THE UNIVERSITY OF READING

Department of Meteorology

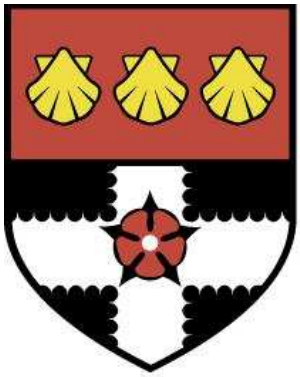

Aircraft Measurements of Saharan Mineral Dust

Claire Louise McConnell

A thesis submitted for the degree of Doctor of Philosophy

February 2009

Declaration

I confirm that this is my own work and the use of all material from other sources has been properly and fully acknowledged.

Claire McConnell

Abstract

Mineral dust is an important component of the Earth's atmosphere, affecting climate through the direct radiative effect and through the deposition of dust to the ocean. Understanding of these processes is limited by a lack of in-situ observations of dust which results in a large uncertainty in the microphysical, optical, chemical and radiative properties of dust.

This thesis presents an analysis of dust measurements obtained during the DODO (Dust Outflow and Deposition to the Ocean) aircraft campaigns which took place in February and August 2006 over West Africa and the tropical East Atlantic Ocean. In-situ and radiative measurements are used to examine the variations in optical, microphysical and radiative properties of the dust in the two seasons. Specific limitations relating to the nephelometer and upper pyranometer are overcome through aircraft, ground-based and model comparisons and appropriate correctional procedures have been applied.

Vertical profiles of dust extinction and size distributions differed between land and ocean areas, and between the dry and wet seasons. Dry season dust was found at low altitudes, whereas wet season dust extended up to $6km$, reflecting the seasonal meteorology.

Measurements of the single scattering albedo for the accumulation mode at $550nm$ are found to range from 0.93 to 0.99. This variation is related to differences in chemical composition and dust sources, but not to changes in the measured size distributions. Optical properties are found to be sensitive to inclusion of coarse mode size distribution measurements.

The range of optical properties observed are modelled in a radiative transfer code in order to investigate their impact on the dust shortwave direct radiative effect. The results are compared to irradiance measurements from the aircraft pyranometers, which have undergone a detailed quality assessment. The range of optical properties cause a difference of up to a factor of five in atmospheric heating, and can alter the sign of the top of atmosphere radiative effect. The variations in the optical properties measured during the campaigns are therefore significant and have implications for accurate dust simulations in models and for satellite retrievals.

Acknowledgements

I would like to say a huge thank you to my supervisor, Ellie Highwood. Firstly, for giving me the opportunity of taking on such an exciting PhD, which gave me the chance to go to Africa not only once, but twice! I have enjoyed every moment of the aircraft campaigns I've been involved in during my PhD. (Well... except for the stomach bug in Dakar!) Secondly, for her continual support and guidance over the past three years, which have made it a pleasure to be working with her. Thanks also to Keith Shine, who managed to find the time to supervise me while Ellie was on maternity leave, which is much appreciated.

A big thanks to Paola Formenti for the use of the dust composition results, for finding funding for me to visit the lab in Paris, and for helpful discussions about the chemistry results. I am grateful for helpful advice and discussions from various Met Office staff: Jim Haywood, Ben Johnson, Simon Osborne and Mark Harrison, with whom discussions over faulty instruments, data processing and dust sources were very useful. Thanks to the members of the radiation group, whose advice and helpful comments on my work has been much appreciated.

The DODO campaigns could never have happened without the energy and commitment of the staff at FAAM and DirectFlight, and the DODO PIs - Ellie, Hugh and Jim, whom I thank. Special thanks go to the BAe-146 pilots, Al and Al, for their expert flying over the Mauritanian desert.

Thanks to the members of the Meteorology Department, especially the PhD students, who have made Reading such a pleasant place to be for the last three years. Thanks to past and present occupants of 2U07 for their help with LaTeX, IDL, unix, and for being great company. A special thanks to the Meteorology frisbee team, who gave me a broken nose in 2007!

I would like to thank my parents, for their commitment to my education since I have been very young, which no doubt helped me to get to where I am now. Finally, thanks to my fianceé, Chris, for helping me to get up at a decent time in the mornings, and for always being there for me.

Contents

Chapter 1

Introduction

1.1 Introduction

Between 1905 to 2006, the Earth's average temperature increased by $0.74°$ (Solomon *et al.*, 2007). This increase in temperature is a response to a perturbation in the energy balance of the Earth-atmosphere system. Two of the most important causes of this perturbation are greenhouse gases, and atmospheric aerosols - small particles suspended in the Earth's atmosphere.

Greenhouse gases act to absorb and emit infrared radiation back towards the Earth's surface, thereby causing a net warming. Aerosols, however, depending on their properties, are able to reflect solar radiation back out to space, causing a cooling, or absorb solar and infrared radiation, which can have a warming effect. These processes are known as the direct aerosol radiative effect. The IPCC 2007 report estimated the direct aerosol radiative effect to be $-0.5 \pm 0.4 Wm^{-2}$, compared to a forcing of $2.63 \pm 0.266 Wm^{-2}$ from greenhouse gases. Anthropogenic aerosols therefore have a significant impact on climate.

Aerosols in the Earth's atmosphere arise from anthropogenic activities, such as combustion of fuels, and include sulphate particles, elemental and organic carbon and nitrate particles. Natural aerosols, such as sea salt, volcanic aerosol and mineral dust are also present in the atmosphere. Mineral dust aerosol consists of solid particles which have been uplifted from arid surfaces and transported by the atmosphere. Eventually they are deposited to the surface, over land or ocean, through wet or dry deposition. North Africa is the dominant global source of dust both in terms of occurrence and intensity (Liu *et al.*, 2008a), supplying around 400-700Tg for atmospheric transport every year (Washington *et al.*, 2003).

The majority of mineral dust is natural aerosol, though models suggest that 5 to 7% of the global dust loading is anthropogenic in origin (Tegen *et al.*, 2004). In the North African region this may increase to 0 to 15% (Yoshioka *et al.*, 2005), where activities such as land use change and overgrazing increase the amount dust which can be uplifted (e.g. Tegen and Fung, 1995).

1.2 Dust in the climate system

The most direct way in which mineral dust can influence global climate is by scattering and absorbing radiation, affecting both regional and global energy balances in the shortwave and longwave spectral regions due to the presence of both sub-micron and super-micron particles. In the shortwave part of the spectrum, dust mainly scatters radiation back to space, but depending on the albedo of the underlying surface, it can either increase (over ocean) or make little difference (over desert) to the total albedo (e.g. Balkanski *et al.*, 2007). The impact in the longwave depends crucially on the surface temperature and the altitude of the dust layer (e.g. Highwood *et al.*, 2003), which may vary with meteorology both within and across seasons.

Other impacts of Saharan dust on the climate system are less well studied and quantified. For example, laboratory studies and field experiments show that dust can act as ice nuclei, so that small concentrations of mineral dust are able to significantly affect cold cloud properties including the radiative properties of cirrus, dehydration of the tropopause and convective cloud dynamics (e.g. Field *et al.*, 2006; DeMott *et al.*, 2003; Richardson *et al.*, 2007).

It has also been hypothesised that dust may provide a surface for heterogeneous chemical reactions to take place. For example, ozone can be destroyed on pure calcium carbonate particles. Salisbury *et al.* (2006) found that daily cycles and absolute concentrations of some oxygenated species were different during dust storms in the MINATROC (Mineral dust aerosol and tropospheric chemistry) project. However, it was impossible to unequivocally attribute this to heterogeneous reactions on the dust itself.

Atmospheric dust also has an impact on ocean biochemistry. Much of the dust leaving the western coast of Africa is deposited in the Atlantic Ocean, where it provides a flux of nutrients such as iron and phosphorus to the ocean. This deposition stimulates nitrogen fixation and relieves iron limitation of phytoplankton activity. The resulting growth of marine biological organisms results in ocean sequestration of carbon dioxide and fluxes of halocarbons, alkynitrate and DMS (dimethyl sulphide) between the atmosphere and ocean (Jickells *et al.*, 2005).

Mineral dust can also play a role in tropical storm development. For example, Jones

et al. (2004) reported indirect observations of the modification of African Easterly Waves by the radiative impacts of dust. Evan *et al.* (2006) showed that mean dust coverage as measured by satellites and tropical cyclone activity are strongly correlated over the North Atlantic. Various mechanisms, including the radiative impact on sea surface temperatures, the alteration of vertical shear and the entrainment of dry dust laden air have been proposed, though none have shown to be the predominant governor of cyclone activity, with sea surface temperatures playing a very large role. The correlation between dust and cyclone activity may stem from them both being driven by a third party, such as Sahelian rainfall from the previous season (e.g. Prospero and Lamb, 2003).

1.3 North African Climatology and Dust Transport

Transport of dust from North Africa varies with season and meteorology. The following sections give an overview of North African climate, and how this affects the seasonal dust uplift and transport.

1.3.1 North African Climate

Tropical climates are, to a large extent, dominated by the movement of the Inter-tropical Convergence Zone (ITCZ) and the associated Hadley circulation. The location of the ITCZ changes throughout the year and is driven by the latitude of most intense solar radiation, which results in deep convection around the ITCZ. As shown in Figure 1.1, the ITCZ is located south of the equator in the northern hemisphere winter, and covers northern Africa in the summer. High levels of precipitation are associated with the deep clouds at the ITCZ, and the precipitation pattern also changes between the summer and winter, as shown in Figure 1.2. Hence the naming of the North African ‘wet’ and ‘dry’ seasons.

The descending part of the Hadley circulation is associated with the subtropical high pressure systems (see Figure 1.3). The location of the centre of the subtropical anticyclones varies with season. The subtropical highs are closest to the equator in winter, and are displaced polewards in summer. The North Atlantic subtropical high, often known as

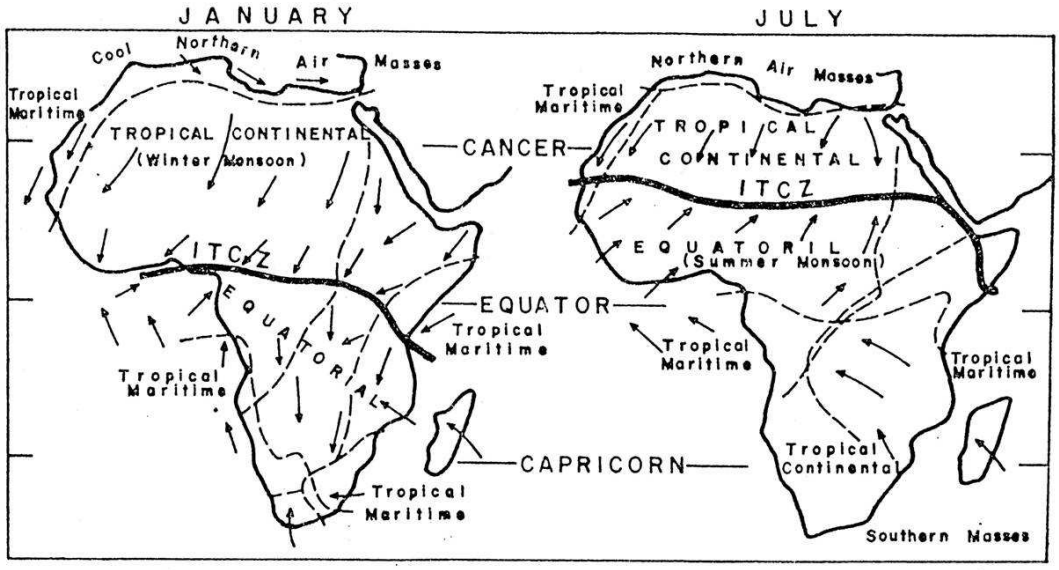

Figure 1.1: *Schematic of mean winds and ITCZ location over Africa in January and July (Das, 1986).*

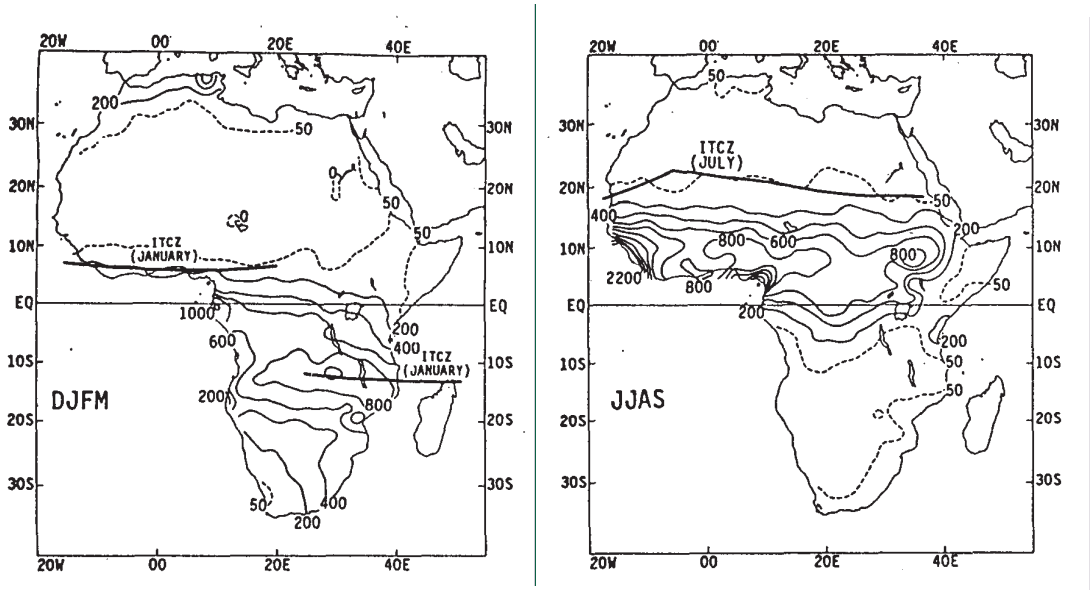

Figure 1.2: *Seasonal rainfall (mm) over Africa during December - March (left) and June - September (right), (Janowiak, 1988).*

the Azores high pressure, shows a northwestward movement during summer, as the ITCZ moves northwards over Africa.

The trade winds constitute the lower-tropospheric equatorward flowing branch of the Hadley circulation. The general pattern is for trade winds to blow from the eastern edges

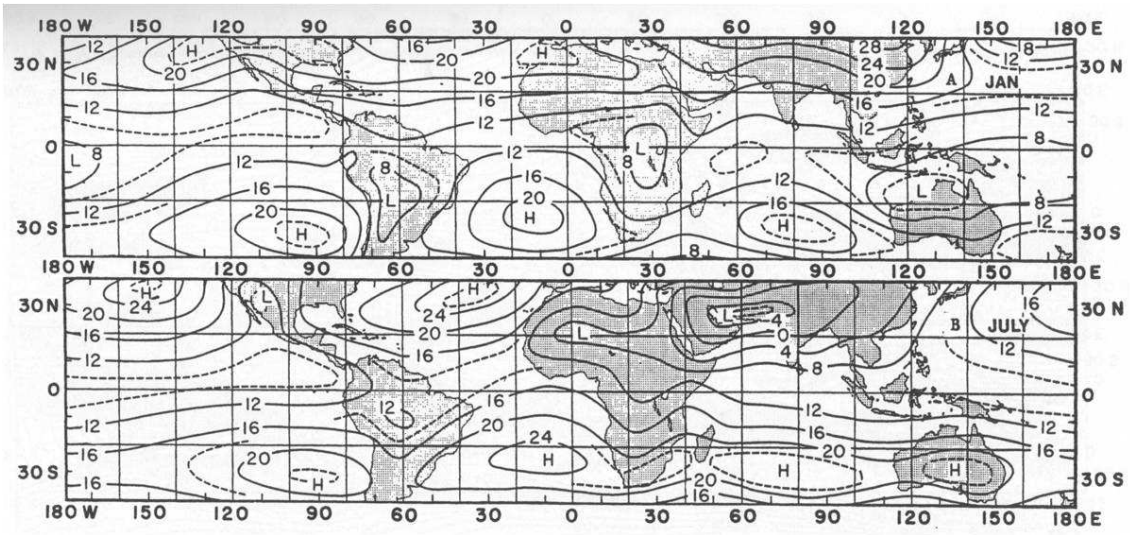

Figure 1.3: *Sea level pressure over the global tropics ($+1000mbar$) (Godbole and Shukla, 1981), during January (top) and July (bottom).*

of subtropical highs towards the southwest (in the northern hemisphere) and towards the ITCZ. During winter, when the subtropical highs are closest to the equator, the meridional pressure gradient is largest, and therefore the trade winds are strongest. In the upstream portion of the trade winds, the flow tends to be subsiding and divergent, resulting in clear skies and low precipitation.

As shown by Figure 1.3, the resulting surface circulation results in north easterly (Harmattan) trade winds over the Sahara, which are particularly strong during the dry season. During the wet season North Africa is subject to more intense convection due to the more northerly location of the ITCZ and more intense solar radiation. Further north, over the Sahara, this is dominated by dry convection, whereas further south this convection will become moister and associated with more precipitation.

During summer, when dry convection over the Sahara is intense, a well-mixed boundary layer can become very deep, extending several kilometres from the surface. As the mid-tropospheric flow is westwards (see Figure 1.3) this dry warm air flows westwards towards the Atlantic, where it is undercut by moister, denser marine air, or the marine boundary layer, and becomes what is known as the Saharan Air Layer (SAL). The boundary between the marine boundary layer and the SAL is characterised by a temperature inversion, which caps any convection resulting from the marine layer. The base of the

SAL is found at altitudes of 1-2km, and the top of the SAL remains at altitudes comparable to the top of the Saharan mixing layer (5-6km) (Carlson and Caverly, 1977). The SAL is transported across the Atlantic over a period of 5-6 days at a typical speed of $8ms^{-1}$, descending as it moves westwards (Carlson and Prospero, 1972).

The African Easterly Jet (AEJ) is found to the south of the SAL, and is an easterly maximum in the mid-troposphere over West Africa throughout the year, but which becomes a more well-defined jet of more than $10ms^{-1}$ from April to November, when it also attains its most poleward position, as shown in Figure 1.4 (Burpee, 1972). The AEJ has a core around $600mb$, is located at around $15°N$, and extends from the Red Sea to the Atlantic Ocean. The AEJ is the result of a positive thermal gradient from the equator towards the Sahara. Instabilities of the AEJ are known as African Easterly Waves (AEWs), have wavelengths of around 2000 to $4000km$, a period of around 3 to 5 days, propagate westwards and are a feature during boreal summer (Hastenrath, 1991). It has been proposed by Carlson and Prospero (1972) that the westward propagation of the SAL results from AEWs crossing the West African coastline.

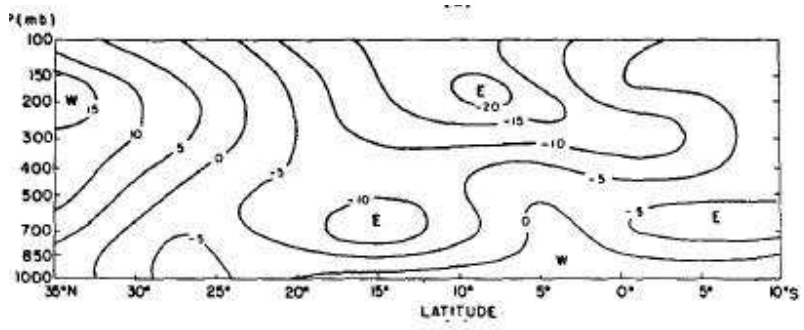

Figure 1.4: *August mean meridional-vertical cross-section of zonal wind component (ms^{-1}) along $5°W$, from Burpee (1972).*

1.3.2 Climate and Dust Transport

Since mineral dust has such wide-ranging impacts on the climate, it is important to be able to understand and predict dust uplift and transport. Dust uplift is governed by soil characteristics and surface windspeeds, the latter having a dependence on meteorology.

As a result of this, dust uplift and transport differ between the North African dry season (November to March) and the wet season (July to September), as shown in the schematic from Stuut *et al.* (2005) in Figure 1.5.

During the dry season dust in North Africa is found mainly at low altitudes (e.g. Chiapello *et al.*, 1995). Uplift can result from strong surface winds along trailing cold fronts associated with low pressure systems passing through the Mediterranean region, and also from northeasterly trade winds (also known as the Harmattan) which are present during the dry season. Factors such as local orography can magnify the dust uplift (e.g. Slingo *et al.*, 2006).

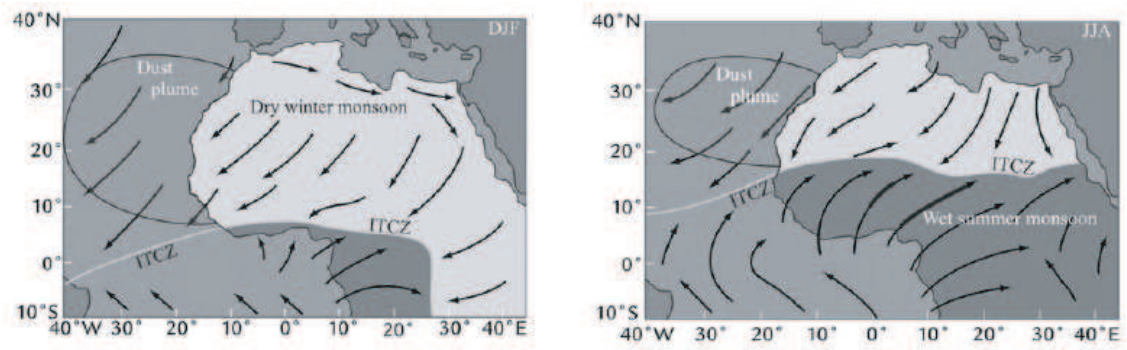

Figure 1.5: *Seasonal variation in latitudinal position of the ITCZ and its consequences for atmospheric conditions over northwestern Africa. Arrows indicate direction of trade winds; dust plumes are indicated by grey shadings. December, January and February are shown on the left, and June, July and August are shown on the right. Figure 2 from Stuut* et al. *(2005).*

During the wet season dust tends to be uplifted by dry and moist convection over the African continent and then transported westwards. Upon reaching the Atlantic Ocean, the dusty air rises above the moist oceanic boundary layer and becomes the Saharan Air Layer (SAL). The SAL is an elevated layer of intensely dry warm air, frequently laden with dust aerosol (Karyampudi *et al.*, 1999).

Recent work has shown that North African dust source regions may vary throughout the year, as the meteorology changes (e.g. Schepanski *et al.*, 2007; Washington *et al.*, 2003; Chiapello *et al.*, 1997). Different source regions appear to respond to different parts of atmospheric dynamics: the activity of the Bodélé Depression in Chad (a major source region for mineral dust) is strongly dependent on the presence and strength of the low level jet (Washington and Todd, 2005; Washington *et al.*, 2006), while dust

production from the western Sahara is more closely related to the degree of low level convergence (Engelstaedter and Washington, 2007b). Differing mineralogy from these different sources may influence the composition, optical properties and the radiative effect of atmospheric dust (e.g. Claquin *et al.*, 1999; Formenti *et al.*, 2008; Highwood *et al.*, 2003).

Satellite measurements of Saharan dust show that transport also varies with season (e.g. Liu *et al.*, 2008a; Herman *et al.*, 1997; Engelstaedter *et al.*, 2006). For example, Liu *et al.* (2008a) showed that in Northern Africa the altitude at which dust was most commonly found varied with season, using space-borne lidar data from 2006-2007. They found dust up to 6km altitude in all seasons, but dust was most frequently found in the 1-2km layer year round, except for December-February when it was most common between 0.2-1km. Of all seasons, winter dust episodes in Northern Africa were the most intense. The observations showed that in spring and summer, the dust layer top was found around 4km, but significant dust still existed up to 6km. During winter the mean dust layer height was 2km, though dust was found up to 4km. They found that in summertime most dust was transported towards North America, predominantly at altitudes above 2km, but that the amount of dust decreased with increasing transport due to deposition and dispersion. Interestingly, they showed that dust concentrations at the lowest altitudes ($< 1km$) did not show significant decreases with westwards transport, indicating that low altitude transport is also important in summer, as well as in winter, and can cover significant distances.

Thus in the different seasons, North African dust is transported by different meteorological mechanisms. The different meteorology may have an effect on determining which dust sources are activated and on whether/how the size distributions change, and will thus have an effect on the optical properties of the dust. Additionally, the differing meteorology means that the vertical profile of the dust will vary between the two seasons (e.g. Karyampudi *et al.*, 1999; Zhu *et al.*, 2007) and this will have an impact on the radiative effect in the longwave, and in the shortwave spectral region if clouds are present (Liao and Seinfeld, 1998). Characterising dust in a range of different meteorological conditions and seasons is therefore very important.

1.3.3 North African Dust Sources

Dust sources are usually associated with topographical lows in arid regions (Prospero *et al.*, 2002). Dust production depends on the available supply of wind-erodible material, usually formed from fluvial erosion followed by subsequent drying and loss or absence of vegetation, which permits small particles to be uplifted into the atmosphere, given high enough windspeeds (Mahowald *et al.*, 2005; Jickells *et al.*, 2005).

Satellite data has frequently been used to identify North African dust source regions (e.g. Prospero *et al.*, 2002; Washington *et al.*, 2003; Engelstaedter and Washington, 2007a; Schepanski *et al.*, 2007). The results indicate numerous sources over both the Sahara and Sahel, some of which appear to have variable emissions over both seasons and years. Some studies have found that most dust is associated with a small number of key preferential source regions (e.g. Herman *et al.*, 1997; Washington *et al.*, 2003; Zhang and Christopher, 2003), an example of which is shown in Figure 1.6. One source of particular importance is the Bodélé Depression, which emits dust all-year round and is likely to be the dominant source of global dust (Washington *et al.*, 2003), being responsible for $6-18\%$ of global dust emissions (Todd *et al.*, 2007). However, as shown in Figure 1.7,the Bodélé Depression is a significant dust source year-round, whereas dust emissions from other smaller, but nonetheless important, dust sources in west Africa appear to be much more variable on a seasonal scale.

The dust emitted from each individual source will be dependent on the parent soil type of the source, and therefore dust emitted from different sources are likely to have differing composition and mineralogy. Direct measurements of soil composition are sparse to non-existent, and therefore other methods have been employed to estimate soil composition. For example, Claquin *et al.* (1999) estimated the mineralogy of North African soils by relating surface mineralogy to classical soil types and found that the fraction of illite, kaolonite, smectite and calcite showed strong north-south variations across the Sahara and Sahel, and that hematite content was particularly high in the Sahel as compared to the rest of the Sahara. Other studies of source mineralogy and composition are mostly based on dust samples measured downwind of sources, which are then traced back to particular geographical regions. For example, Chiapello *et al.* (1997) collected dust samples at Sal,

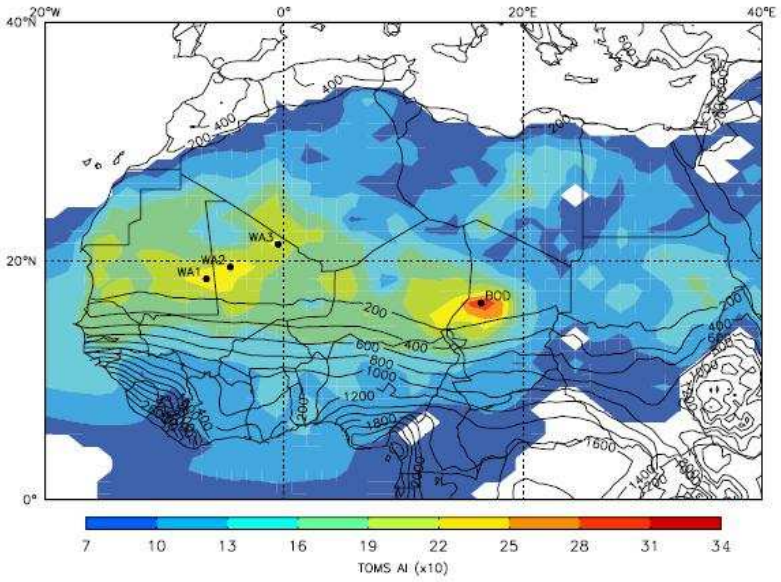

Figure 1.6: *Long term mean (1980-1992) TOMS Aerosol Index over North Africa (colours), precipitation (solid lines) and major dust sources inferred form areas of highest TOMS AI (Figure 1 from Engelstaedter and Washington (2007a)).*

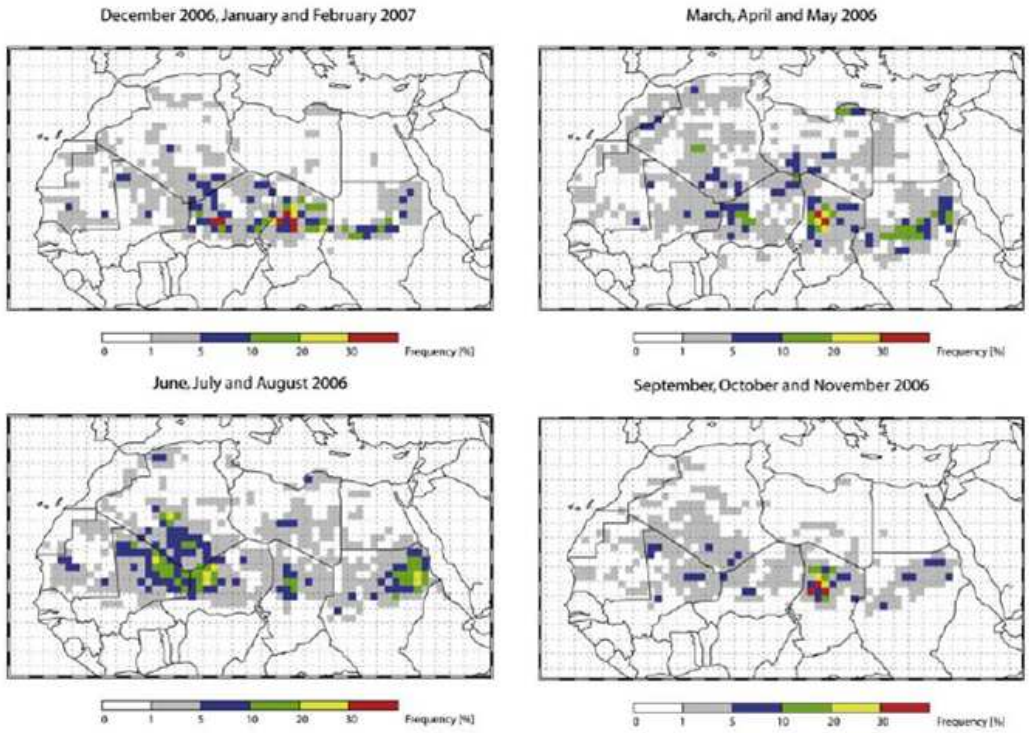

Figure 1.7: *Derived dust sources from SEVIRI MSG IR data by season on a* $1^\circ \times 1^\circ$ *grid. (Figure 1 from Schepanski* et al. *(2007)).*

Cape Verde, and found that as the dust source changed from the Sahel towards the northwest Sahara the calcium content and Si/Al ratio of the samples increased. Caquineau *et al.* (2002) used a combination of ground-based measurements of dust at Cape Verde and Barbados, satellite imagery and back trajectories to show that the illite to kaolonite ratio varied between sources, showing a much higher ratios in the northwest Sahara as compared to the Sahel and eastern Sahara.

Many studies have measured different dust chemistry and/or dust optical properties, which have been traced back to different source regions (e.g. Todd *et al.*, 2007). Kandler *et al.* (2007) found that the amount of calcium within dust sampled at Izaña, Tenerife, was strongly related to the geographical source region indicated by back trajectories, with dust originating from the northern Sahara having a much greater calcium content, a finding corroborated by Formenti *et al.* (2008). Kandler *et al.* (2007) also found that the opposite was true for iron oxide content - dust originating from further south in the Sahara/Sahel had higher iron content. Formenti *et al.* (2008) found that dust originating from the Sahel and Mauritania were enriched in iron oxides in the form of goethite and hematite, in comparison to dust from the Bodélé depression which was iron oxide depleted.

These results all indicate that the mineralogy of dust varies strongly as a function of its source region. Therefore if dust source activity varies seasonally with the dominant meteorology, it is to be expected that the chemistry of dust may also vary seasonally.

1.4 Remote Sensing of Dust

Satellites provide useful information on dust aerosols because of the global nature of their measurements, and their ability to produce data spanning larger time periods than instrumental field campaigns can cover. Previously much knowledge of global dust distribution has been based on passive satellite measurements, such as the Advanced Very High Resolution Radiometer (AVHRR) (Carlson, 1979; Husar *et al.*, 1997), Meteosat (Moulin *et al.*, 1997), Total Ozone Mapping Spectrometer (TOMS) (Prospero *et al.*, 2002), its predecessor, the Ozone Monitoring Instrument (OMI, Torres *et al.* (2007), and the Moderate Resolution Imaging Spectroradiometer (MODIS) (Kaufman *et al.*, 2005). However, these measurements are often limited to making measurements over ocean due to the high

amounts of scattering by highly reflective desert surfaces as compared to that by aerosols, preventing measurements of optical thickness close to dust source regions.

TOMS and OMI are able to make use of measured radiances over desert however, by measuring in the UV spectral region where surface reflectivity is low (Herman *et al.*, 1997; Torres *et al.*, 1998). However, TOMS and OMI measurements are limited because they are strongly affected by the vertical distribution of the aerosol (e.g. Torres *et al.*, 1998; Chiapello *et al.*, 1999; Mahowald *et al.*, 2005) and are also unable to distinguish between dust and biomass burning aerosols (Prospero *et al.*, 2002), which can be a problem in the dry season in West Africa. Passive measurements are also unable to determine the vertical distribution of dust aerosols, which can be important for the radiative effect (Liu *et al.*, 2008a).

The use of multi-angle sensors has also extended the use of single-angle satellite data such as that from MODIS, which can sometimes be unusable due to sun-glint. For example, MISR (Multi-angle Imaging Spectroradiometer) routinely measures global aerosol optical thickness at a resolution of $17.6km$ over land and ocean (Kahn *et al.*, 2007), and does not suffer from sun-glint problems. It has therefore been possible to use MISR data in conjunction with MODIS data to fill in the areas suffering from sun-glint, extending MODIS data coverage by up to 50% (e.g. Kalashnikova and Kahn, 2008). However, the orbit pattern of MISR means that data is available at lower temporal resolution than MODIS data.

Detection of dust over bright surfaces such as deserts is often not possible due to the high surface reflectances, which makes partitioning reflectance between the surface and dust aerosol difficult. However, some progress has been made by using satellite measurements from the blue part of the visible spectrum, where desert surfaces have a much lower reflectance (Hsu *et al.*, 2004). The algorithm of Hsu *et al.* (2004), "Deep Blue," has been applied to MODIS and SeaWIFS (Sea-viewing Wide Field-of-view Sensor) data and allows optical depths over deserts to be calculated.

Developments have also been made in detecting dust over deserts using the infrared part of the spectrum. The SEVIRI (Spinning Enhanced Visible and Infrared Imager) instrument on the Meteosat-8 satellite provides information on dust events in high tem-

poral resolution (Schmetz *et al.*, 2002). Brightness temperature differences are calculated from measurements of narrow band infrared radiances over wavelengths $12.0 - 10.8\mu m$, $10.8 - 8.7\mu m$ and $10.8\mu m$ (Schepanski *et al.*, 2007). The spectral absorption characteristics of dust then allow it to be detected at a temporal resolution of 15 minutes, which is useful in tracking dust storms. The use of infrared radiances also mean that this is possible at night time.

The launch of CALIPSO (Cloud-Aerosol Lidar and Infrared Pathfinder Satellite Observation) in April 2006 (Winker *et al.*, 2007, 2003) carrying the Cloud-Aerosol Lidar with Orthogonal Polarization (CALIOP) has enabled a better understanding of the vertical global and temporal distribution of mineral dust and CALIOP is also able to distinguish between dust and other aerosol types by measuring of the depolarization ration (Sassen, 2000). CALIOP can also detect dust aerosols for any terrestrial surfaces during both day and night (Liu *et al.*, 2008a), and has a vertical resolution of up to $30m$ and horizontal resolution of $1/3km$ below $8.2km$.

Longterm continuous measurements of aerosols have also been achieved through the AERONET (Aerosol Robotic Network) (Holben *et al.*, 1998). AERONET is a worldwide network of ground-based sunphotometers, from which measurements of aerosol optical depth at visible and near infrared wavelengths are available. Retrieval algorithms also allow various other aerosol optical properties and size distributions to be calculated. An advantage of AERONET data with respect to dust measurements is the continuous nature of the measurements, but a sparsity of measurements over deserts where mineral dust is most prevalent.

In summary there has been a large amount of progress in satellite detection and measurement of dust in recent years. Different satellite products benefit and suffer from different issues, though the combination of different satellite products can alleviate this problem. Improvements have also been made in retrieving aerosol properties over deserts, which has previously been problematic. Nevertheless, the use of in-situ measurements, such as examined in this thesis, is vital in order to constrain the optical properties of dust, which are used in satellite retrievals, and to provide opportunities for validation of satellite data for specific case studies.

1.5 Optical Properties of Dust

In order to model the radiative effect of aerosols, it is necessary to know or to be able to calculate their optical properties, which describe how the aerosol particles interact with electromagnetic waves, through scattering and absorption. A brief description of aerosol optical properties is given here, followed by a more detailed review of the estimated values for mineral dust aerosol in the following sections.

1.5.1 Scattering properties of aerosols

When aerosol particles interact with electromagnetic radiation, they are able to scatter this radiation in different directions, or absorb the radiation and re-emit it as thermal energy. The sum of scattering and absorption of this energy is known as extinction, and can be expressed in two ways. The first is in terms of the single-particle extinction cross section, C_{ext} (in m^2), where,

$$C_{ext} = C_{scat} + C_{abs}, \tag{1.1}$$

where C_{scat} and C_{abs} represent the single-particle scattering and absorption cross sections, which is analogous to the shadow the aerosol particle casts on the incident radiation.

The second way the amount of extinction can be expressed is through the dimensionless quantity, Q_{ext}, the extinction efficiency. This is the ratio of the single-particle cross section to the geometric area of the particle, given as

$$Q_{ext} = \frac{C_{ext}}{\pi r^2}, \tag{1.2}$$

where r is the particle radius and Q_{ext} indicates the efficiency of the particle at extinguishing radiation as a function of its size. Q_{scat} and Q_{abs} can be defined similarly.

For a monodisperse sample of aerosols, where there are N particles per cubic metre, the total amount of extinction, or extinction coefficient, can be defined as,

$$\sigma_{ext} = NC_{ext} = \pi r^2 N Q_{ext}, \tag{1.3}$$

where σ_{ext} is measured in m^{-1}. If the aerosol sample is then assumed to be polydispersed,

this then becomes,

$$\sigma_{ext} = \int_{r_{min}}^{r_{max}} \pi r^2 Q_{ext} \frac{dN}{dr} dr, \tag{1.4}$$

where $\frac{dN}{dr}$ is the number of particles per cubic metre in the size range dr, and r_{min} and r_{max} are the minimum and maximum radii that the size distribution covers. σ_{scat} and σ_{abs} can be defined similarly.

The mathematical representation of absorption and scattering of light by spherical aerosol particles with a similar circumference to that of the wavelength of light is described by Mie theory (Bohren and Huffman, 1983). Key parameters that govern the scattering and absorption of light under Mie theory include the wavelength, λ, of the incident radiation, the particle size, frequently expressed as a dimensionless size parameter $\alpha = \frac{2\pi r}{\lambda}$, and the complex refractive index - the optical property of the particle in relation to the surrounding medium, n. It is usually understood that n is given in relation to air, the refractive index of which is almost unity. n is a complex number,

$$n = n_r - n_i i, \tag{1.5}$$

where the real part represents the amount of scattering of energy by a particle, and the imaginary part represents the amount of absorption. Both real and imaginary parts are a function of wavelength. The refractive index of a particle is governed by its chemical composition.

Given the particle size and refractive index, Mie theory can be used to calculate the scattering and absorption properties, Q_{scat} and Q_{abs} of an aerosol population, if the aerosol particles are assumed to be spherical. (Issues arising from non-spherical particles are discussed in Section 1.5.5). In order to calculate irradiances when aerosol is present, three aerosol optical properties, which vary with wavelength, are required:

1. Single Scattering Albedo

   The dimensionless single scattering albedo, ω_0^λ, is the ratio of scattering to extinction of energy, and can be defined as

$$\omega_0^\lambda = \frac{Q_{scat}^\lambda}{Q_{ext}^\lambda} = \frac{C_{scat}^\lambda}{C_{ext}^\lambda} = \frac{\sigma_{scat}^\lambda}{\sigma_{ext}^\lambda}, \tag{1.6}$$

where Q^{λ}_{scat}, C^{λ}_{scat} and σ^{λ}_{scat} are as defined previously in Equations 1.2 and 1.3. Therefore the fraction of light scattered by a particle is ω^{λ}_0, and the fraction absorbed, the co-albedo, is $1 - \omega^{\lambda}_0$. Since the value of ω^{λ}_0 indicates the amount of absorption, and therefore the conversion of light to thermal energy, the value of the single scattering albedo is important in determining the amount of atmospheric heating due to the aerosol. Aerosol particles with a single scattering albedo close to 1 will mostly scatter radiation, whereas particles with lower single scattering albedos will absorb more radiation.

2. Mass Specific Extinction

   The mass specific extinction is the amount of extinction per unit mass of aerosol, usually given in $m^2 g^{-1}$, and indicates how efficient a given mass of aerosol particles are at extinguishing radiation. It is defined as,

$$k^{\lambda}_{ext} = \frac{3Q^{\lambda}_{ext}}{4r\rho_{aer}}, \tag{1.7}$$

   where ρ_{aer} is the density of the aerosol particle, assumed to be $2.65 g cm^{-3}$ (Tegen and Fung, 1995).

3. Phase Function

   The phase function describes the angular distribution of light intensity at a particular angle, θ, given relative to the incident radiation, scattered by a particle at a given wavelength, and normalised by the integral of the scattered intensity over all angles:

$$P(\theta, \alpha, n) = \frac{F(\theta, \alpha, n)}{\int_0^{\pi} F(\theta, \alpha, n) \sin(\theta) d\theta}, \tag{1.8}$$

   where F is is the intensity of the radiation scattered into angle θ, and P is measured in sr^{-1}.

   A more commonly used parameter in two-stream approximations is the asymmetry parameter, g^{λ}, which is the intensity-weighted average of the cosine of the scattering angle:

$$g(\alpha, n) = \frac{1}{2} \int_0^{\pi} \cos(\theta) P(\theta) \sin(\theta) d\theta. \tag{1.9}$$

A value of 1 indicates that radiation is scattered entirely into the forwards direction, whereas a value of -1 indicates that radiation is scattered entirely into the backwards direction. Positive intermediate values indicate that most radiation is scattered forwards, negative values indicate the reverse. If light is scattered isotropically, then $g = 0$.

In terms of the radiative effect of aerosols, the amount of aerosol present in a vertical profile, as well as the amount of extinction caused by the particles, is important. The total amount of extinction due to scattering and absorption caused to incoming radiation at the top of the atmosphere (TOA) due to aerosol particles between the TOA and the surface is defined as the aerosol optical depth (AOD, or τ^{λ}). For a population of polydisperse particles this is defined through aerosol optical properties as,

$$\tau^{\lambda} = \int_{0}^{TOA} \int_{r_{min}}^{r_{max}} \pi r^2 \frac{dN}{dr} Q_{ext}^{\lambda} dr dz = \int_{0}^{TOA} \sigma_{ext}^{\lambda} dz. \tag{1.10}$$

The aerosol optical depth can also be defined using irradiance through the Beer-Lambert law, as,

$$\tau^{\lambda} = ln \left(\frac{I_{SFC}^{clr}}{I_{SFC}^{aer}} \right) \cos(\theta), \tag{1.11}$$

where I is irradiance in Wm^{-2}, SFC indicates the calculation refers to the surface, and θ here is the solar zenith angle. clr and aer indicate the irradiance that would be measured under clear skies (no aerosol present), and with aerosol present. τ^{λ} is therefore the extra extinction that occurs at a particular wavelength due to the presence of aerosol particles.

Additionally another useful parameter to describe aerosol particles is the angstrom exponent, Å, which describes the wavelength dependence of extinction over two wavelengths:

$$\dot{A} = -\frac{log(x_{\lambda_1})/log(x_{\lambda_2})}{log(\lambda_1)/log(\lambda_2)}, \tag{1.12}$$

where x can be τ, σ_{ext} or σ_{scat}. This is useful since scattering and extinction at a particular wavelength tend to be related to the size of a particle - thus if Å is large, it indicates the presence of smaller particles, whereas larger particles will have a smaller, or even negative, value of Å.

1.5.2 Refractive Index of Mineral Dust

1.5.2.1 Real Part

The real part of refractive index, n_r, for Saharan dust is generally better constrained than the imaginary part in the shortwave spectrum. Many studies, such as Shettle and Fenn (1979) and WCP (1983) suggest that n_r^{550} in the visible is 1.53, and is constant over wavelengths 0.2 to $1.0\mu m$. Remote sensing case studies by Tanré *et al.* (2001) and Kaufman *et al.* (2001) have found that using this value leads to consistent results when comparing measurements and model calculations.

However, Dubovik *et al.* (2002) used AERONET (Aerosol Robotic Network) data over a longer period of time (1993-2000) and estimated n_r for Saharan dust to be 1.48 at Cape Verde for optical depths of 0.7 at $440nm$. Laboratory measurements of n_r also deviate from the 1.53 value suggested by WCP (1983) by up to ± 0.05 (e.g. Patterson *et al.*, 1977; Carlson and Benjamin, 1980; Sokolik *et al.*, 1993; Sokolik and Toon, 1999) with measurements by Patterson *et al.* (1977) of n_r ranging from $1.558 - 1.562 \pm 0.004$ at $550nm$.

At least part of this variation is due to the differing mineralogy of samples as well as differences in measurement techniques. Sokolik and Toon (1999) highlighted the effect of mineralogy on the refractive index by showing that based on literature estimates of the most common minerals in dust (except hematite), n_r at $500nm$ varies from 1.49 to 1.7, whereas for hematite n_r varied between 2.8 to 3.3. Despite this uncertainty in n_r, these variations are small in terms of percentages and are thought to be less significant in determining the optical properties of dust than the uncertainties associated with the imaginary part of the refractive index (e.g. Liao and Seinfeld, 1998).

1.5.2.2 Imaginary Part

The value of the imaginary part of the refractive index, n_i, as reported by the literature is much more variable than n_r, showing variations of at least an order of magnitude, and has therefore been the object of much research and discussion.

Calculations of n_i can be divided into two main groups (Sokolik *et al.*, 1993): firstly those based on laboratory analysis of dust samples, and secondly those based on solv-

ing inverse problems using optical and radiative measurements in order to determine the refractive index. Estimates using latter technique are subject to uncertainties relating assumptions of the value of surface albedo, real part of the refractive index and effects of non-spherical dust particles, as well as the averaging of the imaginary part over the atmospheric column (which may contain other aerosol types). The former technique can be separated into two subsections: those using lab techniques to determine the major components of dust samples and then using the known refractive indices of the major components to determine the refractive index, and those using diffuse reflectance methods in the lab to calculate the refractive index. Problems with the latter laboratory technique include factors such as the treatment of samples in order to analyse them.

The most commonly used values of n_i at visible wavelengths for Saharan dust originate from work by Patterson *et al.* (1977), who used lab measurements of diffuse reflectance of dust samples collected at various locations including Tenerife (Canary Islands), Sal (Cape Verde Islands), Barbados, and from a research vessel located at $17°N$, $26°W$. They found similar refractive indices for all sites, with the imaginary part decreasing from $0.025i$ at $300nm$ to $0.0038i$ at $600nm$, with a value of around $0.005i$ at $550nm$. Errors in the value of n_i were estimated to be 40%. Similar laboratory measurements of n_i have been made by Lindberg and Laude (1974); Levin *et al.* (1980) for dust samples from other parts of the world, who found that the value of n_i at 550nm varied between 0.004 to $0.007i$, values in agreement with those of Patterson *et al.* (1977).

Other early estimates of the refractive index were made by Carlson and Caverly (1977) who combined Mie code simulations with ground-based measurements of direct and diffuse radiation with aircraft measurements of size distributions at Sal, Cape Verde, in order to constrain the imaginary part of the refractive index when the real part was assumed to be 1.54. The refractive indices of Carlson and Caverly (1977) of $0.018i$, $0.008i$ and $0.0029i$ at wavelengths of 0.375, 0.468 and $0.610\mu m$ were found to agree very well with those from Patterson *et al.* (1977) within the experimental errors of both studies.

Both these studies indicated significant absorption at visible wavelengths by Saharan mineral dust, and subsequent modelling studies assigned spectral refractive indices accordingly, such as Shettle and Fenn (1979); WCP (1983); d'Almeida *et al.* (1991); Hess

et al. (1998). For example, Shettle and Fenn (1979) and WCP (1983) used a constant imaginary part of the refractive index of $0.008i$ at visible wavelengths (see Figure 1.8). Carlson and Benjamin (1980) included spectral variations of n_i at visible wavelengths, using refractive indices of $1.56 - 0.018i$, $1.54 - 0.008i$, $1.54 - 0.0029i$ and $1.58 - 0.002i$ for the spectral bands $0.32 - 0.42\mu m$, $0.4 - 0.53\mu m$, $0.53 - 0.69\mu m$ and $0.69 - 4\mu m$, respectively.

Various n_i values from the literature have been collated by numerous studies, including Otto *et al.* (2007), as shown in Figure 1.8. They used values of n_i at visible wavelengths from the literature (from Sokolik *et al.* (1993); Patterson *et al.* (1977); Carlson and Benjamin (1980), dotted red lines in Figure 1.8) to compute a spectrally varying average imaginary refractive index (thick red line in Figure 1.8) which resulted in a value of $0.006i$ at $550nm$. Figure 1.8 also clearly shows that most experiments have found dust to be significantly more absorbing in the UV and lower visible wavelengths, with n_i decreasing significantly between $0.3\mu m$ to $0.7\mu m$ (e.g. Carlson and Caverly, 1977; Patterson *et al.*, 1977; Sokolik and Toon, 1999; Dubovik *et al.*, 2002; Yoshida and Murakami, 2008).

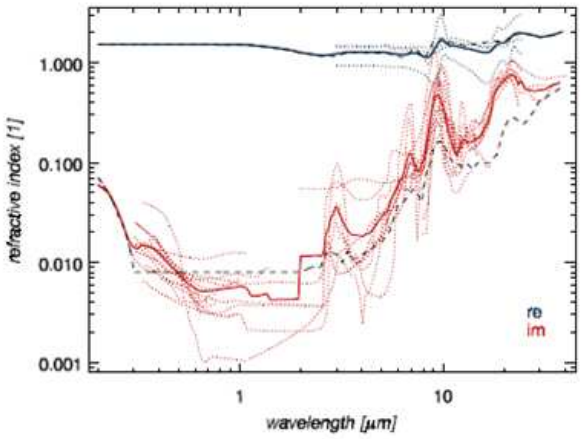

Figure 1.8: *Figure 4 from Otto* et al. *(2007), showing compiled refractive indices from the literature (dotted red lines), and a spectrally varying average of these estimates (solid red line). The black dashed line represents the 'dust-like' refractive index from Shettle and Fenn (1979) and WCP (1983). Values at visible wavelengths from the literature come from Sokolik* et al. *(1993), who compiled various measurements of n_i from around the world, Patterson* et al. *(1977) who measured n_i for Saharan dust and Carlson and Benjamin (1980) who based refractive indices on Carlson and Caverly (1977).*

Estimates of refractive indices from aircraft measurements and remote sensing tech-

niques have suggested significantly less absorption by dust. For example, estimates of n_i from Saharan dust at the Cape Verde AERONET station suggest values of $0.0025i$ and $0.0007i$ at wavelengths of $440nm$ and $670nm$ (Dubovik *et al.*, 2002), with uncertainties of $\pm 50\%$ (Balkanski *et al.*, 2007). These estimates are in agreement with those from Tanré *et al.* (2001) and Kaufman *et al.* (2001) who used AERONET and Landsat satellite data to estimate n_i values. Low values of n_i of $0.003i$ were also found by Levin *et al.* (1980) for a dust storm in Israel by using measurements of size distribution and optical depth, and of $0.001i$ by Otterman *et al.* (1982) using satellite data from Landsat. Aircraft measurements of Saharan dust also indicate much lower absorption of dust, with estimates of $0.0015i$ for n_i at 550nm (Haywood *et al.*, 2003) using size distribution, absorption, scattering and radiometric measurements. Other aircraft studies of mineral dust have found similar values of n_i, for example, Osborne *et al.* (2008) estimated n_i to be $0.0004i$ at $550nm$.

Another approach has been to calculate a bulk refractive index by analysing dust samples for chemical composition, and calculating an overall refractive index based on the volume fraction of various minerals present and their individual refractive indices. For example, using this technique Ivlev and Andreev (1986) found an imaginary refractive index of $0.004i$ at $550nm$. Methods used by Kandler *et al.* (2007), Otto *et al.* (2007) and Otto *et al.* (2009) were similar to this. Kandler *et al.* (2007) made in-situ cascade impactor measurements of Saharan dust at Izaña, Tenerife, and using single particle mineralogy from SEM and TEM analysis and attributed refractive indices based on values for each species based on literature values, estimated the refractive index to be $1.59-0.009i$. Using polar photometry on the same technique led to an estimate of the imaginary part of $0.007i$ at $700nm$. Kandler *et al.* (2007) also showed that composition can change with dust particle size, and calculated their refractive index as a function of particle size, finding that the real part decreased slightly with size for particles larger than $2\mu m$ diameter due to the decreasing amounts of iron oxides, whereas for all particles of sizes between $0.15-10\mu m$ the value of n_i decreased with increasing diameter due to the greater abundance of soot and iron oxides in the smaller particles. Otto *et al.* (2007) used a similar technique for aircraft samples of dust from Morocco and found the opposite: that for particles sized below $0.5\mu m$ diameter the value of n_i was very low due to large amounts of sulphate

present in these size ranges. For extremely large particles of diameter greater than $50\mu m$ they also found low values of n_i due to greater volume fractions of quartz. However, they found much less variation in refractive index for particles sized between $0.5\mu m$ and $50\mu m$ diameter.

Other studies have highlighted the importance of differing mineralogy as well as different measurement techniques in determining the refractive index of dust (Sokolik *et al.*, 1993), since mineral dust can be a complicated mixture of various minerals, with varying optical properties and abundances which can change with dust source, mobilisation processes, and chemical and physical transformation during atmospheric transport (Sokolik and Toon, 1999). For example, Sokolik and Toon (1999) showed that for the most common minerals in dust (except hematite), n_i varies from $0.000075i$ to $0.001i$, whereas hematite was much more absorbing with n_i of $0.9i$. Their results also showed that dust can be much more strongly absorbing when hematite is attached to dust particles in the form of aggregates rather than as an external mixture, further complicating techniques to estimate refractive indices. The complexity of calculating the absorption of dust has been further examined by Lafon *et al.* (2006) who showed that significant differences in single scattering albedo can be caused by differing amounts of free iron contained within dust, as opposed to just the amount of iron oxide present.

Further intricacies have been found by Lafon *et al.* (2006), who found that n_i was different for hematite and goethite, both in terms of magnitude and spectral dependence. Thus the single scattering albedo was strongly affected, though the mass specific extinction coefficient was not. They point out that retrievals of single scattering albedo from optical depth or extinction measurements are unlikely to give satisfactory results due to the different sensitivities of k_{ext} and single scattering albedo to iron oxides. They also found that coarse aggregates had much lower single scattering albedos compared to fine aggregates, due to the size difference as well as coarse aggregates containing more iron oxides than fine ones (contrary to the findings of Kandler *et al.* (2007)). Lafon *et al.* (2006) suggest that transported dust, with preferentially removed larger particles, will therefore have higher single scattering albedo values.

Thus despite many measurements and estimates of the imaginary part of the refrac-

tive index over the past thirty years, there is still much uncertainty over the magnitude and spectral variation of the refractive index, with estimates at $550nm$ varying between $0.0004i$ to $0.01i$, an uncertainty of nearly two orders of magnitude. Nevertheless, some of this variation may be due to variations in composition and mixing state of different samples, and it is also possible that the different techniques used contribute to this range. There is a clear need for a better understanding of the variations observed in the value of n_i.

1.5.3 Size Distribution of Mineral Dust

In modelling studies aerosol particles are often represented by lognormal size distributions (e.g. d'Almeida *et al.*, 1991). This is convenient since it allows a mathematical function to describe the aerosol distribution, rather than many specific numeric values. Lognormal functions are regularly used to represent atmospheric aerosols since they represent the shapes of well observed ambient aerosol size distributions (Seinfeld and Pandis, 2006). The lognormal size distribution is defined as,

$$\frac{dN}{dr} = \frac{N_{tot}}{(2\pi)^{1/2} r \ln \sigma_g} exp\left(-\frac{(\ln r - \ln r_g)^2}{2(\ln \sigma_g)^2}\right). \tag{1.13}$$

Therefore three key parameters govern the characteristics of the lognormal size distribution, which are r_g, the median radius, σ_g, the geometric standard deviation, and N_{tot}, the total aerosol number concentration. Aerosol size distributions can be defined by a single lognormal mode, or a combination of several (Seinfeld and Pandis, 2006). Lognormal size distributions can also be given in terms of surface area, volume and mass, which may result in different values of r_g for the same size distribution.

Another common way of describing aerosol size distributions is through a single parameter, the effective radius (r_{eff}), where,

$$r_{eff} = \frac{\int r^3 \frac{dN}{dr} dr}{\int r^2 \frac{dN}{dr} dr}, \tag{1.14}$$

which allows a straightforward comparison of different measurements.

Dust, unlike most aerosol species, is composed of both sub-micron and super-micron

diameter particles, comprising an accumulation mode containing particles with diameters between around 0.1 to $1-3\mu m$ (e.g. Todd *et al.*, 2007; Fouquart *et al.*, 1987a), and a coarse mode containing particles of diameter between around $1-3\mu m$ and extending up to $100\mu m$ (e.g. D'Almeida and Schtz, 1983; Reid *et al.*, 2003b). The diameter used to separate the two modes varies between studies and is often chosen to separate different aerosol types; for example, Dubovik *et al.* (2002) separate the accumulation and coarse modes at a diameter of $1.2\mu m$, Kaufman *et al.* (2005) used a diameter of $1\mu m$, and Johnson *et al.* (2008) used a diameter of $0.7\mu m$. In terms of mass loadings the coarse mode is found to be more dominant, which is important to aerosol optical depth and deposition of nutrients to the ocean, whereas in terms of particle number different studies find the accumulation mode of varying importance.

The median radius and effective radius of the coarse mode for dust are typically found to be between $1-2\mu m$ by observational studies; for example Dubovik *et al.* (2002) found AERONET derived volume median radii at Cape Verde to be $0.12\mu m$ and $1.9\mu m$ for the fine and coarse modes respectively. Todd *et al.* (2007) found an effective radius of $1.66\mu m$ and median radius of $1.9\mu m$. Measurements of Saharan dust by Haywood *et al.* (2001); Li-Jones and Prospero (1998); Arimoto *et al.* (1997) found the maxima in volume size distributions to range from 1 to $5\mu m$. Dust size distributions with smaller particles were measured by Maring *et al.* (2000), who found median number radii of around $0.1\mu m$ and less, corresponding to a volume mean radius of less than $1\mu m$. Thus it appears that there is some convergence of size distribution measurements, but a large degree of variability is still evident.

Presence of accumulation mode dust particles are extremely important as it is the submicron particles that interact most strongly with solar radiation; for example, Tegen and Lacis (1996) found that the most optically effective particles were in the size range of $0.3-1\mu m$, and that the size distribution is very important in determining the optical properties of dust. Recent studies have highlighted the importance of the coarse mode in terms of optical properties, in that the presence of a larger coarse mode can strongly affect the single scattering albedo at visible wavelengths (e.g. Otto *et al.*, 2007). The amount of coarse mode present is also important in determining the amount of absorption in the

infrared (Tegen and Lacis, 1996). Todd *et al.* (2007) found that aerosol optical depth changes in the Bodélé Depression, Chad, were related to large changes in the amount of coarse mode particles, as well as a shift in the modal radius.

Considering the importance of dust size distribution to both deposition of dust to the ocean and to optical properties, it is of interest to know whether the size distribution of dust changes during transport. Gravitational settling predicts that larger, heavier particles should be deposited on shorter timescales than smaller particles (e.g. Maring *et al.*, 2003a), and therefore large changes in the coarse mode size distribution may be expected with dust transport. Some studies support this, for example, satellite retrievals from AIRS (Atmospheric Infrared Sounder) have show that the coarse mode effective radius of Saharan dust decreased from $2.4\mu m$ to $2\mu m$ during transport from the west coast of Africa to around $50°W$ during April to June 2003 (Pierangelo *et al.*, 2005). Satellite data such as that from CALIPSO (Liu *et al.*, 2008b), MODIS (Remer and Kaufman, 2006),AVHRR and TOMS (Cakmur *et al.*, 2001) consistently show that dust optical depth decreases towards the west with distance from the Sahara, showing that the amount of dust present in the atmosphere is certainly decreasing with transport. CALIPSO lidar data also shows that properties such as the ratio of dust optical depth and backscatter at 1064 to $532nm$, and lidar ratios (the ratio of backscatter at $180°$ to extinction) change during transport, indicating that changes in either composition and/or size distribution are occurring (Liu *et al.*, 2008b) .

However, other studies have found little change in the coarse mode size distribution with transport, such as Reid *et al.* (2008). Maring *et al.* (2003a) found that dust particles smaller than $7.3\mu m$ are not preferentially removed during transport, and the size distribution remains largely unchanged for smaller dust particles, based on measurements over both the Canary Islands and over Puerto Rico. Studies using lidar data to analyse the vertical distribution of dust (e.g. Berthier *et al.*, 2006; Liu *et al.*, 2008b) therefore assume that size distribution is constant in the vertical which means that the lidar ratio and the ratio of backscatter at 1064 to $532nm$ remain constant. The accumulation mode size distribution is also thought not to change significantly during transport over short distances (Tegen and Lacis, 1996).

Additionally Maring *et al.* (2003b) and Reid *et al.* (2002) found dust size distributions to show only a small height dependence. However, this is not in keeping with the modelling study of Tegen and Lacis (1996), who used a height dependent size distributions where the number distribution decreased in magnitude and mean radius between pressures of 950, 470 and $40mbar$, due to gravitational settling of larger particles and their inability to be lifted up to greater altitudes.

1.5.4 Optical Properties of Mineral Dust

Estimation of the true optical properties of dust is complicated due to the dependence of optical properties on factors such as size distribution, refractive index (determined by chemical composition and mixing state) and particle shape, all of which may vary over time and space. It is therefore perhaps not surprising that the optical properties of dust reported in the literature cover a large range of values.

Table 1.1 shows results of optical properties at particular wavelengths measured during several prominent field campaigns based in the North Africa. Table 1.2 gives details of optical properties of dust estimated through other techniques, mostly remote sensing by ground-based instruments and satellites. It is clear that the measurements and estimates of the optical properties are highly variable between different studies; for example, values of single scattering albedo shown in Table 1.1 from measurements range from 0.76 to 0.99 at $550nm$. The range in these estimates of single scattering albedo values for dust is enough to cause either a positive or negative direct radiative forcing (Sokolik and Toon, 1996). Forster *et al.* (2007) estimate the single scattering albedo of global dust to be in the range of $0.9 - 0.99$ with a central global estimate of 0.96 at $670nm$. However, long term AERONET studies suggest that Saharan dust is less absorbing than dust from other parts of the world, with single scattering albedo values of 0.98 at $670nm$ (see Table 1.2) as opposed to values ranging from 0.95 to 0.97 for other parts of the world (Dubovik *et al.*, 2002).

Many initial calculations of the single scattering albedo of North African dust were modelling studies based on the refractive indices of Patterson *et al.* (1977). These studies used various size distributions combined with Mie scattering code and the resulting single

ω_0	g	k_{ext}	λ	Size Range	Campaign, year	Location	Comment	Reference
0.900-0.961	n/a	1.21-0.93	550nm	$< 10\mu m$	NAMMA, Sept 2006	Sal, Cape Verde	Ground-based measurements of size distribution, scattering and absorption	Jeong *et al.* (2008)
0.79	0.79	n/a	$532nm$	AM+CM	SAMUM, May 2006	Morocco	Aircraft measurements of size distribution & ground/aircraft radiometric measurements	Otto *et al.* (2009)
0.99 ± 0.02	0.71	0.76	$550nm$	AM	DABEX, Jan 2006	Niger	Aircraft measurements of scattering and absorption	Osborne *et al.* (2008)
0.98	0.75	0.33	$550nm$	AM+CM	DABEX, Jan 2006	Niger	Aircraft measurements of size distributions, scattering and absorption	Osborne *et al.* (2008)
$0.945 - 0.955$	$0.74 - 0.81$	n/a	"solar wavelengths"	AM+CM	Jul-Aug 2005	Izaña, Tenerife	Ground-based chemical measurements at 2367m asl analysed with polar photometry	Kandler *et al.* (2007)
0.969/0.986	n/a	n/a	$440/670nm$	AM+CM	BODEX, Feb-Mar 2005	Bodélé Depression, Chad	Cimel data with AERONET retrieval algorithms	Todd *et al.* (2007)
0.76	0.81	n/a	$550nm$	AM+CM	ACE2, July 1997	Canary Islands	Aircraft measurements of size distribution	Otto *et al.* (2007)
0.97 ± 0.02	0.72	0.7	$550nm$	AM	SHADE, Sept 2000	Tropical East Atlantic	Aircraft measurements of scattering and absorption	Haywood *et al.* (2003)
0.95	0.74	0.42	$550nm$	AM+CM	SHADE, Sept 2000	Tropical East Atlantic	Aircraft measurements of size distributions, scattering and absorption	Haywood *et al.* (2003)
0.95	0.66	n/a	$0.3 - 2.8\mu m$	AM+CM	ECLATS, Nov-Dec 1980	Niamey, Niger	Aircraft measurements of size distribution & ground/aircraft radiometric measurements, refractive indices based on Carlson and Caverly (1977)	Fouquart *et al.* (1987b)
0.86	0.78	1.0	$530 - 690nm$	$0.2 - 2.4\mu m$	GATE, 1974	Sal, Cape Verde	Measurements of size distribution and refractive indices from Carlson and Caverly (1977)	Carlson and Benjamin (1980)

Table 1.1: *Results from major recent field campaigns where measurements of optical properties of North African dust in the solar spectral region have been performed. AM = accumulation mode, CM = coarse mode. Sizes refer to diameter.*

ω_0	g	k_{ext}, m^2g^{-1}	λ	Location, year	Technique	Reference
0.912/0.976			412/550nm	$10-35°N$, $20°W-30°E$, May-Aug 2003-2006	MODIS data	Yoshida and Murakami (2008)
0.93/0.98	0.73/0.71		440/670nm	Capo Verde, 1993-2000	AERONET	Dubovik *et al.* (2002)
0.94/0.95	n/a	n/a	440/670nm	Capo Verde, 1994-1996	AERONET	Tanré *et al.* (2001)
0.93/0.96	n/a	n/a	440/670nm	Banizoumbou, 1996-1997	AERONET	Tanré *et al.* (2001)
0.97 ± 0.02	n/a	n/a	670nm	Capo Verde, June-Aug 1999 and Tropical North Atlantic Ocean, April 1987	AERONET and Landsat	Kaufman *et al.* (2001)
0.837	0.775	0.37	550nm	n/a	Model study	Hess et al., 1998
$0.95-1.0(0.57-6.3)$	$0.65-0.8$		$0.2-2.5\mu m$	n/a	Refractive indices from literature and modelling of different minerals	Sokolik and Toon (1999)

Table 1.2: *Estimates of dust optical properties from selected remote sensing and modelling studies. For the Sokolik and Toon (1999) data, the value in brackets represents hematite and other values represent a range of size distributions tested for individual minerals rather than a dust mixture.*

scattering albedo values were low, suggesting large absorption by Saharan dust, ranging from 0.63 to 0.89 at $550nm$ (Shettle and Fenn, 1979; WCP, 1983; Koepke *et al.*, 1997; Hess *et al.*, 1998). This range of results highlights firstly the possible absorbing nature of Saharan dust, and secondly the importance of the size distribution in determining the single scattering albedo, since despite these studies using very similar refractive indices, the single scattering albedo results were very different.

Over recent years developments in remote sensing techniques have allowed more estimates of aerosol optical properties, as well as estimates of dust single scattering albedo from data over larger geographical regions and longer timescales. Tanré *et al.* (2001); Kaufman *et al.* (2001); Dubovik *et al.* (2002) used AERONET data to derive high values of single scattering albedo indicating that dust was much less absorbing than previous calculations had shown, from values of 0.93 to 0.94 at $440nm$ (Tanré *et al.*, 2001; Dubovik *et al.*, 2002) to values between 0.95 to 0.98 at $670nm$ (Tanré *et al.*, 2001; Kaufman *et al.*, 2001; Dubovik *et al.*, 2002). Yoshida and Murakami (2008) analysed MODIS data and found high values of single scattering albedo (0.912, 0.976 at wavelengths of 412, $550nm$) over the entire Sahara during 2003-2006 over May-Aug. It should be noted, however, that satellite and AERONET retrievals have errors and assumptions associated with them - for example, since AERONET uncertainties in retrievals of ω_0, g and k_{ext} are high for aerosol optical depths below 0.2, Dubovik *et al.* (2002) discount data from these days. Additionally, non-sampling on cloudy days may create a bias in the results.

The recent estimates of high single scattering albedo values for Saharan dust are mostly backed up by in-situ aircraft and ground-based measurements, as shown in Table 1.1. The most direct measurements of the single scattering albedo come from measurements of scattering and absorption, such as the aircraft measurements of Haywood *et al.* (2003) and Osborne *et al.* (2008). These campaigns find single scattering albedo values of 0.97 and 0.99 at $550nm$ respectively, for the accumulation mode, since aircraft instrument inlets cut-off particles with larger diameters. Table 1.1 shows that these studies find a small decrease in ω_0 when the coarse mode size distribution is included through Mie calculations, though this requires an assumption of the refractive index. Jeong *et al.* (2008) made direct measurements of the single scattering albedo at Sal, Cape Verde, and

found values ranging from 0.9 to 0.96 once the effect of sea salt aerosol particles had been removed from the data.

Various other field campaigns and modelling efforts have measured the size distribution of Saharan dust, and combined this with either estimates of the refractive index from the literature or from chemical composition measurements in order to calculate optical properties using Mie scattering code, such as Carlson and Benjamin (1980); Fouquart *et al.* (1987b); Otto *et al.* (2007, 2009), as shown in Table 1.1. Values of ω_0 from this methodology suggest that dust has a more absorbing nature, with ω_0 values ranging from 0.76 to 0.95. Though these studies include the optical effects of the full size distribution, no measurements of scattering and absorption were made to give direct measurements of the single scattering albedo. Finally, the methodology of Kandler *et al.* (2007) differs from the other calculations described, since polar aerosol photometry was used directly on filter samples to calculate optical properties, including ω_0 , which was estimated to be 0.95.

Note that though the Tables 1.1 and 1.2 give values of single scattering albedo at particular wavelengths, for modelling studies it is necessary to know the full spectral variation. As described in Section 1.5.2.2, most measurements show that dust is much more absorbing in UV wavelengths than in the visible to near infrared (NIR), with n_i decreasing from the UV into the visible. This is reflected in spectral measurements and modelling estimates of ω_0 , with higher single scattering albedo values at larger wavelengths. For example, Dubovik *et al.* (2002) found ω_0 to increase from 0.93 to 0.99 over wavelengths of 440 to $1020nm$ from AERONET retrievals at Cape Verde, and Otto *et al.* (2007) showed that ω_0 increased from around 0.7 at $200nm$ to around 0.97 at $700nm$ (exact values are dependent on the size distribution used), based on refractive indices from the literature shown in Figure 1.8.

It is clear from the literature that there is a wide range of measurements and calculations of single scattering albedo at visible wavelengths. Though part of this range may be due to different measurement techniques being used, it is also possible that some variation is due to changes in size distribution and chemical composition (hence refractive index) of dust in time and space.

Tegen and Lacis (1996) showed that size distribution is very important in determining the optical properties of dust. They used refractive indices from Patterson *et al.* (1977) and varied the effective radius of their size distributions from 0.1 to $9\mu m$, and showed that the extinction efficiency in solar wavelengths was highly dependent on particle size, and that as particle size increased the single scattering albedo decreased, from around 0.95 to 0.65 at $550nm$. In contrast, Sokolik and Toon (1996) estimated that uncertainties in k_{ext} stem mainly from uncertainties in the refractive index, which resulted in values ranging from $0.2 - 2m^2g^{-1}$.

Likewise, the composition (and hence refractive index) strongly influences optical properties. Studies such as Claquin *et al.* (1998, 1999); Sokolik and Toon (1999) emphasise that the way hematite is mixed with quartz or clay is complicated and strongly impacts the resulting absorption. This means that if different source locations are composed of different minerals, and dust transported from different sources is representative of the original source, the resulting optical properties will differ. For example, Todd *et al.* (2007) found that dust transported from the Ennendi region to the east of the Bodélé depression had single scattering albedos around 0.91 at $440nm$, compared to the much higher values of around 0.97 of dust being uplifted from the Bodélé Depression itself. Jeong *et al.* (2008) also found significantly different single scattering albedos of dust (0.9 and 0.96) originating from different source regions in North Africa.

Sokolik and Toon (1999) demonstrate that since the optical properties of the different minerals are very different, the overall properties of a particular dust sample depends strongly on the relative abundance of each mineral. This can have an effect on the magnitude of single scattering albedo and k_{ext} and therefore the optical depth, particularly in large dust loadings. Sokolik and Toon (1999) illustrated that for external mixtures an increase in the proportion of hematite from 0 to 20% for a particular size distribution results in a decrease of the single scattering albedo from over 0.98 to below 0.92. They show that 20% is very high for hematite concentrations, and therefore conclude that values of single scattering albedo as low as 0.8 at $500nm$, as results from using refractive indices from Patterson *et al.* (1977), must be either incorrect, or that the mixing of hematite was not in an external mixture.

Sokolik and Toon (1999) show that when hematite is aggregated with quartz or clay (rather than being an external mixture), this type of mixing can cause much lower single scattering albedos. They found that when hematite was aggregated to clays (1% hematite, 99% kaolonite), single scattering albedo values at $550nm$ were 0.83 to 0.89, in contrast to single scattering albedo of 0.98 for an external mixture. Thus knowing whether hematite is present as an external or aggregated mixture is crucial for calculating the radiative effect of dust. Lafon *et al.* (2006) demonstrate that goethite is also an important iron oxide for optical properties, but is included in studies less often than hematite due to a lack of data availability. Lafon *et al.* (2006) examined optical properties of dust samples based on their mineralogy, and found significantly higher single scattering albedo values to those calculated using refractive indices of Patterson *et al.* (1977).

Sokolik *et al.* (1993) showed that a spread in n_i ranging from $0.003 - 0.009i$ can alter the value of ω_0 of by up to 0.15, and g by up to 0.5 at visible wavelengths for an assumed size distribution. Therefore an increased range of n_i from $0.01i$ to $0.0004i$, as described in Section 1.5.2.2 considerably increases the range of optical properties that could be expected for a particular size distribution, intensifying the problem of representing the optical properties of mineral dust.

In summary, the calculation of the optical properties of dust based on refractive indices is complex. Refractive indices of dust can vary with source, chemical composition and mixing state, with a strong dependence on the amount of absorbing iron oxide present. Additionally the size distribution can have a large effect on the optical properties, which is further complicated since various studies disagree on the amount of change in size distribution for different sources, transport distances and transport altitudes.

1.5.5 Morphology of Mineral Dust

Section 1.5.1 described the procedure for calculating optical properties of aerosols, given spherical particles. While this may be a good assumption for many aerosol types, mineral dust has frequently been found to be composed of non-spherical particles (e.g. Reid *et al.*, 2003b; Kandler *et al.*, 2007; Otto *et al.*, 2009; Chou *et al.*, 2008), which are usually cylindrical, or oblate or prolate spheroids.

Non-spherical particles can result in different optical properties, particularly in the direction of the scattered radiation, or the phase function (e.g. Mishchenko *et al.*, 1997). However, if the phase function is then integrated over hemispheres, differences in the shape of the phase function in determining g become less important. Additionally, if irradiances (rather than radiances) are being modelled, errors due to spherical assumptions will be smaller, on the order of a few percent (Mishchenko, 1993; Mishchenko *et al.*, 1995; Liao and Seinfeld, 1998).

However, in contrast, results for a SAMUM case study from Otto *et al.* (2009) show that non-spherical particles significantly impact radiances, particularly in the back-scattering direction, and that optical depths and the asymmetry parameter were in error by 3.5% and 4% respectively if spherical particles were assumed (though single scattering albedos were only affected by up to 1%).

1.6 Radiative Effect of Dust

The aerosol (or dust) direct radiative effect is a measure of the perturbation to the Earth's energy balance due to the presence of an aerosol. It is defined as the change in net (defined as downwards minus upwards) irradiance (shortwave and longwave) at the top of the atmosphere due to the presence of an aerosol (Forster *et al.*, 2007). The perturbation in the energy balance is frequently defined as "radiative forcing" for anthropogenic aerosols. Since dust is at least in part a natural aerosol, the term "radiative effect" is used (e.g. Haywood *et al.*, 2003).

Atmospheric dust can result in both a shortwave and longwave radiative effect due to the presence of both sub and supermicron particles. In the shortwave spectrum, dust can cause either a cooling or a warming of the Earth-atmosphere system depending on surface albedo and dust optical properties (Balkanski *et al.*, 2007). In the longwave dust causes a positive radiative effect as it emits radiation back towards the surface (Highwood *et al.*, 2003). Therefore the net (shortwave plus longwave) radiative effect of dust can be either positive or negative, depending on the strength of the shortwave or longwave effect (e.g. Tegen and Lacis, 1996; Sokolik and Toon, 1999), both of which are affected by factors such as particle size, dust altitude and chemical composition (i.e. optical properties). For

example, a higher altitude dust layer will cause a more negative TOA radiative effect due to the colder emission temperature.

Large dust events can cause significant perturbations to climate in the shortwave. For example, during SHADE, magnitudes of the local instantaneous direct radiative effect over the ocean reached as much as $-130Wm^{-2}$ at the top of the atmosphere (Haywood *et al.*, 2003), based on a combination of aircraft irradiance measurements and radiative transfer modlling. Slingo *et al.* (2006) also showed top of atmosphere shortwave irradiance increased by $100Wm^{-2}$ during the large dust storm of early March 2006, while the surface solar irradiance at Niamey reduced by as much as $300Wm^{-2}$, values which were based on model estimates and satellite measurements. These are considerable perturbations to the local energy balance, and significantly larger than the accuracy of the measurements. However, the mean global effects are much smaller due to the sporadic spatial and temporal nature of dust storms. For example, the IPCC 2007 report considered the anthropogenic dust top of atmosphere radiative forcing to range between $-0.3Wm^{-2}$ to $+0.1Wm^{-2}$ (Forster *et al.*, 2007), though these numbers include both shortwave and longwave effects. The uncertainty in the net radiative effect of dust stems from uncertainties in dust refractive indices, size distribution, morphology and dust altitude. Additional uncertainties in the radiative forcing come from uncertainties in the proportion of dust which is anthropogenic.

The value of the refractive index, particularly the imaginary part, affects the magnitude and sign of the radiative effect (e.g. Balkanski *et al.*, 2007; Wang *et al.*, 2006; Sokolik and Toon, 1999; Liao and Seinfeld, 1998; Claquin *et al.*, 1998). Liao and Seinfeld (1998) investigated the effect of increasing the imaginary part of the refractive index by 20% around a central value of $0.006i$, and found that over the ocean, this caused a change in the diurnally averaged shortwave TOA radiative effect of $+0.83Wm^{-2}$ due to the extra atmospheric absorption. It should be noted that a 20% change in n_i is not representative of the range of uncertainty associated with n_i in the shortwave, and therefore actual uncertainty in the TOA radiative effect is much larger than this. For example, Claquin *et al.* (1998) found that the range of uncertainties associated with variation in n_i due to different mineralogy in the literature was enough to increase the net TOA shortwave radiative

effect from $-1.39Wm^{-2}$ to $+1.16Wm^{-2}$ due to increased absorption. The value of n_i used is therefore capable of causing a large change in both the magnitude and the sign of radiative effect.

Both the shortwave and net radiative effects are sensitive to the size distribution of the dust (e.g. Tegen and Lacis, 1996; Liao and Seinfeld, 1998; Claquin *et al.*, 1998). Liao and Seinfeld (1998) varied the mass median diameter of the dust size distribution between $1-8\mu m$ and calculated the effect on the TOA shortwave radiative effect. They found that increases in particle size lessened the cooling effect of the dust because of the absorbing nature of larger particles. The same effect was demonstrated by Claquin *et al.* (1998) who found that the mean number radius of a size distribution was critical in determining the net cooling or warming of the atmosphere-Earth system. The critical radius at which this change occurred was found to be $0.5\mu m$ and $0.2\mu m$ over the ocean and desert respectively, though this was due to both effects in the shortwave and longwave spectra. Though there was an important sensitivity to the mean number radius, Claquin *et al.* (1998) found little sensitivity of the radiative effect to the spread of the size distribution.

As a result of uncertainties in refractive indices, size distributions and consequently the optical properties of dust, the current estimate of dust global radiative forcing ($-0.1\pm 0.2Wm^{-2}$, Forster *et al.* (2007)) is not certain in terms of sign, although significant uncertainties in terms of the fraction of dust which is anthropogenic contribute to this range.

1.7 Thesis Approach

Section 1.5 has shown that despite a large number of dust studies, in terms of in-situ measurements, satellite data and modelling studies, the optical properties of North African dust are still not well defined, and there is therefore a need to better understand the processes that cause the optical properties to differ. Additionally, in terms of understanding the climatic impact of dust throughout the year there is clearly a need to establish whether the likely seasonal differences in uplift and transport processes caused by the meteorology lead to any discernible influence in radiative or microphysical properties of North African dust, and to establish whether this may be contributing to the wide spread of optical properties reported in the literature.

This thesis describes the analysis of aircraft measurements of North African dust, obtained during two field campaigns based in West Africa - one in the dry season and one in the wet season. The aim of this analysis is firstly, to determine the optical properties of the dust, and relate these to the chemical and microphysical properties. Secondly, the thesis assesses whether there are any differences in the optical properties of the dust which result from differing seasonal meteorology. Finally, the thesis aims to determine the radiative effect of the dust, and also to relate this to the optical, microphysical and chemical properties, in order that models and satellite retrievals are better able to represent atmospheric dust.

A full description of the aircraft campaigns, instrumentation, flying patterns and meteorology encountered is given in Chapter 2. Chapter 3 describes the vertical profiles of the aerosol encountered, the chemical composition of the dust, and the potential dust sources. Chapter 4 describes the aerosol optical and microphysical properties.

Chapter 5 investigates the quality of the irradiance measurements from the pyranometers on the aircraft, while Chapter 6 uses this data to validate and explore the radiative effect of the dust encountered during DODO. Finally, Chapter 7 presents a summary of the thesis, limitations of the work and suggestions for the future, and a wider discussion of the importance of the findings of this thesis.

Chapter 2

Methodology

2.1 Introduction

This Chapter describes the fieldwork performed during DODO, in terms of flights, meteorology and dust activity (Section 2.2), the instrumentation on the aircraft (Section 2.3), including problems with particular instruments and corrections applied. The criteria used to identify dust aerosol from other aerosol types encountered is also described in Section 2.4.

2.2 Overview of DODO Fieldwork

The aims of the DODO field campaigns were to make aircraft measurements of dust during transport. The DODO aircraft campaigns were based at Dakar Airport, Senegal, with the fieldwork separated into two aircraft campaigns, one in the dry season (DODO1: 3rd February - 16th February 2006) and one in the wet season (DODO2: 21st August - 28th August 2006). Each campaign followed on from other aircraft campaigns based in Niger, Niamey: in the dry season DODO1 followed DABEX (Dust and Biomass Burning Experiment, Haywood *et al.* (2009)) and in the wet season DODO2 followed the aircraft-based part of AMMA (Africa Monsoon Multidisciplinary Analyses, Redelsperger *et al.* (2008)). Thus each part of DODO commenced with a transit flight from Niamey to Dakar, refuelling at Bamako airport in Mali. Both DODO1 and DODO2 were then based from Dakar airport in Senegal, which allowed the BAe-146 aircraft to fly over both the surrounding land and ocean and perform measurements of dust close to local sources and of transported dust over the ocean, in both seasons. The tracks for each flight (including the transit flights) can be seen in Figure 2.1.

The following sections describe the meteorology during the DODO campaigns, the dust activity and how these relate to the flights that were performed during DODO.

2.2.1 Meteorology during DODO

Figure 2.2 shows the 1000 mbar geopotential and the 850 mbar vector winds during the DODO campaigns. Averages over both campaigns are displayed (Figures 2.2(a), 2.2(b), 2.2(g) and 2.2(h)), as well as an average over the first and the last three days during

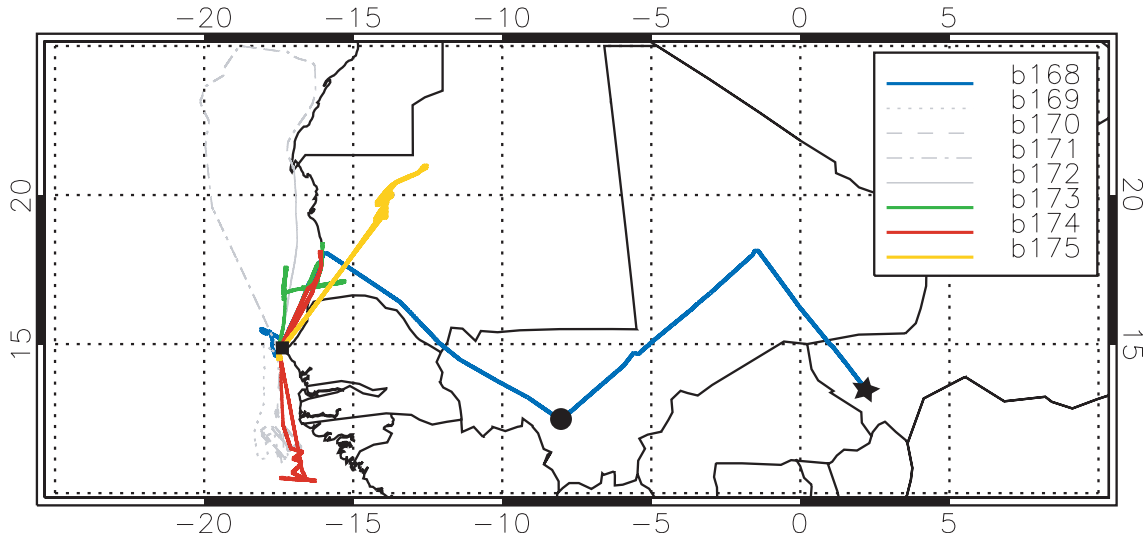

(a) DODO1

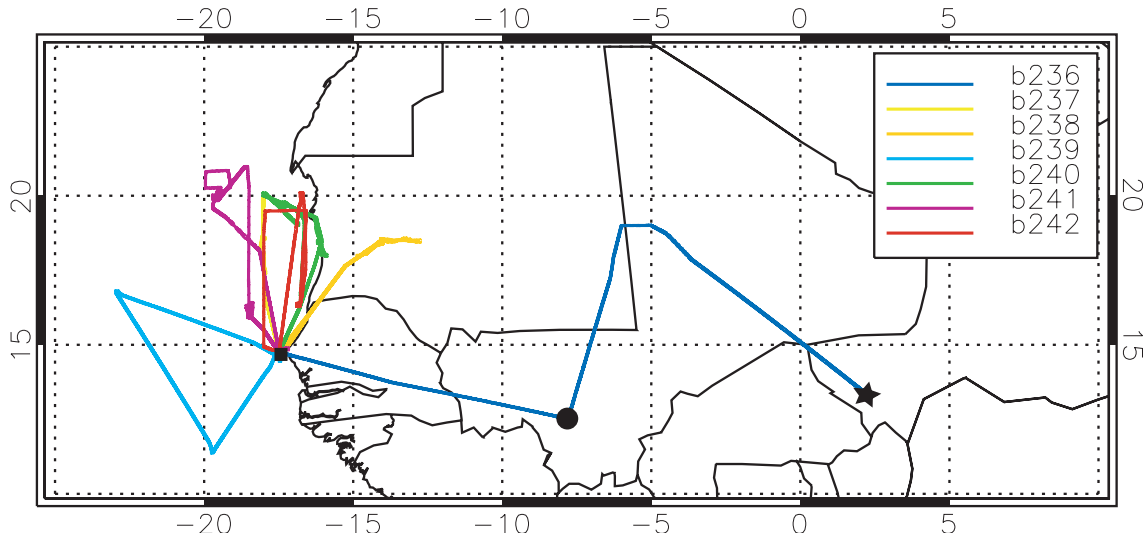

(b) DODO2

Figure 2.1: *Flight tracks for each DODO campaign. Flights which did not encounter dust during DODO1 are shown in grey. Airport locations are indicated by a star (Niamey, Niger), circle (Bamako, Mali) and square (Dakar, Senegal).*

DODO1 (Figures 2.2(c), 2.2(d), 2.2(e), 2.2(f)), since the flow changed significantly during these days and they were also when the only dust flights took place.

During DODO1 the flow changed substantially: for the first week the flow was dominated by an anomalous low-pressure system located over the Canary Islands, shown by the geopotential lines in Figure 2.2(a), which resulted in little offshore flow in the region between Dakar and Nouakchott (Figure 2.2(b)). This is contrary to the predominantly easterly flow that would be expected from climatology, and no dust was sampled during

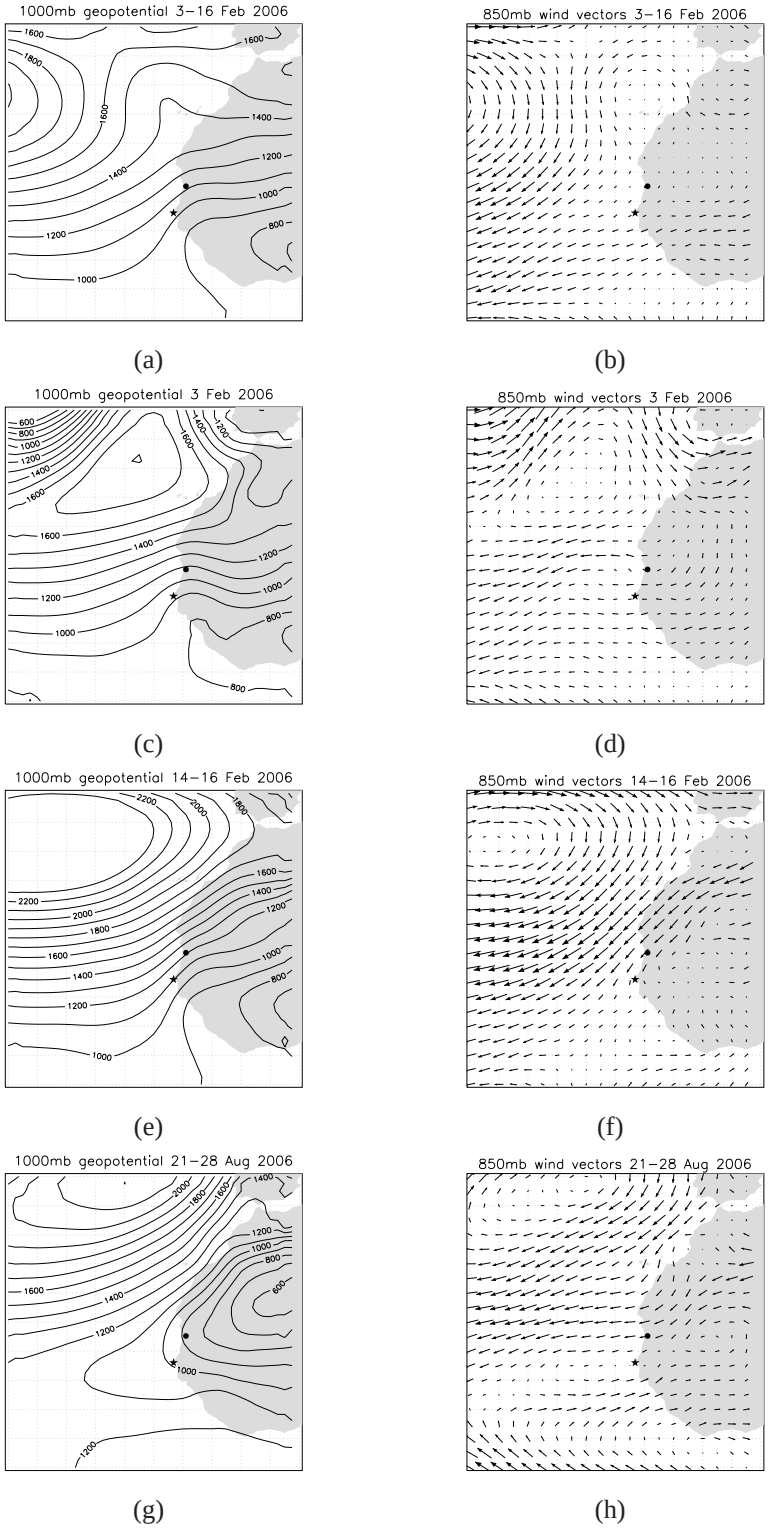

Figure 2.2: *DODO campaign meteorology from ERA operational analyses. The 1000 mbar geopotential ($m^2 s^{-2}$) and 850 mbar wind vectors for: (a) and (b) DODO1 from 3rd-16th February 2006; (c) and (d) DODO1 for 3rd February 2006; (e) and (f) DODO1 from 14th-16th February 2006; (g) and (h) DODO2 from 21st-28th August 2006. Locations of Dakar and Nouakchott are represented by a star and circle respectively.*

this period. Therefore the flights that occurred during this flow regime are coloured grey in Figure 2.1.

The flow changed during the three final days of the campaign, becoming more climatological with northerly/northeasterly flow in the Dakar region (Figures 2.2(e) and 2.2(f)) which resulted in the advection of dust towards the west African coast, which was measured during flights b173, b174 and b175. This flow pattern is not reflected in the DODO1 averages in Figure 2.2(a) and 2.2(b) because of its short time duration. To the south of Dakar the flow was offshore (Figure 2.2(f)) giving rise to the advection of biomass burning aerosol (originating from southern West Africa) at mid-levels in the troposphere, this being sampled during four DODO1 flights (b168, b169, b170, b174) which operated to the south of Dakar.

Dust was also sampled during the transit flight b168 on 3rd February. The meteorology for this day is shown separately in Figures 2.2(c) and 2.2(d), which show a more climatological-like easterly flow between Dakar and Nouakchott (compared to the DODO1 average in Figure 2.2(a)), giving advection of dust over the ocean. This dust was sampled just to the north of Dakar at the end of the transit flight, and was a different dust event to the western-Saharan dust sampled at the end of DODO1.

The geopotential lines in Figure 2.2(g) show the Saharan heat low positioned over Algeria during DODO2. The wind vectors at 850 mbar suggest offshore flow to the north of Dakar, with a recirculation to the south of the region. However, the dust events encountered during DODO2 are more driven by smaller scale convection events, and are more easily described through the satellite imagery shown in Section 2.2.2. The six flights during DODO2 based from Dakar concentrated mainly on the ocean and land areas to the north of Dakar (Figure 2.1), reflecting the largest likelihood of dust sampling.

2.2.2 Dust Activity during DODO

Figures 2.3 and 2.4 show dust forecasts from the Met Office CAMM (Crisis Area Mesoscale Model, Greed (2005)) model at 12Z each day and give a good overview of the dust activity during the campaigns. This information was used for flight planning during DODO. Figure 2.3 shows the surface dust concentration in gm^{-3}, whereas Figure 2.4 shows a

forecast of the aerosol optical depth (AOD) at 550nm, with the different variables shown for each campaign reflecting an update in the flight planning information and model output between the DODO campaigns.

Figure 2.3 shows low forecast concentrations of advected dust over the ocean around Dakar during flights b168, b173 and b174. Dust was forecast to be advected further over the ocean towards the southwest between flight b173 and flight b174, so that the same dust outbreak was sampled on consecutive days. Contrastingly higher concentrations of dust forecast over Mauritania can be seen in Figure 2.3(d) where a heavier dust storm was encountered during flight b175.

Figure 2.4 shows the sequence of forecast dust events that occurred during DODO2. On 21st August high optical depths are forecast over northern Mali which were sampled during the transit flight (b236) between Niamey and Bamako. During 22nd-25th August a tropical depression (Debby) developed and moved westwards from Dakar, and can be seen by the circular area of very low AOD values. This resulted in southeasterly flow across the coastline north of Dakar, transporting dust over the ocean (which had previously been sampled over land during b236), which was sampled in flight b237 (Figure 2.4(b)). High optical depths were forecast over western Mauritania on 23rd August, which were sampled during flight b238 when a heavy dust storm was encountered. Figures 2.4(d) and 2.4(e) show that lower dust AODs were forecast over the ocean during flights b239, b240 and b241 (24th and 25th August). On 26th and 27th August - days when no flights were performed - the main dust outbreaks were not close to the Dakar region. Finally on 28th August (Figure 2.4(h)) there was dust forecast over the ocean to the north of Dakar, which was sampled during flight b242.

Note that though the CAMM forecasts give a good indication of the movement of the dust outbreaks during DODO, and have the advantage of showing dust aerosol only and not being limited by cloud presence obscuring the dust, they do not necessarily represent reality, and for this purpose satellite images must be examined. Indeed, one of the aims of DODO was to validate dust model forecasts (e.g. Greed *et al.*, 2008).

Figures 2.5 and 2.6 show dust product images from the MSG (Meteosat Second Generation) SEVIRI (Spinning Enhanced Visible and Infrared Imager) instrument (Schmetz

et al., 2002). Brightness temperature differences are calculated from SEVIRI measurements of narrow band infrared radiances over wavelengths $12.0 - 10.8\mu m$, $10.8 - 8.7\mu m$ and $10.8\mu m$ (Schepanski *et al.*, 2007). The spectral absorption characteristics of dust allow its detection, and it appears as pink in the false colour images. Therefore dust activity during DODO can be seen and differentiated from other types of aerosol. These images are available in 15 minute time resolution, and therefore are also useful in following the movement of the dust storms which were sampled during DODO, in part to determine whether different flights sampled the same dust plumes. Therefore the images shown in Figures 2.5 and 2.6 are at appropriate times for each flight.

Figures 2.5 and 2.6 clearly illustrate the different meteorology between DODO1 and DODO2. In DODO1 deep convection associated with the intertropical convergence zone (ITCZ) can be seen in the red-coloured cumulonimbus clouds to the south of the equator, whereas during DODO2 these can now be seen over northern Africa. In Figure 2.6(a) the convective cloud of Tropical Depression Debby can also be seen on the left hand side of the image. The large amount of cloud that was frequently present during DODO1 can also be seen in Figure 2.5.

The dust sampled at the end of the transit flight b168 can be seen as a dull pink over the ocean around Dakar. The dust around the coast to the north of Dakar on 14th February (flight b173) and to the south of Dakar on 15th February (flight b174) is difficult to see due to the presence of cloud above the dust. The dust sampled over land on 16th February in Mauritania can just be made out as a light pink colour, just to the west of the band of cloud stretching across West Africa.

Similarly the dust sampled during DODO2 can also be seen in Figure 2.6. On 21st August the dust over Mali that was sampled during b236 (the transit flight) can be seen. By following the succession of 15 minute images (not shown), it can be seen that this dust is the same dust that was then sampled over the ocean to the north of Dakar during flight b237 on 22nd August, and that the skies were clear in this region. Between 23rd - 27th August a large amount of dust can be seen over northern Africa, mostly over northern Morocco and Algeria (note that this was not well forecast by CAMM in Figure 2.4), which appears to have been uplifted in the vicinity of an MCS (mesoscale convective

system) overnight on 22nd August in southern Algeria. This dust developed into a long swathe, part of which broke off and was transported towards Mauritania and encountered during b238 (23rd August). This dust was then advected over the ocean and appears much less intense in the SEVIRI images in Figures 2.6(d) and 2.6(e). Since the dust in Morocco was out of reach of the aircraft, the lower dust concentrations were sampled over the ocean under moderate amounts of cloud on 24th August (b239 and b240) and 25th August (b241, which included an intercomparison with the NASA DC-8 aircraft). Again, for these images (Figures 2.6(d) to 2.6(e)) the dust is difficult to see due to cloud presence.

Three days later on 28th August flight b242 was performed in dust over the ocean in moderate dust loadings, which can be seen in Figure 2.6(h). The 15 minute resolution images can again be used to trace the dust from b242 backwards in time. This does not reveal any obvious source or MCS uplifting the dust, but suggest the dust is traceable to roughly the southern Algeria/eastern Mali area. Again, the frequent cloud coverage prevents being able to fully track the dust outbreak backwards over time.

Figures 2.7 and 2.8 also show the sequence of OMI (Ozone Monitoring Instrument) Aerosol Index (AI) during the DODO campaigns. These are shown since they have the advantage of representing the real situation (as opposed to the model forecasts), and since they are based on UV radiance they are not affected by cloud which limited the detection of dust in the SEVIRI images. The AI is based on the radiance measured at two wavelengths (340 and $380nm$) in the UV, where dust is absorbing, and measurements of the AI over north Africa are made around midday, once per day. OMI can also detect dust aerosol over the desert, due to the low albedo of desert surfaces at UV wavelengths . However, interpretation should be cautious since other aerosol types, including biomass burning aerosol, can also be detected. Additionally the OMI AI is dependent on the height of the boundary layer, and may not detect aerosol if the boundary layer height is very low (e.g. Mahowald and Dufresne, 2004).

Figure 2.7 supports the pictures illustrated by the CAMM forecasts and fills in some gaps from the SEVIRI images. Figure 2.7(a) shows the aerosol sampled during b168 to the south of Dakar. Dust in the same region can be seen in Figures 2.7(b) and 2.7(c),

though in all cases, the presence of biomass burning aerosol is likely to elevate the AI above what it would be for dust alone. Note that the dust encountered to the north of Dakar in flight b173 is not visible in Figure 2.7(b), and this may be related to the dust being at very low altitudes. As with the SEVIRI images, the dust over Mauritania is visible in Figure 2.7(d).

The higher AI values seen in Figure 2.8 reflect the higher dust concentrations found during DODO2 compared to DODO1. The dust sampled in the transit flight b236 over Mali can be seen in Figure 2.8(a), which is then located further west over the ocean on 22nd August during flight b237 (Figure 2.8(b)). The high dust concentrations found during flight b238 over Mauritania can be seen in Figure 2.8(c), where the dust over Morocco is also evident. The lower concentrations of dust over the oceans which were sampled during Flights b239, b240 and b241 (Figures 2.8(d) and 2.8(e)) can also be seen. Finally the higher dust AI over the ocean which was sampled during flight b242 on 28th August can be seen in Figure 2.8(h). During DODO2 when biomass burning aerosol was not dominant, the aerosol detected by OMI is much more likely to be dust.

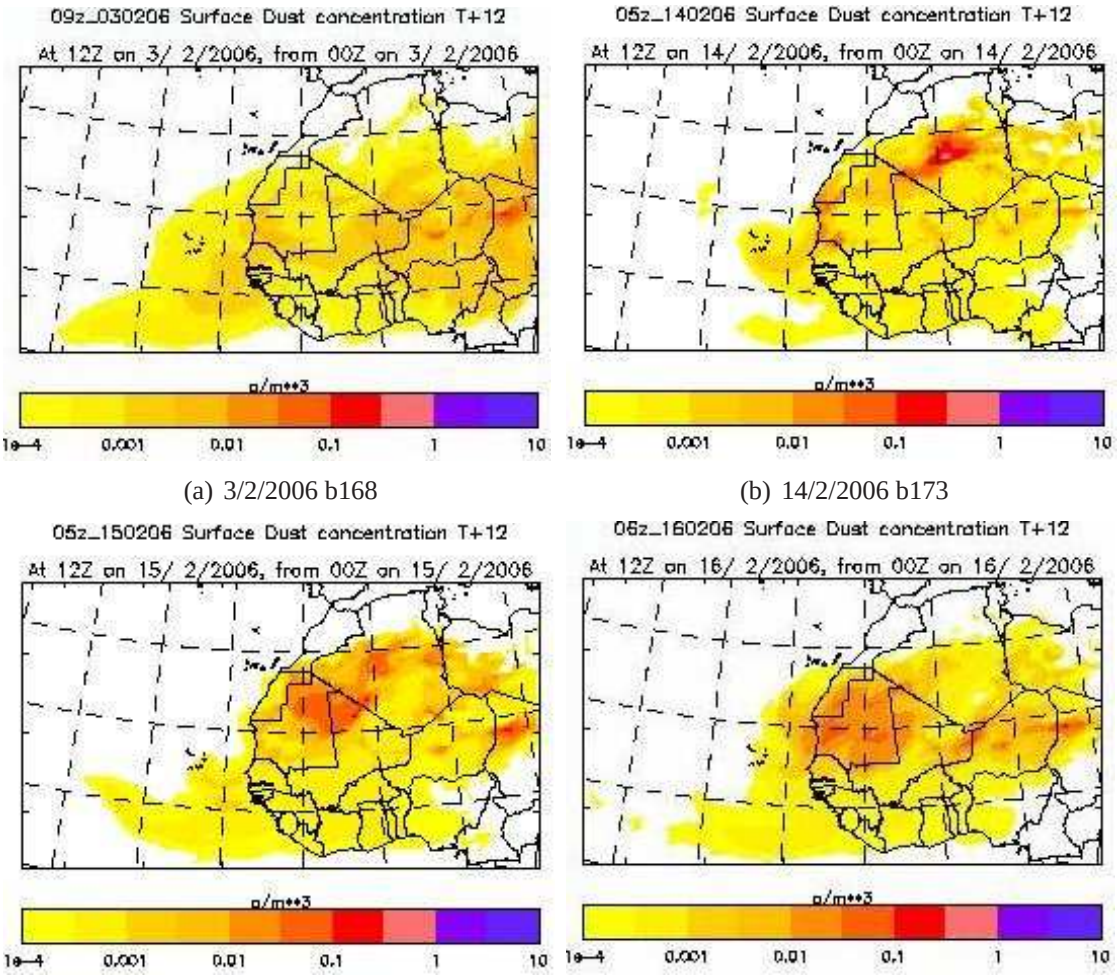

(a) 3/2/2006 b168

(b) 14/2/2006 b173

(c) 15/2/2006 b174

(d) 16/2/2006 b175

Figure 2.3: *12 hour CAMM forecasts of surface dust concentration in gm^{-3} for the days on which dust flights were performed during DODO1. The flight number performed on each day is indicated below each figure.*

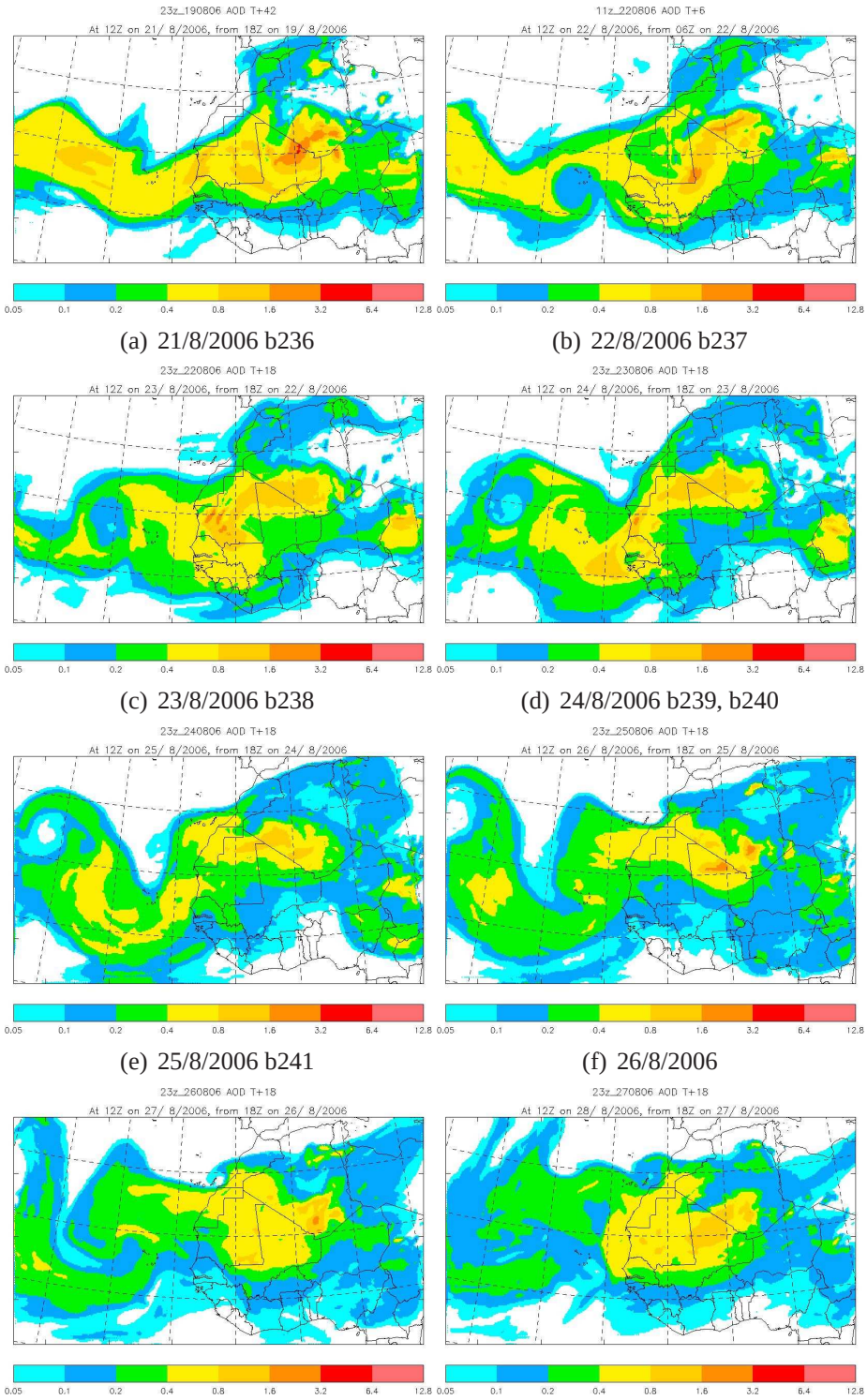

(a) 21/8/2006 b236 (b) 22/8/2006 b237

(c) 23/8/2006 b238 (d) 24/8/2006 b239, b240

(e) 25/8/2006 b241 (f) 26/8/2006

(g) 27/8/2006 (h) 28/8/2006 b242

Figure 2.4: *Forecasts from CAMM of optical depth at 550nm for each day during DODO2. The flight number performed on each day is indicated below each figure.*

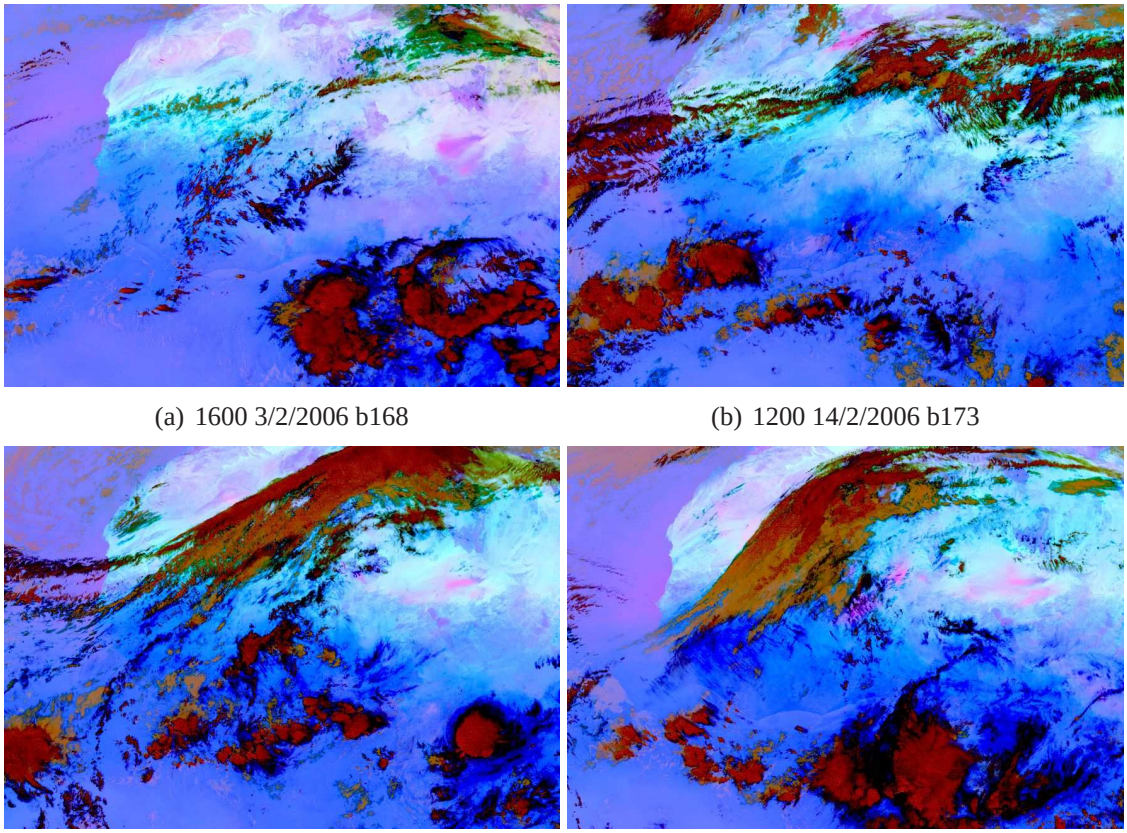

(a) 1600 3/2/2006 b168

(b) 1200 14/2/2006 b173

(c) 1200 15/2/2006 b174

(d) 1200 16/2/2006 b175

Figure 2.5: *SEVIRI Meteosat dust product images for each day dust flights were performed during DODO1. Magenta colours indicate dust, red is high cloud, orange mid-level cloud. The times of the satellite images shown correspond to the DODO flight times.*

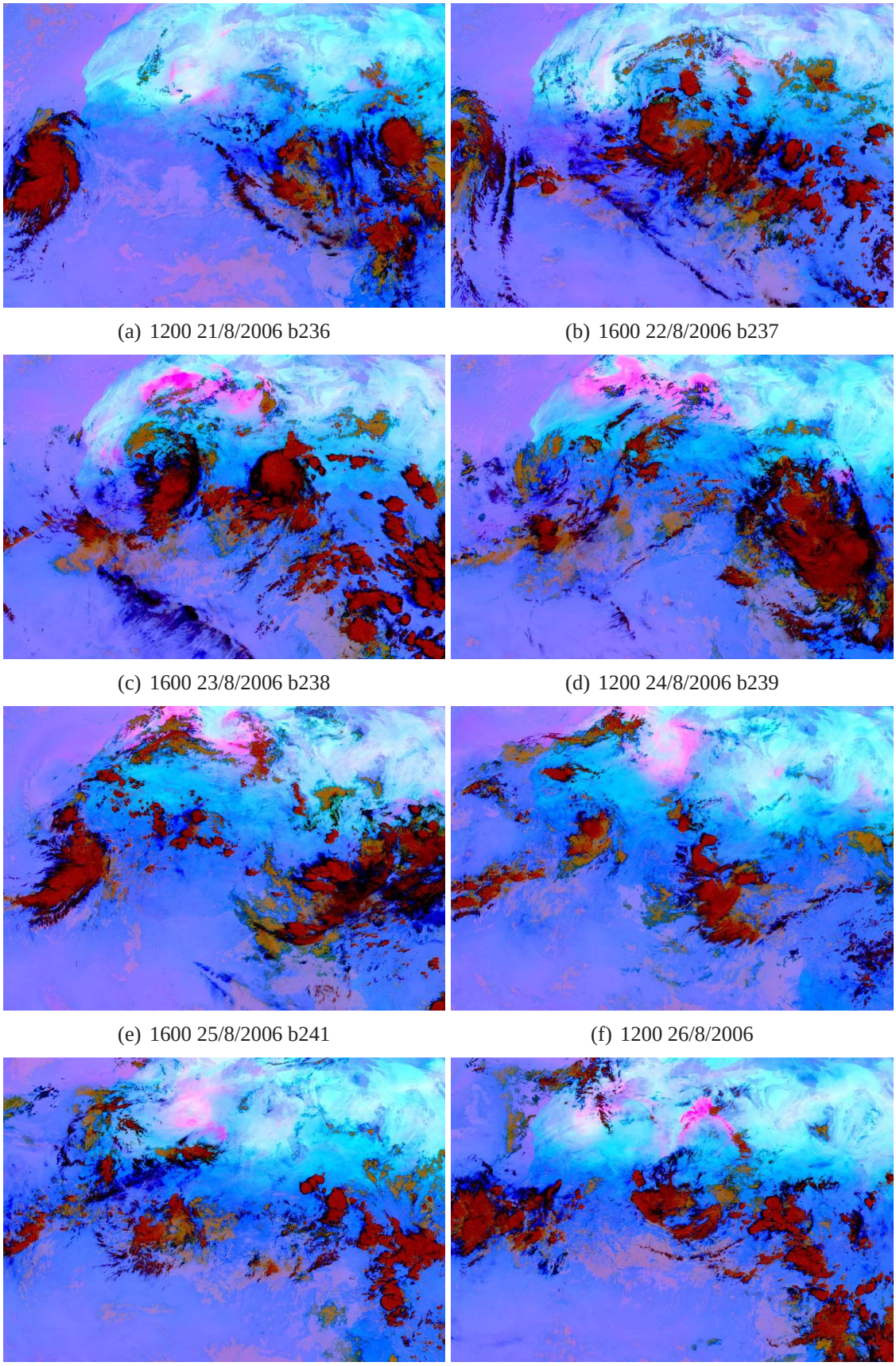

(a) 1200 21/8/2006 b236

(b) 1600 22/8/2006 b237

(c) 1600 23/8/2006 b238

(d) 1200 24/8/2006 b239

(e) 1600 25/8/2006 b241

(f) 1200 26/8/2006

(g) 1200 27/8/2006

(h) 1400 28/8/2006 b242

Figure 2.6: *Same as Figure 2.5 but for DODO2.*

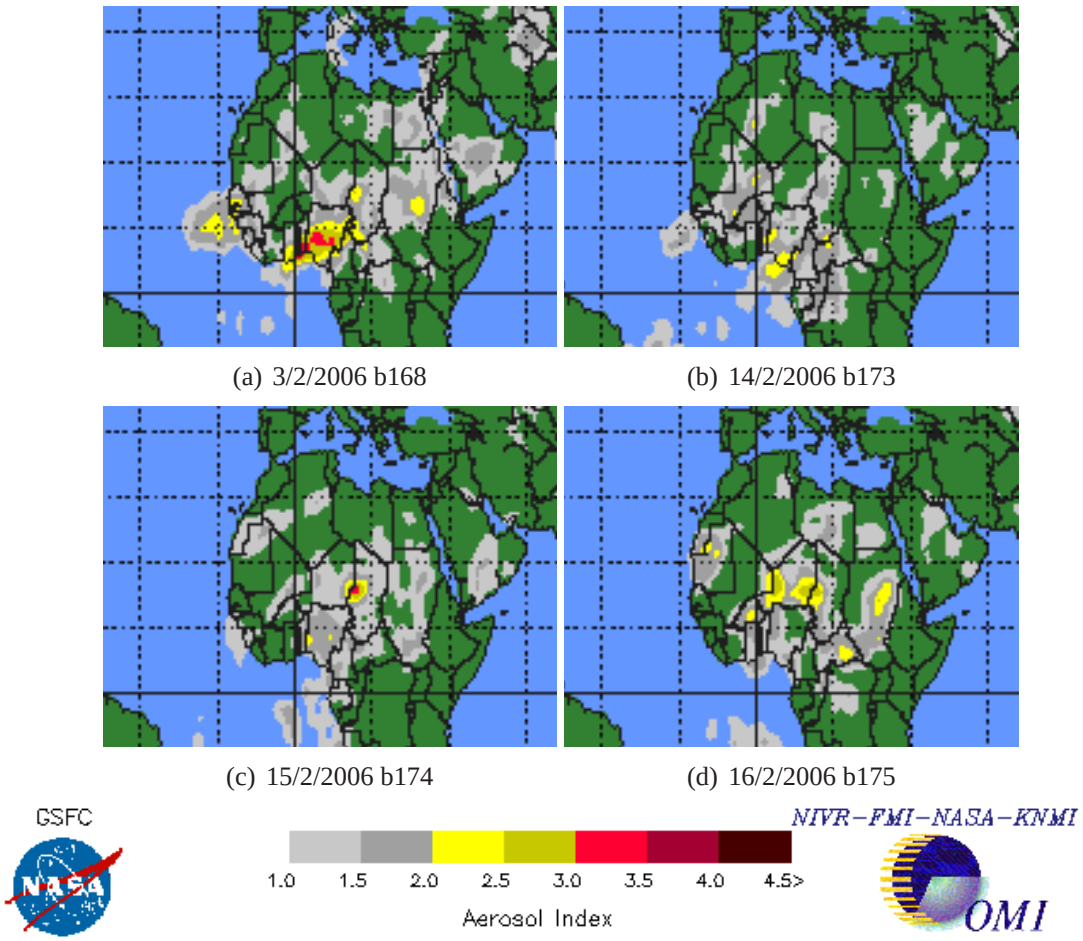

(a) 3/2/2006 b168 (b) 14/2/2006 b173

(c) 15/2/2006 b174 (d) 16/2/2006 b175

Figure 2.7: *OMI Aerosol Index for each day dust flights were performed during DODO1.*

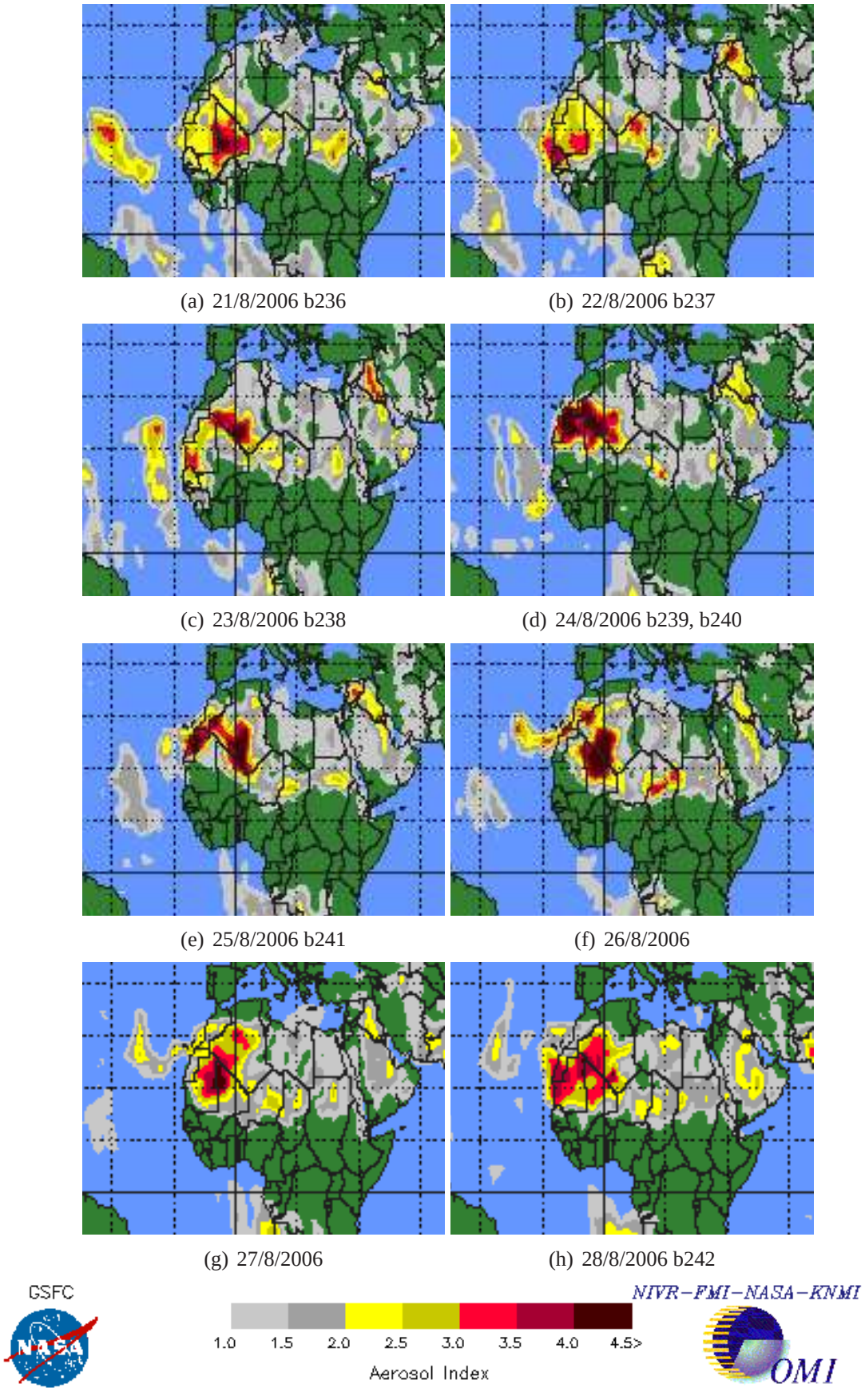

(a) 21/8/2006 b236 (b) 22/8/2006 b237

(c) 23/8/2006 b238 (d) 24/8/2006 b239, b240

(e) 25/8/2006 b241 (f) 26/8/2006

(g) 27/8/2006 (h) 28/8/2006 b242

Figure 2.8: *OMI Aerosol Index for each day during DODO2.*

2.2.3 DODO Flights

During the DODO campaigns a series of flights was performed using the FAAM (Facility for Atmospheric Airborne Measurements) BAe-146 aircraft, over land (desert areas) and ocean. The flight tracks are shown in Figure 2.1 and a summary of the location, duration and nature of the flights is given in Tables 2.1 and 2.2.

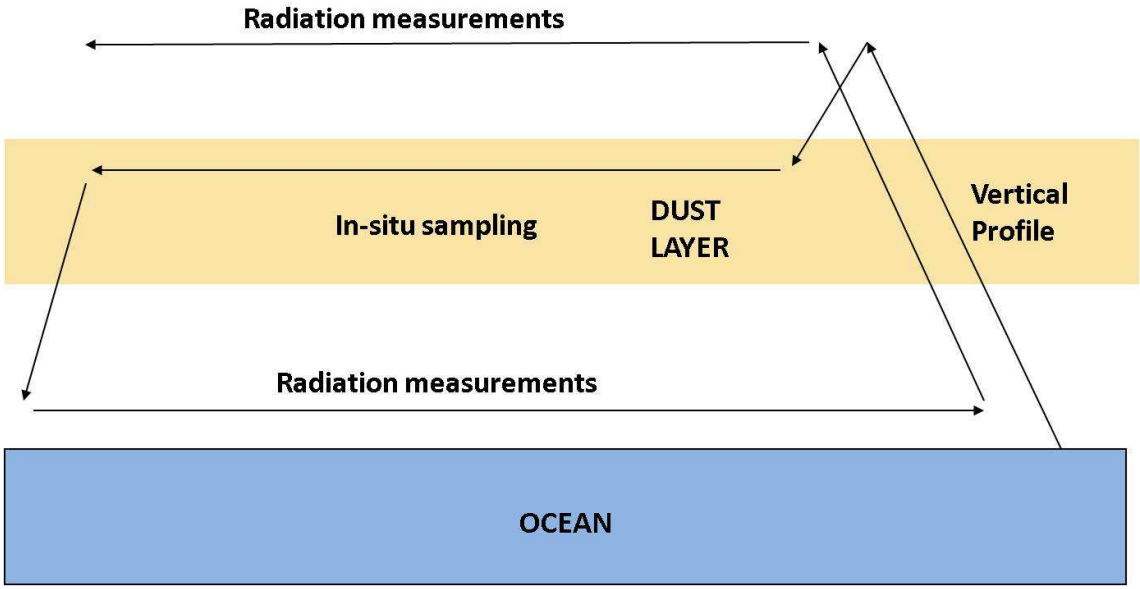

Figure 2.9: *Schematic of typical DODO flight pattern. Arrows indicate aircraft manoeuvres.*

The results and aircraft measurements presented in this thesis come from aircraft manoeuvres consisting of vertical profiles, measuring the vertical distribution of the aerosol, and 'straight and level runs' ('runs' hereafter), where measurements were taken at a constant pressure level or altitude. The straight and level runs usually last for a duration of time between 5 and 30 minutes, covering up to around $300km$, in order to obtain enough data to allow the horizontal variability to be measured, or to collect enough aerosol particles on filter samples. Runs are performed within aerosol layers to take in-situ measurements, and at low and high altitudes to take radiometric measurements, as illustrated in the schematic diagram in Figure 2.9. The aim is for the low level runs to be below all aerosol, and for the high level runs to be above all aerosol with no clouds present. In practice airspace and time limitations may mean that this is not always possible. For example, over the sea the BAe-146 can fly as low as 15m (50ft) during profiles or 30m (100ft) dur-

ing runs, whereas over land the lowest altitude achieved during DODO was 70m (200ft). Additionally the presence of clouds may prevent high altitude radiation work.

Vertical profiles range from either ground level (in the case of take-off or landing) or the aircraft's minimum safe altitude of 20m (50ft) over sea or approximately 70m (200ft) over land, to above the aerosol layer. Since the altitude of the dust varied between seasons, the altitude range of deep profiles also varied between DODO1 and DODO2. The aircraft flies at $110ms^{-1}$ but ascends and descends at $5ms^{-1}$ and therefore covers considerable horizontal distance during a profile, which means that the run data is invaluable in terms of showing the horizontal variation. Most instruments on the BAe-146 sample at least at 1Hz, giving good resolution of data in the vertical and horizontal. The locations of the runs and profiles performed in each flight can be seen in Figure 2.10.

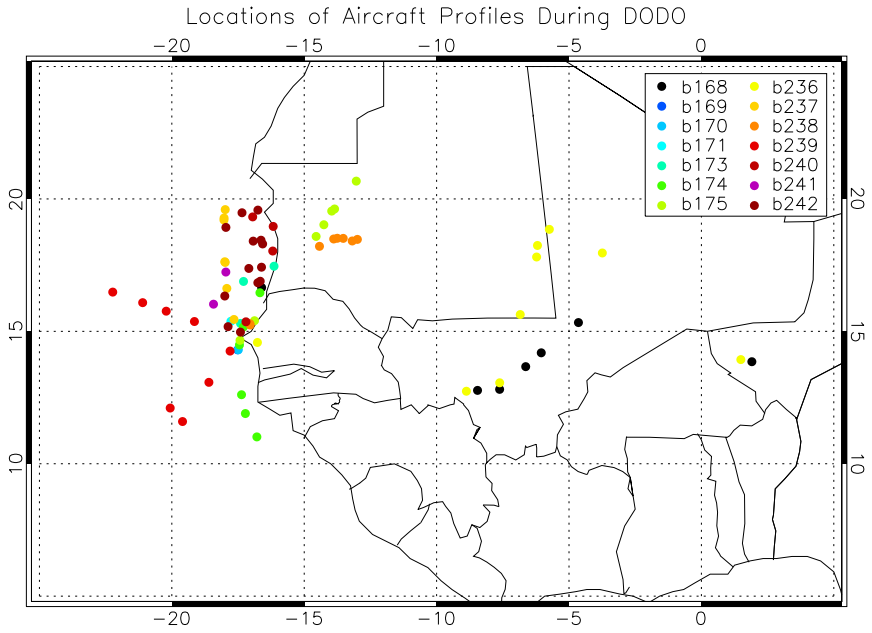

(a)

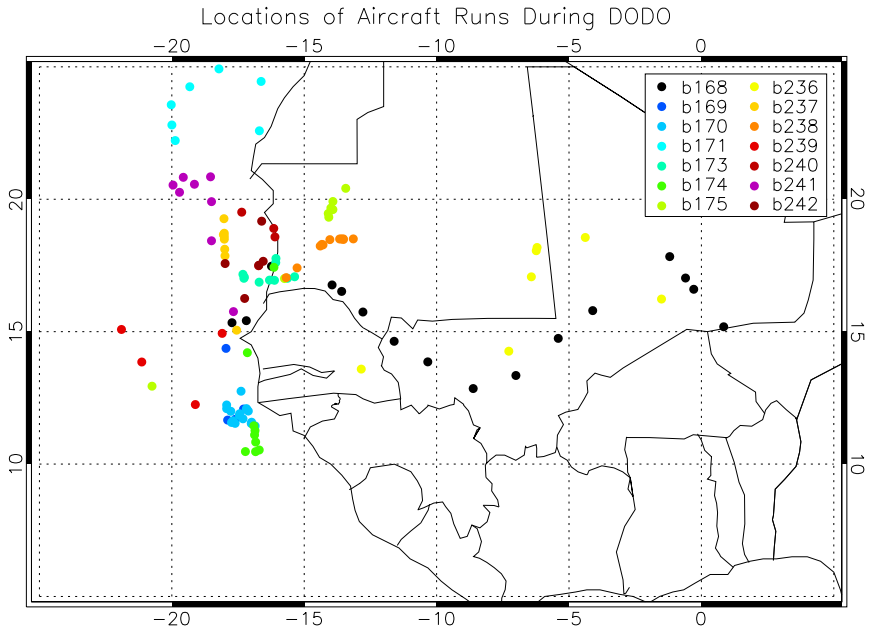

(b)

Figure 2.10: *Locations of (a) profiles and (b) runs during DODO. Each flight is represented by a different colour as indicated in the legend. Circles represent the mean location of a run or profile.*

Flight	Date	Take-off & landing time	Operating Area	Objectives	Cloud present?
b168	3 Feb 2006	074628, 170016	Land areas between Niamey and Dakar, refuel at Bamako	Transit flight (Niamey-Dakar), in-situ and radiometric measurements of dust	yes
b169	7 Feb 2006	112228, 141834	Over ocean south of Dakar	Instrument shake-down, biomass burning aerosol sampling	yes
b170	11 Feb 2006	095447, 145335	Over ocean south of Dakar	In-situ biomass burning aerosol sampling	yes
b171 (b172)	12 Feb 2006	084911, 130656	North of Dakar (up to $25^{\circ}N$), over ocean	Model validation for major dust storm to the north of Dakar. Dust storm not encountered and aircraft lost science power during refuel and therefore no data available for b172	yes
b173	14 Feb 2006	094953, 143615	Coastal region between Dakar and Nouakchott	In-situ sampling of dust over coastline and land	yes
b174	15 Feb 2006	094400, 131354	Over ocean north and south of Dakar	In-situ sampling of dust advected over ocean and biomass burning aerosol, probably same dust event as b173	yes
b175	16 Feb 2006	085143, 141538	Land regions (desert) in northern Mauritania	In-situ sampling and radiometric measurements of dust over desert; moderate dust loadings	no

Table 2.1: *Summary of flights performed during DODO1.*

Flight	Date	Take-off & landing time	Operating Area	Objectives	Cloud present?
b236	21 Aug 2006	072144, 160735	Land areas between Niamey and Dakar, refuel at Bamako	Transit flight (Niamey-Dakar), in-situ and radiometric measurements of dust between Niamey and Bamako. Lack of fuel at Bamako meant a direct flight from Bamako to Dakar	mostly yes
b237	22 Aug 2006	135855, 182401	Over ocean north-west of Dakar	In-situ and radiation measurements of dust over ocean. Possibly same dust event as b236.	no
b238	23 Aug 2006	130025, 173152	Land regions (desert) in northern Mauritania	In-situ and radiometric measurements of dust over desert; high dust loadings and low visibility	mostly no
b239	24 Aug 2006	095141, 135328	Over ocean, between and to the south of Dakar and Sal (Cape Verde Islands)	In-situ measurements of dust over ocean	yes
b240	24 Aug 2006	151619, 193645	Over ocean, to north-west of Dakar	In-situ and radiometric measurements of dust over ocean. No cloud physics data available.	mostly no
b241	25 Aug 2006	135438, 183200	Over ocean, to north-west of Dakar	Intercomparison with NASA DC-8 aircraft and high-altitude calibration of radiometers	mostly no
b242	28 Aug 2006	110243, 153338	Over ocean, to north-west of Dakar	In-situ and radiometric measurements of dust	mostly no

Table 2.2: *Summary of flights performed during DODO2.*

2.3 BAe-146 Instrumentation

2.3.1 Overview of Instruments

The FAAM BAe-146 aircraft was equipped for in-situ aerosol measurements, radiometric measurements and measurements of standard meteorological variables during the DODO campaigns. A summary of the instruments relevant to this thesis is given in Table 2.3, and a full overview of all instruments is given in Haywood *et al.* (2009).

At this point it is necessary to define how the terms 'coarse mode' and 'accumulation mode' will be used in this thesis. The core instruments measuring in-situ aerosol properties (nephelometer , PSAP (Particle Soot Absorption Photometer) and PCASP (Passive Cavity Aerosol Spectrometer Probe)) will be assumed to measure only the fine and accumulation mode, and to exclude the coarse mode. The size range measured by the PCASP is $r = 0.05 - 1.5\mu m$ ($d = 0.1 - 3\mu m$), and therefore this range will be taken to represent the accumulation mode in this thesis. The cut-off radii of the PSAP and nephelometer Rosemount inlets are thought to be around $3\mu m$ diameter (see Section 2.3.4) and therefore the same definition is applied to the PSAP and nephelometer data. Instruments measuring the coarse mode ($r > 1.5\mu m$ or $d > 3\mu m$) are non-core instruments and are described further in Section 2.3.6.

The following sections describe some of the key instrument measurements, corrections and limitations - particularly with regard to the nephelometer which developed a fault during DODO2. A more detailed analysis of the pyranometer data has been carried out and forms the content of Chapter 5.

Type of Measurement	Instrument	Abbreviation	Details	Comment
Aerosol Microphysics	PMS Passive Cavity Aerosol Spectrometer Probe 100-X	PCASP	Size distribution, $r = 0.05 - 1.5\mu m$	Wing-mounted
	Droplet Measurement Technology Cloud Droplet Probe	CDP	Size distribution, measures $r = 0.01 - 31\mu m$, only data from $r = 2.5 - 20\mu m$ used	Mounted on aircraft fuselage. Operated on selected DODO2 flights, corrections applied for non-optimal mounting.
Optical Properties	TSI 3563 Integrating Nephelometer		Total scattering and hemispheric backscattering coefficients (dry) at $450\mu m$, $550\mu m$, $700\mu m$	Supplied by Rosemount inlet. DODO2 data corrected to agree with NASA DC-8 data.
	Radiance Research Particle Soot Absorption Photometer	PSAP	Aerosol absorption coefficient at $567\mu m$	Supplied by Rosemount inlet.
Chemical Composition	Filter Samples		90mm nucleopore filters with $0.4\mu m$ pore size	DODO1 filter samples had larger ($5\mu m$) pore sizes
	Aerodyne Aerosol Mass Spectrometer	AMS	Aerosol mass size distribution of organics, nitrates, ammonium and sulphates ($d = 0.05 - 1\mu m$)	
Radiation	Eppley PSP Clear dome pyranometers		$0.3 - 3\mu m$ up and downwelling hemispheric irradiance	See Chapter 5 for correctional procedures
	Eppley PSP Red dome pyranometers		$0.7 - 3\mu m$ up and downwelling hemispheric irradiance	See Chapter 5 for correctional procedures
Gas Phase Chemistry	Various		Ozone, Carbon Monoxide	TECO 49 UV Photometric Instrument, AL50002 Carbon Monoxide Instrument
Core data	Various		Pressure, altitude (radar, GPS, pressure height), GPS location, temperature, dew point temperature, aircraft pitch & roll.	

Table 2.3: *BAe-146 aircraft instrumentation relevant to this thesis and DODO.*

2.3.2 Uncertainties in PCASP Measurements

The Passive Cavity Aerosol Spectrometer Probe (PCASP) is an optical particle counter which measures aerosol particle concentrations as a function of size, allowing a size distribution to be retrieved. The amount of light scattered by individual particles between scattering angles of $35 - 120^{\circ}$ is measured, and assumed to be dependent on particle size. The scattered radiation is also sensitive to the shape and refractive index of the particles. The PCASP is calibrated using polystyrene latex spheres with a refractive index of 1.588-0.0i. Therefore aerosol particles with a different refractive index, and non-spherical shape may result in inaccurate sizing by the PCASP (McMeeking *et al.,* 2008).

The number of particles measured per second is converted to a number concentration (cm^{-3}) using the flow rate through the PCASP. This is not measured directly during flights, but can be calculated using measurements of ambient temperature and pressure during the flight, if the flow rate through the PCASP has been measured on the airfield before take-off (McMeeking *et al.*, 2008). If this correction is not applied, PCASP data from high altitude runs may be underestimates of the true number concentrations.

It has only recently (in the last month) become evident that the PCASP data from the aircraft had not been corrected to the appropriate flow rate. Therefore data presented in McConnell *et al.* (2008) do not include this correction. However, much of the data from the PCASP is presented in terms of normalised size distributions - i.e. the number concentrations are relative to the total number measured over a run. These measurements will remain unchanged even if flow rate corrections are made to the PCASP data.

The effects of the PCASP flow rate corrections on the number concentrations are greatest at higher altitudes. This has been investigated for data from DODO. Changes to the absolute number size distributions range from very small (under 5%) at low altitudes (under 1km) to very large at high altitudes (increases in particle number concentrations of around 70% at 5 km altitude). Since this only affects data presented in terms of the absolute number concentrations, the only data (and results) affected in this thesis is the analysis of the coarse mode size distributions and optical properties in Chapter 4, Section 4.5. The PCASP data presented there is from an altitude of 1km, where the pressure and temperature changes would result in an increase in particle number concentration of 12%.

This change has been applied to the results, which were not sensitive to a change of this magnitude.

Assigning uncertainty to the PCASP measurements from DODO due to differences in dust refractive index (from latex) and due to non-spherical particles is more difficult due to lack of information on these properties. Osborne *et al.* (2008) investigated uncertainty in PCASP measurements due to non-spherical particles (prolate cylinders and spheroids) and spheres with a refractive index of 1.53-0.0004i and found that there was a tendency for the PCASP to undersize particles by a factor of around 0.8 for particles smaller than $0.2\mu m$ radius. For particles larger than this, the sizing was under-estimated or overestimated by a range of factors from 0.91-1.19 for different sized particles. Therefore the uncertainty in the sizes of particles measured by the PCASP during DODO is likely to be around 20% since the real part of the refractive index of dust assumed here and the aspect ratio of the particles from DODO (Chou *et al.*, 2008) are likely to be similar to those from the tests performed by Osborne *et al.* (2008).

2.3.3 PSAP Corrections

The Particle Soot Absorption Photometer (PSAP) measures particulate absorption by monitoring the change in transmission across a fibrous glass filter. Standard correction procedures have been applied to the PSAP data as described in Bond *et al.* (1999) and Haywood and Osborne (2000). These corrections include adjustments for inaccuracies in the filter spot size, flow rate, overestimations of absorption due to scattering being misinterpreted as absorption, and for multiple scattering. The flow rate on the PSAP on the BAe-146 is set manually, typically to $3Lmin^{-1}$. The flow rate is uncontrolled during profiles, and therefore PSAP data from vertical profiles is not used. During straight and level runs when the flow rate is controlled and therefore this data is used for absorption calcuations.

The PSAP measures absorption at 567nm whereas the nephelometer measures scattering at 550nm. The corrected absorption coefficient measured by the PSAP, σ_a^{567}, has been adjusted to 550nm assuming that σ_a varies as $1/\lambda$ (Haywood and Osborne, 2000), to obtain σ_a^{550}.

2.3.4 Nephelometer Corrections

The TSI 3563 nephelometer on the BAe-146 measures the aerosol scattering coefficient at $450nm$, $550nm$ and $700nm$ wavelengths over scattering angles of $7 - 170^{\circ}$ and is supplied from the aircraft exterior by a Rosemount inlet. The DODO nephelometer has been corrected as advised by Anderson and Ogren (1998) for missed forwards scattering, assuming that the aerosol is submicron particles due to the passing efficiency of the Rosemount inlet.

During DODO2 the BAe-146 flew a wing-tip to wing-tip intercomparison flight (b241) with the NASA DC-8 aircraft which was based at Sal, Cape Verde, during part of DODO2 as part of the NAMMA (NASA African Monsoon Multidisciplinary Analyses) project. The intercomparison part of the flight included three straight and level runs within dust in the SAL to the north of Dakar over the ocean. This provided the opportunity to compare measurements from the nephelometers on the two aircraft.

The DC-8 operated a TSI 3563 nephelometer (identical to that on the BAe-146), but behind a NASA LaRC type inlet, which has been shown to give a 50% loss of dust particles above $3.5\mu m$ aerodynamic diameter, giving an optically equivalent diameter of $2\mu m$ (McNaughton *et al.*, 2007). The BAe-146 Rosemount inlets which supply the nephelometer (and PSAP) have been estimated to have an upper limit for dust particles of around $3\mu m$ in terms of optically equivalent diameter (Haywood *et al.*, 2003), though the true passing efficiency and cut-off are not well defined. However, the estimated inlet cut-off diameters supplying the two nephelometers are similar.

The nephelometer data for the two aircraft have been compared, and is described in McConnell *et al.* (2008). For information purposes, the findings from this comparison are described here. The two nephelometers were found to measure the same variability in the dust layer, but showed significant offsets between the two instruments with the DC-8 nephelometer measuring more scattering by a factor of 7.3, 2.36 and 2.4 at 450nm, 550nm and 700nm respectively. It is thought that the BAe-146 nephelometer developed a fault during AMMA (the campaign preceding DODO2) and lost some sensitivity due to high dust loadings experienced by the BAe-146 when the nephelometer was not closely monitored and may have resulted in the detectors becoming dirty. Additionally the blue

scattering signal was especially low.

Therefore the BAe-146 nephelometer data have been corrected to agree with the DC-8 nephelometer data as described in McConnell *et al.* (2008), for the whole of DODO2.

The underestimation of scattering by the BAe-146 nephelometer can also be shown by comparing aerosol optical depths (AODs) measured by the Dakar AERONET station at Mbour to those obtained by integrating the vertical profiles of scattering as measured by the nephelometer, according to,

$$\tau_{ac}^{550} = \int_0^z \frac{\sigma_s^{550}}{\omega_0^{550}} dz, \tag{2.1}$$

where τ_{ac}^{550} is the optical depth at 550nm measured by the aircraft, σ_s^{550} is the scattering coefficient (including both standard corrections and the DC-8 correction), and ω_0^{550} is the single scattering albedo of dust calculated from a horizontal run in a dust layer at an appropriate altitude, according to,

$$\omega_0^{550} = \frac{\sigma_s^{550}}{\sigma_s^{550} + \sigma_a^{550}}, \tag{2.2}$$

where σ_s^{550} and σ_a^{550} are the scattering and absorption coefficients measured over a run, again corrected for both standard corrections and for the DC-8 correction in the case of σ_s^{550}, since it is not possible to use PSAP data from vertical profiles.

Aircraft-measured optical depths for 13 deep profiles from DODO, either landing or taking off at Dakar airport, have been calculated, and are shown in Table 2.4 with AERONET aerosol optical depth measurements (τ_{AER}^{550}). DODO1 profiles underestimate aerosol optical depth (AOD) by a factor of 1.54 on average in comparison to AERONET measurements. DODO1 data is assumed not to be affected by nephelometer problems, but similarly affected by any inlet losses which may be occurring during DODO2. It is possible that there is a substantial difference in the amount of coarse mode between campaigns which causes this difference. However, the reasonable behaviour of all three nephelometer channels during DODO1, and a realistic zero signal suggest that the nephelometer was behaving normally. Therefore the underestimation of 1.54 is not surprising and is attributed to the loss of coarse mode particles in the Rosemount inlet. This under-

estimation is consistent with that observed during SHADE Haywood *et al.* (2003). Using the DC-8 nephelometer corrections described in McConnell *et al.* (2008) for the DODO2 data, a similar underestimate of 1.35 is obtained. Using data not corrected to agree with the DC-8 data (but still adjusted using standard correctional procedures) results in the AOD being underestimated by an average factor of 3.1 for DODO2.

Flight	Profile	τ_{ac}^{550}	τ_{AER}^{550}	$\tau_{AER}^{550}/\tau_{ac}^{550}$
b168	P17	0.21	0.38	1.83
b169	P1	0.30	0.24	0.81
b171	P1	0.11	0.11	1.00
b173	P1	0.09	0.12	1.34
b174	P10	0.05	0.11	2.03
b175	P1	0.12	0.15	1.19
b175	P8	0.04	0.11	2.56
DODO1 Mean				1.54
b236	P10	0.33	0.23	0.71
b237	P8	0.61	0.64	1.06
b238	P1	0.38	0.68	1.80
b238	P9	0.42	0.48	1.16
b242	P1	0.18	0.42	2.30
b242	P11/P12	0.27	0.29	1.08
DODO2 Mean				1.35

Table 2.4: *Aerosol optical depth at 550nm, from aircraft measurements (τ_{ac}^{550}) for various profiles and from the Dakar (Mbour) AERONET station (τ_{AER}^{550}) at the same times. Also shown is $\tau_{AER}^{550}/\tau_{ac}^{550}$, the ratio between the two measurements of optical depth. All aircraft calculations come from Equation 2.1 and incorporate standard corrections to nephelometer and PSAP data, and DODO2 nephelometer data is corrected based on the NASA DC-8 nephelometer data.*

The variability in $\tau_{AER}^{550}/\tau_{ac}^{550}$ in Table 2.4 is probably related to differing amounts of coarse mode aerosol particles being present, which would result in smaller or greater underestimates of AOD. Some of the variation may also be due to discrepancies in inlet passing efficiency between the two aircraft which would result in a different scaling factor being required for different size distributions.

Hygroscopic growth can result in aerosol particles becoming more scattering in humid environments. Since the nephelometer measures dry humidity, the measured scattering can be an underestimate of the true ambient scattering. Few estimates of hygroscopicity for Saharan dust exist, though it is likely that the effects of humidity are small (e.g. Li-Jones *et al.*, 1998; Carrico *et al.*, 2003). However, when dust is mixed with other aerosol particle types, the effects of humidity can become more important. The effect of hygroscopic growth on the nephelometer measurements has been tested here using

hygroscopic growth values for submicron Asian dust mixtures of Carrico *et al.* (2003) and biomass burning aerosol values from Magi and Hobbs (2003). This resulted in AOD values far greater than those from AERONET, and therefore hygroscopic growth is not accounted for here, though it is acknowledged that it could result in small increases in aircraft calculated AOD.

Another factor contributing to the variability of the values in Table 2.4 could be the distance from the aircraft to the AERONET station - i.e. that the two measurements do not represent an identical aerosol column. Additionally the aircraft covers substantial horizontal distance during a profile. The average distance between the mean point of the aircraft profiles and the AERONET station varies between 29 and 254km with a mean of 114km. However, there is no apparent correlation between distance from AERONET and the correction factor, so this is unlikely to be the main cause of the difference in AOD.

The comparison between aircraft-measured AODs and the AERONET data shows that the behaviour of the nephelometer data throughout DODO2 was consistent and supports the scaling of the BAe-146 nephelometer data described in McConnell *et al.* (2008). Therefore the nephelometer data for the whole of DODO2 has been corrected based on the DC-8 comparison. No corrections for hygroscopic growth in humid environments have been made, since the detailed results using the nephelometer data in this thesis come from straight and level runs within dust layers. These layers were typically very dry (far drier than was experienced in the vertical profiles), with an average relative humidity of 46% during the whole of DODO, which would result in negligible hygroscopic growth (Li-Jones *et al.*, 1998; Carrico *et al.*, 2003).

2.3.5 Filters

Bulk filters were used to collect samples of airborne dust during straight and level runs lasting at least 20 minutes in order to guarantee sufficient loading of the filter samples. The sampling system on the BAe-146 is identical to that from the C-130 and is described in further detail by Andreae *et al.* (2000), and by Formenti *et al.* (2008) with regard to the DODO campaigns. Andreae *et al.* (2000) estimated the inlets to the filter samples to sample 35% of the coarse mode by mass. Aerosol particles were sampled by filtration onto

a stacked filter unit using one stage containing a 90mm Nucleopore filter with a nominal pore size of $0.4\mu m$. Unfortunately the DODO1 samples were mistakenly collected on different filters with pore sizes of $5\mu m$, which means that many particles with diameters smaller than this may not have been sampled.

The filter samples from DODO have been analysed in two ways:

1. Elemental concentrations for the combined accumulation and coarse modes were measured by particle induced X-ray emission (PIXE) at the Laboratorio di Tecniche Nucleari per i Beni Culturali (LABEC) at Florence, Italy (Chiari *et al.*, 2005; Calzolai *et al.*, 2006). PIXE results are available for most of the runs examined in this thesis.

2. Scanning electron microscope (SEM) and transmission electron microscope (TEM) analysis was performed at the Laboratoire Inter-universitaire des Systèmes Atmosphériques (LISA) in Créteil, France on a limited number of samples (see Table 2.5) during a one week period. This allows the composition of single particles to be determined using an energy dispersive X-ray detection system. Further details of the SEM and TEM used can be found in Chou *et al.* (2008).

   The SEM can detect particles with diameter greater than $1\mu m$, whereas the TEM measures the composition of particles smaller than $1.5\mu m$ diameter, so there is some overlap in the particle size measured by each instrument. SEM images of the filter samples have also been used to calculate coarse mode size distributions (see Section 2.3.6).

Flight	Run	SEM	TEM	Comment
b175	R7.1/R7.2	Y	N	Larger pore sizes, but still clear evidence of coarse particles
b237	R2	Y	Y	
b237	R5	Y	Y	
b238	R4.1	Y	N	
b242	R5.1	Y	N	

Table 2.5: *DODO filter samples analysed using the LISA SEM and TEM. Y and N indicate whether SEM or TEM analysis was/was not carried out.*

2.3.6 Coarse Mode Size Distribution Measurements

Measurements of the coarse mode size distribution are much less well defined than those for the accumulation mode (e.g. Reid *et al.*, 2003b), and measurement techniques on the BAe-146 are less well validated. During DODO the coarse mode size distribution was measured by a CDP (flights b237, b238, b239, b240). Additionally it has been possible to use scanning electron microscopy (SEM) on filter samples in order to use particle counting software to calculate a coarse mode size distribution. Each instrument, limitations, and corrections applied, are described below.

1. Cloud Droplet Probe (CDP)

   The CDP is an optical particle counter which uses scattered light to size the particles as they traverse a laser beam. It is mounted non-optimally 10cm away from the aircraft skin which resulted in some initial uncertainty in the sample volume as a function of particle size. Subsequent comparisons with several cloud instruments were used to determine the sample volume which showed a consistent behaviour for droplet sizes below $r = 20\mu m$ (Abel, 2007). On the basis of these comparisons the CDP number concentration for particles up to this size has been adjusted by a factor of 0.35 to account for uncertainties in the sample volume. Above $r = 20\mu m$ the CDP has a shadowing effect due to its position on the aircraft and hence data from sizes larger than this has been discounted. The lower edge of the CDP size bin is not well defined and has also been discounted.

   In cases where full size distributions have been used in this thesis, the CDP size distribution has simply been joined onto the PCASP size distribution, and in most cases the transition from PCASP to CDP size distribution appears smooth. The CDP made measurements roughly every $10s$ during DODO2, and therefore data is available for both straight and level runs, and vertical profiles.

2. Scanning Electron Microscope (SEM)

   Particle counting software was used on SEM images of dust samples (such as Figure 3.7, Chapter 3) to obtain a size distribution. The software uses brightness levels to detect the particles and fits an outline to them. From this the circumference, and

a circular equivalent diameter can be calculated (Chou *et al.*, 2008). The smallest four size bins from the SEM size distribution were defined to be the same as the largest four bins from the PCASP, so that the two size distributions overlapped and could be compared directly.

This is a 2-D procedure which measures geometrical diameter. Non-spherical flat particles are likely to be deposited on the filter samples with the side of largest surface area lying parallel to the filter. This may lead to an overestimate of diameter in comparison to the optical particle counters which measure diameter of particles in all orientations. Measurements of SEM size distributions from specific cases are examined in more detail in Chapter 4.

2.4 Identification of Dust Aerosol

The dominant aerosol types encountered during DODO were mineral dust (both campaigns) and biomass burning aerosols (DODO1 only). In order to isolate runs where the accumulation mode was dominated by dust only, runs where scattering from the nephelometer at 450nm was greater than 550nm and 700nm were removed, on the assumption that these runs were dominated by biomass burning aerosol (where the predominance of smaller particles result in greater scattering at smaller wavelengths).

For the remaining runs, data from the AMS and filter samples (both SEM and TEM analysis) have been used. Filter sample data for SEM samples from flights b175, b237, b238 and b242 have been analysed using the SEM, and do not suggest any mixing of aerosol types or the presence of other components, including sulphate coatings on the dust particles. The results are described in more detail in Chapter 4, but in these samples very few particles other than dust were observed.

AMS data is available for all the runs during DODO1, but not for DODO2. The AMS provides results on the composition in terms of μgm^{-3} of organics, sulphates, nitrates and ammonium, and these results represent the submicron portion of the aerosol. The PCASP size distribution data for these runs has been used to calculate the total submicron mass, from which the percentage of non-dust submicron mass can be calculated using the AMS

data. These results show that the runs selected had less than 15% of the submicron mass constituted by organics, sulphates, nitrates and ammonia, and were therefore dominated by dust. For the runs selected from flights b168 and b175, the submicron mass of the non-dust components reached a maximum of 5%, whereas the dust encountered during flights b173 and b174 reached a maximum of 15% of the mass being supplied by the non-dust components, with the average mass of sulphates contributing between $0.7 - 1.1 \mu g m^{-3}$ for b173 and b174 (low loadings). Thus it appears that the dust from b168 and b175 was much purer dust than was sampled during b173 and b174. This may be related to the trajectory that the air had taken before passing over the Sahara, which appeared to be the Spain/Portugal region (see Chapter 3). However, despite this, it is clear that the samples were dominated by dust.

The results presented in Chapter 3 examine the likely origins of the air masses in which dust was measured. These results were not used in the selection criteria for the runs chosen, but are consistent with the runs chosen being dominated by dust, having origins over the Sahara. The runs selected as being dominated by dust aerosol are described in Table 2.6, and are examined in the following chapters in terms of their microphysical and optical properties.

2.5 Chapter Conclusion

This Chapter has described the meteorology and dust events that occurred during the DODO campaigns, and the instrumentation and relevant correction processes that have allowed measurements of the dust to be made. The following two Chapters describe the dust vertical profiles encountered, dust sources and dust composition (Chapter 3) and the dust microphysical and optical properties (Chapter 4).

Flight	Run	Altitude/km	Comment
b168	R6	0.5	Low level dust over Mali
	R15	0.1	Low level dust north of Dakar over ocean
	R16	1	Low level dust north of Dakar over ocean
b173	R8, R9	0.5	Low level dust, runs parallel to and along Mauritanian coastline
b174	R3.1, R3.2	0.2	Low level dust south of Dakar over ocean
	R4.1, R4.2, R4.3, R4.4, R4.5	0.05	Low level dust south of Dakar over ocean, successive runs nearer to Dakar (upwind)
b175	R2	0.3	Moderate dust storm over Mauritania
	R6	1.5	Moderate dust storm over Mauritania
	R7.1, R7.2	0.25	Moderate dust storm over Mauritania
b236	R2.1	6	Top of well mixed dust layer over Mali/Mauritania
	R5.1	1.5	Bottom of well mixed dust layer over Mali/Mauritania
b237	R2	5	SAL over ocean
	R3	2.5	SAL over ocean
	R4	0.03	Below SAL over ocean
	R5	0.03	Below SAL over ocean
	R6, R7	5	SAL over ocean
b238	R3.1, R3.2, R3.3, R3.4	0.3	Heavy dust storm over Mauritania
	R4.1	1	Heavy dust storm over Mauritania
	R5.1	2.5	Heavy dust storm over Mauritania
	R6.1	3.5	Heavy dust storm over Mauritania
	R7.1	5	Heavy dust storm over Mauritania
b239	R1	2.5	SAL over ocean
	R2-4	2.5	SAL over ocean, three runs of short duration merged
	R5	3	SAL over ocean
	R6	2	SAL over ocean
b241	R2	2.5	Intercomparison with NASA DC-8, SAL over ocean
	R5	0.5	Below SAL over ocean
b242	R1.1	4	SAL over ocean
	R5.1	3.5	SAL over ocean

Table 2.6: *Runs selected (as being dominated by dust aerosol) and used in this thesis for analysis of microphysical and optical properties. Note that no runs from b240 were used due a computer failure resulting in no cloud physics data being available.*

Chapter 3

Dust Vertical Profiles, Sources and Composition

3.1 Introduction

It is important to understand how the meteorology in both seasons affects the vertical profiles of the aerosol and where the dust originates from, as both of these factors affect the transport of the dust, and therefore potentially the size distribution. The chemical composition of the dust is equally important and is examined here, along with potential dust source regions, which are expected to determine (or at least influence) the chemical composition of the uplifted dust. Section 3.2 describes the vertical structure of the aerosol encountered during DODO, Section 3.3 investigates the potential sources of dust measured during DODO, and Section 3.4 describes the results available on the chemical composition of the DODO dust.

3.2 Vertical Profiles

3.2.1 Scattering Profiles

Figure 3.1 shows selected cases of the vertical profiles of aerosol scattering at 550nm from the nephelometer, the Angstrom exponent over wavelengths 550nm to 700nm, and temperature and dew point temperatures. Small or negative Angstrom exponent values indicate larger particles, more likely to be dust, whereas larger values indicate biomass burning aerosols or anthropogenic aerosols. Large amounts of scatter in the Angstrom exponent indicate noise in the scattering signal due to very low amounts of aerosol particles. The structure of the temperature and dewpoint temperature profiles gives an indication of the humidity of the air and can indicate the location of the boundary layer, as well as temperature inversions which can limit vertical mixing. The amount of scattering indicates the amount of aerosol present (though the size of the particles will also affect the scattering).

Over land, close to dust sources, vertical profiles are quite similar for both the dry and wet season (Figures 3.1(a), 3.1(b)), both showing a dust layer close to the surface, indicated by the scattering profiles and small to negative values of Angstrom exponent. Figure 3.1(a) for the dry season shows a thick dust layer extending from the surface to

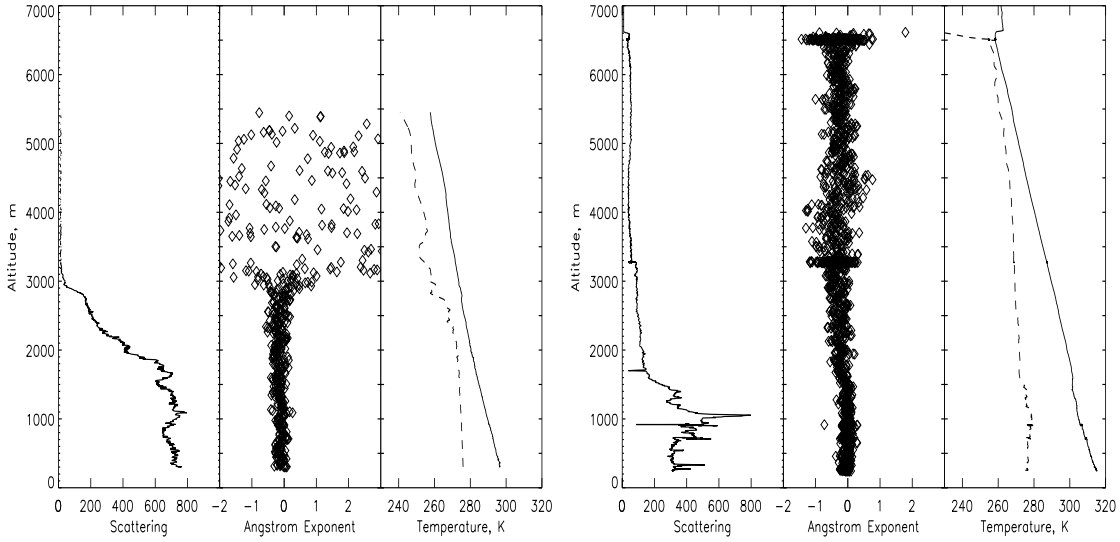

(a) Dry season, desert, b175 P7

(b) Wet season, desert, b238 P3

(c) Dry season, ocean, b174 P6

(d) Wet season, ocean, b237 P2

Figure 3.1: *Vertical profiles of aerosol scattering at 550nm from the nephelometer in Mm^{-1} (corrected as described in Chapter 2), the Angstrom exponent over wavelengths 550nm to 700nm, temperature and dew point temperature. Cases shown are for over desert in Mauritania (top) and over ocean (bottom) in the dry season (left) and wet season (right). Flight numbers and profile names are indicated below each figure.*

3000m with the largest scattering towards ground level. Figure 3.1(b) for the wet season shows a similar layer also extending to around 3km, but with peak scattering at around 1km. Above 3km, low scattering values ($< 100Mm^{-1}$) extend up to 6000m, whereas in the dry season no aerosol was seen above 3000m. The temperature and dewpoint temperature profiles indicate that the altitudes at which the scattering drops off sharply is the same as the altitude where temperature inversions occur - at 6km in the wet season (Figure 3.1(b)) and at 3km in the dry season (Figure 3.1(a)). There is also a minor temperature inversion at around 1500m in Figure 3.1(b), level with the altitude where scattering drops off sharply above the scattering peak at 1km. Thus the boundary layer heights are strongly linked to dust profiles, as would be expected.

Figures 3.1(c) and 3.1(d) show the typical vertical profiles over the ocean during the dry and wet seasons, from flights b174 and b238. There are two aerosol types present in Figure 3.1(c): the lowest aerosol layer below 1km being dust, containing larger particles (indicated by the small to negative angstrom exponent values), and the layers between 1.5 to 4km being biomass burning aerosol dominated by smaller particles (indicated by the much larger Angstrom exponent values of between 0 and 1.7 - see Chapter 2 for a more detailed examination of aerosol species). Carbon monoxide and ozone were also found to be positively correlated with scattering in this upper layer, again indicating biomass burning aerosol. This type of profile was typical of the DODO1 (dry season) flights over the ocean, especially to the south of Dakar, with a low altitude layer of dust, present to varying degrees, and a higher altitude layer(s) of biomass burning aerosol.

In contrast, during the wet season the aerosol profile over the ocean is very different to the dry season. In Figure 3.1(d) there is no biomass burning aerosol present, and instead a layer of weaker scattering particles is present, particularly between 4-6km, which is the Saharan Air Layer (SAL), containing mineral dust, again with small to negative values of the Angstrom exponent. This dust has been uplifted over the Sahara (see Section 3.3) by moist or dry convective activity to altitudes with a high potential temperature, and then advected westwards over the Atlantic Ocean where it becomes separated from the surface by the cooler, moister marine boundary layer. As indicated by the temperature and dewpoint profiles, the SAL is dry and humidities are mostly low (under 60%), and there

is a strong temperature inversion at the top, which is typical of the SAL. Below around 4km dust is still present but with lower scattering values, indicating less dust. Between 1.5km and 4km, it appears from the temperature profile that this is dust within another dry air mass, separated from the layer above by a slightly moister layer. From 6km to 1.5km, the Angstrom exponent shows a gradual decrease from 0 to -1, indicating larger particles present towards the base of the layer. Below 1.5km there is an absence of aerosol particles down to 1km, where the marine boundary layer begins, which also contains dust particles, with negative Angstrom exponents and high humidities (over 80%). Filter samples indicate that this aerosol was indeed dust and that negligible sea salt aerosol was present (see Section 3.4). The very negative Angstrom exponents suggest the presence of larger particles and possibly deposition from the dust layer above. (The origin and chemical properties of this aerosol layer are discussed further in Section 3.3). Though the general picture of wet season dust transport is for the majority of dust to be within the Saharan Air Layer, it appears that dust is also found within the marine boundary layer, as has been suggested by Colarco *et al.* (2003) and found from lidar measurements by Liu *et al.* (2008b).

Figure 3.1 shows a selection of profiles from DODO which were representative of the other profiles performed during the campaigns. During the dry season, dust was not always found below the biomass burning layers, but when present, the vertical extent varied between 500 to $1500m$, and always extended right to the ocean surface (or within the 30m altitude permitted for the aircraft). The vertical structure was mostly a single layer, which dropped off sharply at the top of the layer at the altitude of the temperature inversion. Occasionally two dust layers were observed. The dry season biomass burning aerosol layers were found between a minimum of $1000m$ to a maximum of $5000m$, and the structure varied between a single layer to multiple layers (e.g. Johnson *et al.*, 2008). There was always a 'clean slot' with no aerosol present between the biomass burning aerosol and the lower dust layer. Therefore Figure 3.1(c) is representative of the range of flights during DODO1. The flight over the Mauritanian desert (Figure 3.1(a)) cannot be analysed in terms of representativity, since this was the only dry season flight over the desert. Airborne lidar data, such as that from CALIPSO, will be valuable in evaulating

this.

In the wet season the vertical structure of the dust was more variable. There were frequently several layers in the dust outbreaks over the ocean, and the vertical span of the dust varied from very narrow (around $500m$ during part of flight b239) to very broad ($4000m$ in the case of one profile during b239) and more evenly distributed in the vertical than that for b237. Vertical profiles from flight b236 over the desert show quite a different structure to that from b238 in Figure 3.1(b) - the dust was elevated above $1000m$, and during different profiles peaked at altitudes between $3000m$ to $5000m$, perhaps because the dust was being transported from further afield, rather than being in the process of uplift as in b238.

The vertical profiles shown in Figure 3.1 are broadly consistent with what is expected from West African seasonal dynamics, with the greater convective activity during the wet season allowing dust to be uplifted to higher altitudes, and with low-level dust transport in the dry season. The seasonal variation in vertical profiles will have important effects in terms of the longwave radiative effect, which depends on the altitude of the dust layer (e.g. Highwood *et al.*, 2003), and also on deposition of nutrients to the ocean, a process which might be expected to take longer for a higher altitude dust layer. However, considerable variation within this idealised picture is evident, such as the deeper dust layer shown in Figure 3.1(a) extending to 3km and dust within the marine boundary layer in Figure 3.1(d). A ubiquitous biomass burning aerosol layer was detected by the instrumentation and clearly visible by eye during almost all the flights during the dry season, but notably not during the more northerly flights, including flight b175 over the desert in Mauritania. The difference between vertical profiles over land and ocean is apparent, in particular with the warm dusty SAL air overlaying the marine boundary layer in the wet season but not in the dry season. The differences shown in Figure 3.1 demonstrate that dust was being transported differently during each campaign during DODO, and may have different impacts on the size distributions between campaigns.

Additionally the differences in the height of the boundary layer containing the dust between the two seasons is of importance. Several studies have located dust sources based on the TOMS Aerosol Index (AI) (e.g. Herman *et al.*, 1997; Prospero *et al.*, 2002; Ginoux

et al., 2001; Goudie and Middleton, 2001; Engelstaedter *et al.*, 2006), by locating regions of North Africa with persistently high AI values as dust sources. However, as pointed out by Mahowald and Dufresne (2004), the TOMS AI is sensitive to the boundary layer height, with higher boundary layers leading to greater values of AI. The results shown here confirm that dry season dust is found at low altitudes, with the boundary layer and dust top level varying between 500m-3km. Thus, as shown by Mahowald and Dufresne (2004), low boundary layer heights in the dry season are likely to lead to dry season dust sources being underestimated. For example, the TOMS AI images in Chapter 2 do not show the dust encountered over the coast during flight b173, which reached altitudes of $1.5km$, wherease they did show the b175 dust which extended to $3km$. Comparison with dust from the other dry season flights is not straightforward due to the presence of biomass burning aerosol above the dust layers, which TOMS also detects. However, very recent studies using new space-borne lidar data (such as Liu *et al.* (2008b)) to examine dust outbreaks should provide a good way to overcome this limitation.

3.2.2 Size Distribution Profiles

Figure 3.2 shows how the measured size distributions change in the vertical. The colours indicate the number concentration at a particular radius. This figure format is used as it provides a detailed view of how the size distributions change in the vertical, without having to average over layers. (See Section 4.2.3 for conventional plots of size distribution changes in the vertiacl). The accumulation mode size distribution is measured by the PCASP, and extends to a radius of $1.5\mu m$. The CDP was available only during DODO2 and covers the range $r = 1 - 20\mu m$. As described in Chapter 2, the CDP was an experimental instrument during DODO2 and cannot be accurately relied upon, which explains why the CDP and PCASP overlap is not always smooth in Figure 3.2. It does, however, give a good qualitative indication of the vertical changes in coarse mode size distribution, particularly since the profiles shown in Figure 3.1 do not provide any information on the coarse mode particles.

In general, the size distribution profiles are complimentary to the scattering profiles shown in Figure 3.1. Over land, it is clear that the peak dust concentrations were found closest to the surface, with both the number concentration and the contribution from larger particles decreasing with altitude. In Figure 3.2(a), the number of particles larger than $0.2\mu m$ drops sharply at 3km, consistent with the sharp drop seen in the scattering profile in Figure 3.1(a). Interestingly, the PCASP data shows the presence of particles smaller than this up to 5km, though since this is not seen in the nephelometer scattering data it indicates that these particles are not very optically effective. In Figure 3.2(b) there is a significant number of particles all the way up to 6.5km, consistent with the altitude in 3.1(b) at which scattering drops off sharply and the temperature inversion occurs. For both profiles in the dry season, the greater number of larger particles closer to the surface is consistent with Stokes' theory that smaller particles, requiring smaller uplift velocities, can be uplifted to greater altitudes.

Over the ocean the profiles of size distribution are also consistent with the scattering and temperature profiles. Figure 3.2(c) clearly shows the biomass burning aerosols between 1-4km with radii smaller than around $0.2\mu m$. The dust layer can be seen below 1km, with more particles of radius greater than $0.2\mu m$ in comparison to the biomass burn-

ing layer. There is a sharp decrease in the number of particles at around $500m$ where the dust layer ends - this occurrs at all radii (though due to the choice of colour bar the drop in number concentrtion in the orange colours appears more obvious). In the wet season, the very different profile can be seen in Figure 3.2(d). Here peak number concentrations in the coarse mode are found between around 3.5-4.5km, slightly lower than the peak in accumulation mode particles and in scattering from Figure 3.1(d). This is an indication that the nephelometer is reacting more strongly to particles in the accumulation mode, and that variations in scattering due to coarse mode particles are not reflected in the scattering data. The cleaner layer seen in Figure 3.1(d) between 1-1.5km is also seen in Figure 3.2(d). Here the number concentration of coarse mode particles, and accumulation mode particles in the range $r = 0.5 - 1.5\mu m$ drops off sharply. This may be because the two layers are being transported from different locations and under different meteorological conditions. The temperature inversion then prevents them from merging. Below 500m, there is a sudden increase in the number of coarse mode particles which is not so marked in the accumulation mode data. This increase in large particles may be due to the dust layer above depositing larger particles.

In summary, the vertical profiles of size distribution differ between the two DODO campaigns and between land and ocean cases, and can be explained by the differing meteorology between the dry and wet season. It is clear that the different meteorology results in a different vertical structure to the dust, different transport mechanisms, and different size distributions.

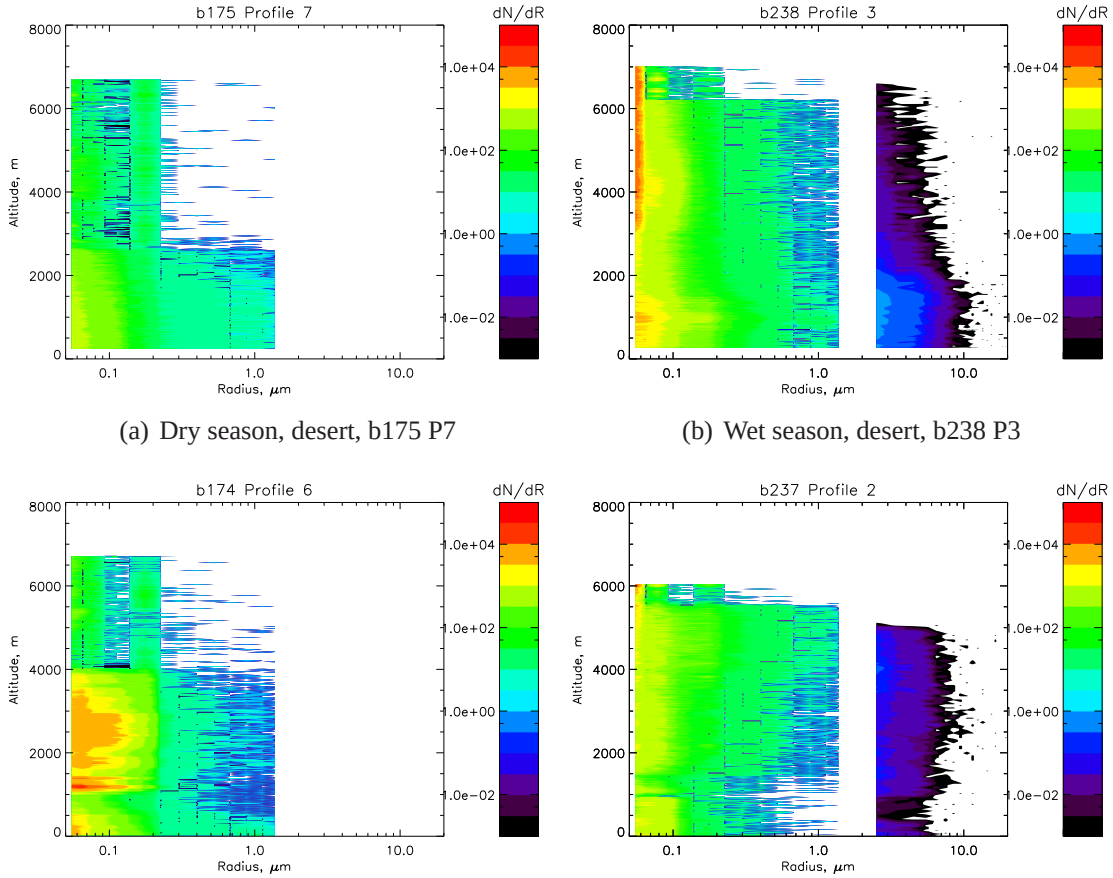

(a) Dry season, desert, b175 P7

(b) Wet season, desert, b238 P3

(c) Dry season, ocean, b174 P6

(d) Wet season, ocean, b237 P2

Figure 3.2: *Vertical profiles of size distribution for the same cases as shown in Figure 3.1. Colours indicate number concentration ($\frac{dN}{dr}, cm^{-3}\mu m^{-1}$). Size distributions are covered by the PCASP for the accumulation mode (up to $r = 1.5\mu m$) and the CDP for the coarse mode ($r = 1 - 20\mu m$). CDP data is only available for DODO2 flights. Corrections to CDP data are described in Chapter 2.*

3.3 Source Attribution using NAME

3.3.1 Methodology

The origin of the air masses observed during DODO have been investigated using the Met Office Numerical Atmospheric-dispersion Modelling Environment (NAME) (Ryall and Maryon, 1998). This is a Lagrangian particle model in which emissions from pollutant sources are represented by air parcels driven backwards in time by meteorological fields from the Unified Model (Cullen (1993)). Although NAME was initially designed as an emergency response tool, it has subsequently been developed for numerous applications, including tracing the origin of air masses containing aerosols (e.g. Gloster *et al.*, 2007; Witham and Manning, 2007; Webster *et al.*, 2007).

NAME has been used for DODO by tracing air masses backwards over five days from locations where the aircraft sampled dust, in order to gain an understanding of the possible dust source locations. This has been done using the locations of runs where the aircraft measured dust, since data from these runs have been used to calculate the dust optical properties in Chapter 4. NAME was initiated at times corresponding to the duration of the aircraft runs, and at locations (latitude, longitude and altitude) corresponding to that of the aircraft over the entire run. The trajectories of particles released within this volume are then followed backwards in time by NAME, over 5 days - a typical lifetime of dust in the atmosphere. When the particles enter a layer close to the surface, chosen to be altitudes of 0-200m, the location of the particles has been recorded and mapped. Thus the origin of the air masses sampled can be traced back to when they were close to the surface, which is likely to indicate the location of dust uplift.

Caution should be exercised when interpreting the NAME results, however. The results indicate where the airmasses were close to the surface, not where dust was actually uplifted. Dust uplift is dependent on many factors, such as surface windspeeds and surface moisture. Since NAME is not a dust uplift model, these factors are not taken into account in the results shown in Section 3.3.2. Therefore the results shown in Section 3.3.2 should be interpreted as showing locations where possible dust uplift may have occurred, had sediment availability and uplift conditions been favourable. Therefore if source regions

occur over the ocean, this indicates only that air originated over the ocean, not that the ocean is a dust source.

3.3.2 NAME Results

Results from NAME are shown in Figures 3.3, 3.4 and 3.5. They show the locations of the air masses when they were close to the surface, in the lowest 200m of the atmosphere, in order to give an indication of possible dust uplift locations for the dust measured by the aircraft.

Figure 3.3 shows that during the dry season the dust laden air sampled by the aircraft had been transported in well defined plumes from a northeasterly direction, consistent with climatological winds over North Africa. Thus most of the dust sampled during DODO1 is likely to have been uplifted in Mauritania, Morocco, Western Sahara and Algeria. The dust sampled during b168 appears to have a less northerly trajectory than the rest of the DODO1 dust, with sources also including northern Mali. The overall picture of dust transport during DODO1 is consistent for all cases examined, with dust being transported by a well-defined plume from the northeast.

NAME results in Figures 3.4 and 3.5 indicate that this is not the case for the wet season. Dust sampled during the various runs appears to have originated from a variety of widespread geographic locations. This indicates that both dust sources and transport mechanisms were different and more varied during DODO2. The cases of dust measured during flights b237 and b238 shown in Figure 3.4 show that even within single flights, the dust measured at different altitudes originated from different parts of Africa. For both b237 and b238 the dust encountered at higher altitudes had been transported from further east than dust measured at low altitudes.

Interestingly, all the cases where dust was found at low altitudes during the wet season (Figures 3.4(a), 3.4(d), 3.4(e) and 3.5(g)) appear to have northeasterly origins with obvious plume patterns, in a similar way to the DODO1 results. In the case of b237 R5 and b241 R5 (Figures 3.4(a) and 3.5(g)) the principal origin of the airmasses where dust was sampled appears to be over ocean, though some air for b237 R5 does originate from Western Sahara and Morocco and some air for b241 R5 also originates from Mauritania,

Mali and Niger. Note that these runs have been identified as dust from the procedure described in Chapter 2. In particular, the case of b237 R5 will be examined in more detail in terms of composition in Section 3.4.

It is interesting to note that the dust found during flight b242 and b241 R2 has more southerly origins (b242 - southern Algeria, Mali and Niger, b241 - Mauritania, Senegal, southern Mali, Burkina Faso, southern Niger and western Chad) than the other flights. Since dust originating from more southerly sites in the Sahara/Sahel are thought to have higher contents of absorbing iron oxides (e.g. Claquin *et al.*, 1999; Alfaro *et al.*, 2004; Lafon *et al.*, 2006), this is of interest, and will be discussed further with respect to the optical properties in Chapter 4.

It is noticeable that the plumes from flights b173 and b174 have origins towards Spain and Portugal as well as over northwest Africa, and that the air may therefore contain anthropogenic European pollution or aerosols. Filter samples from these flights have not been analysed and therefore cannot confirm this. However, the AMS submicron mass percentage of sulphates was higher for the runs in b173 and b174 (Chapter 2), which is consistent with the NAME results. However, the total percentage of non-dust mass was still very low.

In order to account for the NAME results not including uplift potential, forward model runs were undertaken for the cases in flight b238, which incorporated a dust uplift scheme (Athanassiadou *et al.*, 2006). In this dust model, dust is dynamically lifted, transported and deposited on the basis of the surface properties and meteorology. The results indicated that essentially all the dust observed at low altitude (Run 3.3) originated from the region west of $0^{\circ}E$. This region accounted for approximately 80% of the dust observed at mid level runs (Run 5.1), but only 10% of the dust observed at high altitudes during Run 7.1, with the remainder having been transported from further east. Therefore these dust model results support the hypothesis drawn from the NAME air mass origin results that for b238 the high altitude dust had been transported over larger distances than the dust sampled at lower altitudes, and also that the dust sources were different at different altitudes.

The dust sampled during b173 and b174 appear to have very similar air mass ori-

gins, both having sources in northern Mauritania, northern Western Sahara, and southern Morocco. Thus it appears that the same dust event was encountered on consecutive days, with b173 encountering it along the west African coast and b174 sampling it further downstream to the southwest of Dakar. This makes these two flights particularly interesting, as they can be potentially used to analyse the direct effects of transport on dust, which will be examined in more detail in Chapter 4.

In summary, the dust measured appears to have different sources between the two DODO campaigns. This suggests firstly that the dust may have different composition, if the properties of the parent soils differ, and secondly that the transport distances are different, which may affect the size distributions. Additionally during the wet season there is a greater variation in the suggested location of the sources, both for different flights and within a single flight. Thus if this causes variation in the microphysical and chemical properties of the dust, the optical properties could be expected to be more varied during DODO2 than during DODO1. However, it should be noted that more dust flights were operated during DODO2 than DODO1, and differences between the two campaigns may be partly due to the limited meteorology experienced during DODO1, rather than a true seasonal difference.

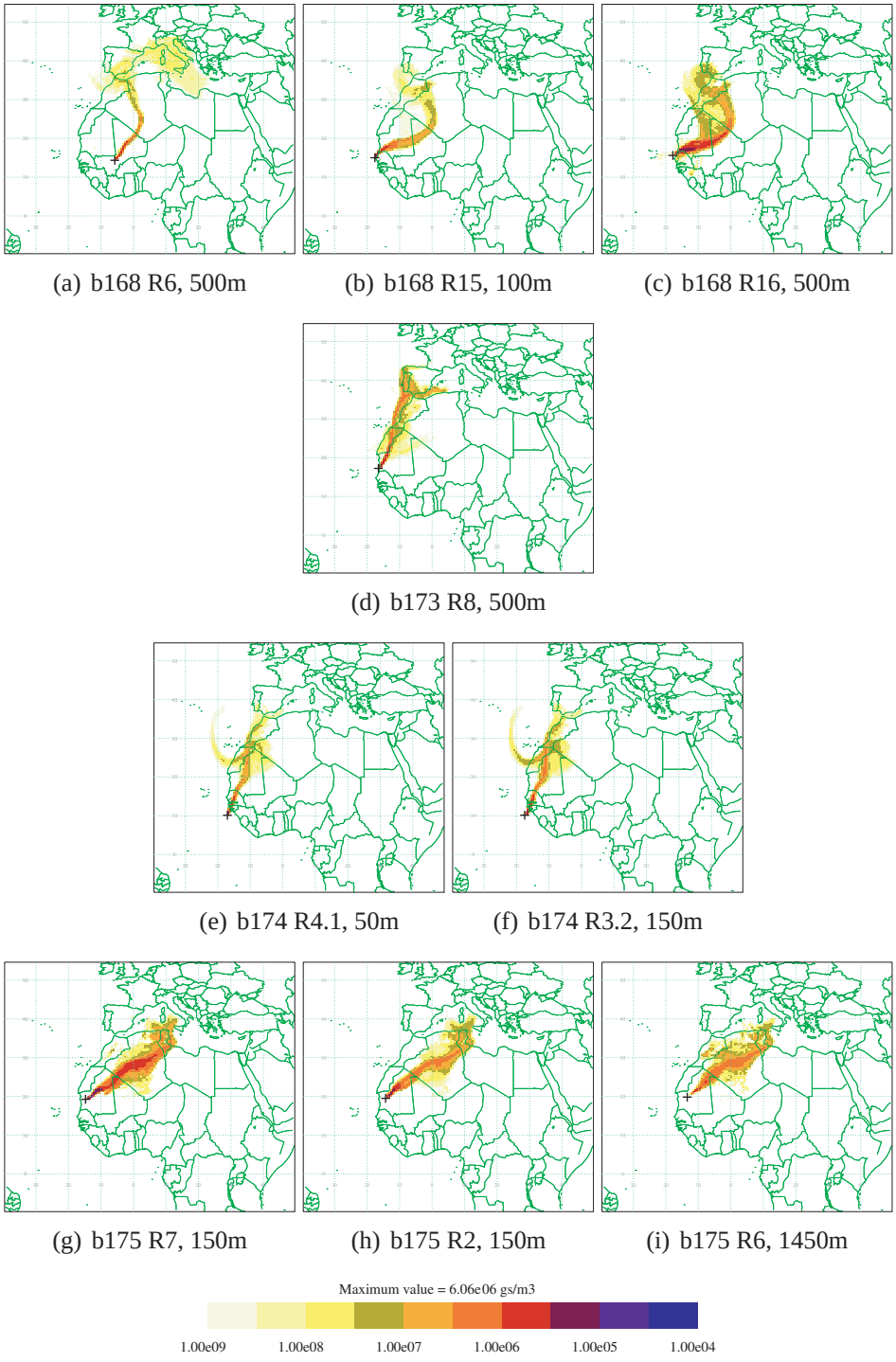

(a) b168 R6, 500m (b) b168 R15, 100m (c) b168 R16, 500m

(d) b173 R8, 500m

(e) b174 R4.1, 50m (f) b174 R3.2, 150m

(g) b175 R7, 150m (h) b175 R2, 150m (i) b175 R6, 1450m

Figure 3.3: *Dry season results of five day particle release experiments from the UK Met Office NAME model, indicating the likely origin of dust encountered during runs where the aircraft sampled dust. Colours indicate particle concentration within the lowest 200m of the atmosphere. Results from the same flight are grouped by line, starting with dust found at the lowest altitudes from the left. Text below each figure indicates flight and run number, and altitude of the run where dust was measured. Altitudes correspond to the runs where optical properties are calculated, as described in Chapter 2. Units are arbitrary, but should be interpreted as the number of particles within the 0-200m layer. Black cross indicates the location where the aircraft measured the dust.*

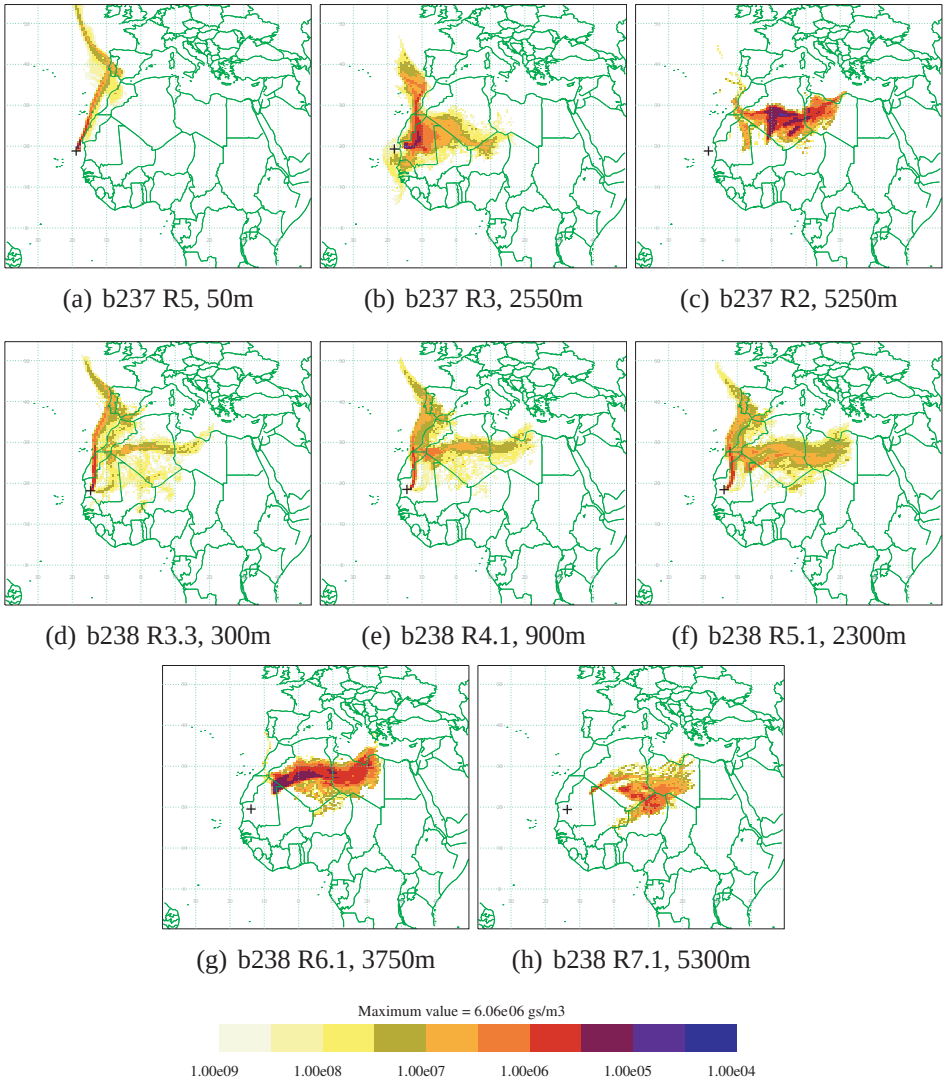

(a) b237 R5, 50m (b) b237 R3, 2550m (c) b237 R2, 5250m

(d) b238 R3.3, 300m (e) b238 R4.1, 900m (f) b238 R5.1, 2300m

(g) b238 R6.1, 3750m (h) b238 R7.1, 5300m

Figure 3.4: *Same as Figure 3.3 but for flights b237 and b238 during the wet season.*

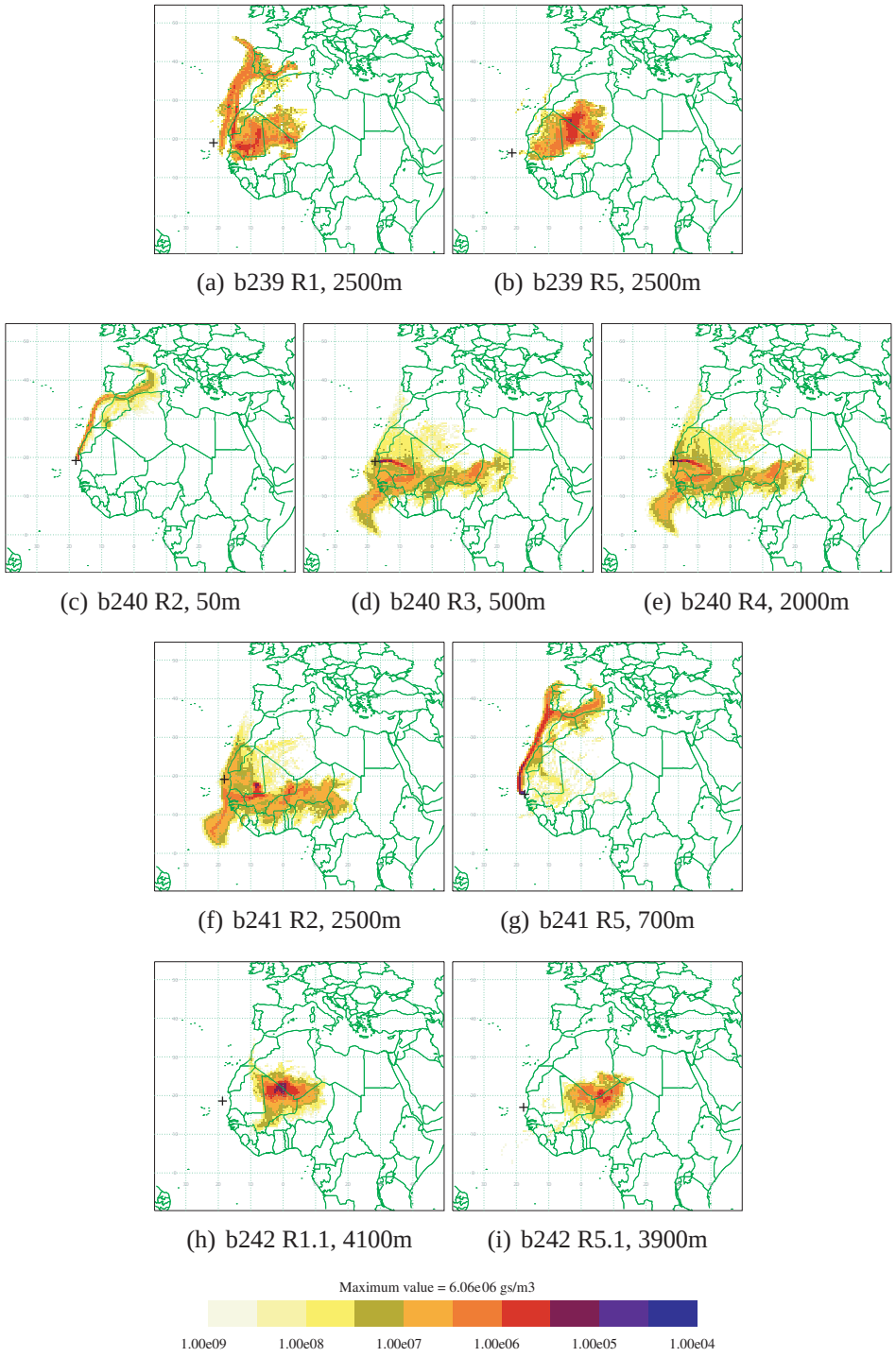

(a) b239 R1, 2500m (b) b239 R5, 2500m

(c) b240 R2, 50m (d) b240 R3, 500m (e) b240 R4, 2000m

(f) b241 R2, 2500m (g) b241 R5, 700m

(h) b242 R1.1, 4100m (i) b242 R5.1, 3900m

Figure 3.5: *Same as Figure 3.3 but for flights b239, b241 and b242 during the wet season.*

3.4 Composition of DODO Dust

3.4.1 Elemental Ratios

Elemental concentrations for the combined accumulation and coarse modes were measured by particle induced X-ray emission (PIXE) at the Laboratorio di Tecniche Nucleari per i Beni Culturali (LABEC) at Florence, Italy (Chiari *et al.*, 2005; Calzolai *et al.*, 2006). Ratios of elemental concentrations usually associated with dust have been calculated for the same cases as those described in Chapter 2 and are shown in Table 3.1 along with similar results from other work. Elemental ratios are useful in understanding the composition of the dust, as well as giving an insight into different dust source locations (e.g. Chiapello *et al.*, 1997). Note that the ratios here are for runs corresponding to the runs examined in terms of optical properties in Chapter 4, and differ from the DODO results presented in Formenti *et al.* (2008), who present results from the whole of DODO.

Campaign/Measurement Location	Reference	Si/Al	Ca/Al	K/Al	Fe/Al
DODO1		2.7 (0.2)	1.1 (0.4)	0.3 (0.1)	0.7 (0.1)
DODO2		2.6 (0.3)	0.5 (0.2)	0.2 (0.1)	0.7 (0.1)
DABEX	Formenti *et al.* (2008)	3.0 (0.6)	0.5 (0.3)	0.3 (0.2)	0.7 (0.3)
Banizoumbou, Niger	Formenti *et al.* (2008)	2.7 (0.3)	0.4 (0.1)	0.2 (0.05)	0.59 (0.06)
Izana, Tenerife	Kandler *et al.* (2007)	2.14	0.28	0.2	0.58
SHADE, Eastern Tropical Atlantic	Formenti *et al.* (2003)	2.18	0.35	0.21	0.53
Barbados	Reid *et al.* (2003a)	2.13	0.38	0.17	0.3
Sahelian dust at Sal	Chiapello *et al.* (1997)	2.03 (0.09)	0.2 (0.1)		
North Saharan dust at Sal	Chiapello *et al.* (1997)	2.32 (0.05)	0.6 (0.19)		

Table 3.1: *Mean elemental ratios measured from PIXE for DODO filter samples corresponding to the runs examined in Chapter 4. Values in parentheses represent one standard deviation of the sample. Elemental ratios of Saharan dust for other studies are also shown.*

Average ratios for Si/Al are 2.7 ± 0.2 and 2.6 ± 0.3 for DODO1 and DODO2 respectively. These are somewhat higher than previous results from SHADE in Formenti *et al.* (2003) and from the range of results for different origins given by Chiapello *et al.* (1997), but less than the value in crustal rock Mason (1966) - rock which has not been uplifted. It is possible that transport affects this ratio, since some of DODO1 and DODO2 samples were much closer to the source of the dust than those in the previous studies. It is also possibly due to different source regions having different characteristics. Chiapello

et al. (1997) suggest that dust from the northern Sahara has higher Si/Al ratios based on the lower kaolonite content in the soil. Of all the clay minerals, kaolonite has the lowest Si/Al ratio. However, despite some of the DODO2 sources appearing to be more towards the Sahel, there is no significant difference between the DODO1 and DODO2 samples for Si/Al, or indeed between the ratios for the individual flights (not shown). Formenti *et al.* (2008) examined illite to kaolonite ratios for b238 dust compared to other ground-based samples taken at Banizoumbou, Niger, and aircraft measurements from DABEX flights over northern Niger, and found b238 to have much higher illite to kaolonite ratios (0.6) compared to the other samples (0.1-0.3), indicative of sources in northern Africa. This is in agreement with the NAME results for this flight in Figures 3.4(d), 3.4(e) and 3.4(f) suggesting sources in northern Africa.

DODO1 shows substantially higher Ca/Al ratios (1.1 ± 0.4) compared to DODO2 (0.5 ± 0.2). Work by Formenti *et al.* (2008); Rajot *et al.* (2008) indicates from dust measured in Niger during AMMA that sources in northwest Africa are richer in calcium. Analysis of soil samples by Schütz and Sebert (1987) and Gomes (1990) also suggest that soil from the northern Sahara is rich in calcite. This fits in with the dust sources indicated in Section 3.3, with DODO1 sources being based more towards northwest Africa (Morocco, Western Sahara, northern Mauritania and northwest Algeria) than the DODO2 sources. DODO1 was particularly high in calcium compared to the other results shown in Table 3.1, though the average ratio falls within the total range of results shown by Chiapello *et al.* (1997). The Ca/Al ratio for b173 R8/R9 was particularly high at 1.9, though this has little effect on the DODO1 average due to the large number of samples.

The K/Al ratios are low at (0.3 ± 0.1) and (0.2 ± 0.1) for DODO1 and DODO2, similar to the other results for Saharan dust shown in Table 3.1. Fe/Al ratios are similar for DODO1 and DODO2 at (0.7 ± 0.1) for both campaigns. These values are slightly higher than was found from other measurements as shown in Table 3.1. The different source regions for the two campaigns as indicated by NAME do not appear to affect the Fe/Al ratios. This agrees with results from Formenti *et al.* (2003) who show that the Fe/Al ratio is not sensitive to the source region, whereas the iron oxide to iron ratio is. The DODO results appear to have higher Fe/Al ratios than the other results shown in

Table 3.1. This may affect the optical properties, though it is the amount of absorbing iron oxide that is thought to be important to this, rather than the total amount of iron (e.g. Lafon *et al.*, 2006). The iron content is explored further in Section 3.4.3.

It is interesting to note that Chiapello *et al.* (1997) find a good relationship between the K/Ca and Ca/Al ratios, with Sahelian dust having low Ca/Al but high K/Ca ratios, and North Saharan dust the reverse. The DODO elemental ratios fit into this relationship nicely, as shown in Figure 3.6 - the DODO1 samples orignating from the Northern Sahara have high Ca/Al values (an average of 1.1) and low K/Ca values (0.3 average) whereas the DODO2 dust, orginating from sources further south, has average values of 0.5 and 0.5 respectively, consistent with the 'central Saharan' dust classification of Chiapello *et al.* (1997). Figure 3.6 shows the results from all the runs used for these averages, and shows that there is some distinction between the two campaigns. In particular, the results for b241 would be interpreted as having sources most southerly of all the flights under the conclusions from Chiapello *et al.* (1997), which is in agreement with the NAME results in Figure 3.5(f) which show the most southerly air mass origins of all the NAME results.

Contrastingly, Chiapello *et al.* (1997) also found that Fe/Ca and Si/Al ratios were also a good indicator of dust source, with Si/Al values decreasing towards the Sahel, while Fe/Ca values increased. Though the Fe/Ca value for DODO dust increased from 0.7 to 1.5 from the dry to wet season, consistent with northerly sources being higher in Ca, the lack of Si/Al change seen during DODO is not consistent with this, though this may be related to the greater number of data points used in Chiapello *et al.* (1997).

Therefore the main differences in elemental ratios between DODO1 and DODO2 are in the Ca/Al ratio, which reflect the DODO1 dust origins being located in northwest Africa. This suggests that the composition of dust during the two DODO campaigns differed, and may have an impact on the optical properties. Conclusions about differences between different flights and runs are difficult to draw since generally the elemental ratios show low variability between different filter samples within each campaign, and only a few samples are available for each flight.

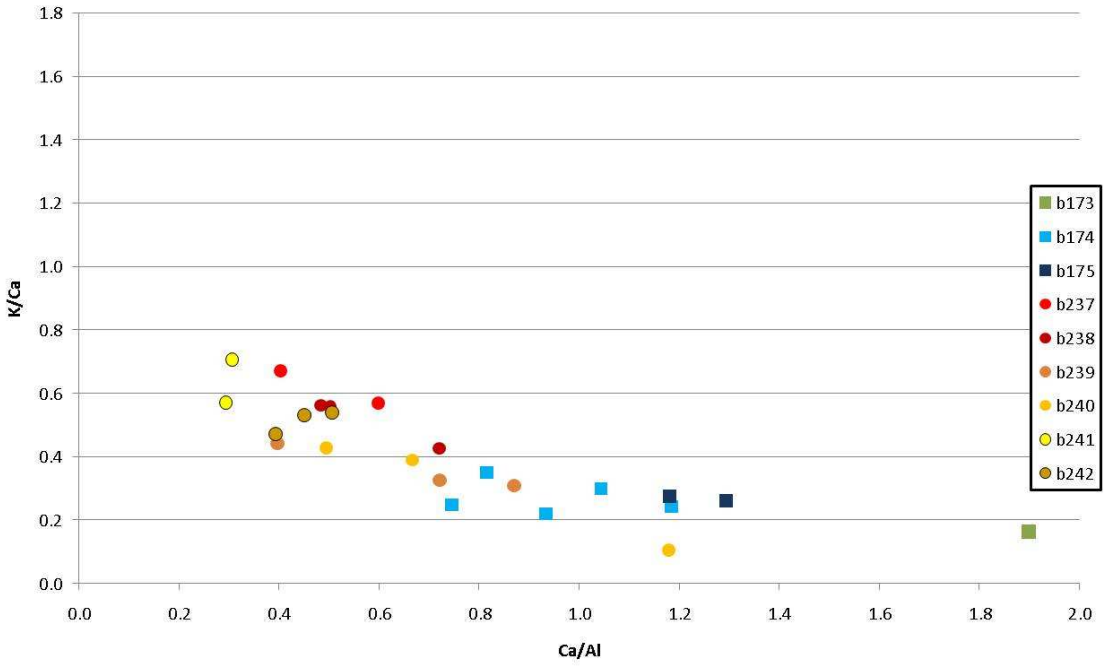

Figure 3.6: *Elemental ratios of K/Ca and Ca/Al separated by flight and DODO campaign, using the same axes as shown in Figure 6 in Chiapello* et al. *(1997). Squares indicate DODO1 flights, circles indicate DODO2 flights. Low K/Ca and high Ca/Al ratios are expected to indicate dust sources in northwest Africa while the reverse indicate Sahelian sources.*

3.4.2 Mineralogy

3.4.2.1 Technique

It has been possible to analyse a limited number of filter samples for mineralogy using a scanning electron microscope (SEM) and transmisson electron microscope (TEM) at LISA, Paris (as described in Chapter 2. This allows the composition of single particles to be determined. In contrast to the results presented in Section 3.4.1, the SEM and TEM results can be analysed in terms of particle number (rather than by mass), and can be separated into fine and coarse modes. The composition of particles has been categorized based on those described in Kandler *et al.* (2007) and Otto *et al.* (2009) using SEM and TEM analysis, and is also similar to that used by Chou *et al.* (2008). An example SEM image is shown in Figure 3.7.

Dust was collected on 90mm diameter Nucleopore filters with pore sizes of $0.4\mu m$ during DODO2. However, DODO1 samples were mistakenly collected on different filters with pore sizes of $5\mu m$, which means that many particles with diameters smaller than

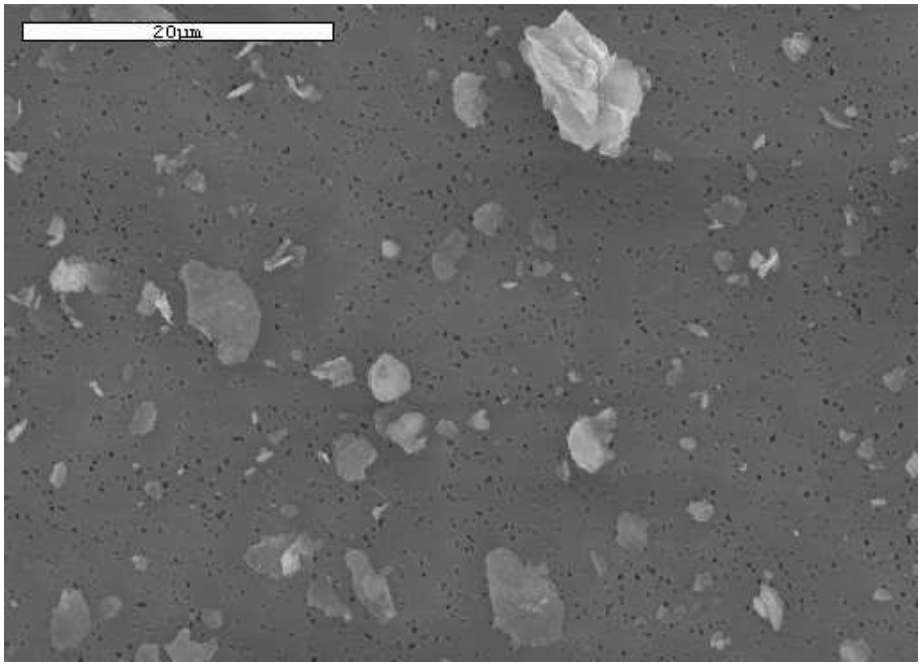

Figure 3.7: *An example of a SEM image from b238 R4.1. Bar on image indicates scale. Small black holes are pores on the filter, larger lighter shapes are dust particles.*

this may not have been sampled. However, it was clear from the b175 sample (the only DODO1 sample analysed) that many particles smaller than this size were still present, though they may not be representative of all particles.

Five samples from runs during DODO have been analysed and are shown in Figure 3.8, as well as two from DABEX which are also shown for comparison purposes. Time limitations prevented further samples being analysed, and also limited the number of particles per sample which could be analysed, which are shown in the legend in Figure 3.8. This number also varied between flights due to the density of dust particles on the filter samples. It is clear that these numbers are not large enough to be statistically rigorous, especially for the DABEX flights where the density of dust particles on the filter samples was lower. The data do, however, give some indication of the main mineralogy of the dust and of the contribution from different minerals.

The SEM data represent composition of particles with diameter greater than $1\mu m$, which covers the upper portion of the measured PCASP size distributions as well as the coarse mode. The TEM data represent particles smaller than $1.5\mu m$ diameter, so there is some overlap in the particle size measured by each instrument. Particles have been

classified according to the the main signal from both SEM and TEM. This means that the presence of trace minerals is not represented in these results - for example, Fe was often evident in the signal even though Silicon and Aluminium were the principal components. Therefore these results are not exclusive, and more sophisticated techniques such as those described in Formenti *et al.* (2008) are required to fully analyse the chemistry of the dust samples. However, Formenti *et al.* (2008) only examine b238 data, so the results presented here are useful for contrasting the various DODO flights.

3.4.2.2 Mineralogy Results

Both Figures 3.8(a) and 3.8(b) show that most particles are alumino-silicate clays. This is consistent with other measurements of African dust (e.g. Formenti *et al.*, 2003; Kandler *et al.*, 2007; Formenti *et al.*, 2008; Otto *et al.*, 2009). Figure 3.8(a) suggests much more variation in the minerals present in DODO dust in comparison to the DABEX samples, with contributions in the DODO dust from gypsum, quartz, NaCl (which may be sea salt or mineral halite), calcium rich particles, and calcium carbonates. This suggests different sources and composition between DODO and DABEX. Some differences between flights are also evident. For b175 (R7.1/7.2, the only DODO1 sample analysed), contributions from non-silicate minerals are much greater than for the DODO2 flights. Differences in composition between the DODO2 flights are also evident, including differences between the two samples analysed from flight b237, which were collected at different altitudes. R2, performed at 5km, found more contribution from gypsum, quartz and Ca-rich particles, whereas R5 performed at 50m was much more dominated by silicates.

The TEM results in Figure 3.8(b) show some differences to the SEM results. Particles composed of carbon, iron and mixtures are now present, whereas they were not in the larger particles. Notably no sulphate particles are present in the fine mode, indicating a lack of anthropogenic pollution in the dust sampled. This is consistent with Formenti *et al.* (2008) finding a lack of coatings on dust particles, but contrasts with Kandler *et al.* (2007) who did find sulphate coatings. No contribution from quartz, NaCl or Ca-rich particles was found in the TEM results, which indicates that these minerals are likely to be larger particles.

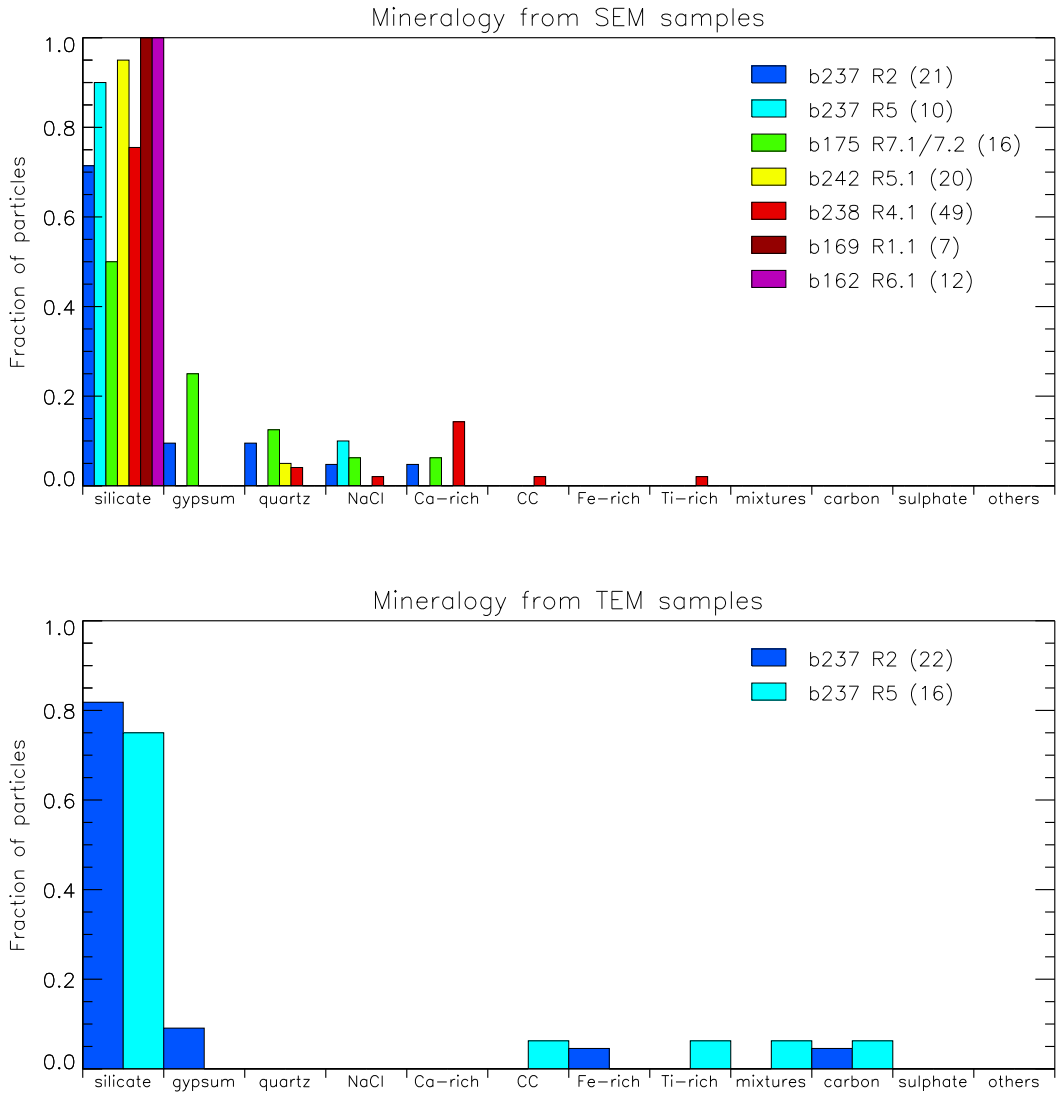

Figure 3.8: *Particle minearlogy for selected flights from scanning electron microscope (SEM) and transmisson electron microscope (TEM) analysis as a function of the fraction of particles analysed. CC indicates calcium carbonates, numbers in parentheses indicate number of particles counted. b162 and b169 were flights from DABEX and are shown for comparison.*

It is interesting to contrast the results for b237 against those measured at 5km (R2) and 50m (R5) altitudes, and between the fine and coarse composition results, especially if the R5 results are indeed for dust being deposited to the ocean from the layer above. If this is the case, these results suggest that the particles being deposited have different composition to those still at higher altitudes. Though both layers are rich in silicate particles, a difference is that the lower layer was lacking in gypsum, quartz Ca-rich and Fe-rich particles, which could have an impact on ocean nutrient supply, particularly through iron. Though the results shown here are not representative of enough particles to form strong conclusions, the results certainly suggest different dust composition in layers of different altitudes.

3.4.3 Iron Content

It has been possible to gain an insight into how the amount of absorbing iron oxide is related to the optical properties of the dust measured through a combination of the SEM and TEM results, and the iron oxide content measured from the filter samples.

Figure 3.9 shows the fraction of particles (of those analysed) from various runs and flights, which were found to contain Fe, even if it was not the main element in each dust particle. For the SEM results (representing particles sized $r > 0.5\mu m, d > 1\mu m$) most iron particles were found for b242, b238 and for b237 R2 (in the elevated dust layer). Significantly fewer Fe particles were found in the DABEX flights (b169 and b162), b175 (DODO1 - though the usage of different filters for this flight prevents proper comparisons), and b237 R5 (in the lower dust layer). This is interesting, since it firstly supports that the wet season dust had different sources and composition to that from DODO1 and DABEX, and suggests that the wet season dust may have been more absorbing than dust from the dry season, if the number of particles containing Fe is representative of the amount of absorbing iron oxide present. Secondly, a large contrast in the number of Fe particles is seen between the two layers of dust in b237, with the upper layer containing more Fe particles. Therefore it appears that the two dust layers observed during b237 had different dust sources, different size distributions, and different composition. Thirdly, b242 R5.1 shows the largest number of Fe particles of all the flights for the SEM results,

which may be linked to the more southerly dust sources suggested by the NAME results.

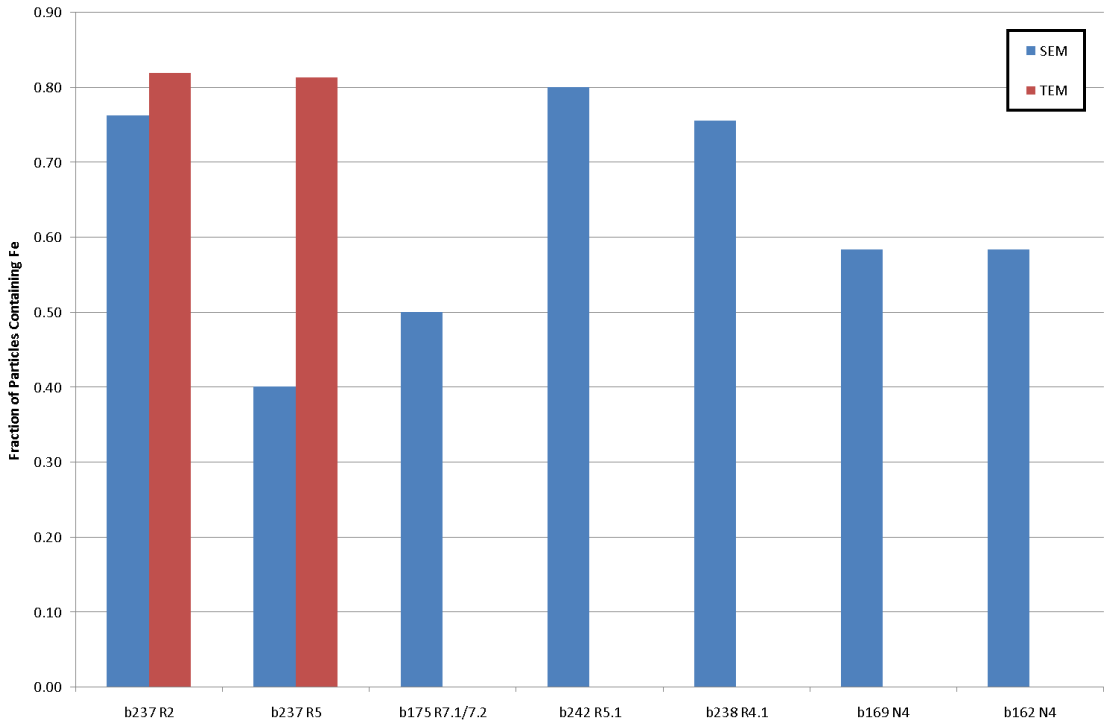

Figure 3.9: *Fraction of particles which were found to contain iron from SEM and TEM analysis. Note that b175 filters had a larger pore size and therefore may under-represent the smaller particles.*

It is also interesting that the TEM results, for particles sized $r < 0.75\mu m, d < 1.5\mu m$, show many more particles containing Fe than occur for the larger particles from the SEM results. There is not much difference in the fraction of particles containing Fe between the two b237 runs examined. This does suggest that there is a composition difference between the accumulation mode and the coarse mode, however, particularly for the lower dust layer in b237.

It should be noted that only a small number of particles have been counted in determining these statistics (as shown in Figure 3.8), and that therefore they are not stastically representative. Nevertheless, it is useful to observe the composition differences between the accumulation mode and coarse mode, and also the differences between flights. In order to draw firm conclusions, a larger number of particles would need to be analysed.

Iron oxide content, in relation to the amount of iron and aluminium, has been calculated from the filter samples for a few selected flights and runs (courtesy of P. Formenti),

and is shown in Table 3.2. This data is valuable since it is thought to be the amount of absorbing iron oxide present in dust, rather than the total amount of iron, that is important to the optical properties (e.g. Lafon *et al.*, 2006).

Flight & Run	Iron oxide/total Iron	Iron oxide/total Aluminium
b238 R3.1/3.2	0.52	0.35
b238 R4.1	0.56	0.38
b238 R5.1	0.53	0.35
b242 R1.1	n/a	0.33
b242 R5.1	0.59	0.39

Table 3.2: *Iron oxide content for selected runs with respect to the total mass of iron and aluminium, courtesty of P. Formenti.*

In terms of both iron oxide content in relation to total iron and total Aluminium, the ratios for b242 R5.1 are higher than those from b238. This supports that the dust measured during b242 had different sources to that from the rest of DODO2, and as expected, the greater iron oxide ratios are higher for more Sahelian sources. This also implies that the dust may be more absorbing, and will be examined in Chapter 4. Surprisingly b242 R1.1 shows much lower iron oxide ratios, lower even than the b238 ratios. Considering that the NAME results showed similar sources for these two b242 runs, the differences in iron oxide ratios are surprising, but may be a result of the NAME results showing sources covering a large area, when in reality only small parts of those areas may have the appropriate soil moisture and surface wind conditions to enable dust uplift.

3.5 Chapter Conclusion

This chapter has examined the vertical profiles of some example cases from DODO, the source locations of the dust encountered, and a limited amount of chemical composition data.

The vertical profiles of scattering and size distribution clearly show differences between the two seasons. Dust in the dry season was found close to the surface over land and ocean, mostly below 1 km, though dust extended up to 3 km in the deeper boundary layer above the desert in flight b175. Contrastingly, in the wet season, dust was found up to 6 km over both land and ocean, though the profiles were distinctly different with dust over

the land having peak concentrations towards the surface and dust over the ocean having peak concentrations above 4 km, within the Saharan Air Layer. This seasonal contrast is due to the different seasonal meteorological dynamics, with more intense solar insolation driving deeper convection in the wet season. The different vertical profiles will have an impact on the longwave radiative effect, which depends on the altitude of a dust layer, and possibly on the shortwave radiative effect depending on whether clouds are present above or below the dust layer. The altitude of the dust layer may also affect the rate of deposition of dust to the ocean, which affects marine biology. The transport of dust at different altitudes may also affect the particle size distribution, and therefore the optical properties of the dust.

The air mass origins shown by the NAME results suggest that the dust was transported differently, and from different sources, between the dry and wet seasons. DODO1 dust was transported from the northeast (in varying degrees) within an well defined plume, consistent with the meteorology from the campaign, and typical winter climatology, described in Chapter 2. Considering the meteorology of the dry season, with northeasterly surface winds associated with the subtropical high, it is perhaps not surprising that DODO1 dust sources were mostly from northwest Africa, including Mauritania, Western Sahara, Morocco and Algeria. It is likely that dust originating from sources further east (such as the Bodele Depression) is also transported by northeasterly winds in the dry season and would therefore cross the African coast further south and east than the area around Dakar (for example as described in Kaufman *et al.* (2005)), which was of focus during DODO. Therefore the location of possible dust sources for the DODO1 dust may well be due to the location of sampling, rather than being representative of all dust uplift during the dry season. Nevertheless, there is a clear and well defined source area for dust sampled during DODO1.

During DODO2 in the wet season the dust sources were a lot more varied than DODO1, with dust being transported from both western and central North Africa, and with dust sampled during some flights originating from much further south (such as b241 and b242). Therefore it is likely that the microphysical and chemical properties of DODO2 dust will be much more varied due to the greater variation in dust source

(likely to affect chemial composition) and transport distances and altitudes (likely to affect size distribution). It is also evident from the NAME results that dust encoutered at different altitudes during b237 and b238 had different dust sources.

Both the NAME and the chemical composition (elemental ratios and mineralogy) point towards dust sources being different between DODO1 and DODO2. DODO1 dust, originating from northwest Africa had much higher calcium content than DODO2 dust. Other studies (e.g. Chiapello *et al.*, 1997; Formenti *et al.*, 2008; Rajot *et al.*, 2008) have also found northwestern Saharan dust to be richer in Calcium than those further south and east. There was no difference in the Fe/Al ratios between the DODO campaigns, though this is not necessarily an indicator of absorption. Iron oxide content was found to vary between the two flights analysed. The mineralogy results from limited DODO cases also show that there is some variation in the dust composition between flights and between the fine and coarse modes. This suggests that it may not be appropriate to model the dust using one refractive index for all dust cases and particle sizes.

Chapter 4

Dust Microphysical and Optical Properties

4.1 Introduction

This Chapter examines the microphysical and optical properties of the dust encountered during DODO, both from measurements and through modelling. The microphysical and optical properties will be examined in terms of the means from each campaign, as well as the variability observed during and between the two campaigns. Section 4.2 examines direct measurements of single scattering albedos and size distributions of the accumulation mode and the variability of both, Section 4.3 describes the average optical properties for the two campaigns, Section 4.4 examines the contribution from size distribution and chemical composition to the optical properties, and Section 4.5 investigates the effect of the coarse mode size distribution on the optical properties. The larger part of the findings reported in this Chapter have been published in McConnell *et al.* (2008) (see Appendix).

4.2 Measured Optical and Microphysical Properties

In this Section, optical properties which have been measured directly (i.e. single scattering albedo at 550nm for the accumulation mode) and the measured dust size distributions are presented.

4.2.1 Measurements of Accumulation Mode Single Scattering Albedo

The single scattering albedo at 550nm (ω_0^{550}) can be calculated directly from measurements on the aircraft. In order to do this, data measured over the duration of a straight and level run (selected and identified as dust, as described in Chapter 2) have been averaged. Averaging the data over a run lasting at least 5 minutes provides data that is more spatially representative of the dust encountered than the data from the profiles, and can also give a measure of the horizontal variability through the standard deviation around the mean. For each run, data from the nephelometer and PSAP have been averaged and corrected as described in Chapter 2.

The single scattering albedo has then been calculated according to Equation 4.1 using the corrected absorption coefficient $\sigma_{a_{corr}}^{550}$ from the PSAP and the corrected scattering coefficient $\sigma_{s_{corr}}^{550}$ from the nephelometer. Note that due to the aircraft inlet cut-off diameters

(see Chapter 2), these single scattering albedos most likely only describe the accumulation mode. The uncertainty in ω_0^{550} due to instrumental error (see Chapter 2) and atmospheric variability (defined as one standard deviation over a run) have also been calculated. The results for ω_0^{550} and the associated errors are shown in Figure 4.1. The dashed lines show the average single scattering albedo values for each campaign, excluding the transit flights (b168 and b236) since this data was not necessarily collected in the Dakar area.

$$\omega_0^{550} = \frac{\sigma_{s_{corr}}^{550}}{\sigma_{s_{corr}}^{550} + \sigma_{a_{corr}}^{550}} \tag{4.1}$$

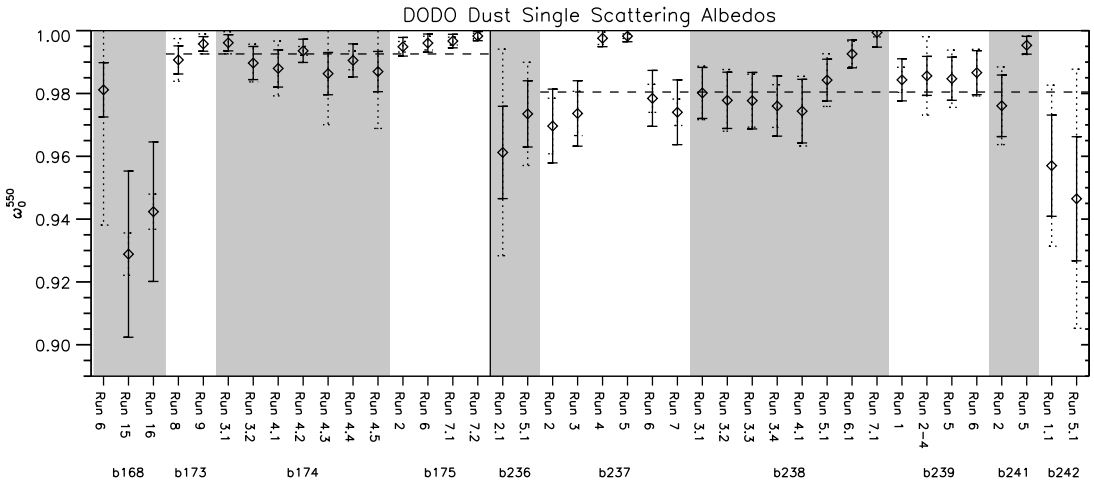

Figure 4.1: *Single scattering albedo values of dust measured during DODO at 550nm. Shaded panels indicate different flights. Solid error bars indicate instrumental error, dashed error bars indicate atmospheric variability. The two horizontal dashed lines indicate DODO1 and DODO2 campaign average single scattering albedo values (and campaign standard deviations) of* 0.99 ± 0.001 *and* 0.98 ± 0.013 *respectively. These averages do not include results from the transit flights of b168 and b236 where dust was not always measured in the Dakar area.*

The horizontal dashed lines in Figure 4.1 show the campaign average single scattering albedo values of 0.99 ± 0.001 and 0.98 ± 0.013 for DODO1 and DODO2 respectively, with errors representing one standard deviation over the runs contributing to this average (as opposed to the range of values shown in Figure 4.1). Thus DODO2 dust was more absorbing than DODO1 dust on average, though the errors do overlap. This may be caused by the chemical composition or size distributions (or both) varying between the campaigns. Chapter 3 showed that the source regions and composition for DODO1 and DODO2 were indeed different. Section 4.2.2 will examine the difference in size distribu-

tions.

Figure 4.1 shows that there was much more variability in the single scattering albedo during DODO2 than DODO1, with DODO1 single scattering albedo values never dropping below 0.985 for b173, b174 and b175 and DODO2 values ranging form 0.94 to 0.99. The greater variability observed in the DODO2 single scattering albedo values is consistent with the greater variability in transport distances and dust sources shown in the NAME results in Chapter 3, which are likely to affect composition and size distribution, and therefore the single scattering albedo. The lack of variability seen during DODO1 (in flights b173, b174 and b175) is also consistent with the well defined, less variable, dust transport from the northeast from less varied dust sources. Therefore it appears that the variability of the optical properties of the dust measured by the BAe-146 in the Dakar region during DODO1 are affected by the seasonal meteorology through upwind dust sources and transport processes.

It should be noted, however, that the DODO2 dust flights were performed over a period of 8 days, whereas the DODO1 dust flights were performed over 4 days, with one flight on the 3rd February 2006 and the three other flights between 14th-16th February 2006. Therefore the DODO1 measurements may be limited in the amount of variability of both the meteorology and the dust that was uplifted, which may result in the data presented here for DODO1 being less varied. During the days when DODO1 dust was collected, the flow was as would be expected from the climatology.

Figure 4.1 shows that the single scattering albedo values for b168 (0.93, 0.94) were significantly lower than those measured during flights b173, b174 and b175, and the error bars (both atmospheric variability and instrumental error) do not overlap. These values (for Runs 15 and 16) were performed at the end of the transit flight, just to the north of Dakar, with the flow at this point in the campaign being much more easterly than in the subsequent weeks. This is reflected by the air mass origins for these runs from NAME as shown in Chapter 3, which were southern Mauritania and northern Mali. This suggests that the source region is affecting the chemical composition, and therefore the single scattering albedo of the dust in flight b168. This is interesting, considering current thought that dust from Sahelian sources is higher in absorbing iron oxides (e.g. Claquin

et al., 1999; Alfaro *et al.*, 2004; Lafon *et al.*, 2006).

It is interesting to note that in the same way that dust source varied with altitude for some flights (as shown in Section 3.3), the single scattering albedo shows the same pattern. For example, Figure 4.1 shows much higher single scattering albedo values (over 0.99) for b237 Run 4 and Run 5 (performed at 50m) compared to the other runs for that flight (performed between 2.5 - 5km, ω_0^{550} ranging from 0.97-0.978). Figure 3.4(a), 3.4(b) and 3.4(c) show that the dust measured in Run 5 (also representative of Run 4 due to the similar timing, location and altitude) had significantly different air mass origins to the dust measured in Runs 2, 3, 6 and 7. The SEM and TEM results also showed somewhat different mineralogy for the runs at lower altitude, compared to the runs at 5km. Thus it appears that during b237 the upper layer of dust (shown in Figure 3.1(d)) had composition and transport processes which led to significantly different optical properties to the dust in the layer below 1km, sampled during Runs 4 and 5.

Similar features are also seen for b238 over land during DODO2. Here a series of stacked runs was performed, measuring the properties of dust at various altitudes. Runs 3.1-3.4 were performed at 300m (as close as the aircraft was permitted to the surface over land), Run 4.1 at 1km, Run 5.1 at 2.5km, Run 6.1 at 3.5km and Run 7.1 at 5km. For b238 it is noticeable that as the altitude of the dust increases the single scattering albedo increases. The NAME results in Chapter 3 also showed different sources at the different altitudes, with dust at higher altitudes having sources further east. Thus the dust observed at the different altitudes may have different composition. It may also be expected that the size distribution would change with altitude, with larger particles not being uplifted to such large heights as smaller particles. The variation in optical properties with altitude seen during b238 may therefore be related to the dust at different altitudes having different composition, size distribution, or both.

During DODO1 the dust was confined to a smaller range of altitudes - always below 1km, except in the case of b175 over Mauritania. During flight b175 runs were performed at altitudes of 150m (R2, R7.1, R7.2) and 1450m (R6) and during flight b174 runs were performed at 150m (R3.1, R3.2) and 50m (R4.1-4.5). Despite this the measured single scattering albedos shown in Figure 4.1 do not change much. Figure 4.2 shows ω_0^{550} as

a function of altitude. This reinforces the picture that all the DODO1 dust was found at low altitudes, whereas DODO2 dust was found at a much wider range of altitudes, and also had varying ω_0^{550}. There appears to be no evidence of DODO1 ω_0^{550} changing with altitude, whereas during DODO2 there is a suggestion of decreased ω_0^{550} at higher altitudes, contrary to the pattern seen in b238.

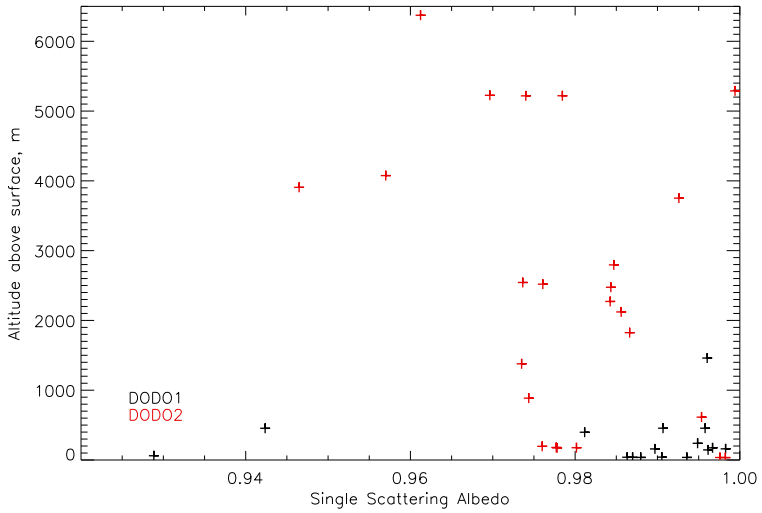

Figure 4.2: *Single scattering albedo values at 550nm versus altitude. Black indicates DODO1, red indicates DODO2.*

It is interesting that both b237 R5 and b241 R5 have high single scattering albedos (greater than 0.99), and both these runs were distinct in their air mass origins, with most air originating from over the ocean to the northeast of the aircraft, and limited particles being traced back to desert areas by NAME in Chapter 3. It has been hypothesised that the b237 R5 dust was being deposited from higher altitudes, and may have different chemical composition to the dust above as a result of size dependent composition. It is equally possible that this dust (both b237 R5 and b241 R5) originated from sources in northwest Africa, similar to those which were active during DODO1, resulting in different size distributions and/or composition which result in higher single scattering albedos. Despite being limited in terms of composition data (particularly for b241), it is clear that the optical properties as well as potential source locations for these two runs are different to the other samples from DODO2.

Single scattering albedo values for b242 (0.957 and 0.946) are lower than those for

the rest of DODO2. The NAME air mass origins for this flight were further south than others, with sources in southern Algeria, but also extending as far south as southern Mali and southern Niger. This is interesting since Sahelian dust has a higher content of absorbing iron oxides, which may lower the single scattering albedo. Indeed, of the iron oxide ratios (with respect to the mass of Aluminium) available from the filter samples shown in Chapter 3, the highest value was measured for b242 R5.1, suggesting a dependence of the lower ω_0^{550} values on the amount of absorbing iron oxide present.

b241 R2 also showed some air having originated from much further south - in fact with a greater proportion of the air originating from further south than that for b242 - though some air had also come from Mauritania and Western Sahara. Interestingly ω_0^{550} for b241 R2 is not particularly lower than other DODO2 values - as would be expected if there was a greater amount of absorbing iron oxide in the dust. It does appear though, that of the NAME runs with southerly sources (b168, b241 and b242), two out of these three flights show significantly lower ω_0^{550} values.

It should be pointed out that optical properties would be expected to vary if factors such as sulphate coatings on dust particles, mixing of dust with other aerosol types (such as anthropogenic pollution or biomass burning aerosol) were occurring. As described in Chapter 2, these cases have been selected for analysis based on the principal component being dust, with runs being affected by biomass burning aerosol removed, with no sulphate coatings observed on the filter samples that were analysed (Formenti *et al.*, 2008), and very few anthropogenic particles observed.

In conclusion, a variety of single scattering albedo values at 550nm have been measured during DODO for the accumulation mode, ranging from 0.93 to 0.99. Differences in the single scattering albedo are observed between the DODO campaigns, between different flights (i.e. day to day) and between dust at different altitudes (during DODO2). These differences appear to be related to variations in the dust source, as supported by the NAME results from Chapter 3, which are well defined during DODO1 and more variable during DODO2. The variation in dust source is likely to impact both the chemical composition and dust size distribution, which could then affect the single scattering albedo (and other optical properties). Though it is clear that the dust source has a strong impact

on ω_0^{550}, it is unclear whether this is due to different chemical composition or different size distributions at this stage. Limited chemical composition results (Chapter 3) support a difference in composition between DODO1 and DODO2, and between different flights during DODO2. The following Section investigates the measured size distributions from DODO.

4.2.2 Observed Size Distributions (Accumulation Mode)

Size distributions measured by the PCASP instrument covering radii from $0.06\mu m$ to $1.5\mu m$ were used to calculate the average size distribution for each DODO campaign. Data from the same runs as used in the averages from Section 4.2.1 and McConnell *et al.* (2008) were averaged over each run to calculate the average size distribution for each run. The size distributions were then normalised by the total average number of particles measured by the PCASP over the run in order to allow comparisons between runs where the total dust loading differed. These normalised size distributions are shown in Figure 4.3, along with the campaign averages (bold lines in Figures 4.3(a) and 4.3(b), and compared together in Figure 4.3(c)).

Figure 4.3 shows that DODO1 size distributions show less variability than those for DODO2. The fine mode size distributions ($r < 0.2\mu m$) for DODO1 show very little variability indeed. Most variation in the DODO1 size distributions are seen at $r > 0.2\mu m$. Contrastingly, the DODO2 size distributions show variation over the whole range measured by the PCASP, and also show much more variability compared to DODO1. This is likely to be related to the NAME results and vertical profiles from Chapter 3 which showed dust at a greater range of altitudes during the wet season, and showed dust being transported over distances which varied from quite local (Mauritania, Western Sahara) to much further north and east. It is logical that the greater range of transport distances (both horizontal and vertical) cause a greater variation in the size distribution in the wet season, which may also result in more variation in the optical properties.

The average size distributions shown in Figure 4.3(c) show small differences between the two DODO campaign average size distributions. The differences are observed at $r > 0.2\mu m$; the fine mode size distributions at radii smaller than this are very similar.

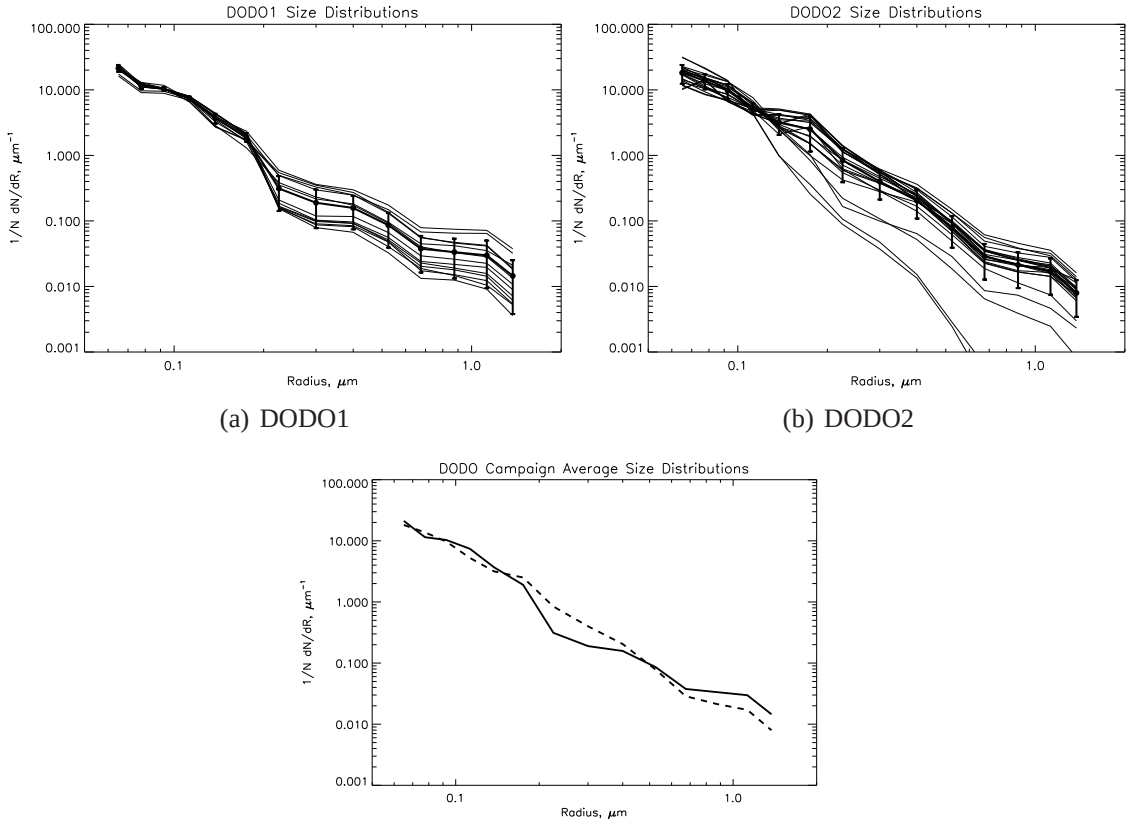

(a) DODO1

(b) DODO2

(c) Both campaigns

Figure 4.3: *(a) & (b) Normalised size distributions measured by the PCASP (fine and accumulation modes) on all runs determined to be dust using nephelometer and SEM analysis, for each DODO campaign. Campaign average size distributions and errors (one standard deviation) are shown by the heavy lines. (c) Campaign average normalised size distributions for DODO1 (solid line) and DODO2 (dashed line).*

DODO1 shows more particles at the large end of the accumulation mode, in the largest two size bins of the PCASP (radius $1.0 - 1.5\mu m$), while DODO2 has a greater proportion of particles at the lower end of the accumulation mode, between $0.2 - 0.35\mu m$ radius. This difference in the average size distribution may be important in determining the reasons for any differences in optical properties between campaigns.

4.2.3 Effects of Transport on Size Distribution

Figures 4.4 and 4.5 explore in greater detail how the measured accumulation mode size distributions change with transport and season. In order to do this the average size distributions for various runs have been combined to build up a better picture from the DODO

data. Details of the runs used to calculate each average can be found in Table 4.1.

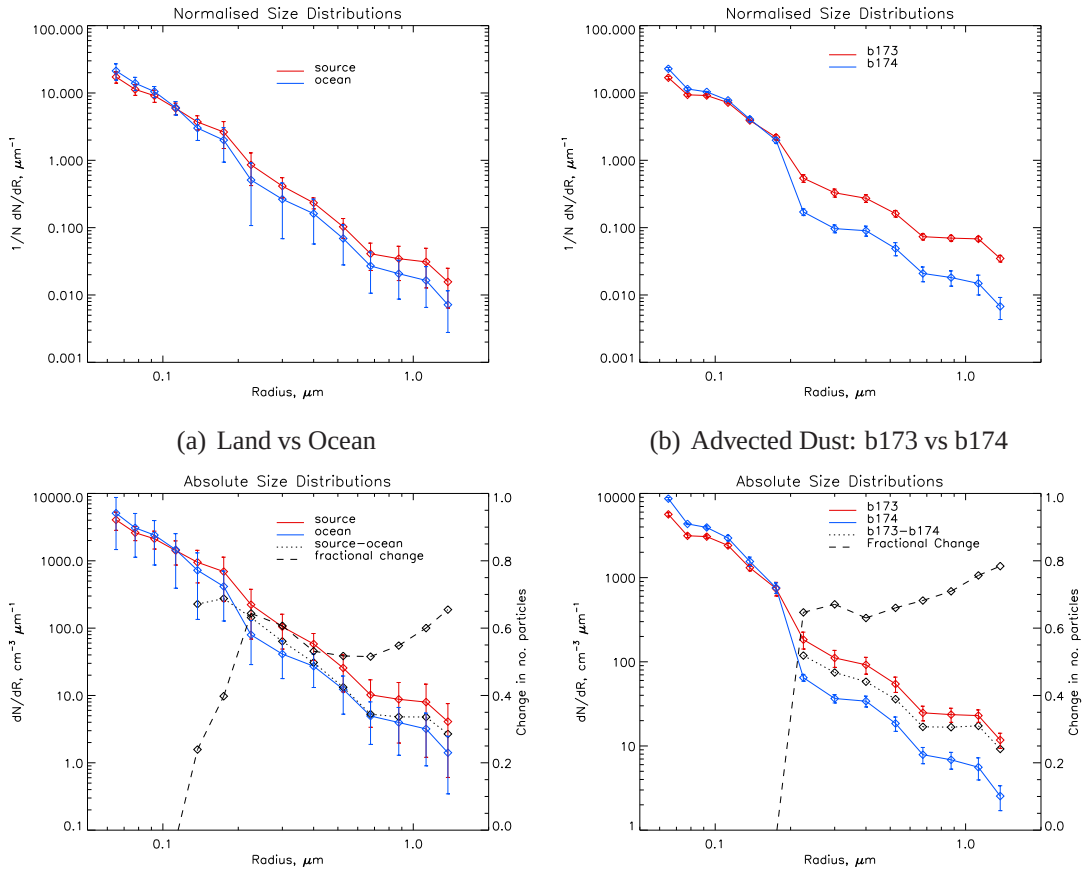

(a) Land vs Ocean

(b) Advected Dust: b173 vs b174

(c) Land vs Ocean

(d) Advected Dust: b173 vs b174

Figure 4.4: *DODO accumulation mode size distributions averaged by various categories of interest (see Table 4.1 for details of runs used). Error bars represent one standard deviation of the distributions used to calculate the averages. Note the different y-axis on Figures 4.4(c) and 4.4(d). Figures 4.4(a)-4.4(b) show normalised size distributions, Figures 4.4(c)-4.4(d) show absolute size distributions and fractional change in particle number.*

Figure 4.4(a) shows the differences in the size distributions measured over land and ocean in both campaigns. Though the error bars overlap, it is clear that on average there are more particles found over land at radii greater than $0.2\mu m$. This is consistent with the deposition of particles to the ocean (and land) as dust is transported westwards. Figure 4.4(b) expands on this idea by focusing on the size distributions from b173 and b174. Here it is likely that the same dust outbreak was sampled, having origins in northern Western Sahara and southern Morocco (see Chapters 2 and 3). Therefore it follows that the aircraft sampled part of the same dust outbreak on consecutive days, the first to the north of Dakar, the second to the south of Dakar. Figure 4.4(b) shows that there had been a significant

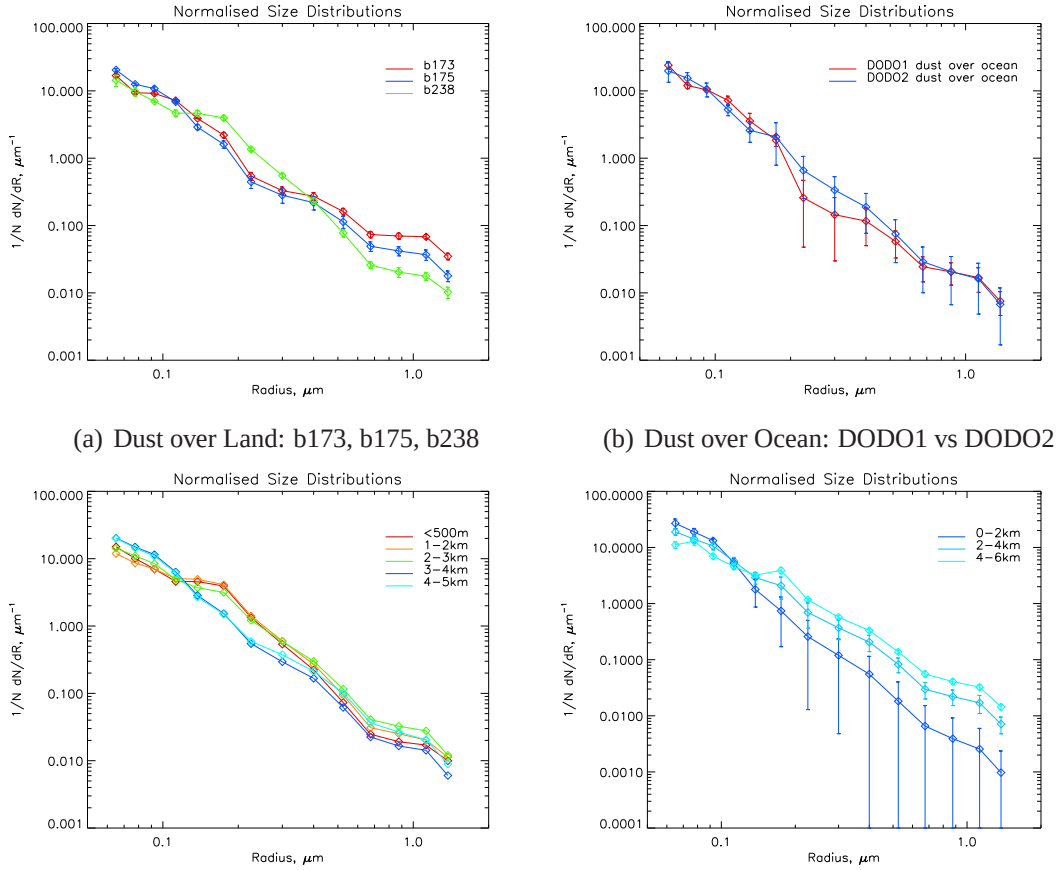

(a) Dust over Land: b173, b175, b238

(b) Dust over Ocean: DODO1 vs DODO2

(c) b238 dust: Different altitudes

(d) DODO2 Dust over Ocean: Different altitudes

Figure 4.5: *DODO accumulation mode normalised size distributions averaged by various categories of interest (see Table 4.1 for details of runs used). Error bars represent one standard deviation of the distributions used to calculate the averages.*

change in the size distribution between the two flights, with relatively more particles (at $r > 0.2\mu m$) being found on the first day and fewer during b174 a day later - likely due to dry deposition of dust to the ocean. Interestingly there is no significant change in the observed single scattering albedo between these two flights, despite the change in the size distribution. This finding is consistent with other studies such as Liu *et al.* (2008b) who showed that dust optical properties remained relatively unchanged during the first 3 days of transport over the Atlantic during an August 2006 case study.

Figures 4.4(c) and 4.4(d) show number size distributions for the same runs (not normalised here), in order to show the change in the absolute size distributions for the same cases. In the case of both b173/b174 and all of DODO land vs ocean flights, the trends are the same. Using these size distributions, the difference between the two lines has been

Category	Figure	Runs Used
Dust over land	4.4(a)	b173 (R8,R9), b175 (R2,R6,R7.1,R7.2), b238 (R3.1-R3.4,R4.1,R5.1,R6.1,R7.1)
Dust over ocean	4.4(a)	b168 (R15,R16), b174 (R3.1,R3.2,R4.1-R4.5), b237 (R2,R3,R4,R5,R6,R7), b239 (R1,R2-4,R5,R6), b241 (R2,R5), b242 (R1.1,R5.1)
b173	4.4(b)	b173 (R8,R9)
b174	4.4(b)	b174 (R3.1,R3.2,R4.1-R4.5)
b173 source	4.5(a)	b173 (R8,R9)
b175 source	4.5(a)	b175 (R2,R6,R7.1,R7.2)
b238 source	4.5(a)	b238 (R3.1-R3.4,R4.1,R5.1,R6.1,R7.1)
DODO1 dust over ocean	4.5(b)	b168 (R15,R16), b173 (R1), b174 (R3.1,R3.2,R4.1-R4.5)
DODO2 dust over ocean	4.5(b)	b237 (R2,R3,R4,R5,R6,R7), b239 (R1,R2-4,R5,R6), b241 (R2,R5), b242 (R1.1,R5.1)
b238 $< 500m$	4.5(c)	b238 (R3.1-3.4)
b238 $1-2km$	4.5(c)	b238 (R4.1)
b238 $2-3km$	4.5(c)	b238 (R5.1)
b238 $3-4km$	4.5(c)	b238 (R6.1)
b238 $5km$	4.5(c)	b238 (R7.1)
DODO2 dust over ocean $0-2km$	4.5(d)	b239 (R6), b237 (R4,R5), b241 (R5)
DODO2 dust over ocean $2-4km$	4.5(d)	b237 (R3), b239 (R1,R2-4,R5), b241 (R2), b242 (R1.1,R5.1)
DODO2 dust over ocean $4-6km$	4.5(d)	b237 (R2,R6,R7)

Table 4.1: *Runs used in creating the average size distributions for each category as shown in Figures 4.4 and 4.5.*

calculated, and is also shown (black dotted line). This represents the size distribution of dust which would be lost through deposition. Additionally, the fraction of particles lost for each size bin is shown (black dashed line) in order to give an indication of the size dependence of deposition. For Figure 4.4(d) these measures assume that the same dust outbreak was sampled during both flights, and that the difference in size distributions was due to deposition. For Figure 4.4(c) where a number of flights were used, and from both seasons, no direct continuity is applicable and the results show a general picture of what could be expected in terms of the number and sizes of particles being deposited near the west coast of Africa.

It is clear that in both cases the largest fraction of particles deposited come from the larger particles, with the fraction deposited greater than 0.5 for $r > 0.2\mu m$. This is consistent with expectations that larger particles have greater settling velocities and are therefore deposited more rapidly. Whereas the case study of b173-b174 shows that as radius increases the proportion of each size bin being deposited increases (to a maximum

of almost 0.8 of the particles present), the results averaged over the whole of the DODO campaign show a double peak in deposition fraction. The PCASP size bins centred at radii of $0.225\mu m$ and $1.375\mu m$ both suggest a difference of around 70% in the number of particles present between land and ocean flights. In terms of the size distribution deposited, the number concentrations are highest for smaller particles, consistent with the measured size distributions (though the mass size distribution would be dominated by the larger particles). It should be noted that for Figure 4.4(c) the error bars overlap between land and ocean, and therefore that the deposition results may be variable. Additionally these results only show data for the accumulation mode (up to $r = 1.5\mu m$), and therefore give no information on the coarse mode size distribution, where most of the mass would be expected to reside. However, Baker and Jickells (2006) show that the primary control on aerosol iron solubility is the surface area to volume ratio of particles, which is higher for smaller particles, and therefore the importance of deposition of smaller particles is not to be ignored.

Figure 4.5(a) shows the size distributions measured over land from flights b173, b175 and b238. A reasonable amount of variability is see in these size distributions, with b173 (followed by b175 and b238) having the largest amount of particles greater than $0.6\mu m$ present, and the same sharp drop off in size observed during the DODO1 flights as shown in Figure 4.3(c) for DODO1, whereas DODO2 shows a more gradual slope. The variability in size distribution seen over land is likely to be dependent on parent soil and uplift characteristics, which would be expected to vary with source.

Figure 4.5(b) contrasts the size distributions between DODO1 and DODO2 from flights over the ocean only. Interestingly now, the main difference between DODO1 and DODO2 is between radii of $0.2 - 0.5\mu m$, with no difference at radii greater than $0.6\mu m$ (as seen in Figure 4.3(c)). Thus DODO2 transported oceanic dust appears to be composed of many more smaller particles than DODO1 dust. This may be because the wet season dust is transported from sources located further east than the dry season dust, and so by the time the dust reaches the Atlantic a greater proportion of larger particles have been deposited.

Figures 4.5(c) and 4.5(d) show size distributions from DODO2 measured over the

desert (b238) and ocean (various flights), separated by the altitude where the dust was found. These results reflect the size distribution profiles shown in Figure 3.2 in Chapter 3, where the largest particles peak in terms of number concentrations at higher altitudes over ocean, but at lower altitudes over the desert. In terms of the largest particles measured by the PCASP during b238, the largest proportion of particles with radii greater than $0.6\mu m$ were found at altitudes of 2-3km, with lower proportions at higher and lower altitudes than this. At radii between $0.1 - 0.4\mu m$ there is also a separation in the size distributions with altitude, with the runs performed above 3km having fewer particles in this size range. This is surprising, since it would be expected that smaller particles are uplifted to greater altitudes more easily. Over ocean, lower altitudes appear to have significantly lower proportions of particles over $r = 0.2\mu m$, with most of the larger particles residing aloft within the Saharan Air Layer, contrary to some speculation in the literature (e.g. Stuut *et al.*, 2005). This raises interesting questions about the transport of dust across land/ocean interfaces, and whether the dust present in the lower layer is being deposited from higher altitudes, or just being transported at low levels.

Also of note is the very different size distribution in Figure 4.5(d) for dust at altitudes between $0 - 2km$. Three of the three runs used for this average (b237 R4 and R5, b241 R5) also had much higher single scattering albedo values (over 0.99), in contrast to the rest of DODO2. Thus it is possible that the different size distributions of dust at low altitudes in the wet season are contributing to the optical properties here.

In conclusion, the various plots in Figures 4.4 and 4.5 show that the principal cause of the variation seen in DODO2 size distributions are due to variations with altitude. It is also evident that the size distributions are different between land and ocean (in both seasons), with fewer particles being measured over the ocean due to loss from deposition.

4.3 Campaign Average Optical Properties

This section examines the average optical properties (for the accumulation mode) for each campaign in an attempt to identify seasonal variations in the optical properties.

4.3.1 Mie Code Procedure

The average size distributions shown in Figure 4.3(c) have been used in a Mie scattering code to calculate the optical properties for each campaign. In order to do this the PCASP size distributions from Figure 4.3(c) were each fitted with a logfit curve, which is the sum of four individual lognormal modes described by Equation 4.2, summed according to Equation 4.3, where N_{tot_i}, σ_{g_i} and r_{g_i} represent the total number of particles, the geometric standard deviation and the geometric mean radius of each mode (i) respectively.

$$\left(\frac{dN}{dr}\right)_i = \frac{N_{tot_i}}{(2\pi)^{1/2} r \ln \sigma_{g_i}} exp\left(-\frac{(\ln r - \ln r_{g_i})^2}{2(\ln \sigma_{g_i})^2}\right) \tag{4.2}$$

$$\frac{dN}{dr} = \sum_{i=1}^{4} \left(\frac{dN}{dr}\right)_i \tag{4.3}$$

A logfit curve, rather than the raw size distributions, was used firstly to smooth out any noise which can occur in the PCASP size distributions, secondly so that the size distributions can be easily reconstructed (for example by modellers) by using the lognormal mode parameters, and thirdly, so that the size distribution for input to the Mie scattering code has a higher resolution for more accurate scattering calculations.

The parameters for the lognormal modes were chosen so that the logfit curve fitted the measured size distribution as closely as possible, as shown in Figure 4.6. The lognormal modes and logfit curve for each campaign can be seen in Figure 4.6, and the details of each lognormal mode, including the weight, w (calculated from N_{tot_i}), given to each mode are shown in Table 4.2.

The inputs required for the Mie scattering code as shown in the flow chart in Figure 4.7 are firstly the size distribution, which is input in terms of the lognormal fitted curve described above, and secondly, a complex refractive index. Optical properties have been

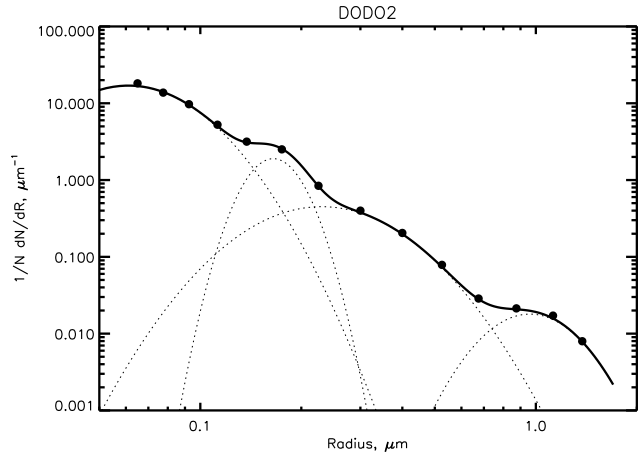

(a) DODO1

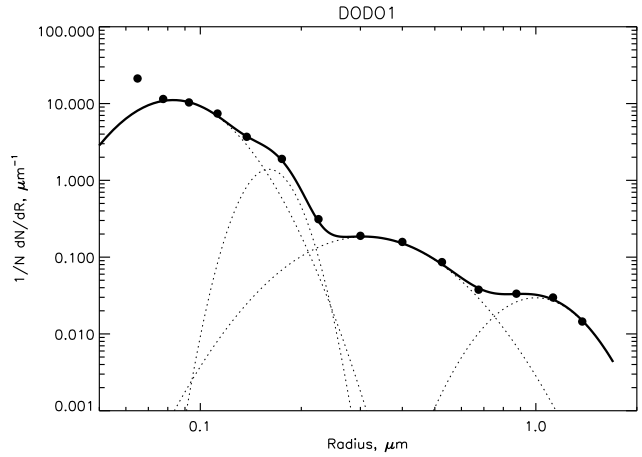

(b) DODO2

Figure 4.6: *PCASP average normalised size distributions for each campaign (circles) with logfit curves (heavy lines) created by summing four lognormal modes (dotted lines).*

	Mode	$r_g, \mu m$	σ_g	w
DODO1	1	0.083	1.36	0.815
	2	0.160	1.16	0.095
	3	0.310	1.50	0.067
	4	1.000	1.31	0.023
DODO2	1	0.061	1.47	0.797
	2	0.165	1.18	0.104
	3	0.230	1.54	0.089
	4	0.960	1.32	0.010

Table 4.2: *Lognormal mode parameters used to construct the logfit size distributions shown in Figure 4.6*

calculated at wavelengths of $450nm$, $550nm$ and $700nm$ to coincide with the wavelengths at which the nephelometer measures scattering. The refractive index has been assumed to be spectrally constant over these wavelengths, as in WCP (1983). Sensitivity tests showed that using a full spectral refractive index did not change the results significantly. Additionally the logfit curve has been truncated at radii greater than $1.5\mu m$ and less than $0.03\mu m$ to coincide with the size range over which the PCASP measures and the cut-off size of the nephelometer and PSAP inlets. Therefore the optical properties calculated will cover the fine and accumulation modes only. The resulting optical properties also assume spherical particles, due the difficulties in modelling non-spherical particles and on the assumption that when integrated over all scattering angles, non-sphericity has less effect (e.g. Mishchenko *et al.*, 1995).

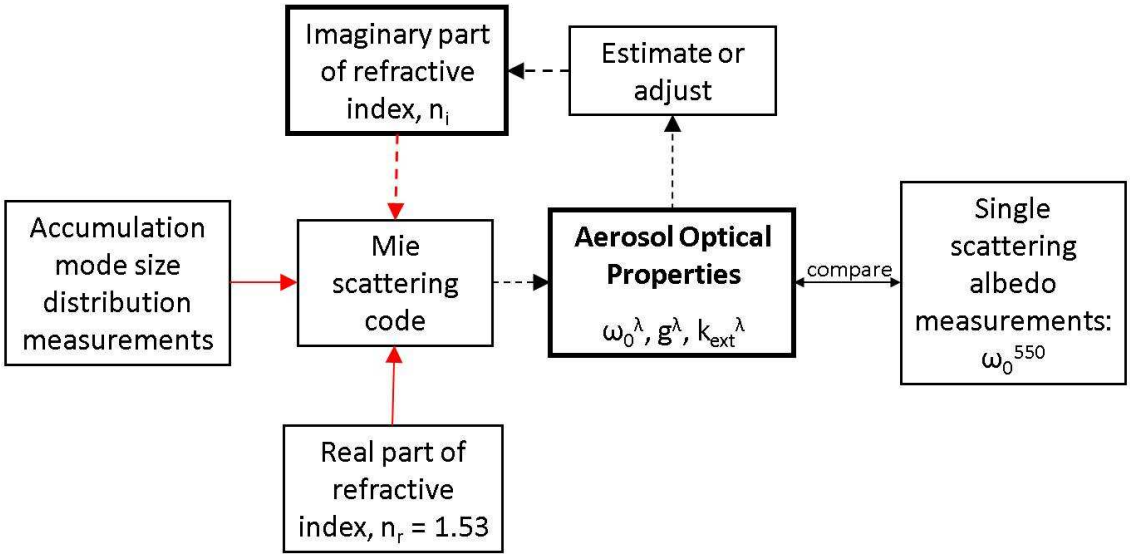

Figure 4.7: *Schematic showing methodology to calculate optical properties for the accumulation mode and derived imaginary part of refractive index. Inputs to Mie code are shown by red arrows. Iterations are shown in dashed arrows. Initial inputs of measured size distribution, the real part of the refractive index (1.53) and an estimated imaginary part of the refractive index are used.* n_i^{550} *is then adjusted iteratively until the measured and modelled* ω_0^{550} *are in agreement.*

Since the value of the refractive index is not known, some iteration is required, and is depicted in Figure 4.7. The real part of the refractive index is assumed to be 1.53, since this is relatively well known. Initially the complex refractive index is estimated, and input into the Mie code. The resulting single scattering albedo at 550nm from Mie code is then compared to the observations of single scattering albedo at 550nm from the nephelometer

and PSAP measurements described in Section 4.3. The imaginary part of the refractive index is then adjusted, and the process is iterated until the single scattering albedo from the Mie code and the observations are in agreement. This results in a derived refractive index at 550nm, given a real part of 1.53. Finally the other optical properties, including the asymmetry parameter (g^{550}) and mass specific extinction (k_{ext}^{550}, m^2g^{-1}) are output, assuming a reasonable dust density of $2.65gcm^{-3}$ (Tegen and Fung, 1995).

4.3.2 Results of Campaign Average Optical Properties

Table 4.3 shows the campaign average results of the modelled and observed optical properties for the fine and accumulation mode dust particles. The results from DODO show that there is a small difference between the single scattering albedos measured and modelled between both campaigns of 0.1. However, although the difference in the single scattering albedo value is small, it should be noted that the difference in the co-albedo ($1 - \omega_0$) is a factor of two between the two campaigns. This points to significant differences in the amount of absorption occurring in each campaign, and is reflected in the differences in the inferred refractive index from the Mie code results. The imaginary part of the refractive index for DODO2 dust is $0.0014i \pm 0.0001i$, while the DODO1 value is much lower at $0.0005i \pm 0.0001i$, indicating far less absorption by dust in the dry season.

	Observed	Modelled				
	ω_0^{550}	ω_0^{550}	g^{550}	k_{ext}^{550} , $g^{-1}m^2$	$n_r^{550} - n_i^{550}$	Uncertainty in n_i^{550}
DODO1	0.99 ± 0.004	0.99	0.68	0.85	1.53-0.0005	0.0001
DODO2	0.98 ± 0.013	0.98	0.68	1.14	1.53-0.0014	0.0001

Table 4.3: *Optical properties of mineral dust at 550nm from DODO1 and 2.n_i^{550} and n_r^{550} are the real and imaginary part of the refractive indices respectively. Errors on ω_0^{550} represent one standard deviation of measured values over the campaign. Error in the imaginary part of the refractive index is calculated using the range of refractive indices that would be required to allow the modelled single scattering albedo values to fall within the range of observed single scattering albedo uncertainty.*

The mass specific extinction also varies considerably between DODO1 and DODO2 ($0.85g^{-1}m^2$ and $1.14g^{-1}m^2$ respectively). This may be attributable to the extra amount of absorption occurring during DODO2 (indicated in both the lower ω_0^{550} and the higher n_i^{550} values), and possibly to the size distribution as well. Figure 4.3(c) shows that DODO2

has more particles in the $0.2 - 0.4\mu m$ radius range, the region where there is likely to be most interaction with visible radiation, while DODO1 has a greater proportion of particles in the accumulation mode in the radius range $r > 0.675\mu m$. It is hypothesised that the difference in size distribution in the $0.2-0.4\mu m$ range may be more important as particles in this range will be more efficient at extinction per unit mass. This has been examined for a specific case (b238 R4.1) by changing the size distribution one mode at a time, and examining how the size distribution for each mode affects the optical properties. The results showed that changes in the second and third mode (in the size range roughly $r = 0.1 - 0.5\mu m$) had a large effect on k_{ext}^{550}, and that relatively more particles in this size range led to a higher value of k_{ext}^{550}. Particles sized $r > 0.675\mu m$ contribute to a higher extinction coefficient (m^{-1}) in DODO1, but this effect is outweighed by the greater mass of the larger particles which lowers k_{ext}^{550}. The effect of both size distribution and refractive index on the optical properties are examined in more detail in Section 4.4.

The asymmetry parameter (0.68) does not change between campaigns. This indicates that neither the size distribution nor the refractive index differ enough between DODO1 and DODO2 to warrant a change in g, and that g is also less sensitive to changes in the size distribution and refractive index than k_{ext}^{550} and ω_0^{550}.

Uncertainties in the results exist due to assumption of spherical particles. Otto *et al.* (2009) found that non-spherical particles resulted in 1% changes in ω_0^{550} and 4% changes in g^{550}. Therefore the Mie code values of ω_0^{550} may change by a few percent, which would result in different values of n_i^{550}, and potentially also g^{550} and k_{ext}. However, changes of this size are smaller than the measured variations in ω_0^{550} from the campaigns, and therefore the uncertainty shown in Table 4.3 for n_i^{550} will most likely remain the same.

4.3.3 Evaluation of Campaign Average Optical Properties

In summary, there appears to be a difference in the average optical properties between the two DODO campaigns, with the dry season having higher single scattering albedo values, lower k_{ext}^{550} and lower n_i^{550}, with little difference in g^{550} between the two seasons. These differences can be traced back to differences in both the composition (and dust sources) and the size distributions for each DODO campaign. However, it should be noted

that the variation in optical properties between the different runs within each campaign, particularly DODO2, is much greater than the average differences between the campaigns.

The two factors contributing to the optical properties are the size distribution and the chemical composition (represented in the Mie code through the refractive index). It is clear that there is a difference in both these properties between DODO1 and DODO2, and also a difference in the average optical properties (k_{ext}^{550} and ω_0^{550}). The relative roles of the size distribution and the refractive index in causing the differences in the optical properties is examined in Section 4.4. The differences in the single scattering albedo are also much greater within in each campaign compared to the differences between the campaign, and this is also examined in terms of size distribution and composition in Section 4.4.

A natural comparison of the campaign average properties is against dust measurements from aircraft campaigns using the same instrumentation, and therefore also representing the accumulation mode only. SHADE (SaHAran Dust Experiment, Haywood *et al.* (2003)) took place in the Dakar/Sal region during September 2000 using the same instrumentation but on a different aircraft (the C-130). DABEX (Dust And Biomass EXperiment, Osborne *et al.* (2008)) took place in Niamey, Niger during January 2006, using identical instrumentation and the same aircraft as DODO.

DABEX measured consistently high ω_0^{550} with an average of 0.99, and SHADE an average of 0.97 with a range of $0.95 - 0.99$. These are in line with the DODO results, and it therefore appears that dust measured in the dry season has higher ω_0^{550} than the wet season values, which seem to be more variable. The values of n_i^{550} inferred from SHADE and DABEX (0.0004 and 0.0015 respectively) reflect the ω_0^{550} values, with SHADE in the wet season showing more absorption, similar to DODO2. It therefore appears that the composition differed significantly between SHADE and DODO2 to DABEX and DODO1, leading to differences in n_i^{550} and ω_0^{550} . The asymmetry parameters for SHADE and DABEX are 0.72 and 0.71, slightly higher than DODO values of 0.68, indicating that more radiation is scattered in a forward direction for DABEX and SHADE dust. The reason for this could be size distribution differences. The values of k_{ext}^{550} , 0.76 and 0.70 for SHADE and DABEX respectively, are lower than DODO values, possibly due to the presence of a greater proportion of larger particles in the PCASP size range which are less efficient per

unit mass at extinguishing visible radiation.

However, it is important to remember that these campaigns are of short duration (7-20 days), and are not necessarily climatologically representative. The particular results obtained for each campaign may be strongly affected by the particular sources which are activated at the time. This is illustrated by the contrasting optical properties between b168 and the rest of DODO1, which took place under different wind directions, and also the greater variability during DODO2 when dust was measured over a longer time period.

In comparison to measurements of optical properties from the literature, the values of ω_0^{550} and n_i^{550} are at the high and low end respectively, indicating that the DODO accumulation mode dust was more scattering and less absorbing than most measurements and estimates. The DODO values of ω_0^{550} are in agreement with some recent satellite and AERONET estimates of ω_0, roughly in the range of $0.93 - 0.98$ over wavelengths $440-670nm$ (Tanré *et al.*, 2001; Kaufman *et al.*, 2001; Dubovik *et al.*, 2002; Forster *et al.*, 2007). In contrast, the ω_0^{550} measurements and n_i^{550} estimates from DODO are rather different from the more absorbing dust measured in other studies (e.g. Patterson *et al.*, 1977; Shettle and Fenn, 1979; WCP, 1983; Hess *et al.*, 1998; Otto *et al.*, 2007, 2009). However, note that the DODO estimates are solely for the accumulation mode, due to the inlet limitations of the nephelometer and PSAP. The addition of the coarse mode is expected to decrease the value of ω_0^{550} (e.g. Haywood *et al.*, 2003; Otto *et al.*, 2007), and is examined in Section 4.5.

4.4 Role of Composition and Size Distribution in Determining Optical Properties

4.4.1 Introduction

Modelling studies (e.g. Tegen and Lacis, 1996; Liao and Seinfeld, 1998; Balkanski *et al.*, 2007; Otto *et al.*, 2007) have illustrated the complexity of modelling the optical properties of dust due to variations in size distributions and refractive indices. The previous sections have shown that the optical properties, size distributions and derived refractive indices all

varied during DODO. Therefore it is important to use the observational data from DODO to examine the contribution of both size distribution and refractive index to the optical properties. This section tackles this issue, with the aim of determining which has most effect on the variation in optical properties observed during DODO.

4.4.2 Calculation of Optical Properties for Individual Runs

In order to examine the contribution of refractive index and accumulation mode size distribution to the optical properties, Mie code calculations have been performed for all the runs shown in Figure 4.1. The same method as described in Section 4.3.1 has been individually applied to each case shown in Figure 4.1. Thus the size distribution for each run was fitted with a lognormal curve (comprised of four modes, extending to $r = 1.5\mu m$), and input into a Mie scattering code with an assumed imaginary refractive index. The imaginary part of the refractive index was then iterated until the single scattering albedo from the Mie code and that from the observations for the particular run were in agreement. Again, the real part of the refractive index was assumed to be 1.53, and the refractive index was spectrally constant between $350 - 700nm$. The limitations of this technique are the same as those for the campaign average optical properties - firstly that the Rosemount inlet cut-off is such that the nephelometer and PSAP measure the same size distribution as the PCASP, and secondly that the particles are assumed spherical.

Thus it has been possible to model the optical properties for all the individual runs shown in Figure 4.1. These are shown in Figures 4.8 and 4.9 as a function of flight and run, along with the single scattering albedo observations measurements from Figure 4.1 which are repeated here for comparison purposes. The derived imaginary part of the refractive index at 550nm is also shown in Figure 4.9.

The error in ω_0^{550} , k_{ext}^{550} and n_i^{550} has also been calculated. All these parameters are constrained by the ω_0^{550} observations, which themselves have an uncertainty, as shown in Figure 4.8(a). The maximum and minimum range in ω_0^{550} shown in Figure 4.8(a) have been used to determine the maximum and minimum value of n_i^{550} . This range in n_i^{550} has then been used to calculate the uncertainty in k_{ext}^{550} and g^{550} , as shown in Figures 4.8(a) and 4.9((d). In cases where the atmospheric variability in ω_0^{550} is very large, this also results

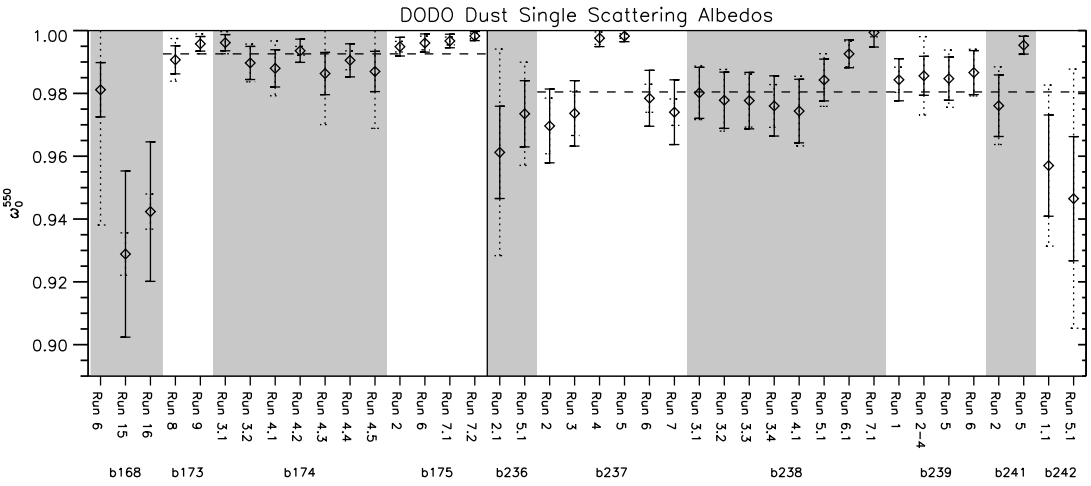

(a)

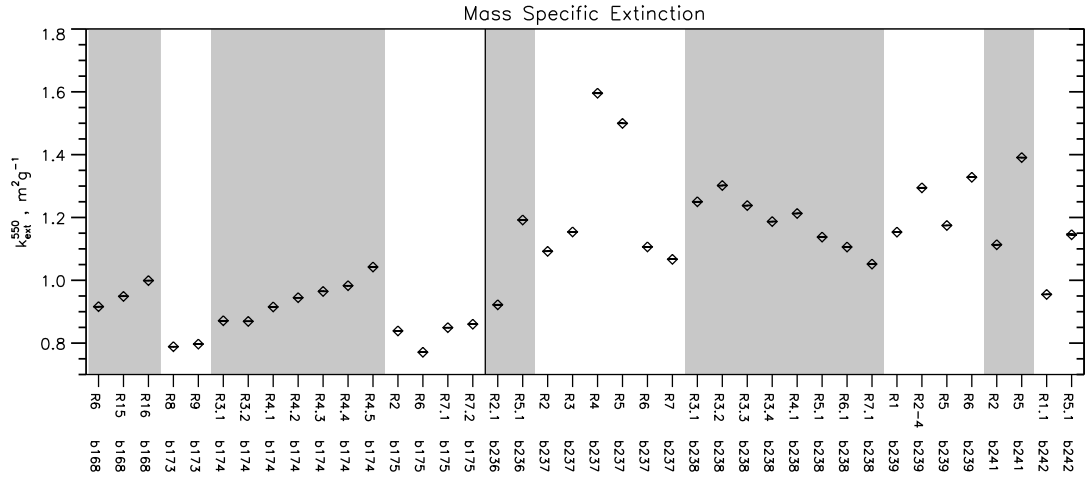

(b)

Figure 4.8: *Optical properties and refractive index for DODO accumulation mode dust for individual runs. (a) Observed single scattering albedo values at 550nm (as in Figure 4.1), (b) mass specific extinction values at 550nm from Mie code. Error bars indicate uncertainty in k_{ext}^{550} due to the range of instrumental and atmospheric variability of ω_0^{550} as shown by the error bars in Figure 4.8(a).*

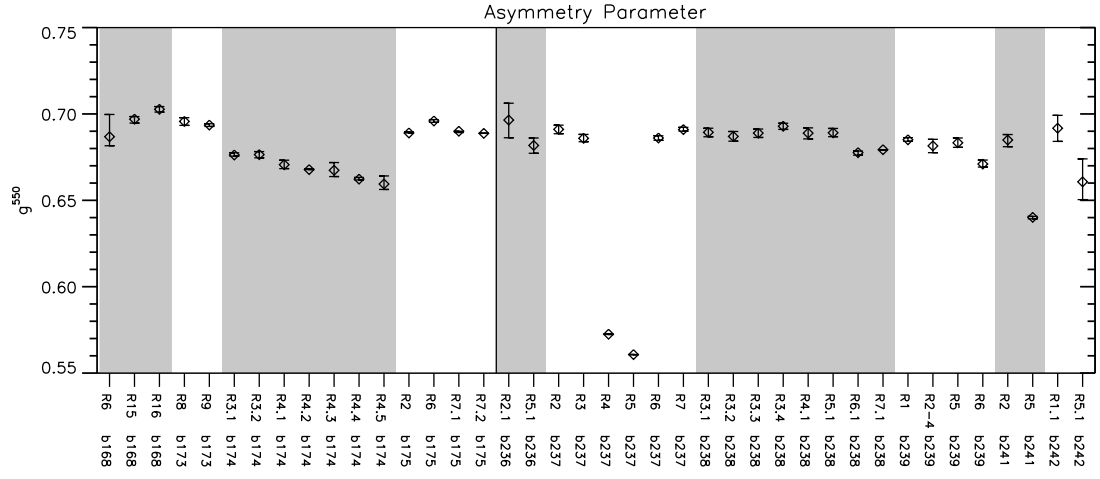

(a)

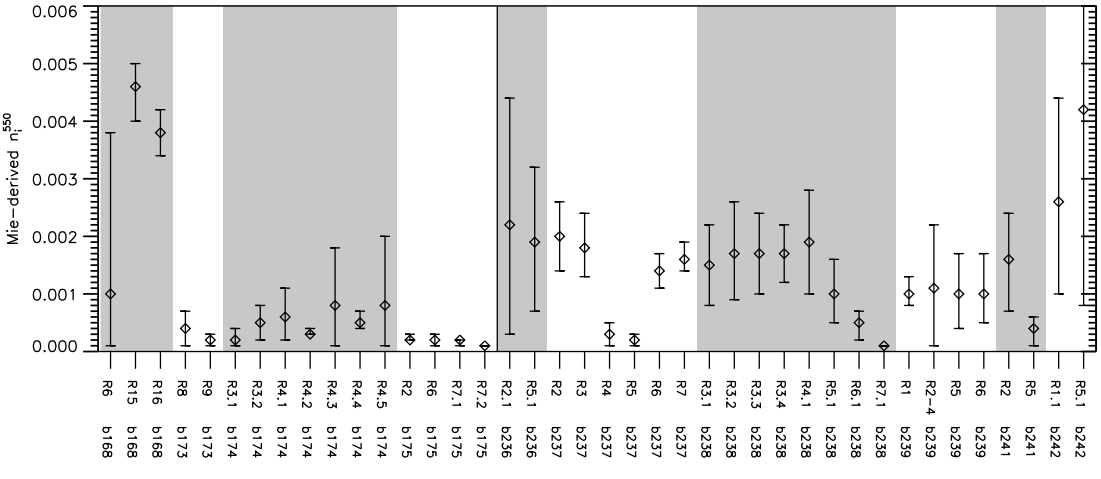

(b)

Figure 4.9: *Optical properties and refractive index for DODO accumulation mode dust for individual runs. (a) asymmetry parameter values at 550nm from Mie cod , (b) derived imaginary part of the refractive index at 550nm (n_i^{550}) from Mie code. Error bars indicate uncertainty in n_i^{550} and g^{550} due to the range of instrumental and atmospheric variability of ω_0^{550} as shown by the error bars in Figure 4.8(a).*

in large errors in n_i^{550} , for example as shown for b236 R2.1 and b242 R5.1. The errors in g^{550} and k_{ext}^{550} are very small, probably due to a small dependence on the value of n_i^{550} used. It is possible that uncertainties in the measured size distribution could contribute to larger errors than shown here for k_{ext}^{550} and g^{550} , but this has not been quantified.

Generally the results shown in Figures 4.8 and 4.9 are consistent with the average DODO1 and DODO2 optical properties shown in Table 4.3. For example, the mass specific extinction values are generally higher for DODO2 than DODO1, there is little variation in the asymmetry parameter and the values of n_i^{550} are generally much lower for DODO1 than DODO2 (with the exception of b168).

However, the purpose of Figures 4.8 and 4.9 is to show the variability of the optical properties for various runs during DODO. Two runs that stand out in particular are R4 and R5 from b237, which were performed at 50m above the ocean in a lower layer of dust. These two runs have been singled out previously for having ω_0^{550} values higher than 0.99 (in contrast to much of DODO2). Figure 4.8 also shows that these runs had high values of k_{ext}^{550} (1.60, 1.50), lower values of g^{550} (0.57,0.56), and a lower values of n_i^{550} (0.0003, 0.0002). Similar trends can also be seen for b241 R5 which was also performed at an altitude of 500m, also below the main dust layer.

Variations in k_{ext}^{550} can also be seen between the two DODO campaigns, between different flights, and within the same flight, showing the same sort of variability as was seen for the single scattering albedo measurements in Section 4.2. Similarly the refractive indices show variation on the same scales, with b168 (R15 and R16) and b242 (both runs) showing much larger values, indicating more absorption, which fits with the lower single scattering albedos for these flights. This indicates that significantly different composition for dust was measured during these flights which contributed to the lower single scattering albedos.

It has been possible to calculate refractive indices from filter samples for five different cases, which are shown in Table 4.4. These have been calculated assuming an external mixture of calcium carbonates, quartz and clays, and that iron oxides are internally mixed with the clays. These have been calculated using elemental concentrations from PIXE analysis, and laboratory measurements of iron oxide amounts. Using a simplified version

of the technique described by Lafon *et al.* (2006), the refractive index has then been calculated. Due to lack of information on the partitioning of clays and iron oxides, initially all iron oxides were assumed to be hematite, and all clays assumed to be illite. Other combinations involving kaolonite and goethite are also possible, and the range in n_i^{550} due to these assumptions has been calculated for b238 R4.1, and is also shown in Table 4.4. Note that the combination of hematite and illite leads to the most absorbing combination of iron oxides and clays (Lafon *et al.*, 2006).

Flight	Run	Mie Code n_i^{550}	Mie Code Min/Max n_i^{550}	Filters n_i^{550} (HI)	Filters range in n_i^{550}
b238	R3.1,R3.2	$0.0015, 0.0017$	$0.0008/0.0022$, $0.0026/0.0009$	0.0032	
b238	R4.1	0.0019	$0.0010/0.0028$	0.0032	$0.0016 - 0.0032$
b238	R5.1	0.0010	$0.0005/0.0016$	0.0031	
b242	R1.1	0.0026	$0.0010/0.0044$	0.0030	
b242	R5.1	0.0042	$0.0008/0.0100$	0.0036	

Table 4.4: *Comparison of imaginary refractive indices derived from Mie code for the accumulation mode against values calculated from filter samples (courtesy of P. Formenti, LISA) incorporating the full size distribution. HI indicates that the composition was assumed to be hematite only in iron oxides, and illite only in clays (the most absorbing combination). The range in filters n_i^{550} shows the range in that would result if other combinations of hematite, goethite, illite and kaolonite were assumed, where data is available.*

The results in Table 4.4 provide an important validation of the refractive indices shown in Figure 4.9, despite the uncertainties in the filters values of n_i^{550} due to the assumptions made. For all cases other than b242 R5.1, the Mie code n_i^{550} values underestimate those from the filters. However, the case of b238 R4.1 demonstrates that assumptions of combinations other than that of hematite and illite can significantly lower n_i^{550} , bringing n_i^{550} for the Mie code results within those for the filters. It should also be noted that the filter samples represent the whole size distribution (most likely) whereas the Mie code values represent only the accumulation mode. Changes in composition with size may therefore explain some of the differences. Interestingly the variability shown in the Mie code n_i^{550} values in Table 4.4 is not reflected in the filters values, though this may change when other iron oxides and clays are considered for the remaining four cases. Overall the n_i^{550} values from the filter samples support the values derived from Mie code in this study, when both different combinations of clays and iron oxides are considered, and when the different size distributions contributing to each are considered.

4.4.3 Factors Influencing ω_0^{550}

This section investigates the relative contributions from the imaginary part of the refractive index and the size distribution to the optical properties. In order to represent the size distribution through one variable, the effective radius has been used (as in McFarquhar and Heymsfield (1998); Pierangelo *et al.* (2005); Petzold *et al.* (2009), for example), and is defined as:

$$r_{eff} = \frac{\int_{r_{min}}^{r_{max}} r^3 \frac{dN}{dr} dr}{\int_{r_{min}}^{r_{max}} r^2 \frac{dN}{dr} dr}, \tag{4.4}$$

where r_{min} and r_{max} are defined as the upper and lower cut-off radii of the PCASP size bins which have been used for the size distribution, $0.06\mu m$ and $1.5\mu m$ respectively.

Figure 4.10 shows a scatter plot of the measured single scattering albedo values at 550nm against the effective radius of the size distribution (two completely independent variables). It is clear that there is no relationship between ω_0^{550} and r_{eff} for these results, and therefore that the size distribution variations seen during DODO are not strongly influencing the variations observed in ω_0^{550} .

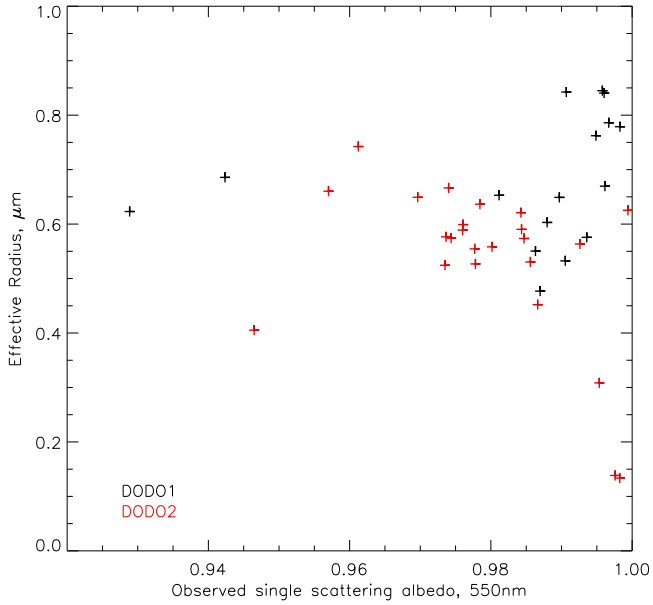

Figure 4.10: *Relationship between ω_0^{550} (directly from measurements) and effective radius (r_{eff}). Results represent accumulation mode only. DODO1 data shown in black, DODO2 in red. The two axes are independent measurements.*

Different variables representing the size distribution have also been tested. For example, the number of particles present greater than a particular radius may have more of an effect on the optical properties than r_{eff}, which is a measure of the whole size distribution. Therefore similar scatter plots were created showing ω_0^{550} against the fraction of the size distribution greater than a particular radius, with this radius varying from $r = 0.3\mu m$ and $r = 0.675\mu m$. These results are not shown, since they all showed no relationship between the various measures of the size distribution and ω_0^{550}. Therefore it appears robust that the variability in size distributions seen during DODO does not explain the variations seen in ω_0^{550} and were therefore not the dominant factor in governing the single scattering albedo. Note that this conclusion applies only to the accumulation mode.

Figure 4.11 shows the relationship between the imaginary part of the refractive index at 550nm and ω_0^{550}. In contrast to Figure 4.10, there is a strong relationship between n_i^{550} and ω_0^{550}, with larger absorption (greater n_i^{550}) corresponding to lower single scattering albedo values. The linear Pearsons correlation coefficient between n_i^{550} and ω_0^{550} is -0.987, indicating a very linear relationship.

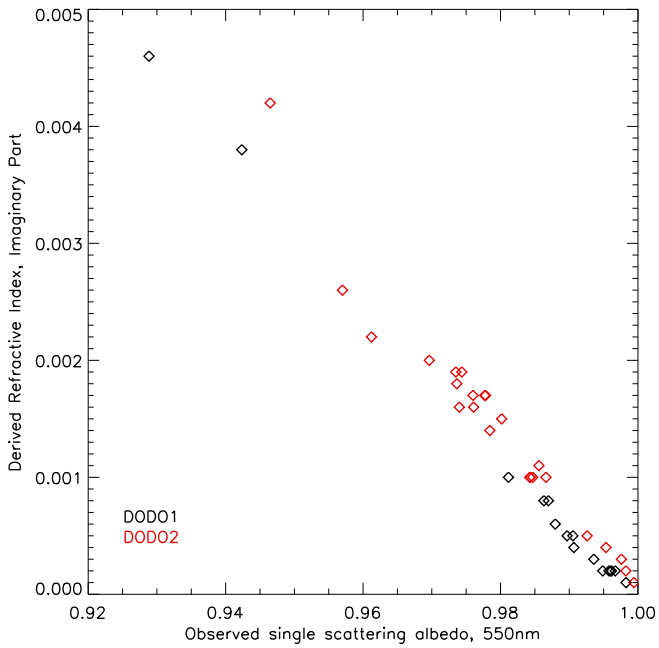

Figure 4.11: *Relationship between ω_0^{550} (directly from measurements) and derived imaginary part of the refractive index (n_i^{550}) from Mie calculations. Results represent accumulation mode only. DODO1 data shown in black, DODO2 in red. Linear Pearson correlation coefficient is -0.987.*

It is to be expected that greater absorption is related to lower single scattering albedo values. However, considering the number of modelling studies where optical property determination is complicated by the uncertainties in both size distribution and refractive index, both of which affect single scattering albedo (e.g. Tegen and Lacis, 1996; Liao and Seinfeld, 1998; Balkanski *et al.*, 2007), it is important to use observations to close in on these uncertainties. Despite the expected relationship between ω_0^{550} and n_i^{550}, the lack of a relationship between size distribution and ω_0^{550} is important, and implies that the single scattering albedo variations seen during DODO are determined principally by the refractive index, through the chemical composition of the dust. Note that this only applies to the accumulation mode (up to $r = 1.5\mu m$ here), since these measurements only cover this range of sizes.

The importance of the results shown in Figures 4.10 and 4.11 is firstly, that the variation of the single scattering albedo values for the accumulation mode from DODO can be explained mostly by the variation in the chemical composition. The chemical composition results, though not numerous, do show chemical variation occurring between DODO1 and DODO2, and between different flights, which supports this conclusion. The refractive indices from Table 4.4 also show that the chemical and microphysical data are in broad agreement of the values of n_i^{550}. This means that in future greater emphasis should be put on both defining the composition, and therefore the refractive index of dust accurately, in order to represent the single scattering albedo of the accumulation mode as accurately as possible, and to obtain closure on the optical properties through scattering and absorption measurements of the same size ranges. Exact representation of the accumulation mode size distributions is less important for modelling ω_0^{550} (again, accumulation mode only), though not necessarily for k_{ext}^{550} and g^{550} (see next Section).

Secondly, the lack of influence of the variability of size distribution on ω_0^{550} brings up the question of whether the variations in size distribution seen during the DODO campaign timescale are a good representation of the true variations in dust accumulation mode size distributions. It may be that the DODO size distribution measurements only represent a limited portion of the true variability, in which case the strong relationship between n_i^{550} and ω_0^{550} for the accumulation mode shown here may not always hold. However,

in comparing the size distributions to those from SHADE (Haywood *et al.*, 2003) and DABEX (Osborne *et al.*, 2008), the variations seen during DODO are not dissimilar. If the DODO accumulation mode size distributions are representative of the true variability in the atmosphere, then these results show a straightforward way to represent the refractive index using single scattering albedo measurements of the accumulation mode. Further size resolved chemical data would be needed to determine size-dependent changes in n_i , however.

4.4.4 Factors Influencing k_{ext}^{550}

In order to determine the dominant factors influencing the values of k_{ext}^{550} , similar scatter plots comparing the value of k_{ext}^{550} to measures of the size distribution and n_i^{550} have been created. Additional measures of the size distribution have been used here to represent the fraction of particles between particular radii. Here these radii are defined as $r_{min} = 0.06\mu m$, $r_1 = 0.3\mu m$, $r_2 = 0.675\mu m$ and $r_{max} = 1.5\mu m$, where r_{min} and r_{max} are the lower and upper ends of the PCASP size range. r_1 corresponds to the threshold radius used in Johnson *et al.* (2008) to differentiate between the fine and accumulation modes, and r_2 has been chosen to correspond to the mid point of one of the PCASP size bins, at which there appears to be a natural change in the size distributions, as shown in Figure 4.12. Figure 4.12 also shows the threshold radii in relation to the average DODO size distributions. The number of particles within each of these sections is defined as N_1, N_2 and N_3.

Figure 4.13(a) shows the mass specific extinction as a function of n_i^{550} , r_{eff} and the ratio of N_3 to N_2. It is clear from Figure 4.13(a) that there is no obvious relationship between the derived imaginary refractive index and the mass specific extinction, indicating that the composition is having little effect in determining k_{ext}^{550} .

In contrast, Figures 4.13(b) and 4.13(c) show a stronger relationship between measures of the size distribution and k_{ext}^{550} . As the effective radius increases, the mass specific extinction decreases, with DODO2 data having greater values of k_{ext}^{550} and lower values of r_{eff} than DODO1 in general. This implies that it is the size distribution which has a major effect on the value of k_{ext}^{550} , as opposed to the refractive index (and therefore chemical

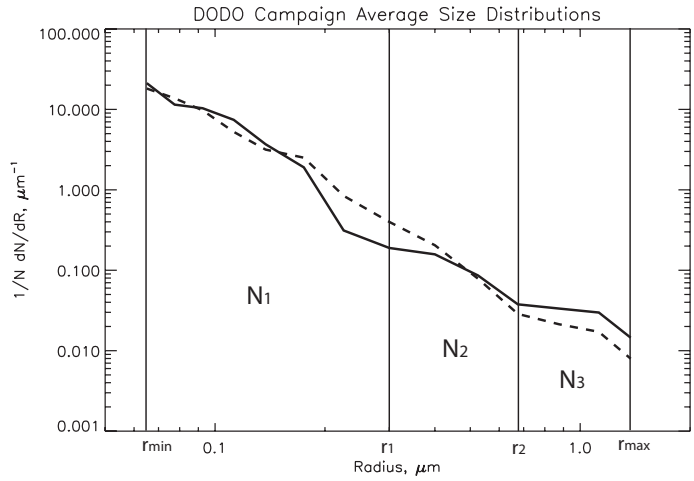

Figure 4.12: *Average DODO1 and DODO2 accumulation mode size distributions (same as Figure 4.3(c), with solid line representing DODO1 and dashed line DODO2) but with threshold radii marked on.* N_i *indicates the number of particles within each section of the size distribution.*

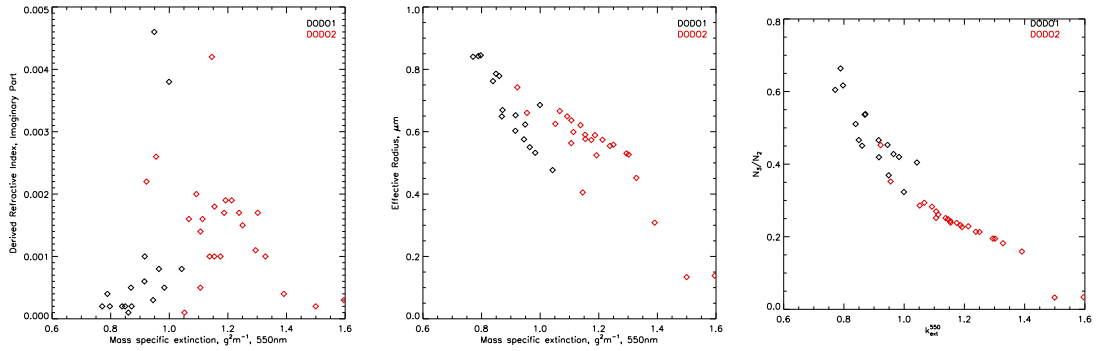

(a) (b) (c)

Figure 4.13: *Relationship between mass specific extinction at 550nm from Mie calculations (*k_{ext}^{550}*) and (a) Derived refractive index from Mie calculations, (b) effective radius (*r_{eff}*) from measurements and (c) the ratio of* N_3 *to* N_2 *(see text). Results represent accumulation mode only.*

composition).

A theoretical framework consistent with this observed relationship can be derived from simple definitions of extinction for a monodisperse sample, as follows:

$$\sigma_{ext} = \pi r^2 N Q_{ext}(r) \tag{4.5}$$

$$k_{ext} = \frac{\sigma_{ext}}{vf\ \rho_{dust}} = \frac{\pi r^2 N Q_{ext}(r)}{(4/3)\pi r^3 N \rho_{dust}} = \frac{3Q_{ext}(r)}{4r\ \rho_{dust}}, \tag{4.6}$$

where N is the number of particles per cm^3, σ_{ext} is the extinction coefficient in m^{-1}, Q_{ext}

is the extinction efficiency, ρ_{dust} is the density of dust, and vf is the volume fraction, or the volume of dust per m^3 air. If $r = r_{eff}$, as with a monodisperse sample, then,

$$k_{ext} = \frac{3Q_{ext}(r_{eff})}{4r_{eff}\,\rho_{dust}}, \tag{4.7}$$

and

$$r_{eff} = \frac{3Q_{ext}(r_{eff})}{4k_{ext}\,\rho_{dust}}, \tag{4.8}$$

so that

$$r_{eff} \propto \frac{1}{k_{ext}}, \tag{4.9}$$

since for a particular r_{eff} and wavelength the other variables are constant.

The same can be shown for a polydisperse sample using Equation 4.6 and 4.4, but where,

$$\sigma_{ext} = \pi \int_{r_{min}}^{r_{max}} r^2 \frac{dN}{dr} Q_{ext}(r) dr, \tag{4.10}$$

$$vf = \frac{4\pi}{3} \int_{r_{min}}^{r_{max}} r^3 \frac{dN}{dr} dr \tag{4.11}$$

are used to include the full size distribution, resulting in,

$$r_{eff} = \frac{3\int_{r_{min}}^{r_{max}} Q_{ext}(r) dr}{4\pi k_{ext}\,\rho_{dust}}. \tag{4.12}$$

Therefore, if Q_{ext} is not strongly influenced by differing chemical composition in each case, it could be expected that $r_{eff} \propto \frac{1}{k_{ext}}$. Due to the slight spread of data away from a perfect curve in Figure 4.13(b), it is likely that the chemical composition still retains some control over k_{ext}^{550} in the DODO results.

In addition to k_{ext}^{550} and r_{eff} showing an inverse relationship, the relation can be strengthened if the size distribution is represented by the ratio of the fraction of particles within two size ranges, in particular between the ratios of N_3 to N_2 (as shown in Figure 4.12). Again there is a distinction between the DODO1 and DODO2 data, with DODO1 data having lower values of k_{ext}^{550} and a smaller N_3 to N_2 ratio (DODO1 dust had more larger particles). The N_3 particles have a larger mass, so that their greater extinction is outweighed by their greater mass, making them less optically effective per unit mass. Con-

trastingly particles in the N_2 range are large enough to cause significant extinction, but small enough that their mass is not big enough to cause a low mass specific extinction. Thus a high ratio of N_3/N_2 yields a low value of k_{ext}^{550} , and vice versa. It seems that there is a threshold size, over which particles contribute more to the mass and lower k_{ext}^{550} , and below which particles contribute more to the extinction and less to the mass, increaseing k_{ext}^{550} .

4.4.5 Conclusion

The results presented for this section show that the observed variations in the single scattering albedo during DODO were largely determined by the imaginary part of the refractive index, whereas the variations in the modelled values of k_{ext}^{550} were much more influenced by the variations in size distribution for the accumulation mode.

In view of the single scattering albedo, this highlights the importance of the chemical composition and accurate assessments of the refractive index for dust (particularly concerning the wide range of estimates from the literature). Measurements of composition and refractive index of dust from different, but well-defined, source locations are also important, but are challenging considering the remoteness of many Saharan dust sources.

It should be noted that this work only considers the accumulation mode, since this is the size range over which closure of the refractive index is possible, due to measurements of both size distribution, scattering and absorption. The following section examines the effect of the coarse mode on optical properties, but this cannot be explored in the same level of detail as the accumulation mode due to lack of scattering and absorption measurements covering the full size range.

4.5 Effect of Coarse Mode on Optical Properties

The optical properties examined so far have covered size distributions in the fine and accumulation modes due to the size ranges measured by the nephelometer and the PCASP ($r = 0.06 - 1.5\mu m$) instruments. During DODO2 the coarse mode was measured by a number of instruments and techniques on the BAe-146, considered as experimental (see

Chapter 2). The impact of the coarse mode size distribution in addition to the fine and accumulation mode size distribution on the optical properties is tested here, for a single case study.

4.5.1 Coarse Mode size distributions for b238 Case Study

For this investigation Run 4.1 from flight b238 at an altitude of 1km was chosen, firstly since coarse mode data is available for both the CDP (Cloud Droplet Probe) and SEM (Scanning Electron Microscope) analyses. Secondly, b238 took place over desert in Mauritania where dust loadings were high, and coarse mode size distributions were likely to be greatest, and may therefore have the greatest impact on optical properties.

In order to generate a size distribution spanning the range from fine to coarse mode distribution it has been necessary to combine the coarse mode size distributions with the PCASP size distribution measurements. This has been done in the following ways for each instrument:

- **CDP**

  Figure 4.14(a) shows the size distributions as measured by the CDP and the PCASP. As described in Chapter 2, the first size bin and size bins greater than $r = 20\mu m$ for the CDP are not used. The CDP has been found to give reliable measurements over this size range (Abel, 2007). There appears to be a smooth transition between the PCASP and the CDP data. In order to create the full size distribution the CDP size distribution has simply been joined onto the PCASP size distribution.

- **SEM**

  Figure 4.14(b) shows that there is not a good agreement between the PCASP size distributions and the raw SEM size distribution, with the SEM dN/dR values being around two orders of magnitude greater than those measured by the PCASP. This could be due to a number of factors, including that the SEM shows geometric diameter whereas the PCASP gives an optical diameter. Accounting for changes in PCASP flow rate with pressure makes negligible difference to the discrepancy between the PCASP and SEM size distributions. Non-sphericity may also affect

both size distributions, though the effect for the PCASP has been shown to be small (Osborne *et al.*, 2008).

Since quantifying these problems is difficult the SEM size distribution has been scaled to agree with the PCASP size distribution which is thought to be more reliable. Since the smallest four size bins of the SEM size distribution have been defined to be the same as the largest four bins of the PCASP, a scaling factor necessary to match the four overlapping bins was calculated. The whole SEM size distribution was then scaled down using this scaling factor allowing a fit to the PCASP size distribution, as shown by the red line.

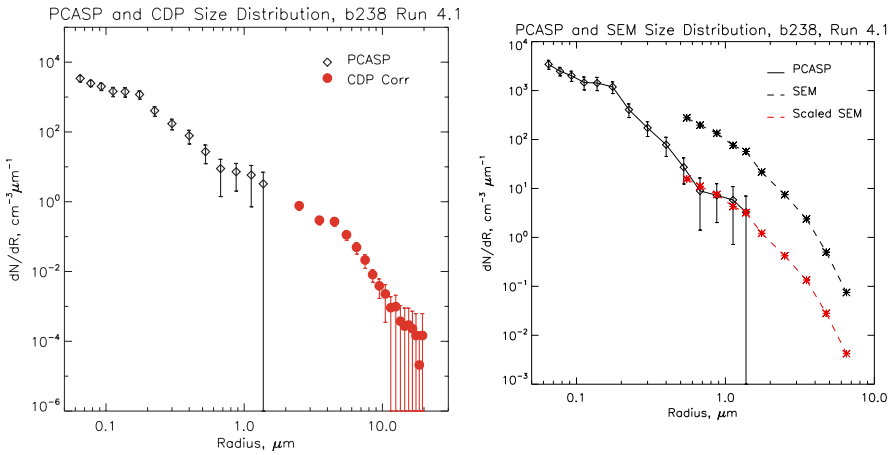

Figure 4.14: *Size distributions for coarse mode instrumentation from run 4.1, flight b238 at 1km altitude. (a) Number size distributions from the PCASP and CDP (corrected by a factor of 0.35 - see Chapter 2 for details). (b) Number size distributions from the PCASP and SEM, showing raw SEM data (black dashed line) and scaled SEM data (red dashed line) in order to obtain agreement with the PCASP. Error bars represent one standard deviation of the variability over the run. No time-resolved data is available for SEM data, therefore no error bars are shown.*

Figure 4.15(a) compares the resulting size distributions from the CDP and SEM, showing that although there is some agreement between the two instruments, the difference amounts to an order of magnitude in places. As described in Chapter 2, there are limitations in the CDP data due to the positioning of the instrument on the aircraft, and in the SEM due to the 2-D sampling technique which may overestimate diameter. Additionally there are further differences since the SEM size distribution is a geometrical measure, whereas the CDP size distribution is an optical measure.

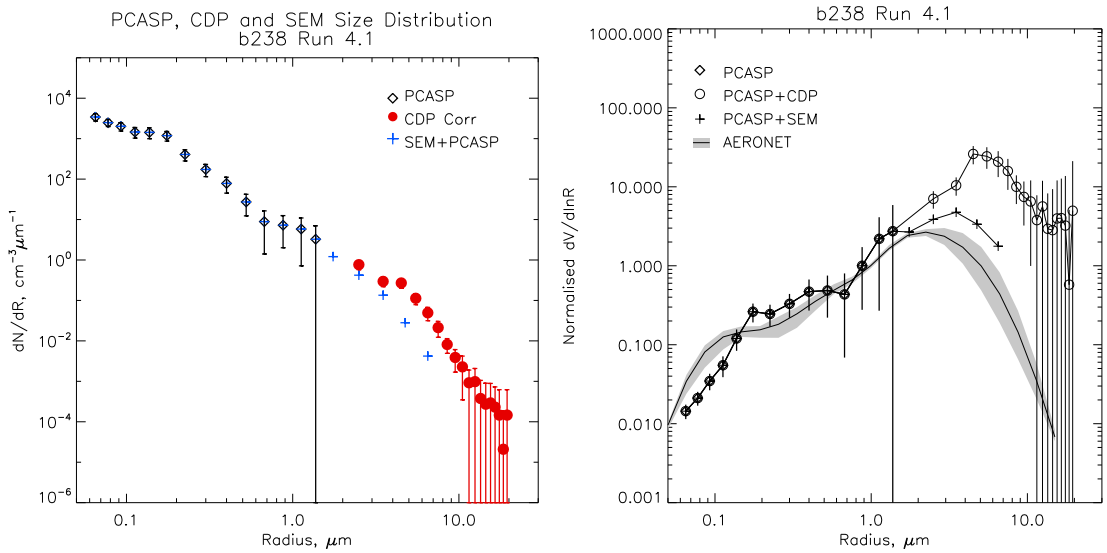

Figure 4.15: *Full size distributions for Run 4.1, flight b238, using data from the PCASP, CDP and SEM. (a) Number size distribution for each instrument, showing corrected CDP and SEM data. Error bars represent one standard deviation of the variability across the run. No time-resolved data is available for SEM data, therefore no error bars are shown. (b) Normalised volume size distributions for the same size distributions. Size distribution retrievals from the ground-based AERONET station at Dakar are shown, with grey shading representing the range in size distributions over the retrieval times used. Aircraft-measured size distributions have been normalised by the value at $1\mu m$ to allow meaningful comparisons with AERONET data.*

The full size distributions have also been compared to size distribution retrievals from the Dakar AERONET station, as shown in Figure 4.15(b). In doing this it should be noted that firstly that AERONET size distributions represent a column average, whereas the aircraft measurements were made at $1km$ altitude during a heavy dust storm, where the size distribution varied strongly with height (see Chapter 3). Therefore the aircraft size distributions have been converted to volume size distributions to match the AERONET size distributions, and normalised by the value at $1\mu m$. This avoids normalising by either the smallest PCASP size bin, which is known to be the least reliable of the PCASP bins (due to noise), or the larger size bins, which places too much faith in the coarse mode measurements, given the large range shown.

Secondly the Dakar AERONET station is located around $580km$ from where the aircraft was during flight b238. Satellite images also show that the main dust event did not pass directly over Dakar. Therefore the size distributions can only be expected to be broadly similar.

Although there are limitations associated with each measurement technique, Figure 4.15 shows the large range of coarse mode size distributions (in terms of both number and volume). The CDP measures significantly more supermicron particles than the SEM. The volume size distributions are different in both magnitude and radius, centred around $3.5\mu m$ and $4.5\mu m$ respectively for the SEM and CDP. These peaks are not so evident in the number size distributions in Figure 4.15(a) which show much smoother size distributions.

In comparison to the AERONET size distribution, the aircraft data are in agreement (within error bars) between radii of $0.2 - 2\mu m$. Below $0.2\mu m$ AERONET measures more particles than the aircraft - possibly due to the proximity to Dakar and associated pollution. For the coarse mode AERONET measures significantly fewer particles, which is not surprising considering that the main dust outbreak did not pass over Dakar. Because of limitations associated with each coarse mode measurement technique, the various coarse mode size distributions are regarded as a range of estimates. The following section examines the optical properties of the full size distribution, with respect to the uncertainties in the coarse mode measurements.

4.5.2 Calculation of Optical Properties for b238 Case Study

In order to calculate the optical properties of the full size distributions including the coarse mode, Mie code calculations have been performed using the different coarse mode size distributions and an appropriate refractive index.

In order to represent the measured size distributions, lognormal modes were fitted to the full size distributions (in the same way as described in Section 4.3.1). Firstly four lognormal modes were used to make a fitted curve which matched the size distribution from the PCASP for Run 4.1. A fifth mode was then added so that the new fitted curve from all five modes matched the full size distribution (including coarse mode) for the CDP as closely as possible. The full logfit curve was fitted to the measured size distribution by eye. The parameters for the first four lognormal modes were kept constant in each case so as to solely vary the coarse mode contribution. The same technique was then applied to the PCASP+SEM size distribution. The lognormal mode parameters used are shown

Mode	$r_{pg}/\mu m$	σ_g	N/cm^{-3}
1	0.062	1.49	190.0
2	0.153	1.24	89.0
3	0.225	1.52	47.0
4	0.960	1.35	4.6
5 (SEM)	1.800	1.60	1.0
5 (CDP)	2.200	1.50	1.8

Table 4.5: *Lognormal mode parameters used in calculation of fitted curves to represent full size distributions including the coarse mode, for B238 Run 4.1, as shown in Figure 4.15. Mode 1-4 values were established using the PCASP size distribution. Different parameters were used for mode 5 in the case of the SEM and CDP size distributions.*

for each test in Table 4.5.

In order to analyse the effect of the coarse mode over the same size distribution ranges, in the two coarse mode cases the size distributions were cut off at values of $30\mu m$ radius. For the case of the PCASP-only size distribution, the maximum radius value used was $1.5\mu m$, consistent with the optical properties previously calculated in Sections 4.3 and 4.4.

In order to calculate the optical properties of the size distributions shown in Figure 4.15 a refractive index is also needed. The derived imaginary refractive index of $0.0019i$ shown in Figure 4.9 for b238 Run 4.1 has been used with a real part of 1.53. This refractive index is representative of the accumulation mode, and therefore extending it to the coarse mode assumes that the composition does not vary with particle size. This may not be the case, and the chemical data for b237 suggests otherwise. However, due to the lack of data for b238 on the size resolved composition and refractive index, the value of $0.0019i$ is used as a best estimate. The refractive index used is constant over all wavelengths between $450 - 700nm$, and is not defined at wavelengths outside this range since only the optical properties at 550nm are examined. Sensitivity tests have showed that including the WCP (1983) variations of imaginary refractive index at greater wavelengths than the visible has negligible effect on the resulting optical properties. For simplicity spherical particles have been assumed for this test case, though the filter samples from b238 clearly show that many non-spherical particles were present.

Instrument measuring coarse mode	ω_0^{550}	g^{550}	k_{ext}^{550}, m^2g^{-1}
No coarse mode (PCASP only)	0.98	0.69	1.22
SEM	0.96	0.72	0.46
CDP	0.90	0.77	0.20

Table 4.6: *Optical properties at 550nm for coarse mode size distributions from B238, R4.1, as shown in Figure 4.15 and in Table 4.6.*

4.5.3 Optical Property Results for b238 Case Study

Table 4.6 shows the optical properties resulting from the different measurements of coarse mode size distribution, as well as the optical properties that result from Run 4.1 when no coarse mode (i.e. PCASP size distribution only) is included.

It is clear that the addition of a coarse mode results in a lower single scattering albedo (due to greater absorption from large particles), a lower mass specific extinction (due to the extra mass from large particles) and higher asymmetry parameter (due to larger particles scattering radiation in a more forward direction), as has been found previously (e.g. Tegen and Lacis, 1996; Haywood *et al.*, 2003; Otto *et al.*, 2007; Osborne *et al.*, 2008). The larger the coarse mode present, the more marked the change in the optical properties. For example, ω_0^{550} drops from 0.98 to 0.96 when the SEM coarse mode size distribution is included, whereas it drops further to 0.90 when the CDP coarse mode is included, since the SEM measurements showed less material in the coarse mode than the CDP.

Though the trend of the change due to adding the coarse mode fits in with that found in other literature, the magnitude of the change in optical properties, particularly ω_0^{550} , is much greater than has been found for previous aircraft campaigns (e.g. SHADE (Haywood *et al.*, 2003) and DABEX (Osborne *et al.*, 2008)). For the two dust cases examined in SHADE ω_0^{550} was found to drop from 0.96 to 0.92 in the first case, but did not drop at all from 0.95 in the second case. For DABEX, ω_0^{550} dropped from 0.99 to 0.98 when the coarse mode size distribution was included. Therefore the DODO results for b238 suggest that the differing effects of the coarse mode on the optical properties seen from these different campaigns are related to the amount of coarse mode present (or measured), and imply that the exact size distribution of the coarse mode is extremely important in deter-

mining the optical properties of dust.

There may be additional differences between ground (in-situ) measurements and aircraft measurements, should the coarse mode size distribution vary with height, as was found during DODO in Chapter 3. It is to be expected that large variations in the amount of coarse mode present occur, which may explain some of the differences in the reported values of ω_0^{550}, such as by Slingo *et al.* (2006) who took radiative measurements during an extremely heavy dust storm where a large coarse mode is to be expected, and derived ω_0^{550} values in the range 0.89-0.95. Aircraft studies measuring transported dust (such as Haywood *et al.* (2003)) may encounter less coarse mode and therefore measure higher single scattering albedos.

Despite the large sensitivity in ω_0^{550} to the coarse mode size distribution that has been illustrated by these results, the range in ω_0^{550} for b238 R4.1 (0.90-0.98) does not cover the range of single scattering albedo values from the literature (0.63-0.99). However, it likely that other factors may cause ω_0^{550} values lower than those shown in Table 4.6, such as a lower refractive index (such as the cases of b168 and b242) which would result in ω_0^{550} for the full size distribution being even lower. Therefore the ω_0^{550} values shown in Figure 4.1 can be viewed as an upper limit since they do not include any contribution from the coarse mode.

Additionally, it is entirely possible that the refractive index varies with particle size due to particle composition changes. For example, the SEM and TEM filter samples from DODO showed that iron oxide particles were present in the accumulation mode but not in the coarse mode, and are important due to their ability to absorb UV and visible light (e.g. Sokolik and Toon, 1999; Lafon *et al.*, 2006). If this was the case for the DODO results, it would result in the value of ω_0^{550} for the full size distribution being higher than the values shown in Table 4.6. Kandler *et al.* (2007) and Otto *et al.* (2009) also found (from chemical measurements) that the imaginary part of the refractive index decreased with particle size, due to the decreasing presence of soot and iron oxide in the case of Kandler *et al.* (2007).

It is also possible that the results here are dependent on the spherical assumptions. However, Otto *et al.* (2009) found that non-sphericity altered ω_0 by up to 1%, which would

result in a maximum change in ω_0^{550} of 0.01 for the b238 R4.1 CDP case.

In conclusion, the results in Table 4.6 show that the coarse mode is extremely important in determining the optical properties of dust, and therefore future aircraft campaigns should place strong emphasis on operating fully calibrated aerosol probes which are able to measure particles at least up to $20\mu m$ radius.

4.6 Chapter Summary

This Chapter has explored the microphysical and optical properties, both measured and modelled, of dust measured during the DODO campaigns. The key findings are as follows:

1. The accumulation mode size distributions measured during the wet season show more variability than those from the dry season, which is related to the greater range in transport altitudes during DODO2. This results in a greater fraction of the larger accumulation mode particles residing at higher altitudes, with fewer at lower altitudes.

2. There is a difference in accumulation mode size distributions between measurements made over land and ocean. Fewer particles at $r > 0.2\mu m$ are found over the ocean, due to loss from deposition, which is most marked at greater radii.

3. Differences in accumulation mode ω_0^{550}, k_{ext}^{550} and n_i^{550} are seen between the two campaigns, with the dry season flights generally showing higher ω_0^{550}, lower k_{ext}^{550} and lower n_i^{550}. No differences in g^{550} were found between campaigns.

4. Variability in optical properties was much greater during DODO2 than DODO1, which is fitting with the dust sources, chemical composition and size distributions being more variable.

5. ω_0^{550} values for the accumulation mode ranged from $0.93 - 0.99$, which is at the upper range of estimates from the literature.

6. The variability of ω_0^{550} observed during DODO can be attributed to variations in n_i^{550} and therefore variations in the composition and source of the dust. The contribution from the accumulation mode size distribution to the variations in ω_0^{550} have been shown to be negligible. This highlights the importance of accurate and representative measurements of the refractive index in order to correctly model Saharan dust. It also suggests that if the composition does not change with further transport, ω_0^{550} will not change substantially across the Atlantic (at least for the accumulation mode).

7. The variability of k_{ext}^{550} during DODO can be attributed mostly to variations in the accumulation mode size distribution. Due to changes in the size distribution with dust transport, this would mean that k_{ext}^{550} may change substantially across the Atlantic.

8. The coarse mode size distribution has been shown to have a large effect on the optical properties of dust, particularly for ω_0^{550} where the decrease due to the addition of the coarse mode is larger than has previously been seen in aircraft campaigns. Therefore the accumulation mode measurements of ω_0^{550} in the range $0.93 - 0.99$ should be viewed as an upper limit.

9. The varying values of ω_0^{550} from the direct measurements of the accumulation mode, and the coarse mode tests go some way to explaining the variation in ω_0^{550} in the literature. Depending on the amount of coarse mode present and the technique for measuring (or not measuring) the coarse mode, the resulting single scattering albedo may vary.

10. Good quality measurements of the coarse mode size distribution from calibrated aircraft probes are of great importance when measuring dust. Scattering measurements of the full size distribution (i.e. including coarse mode) are also valuable.

11. The varied values of ω_0^{550} , k_{ext}^{550} and n_i^{550} may have significant effects on the radiative effect of the dust.

Chapter 5

Assessment of Pyranometer Data Quality

5.1 Introduction

5.1.1 Reasons for Quality Assessment

During DODO the BAe-146 was equipped with upper and lower pyranometers in order to measure downwelling and upwelling shortwave irradiances. Pyranometer measurements can be used in conjunction with computed irradiances from radiative transfer models in order to validate model results and so obtain radiative closure (as described in Chapter 6). Therefore the availability of accurately measured, reliable irradiance data from the pyranometers is critical. If the pyranometer data is to be used in this way however, it is essential to ensure that the pyranometer data is accurate and to know the uncertainty in the measurements.

Recently it has become evident that some problems exist with the BAe-146 pyranometer data. During flights in the UK following the DODO campaigns it was noticed that the pyranometer domes had suffered from sand-blasting (degradation of the dome surface due to heavy aerosol impaction) on their forward-facing side (personal communication, Jim Haywood). This chapter shows that the pyranometer-measured irradiances did not always agree with other measured and modelled irradiances, and that standard procedures presently used to correct the BAe-146 pyranometer measurements may not be appropriate. Alternative methods are investigated, as are uncertainties in the measured irradiances.

5.1.2 Summary of Data, Instruments and Flights

Measurements of down-welling and up-welling irradiance on the BAe-146 were made using Eppley Precision Spectral Pyranometers (PSPs) mounted both above and below the fuselage (see Table 5.1). Each pyranometer was covered with Schott glass which protects the surface of the thermopile and defines the operating wavlength range, shown in Table 5.1.

The overall accuracy of the BAe-146 pyranometers is not well defined. The accuracy of standard Eppley PSPs are frequently defined at $\pm 1\%$ (Burns *et al.*, 2000), and the Baseline Surface Radiation Network (BSRN) requirements on pyranometer accuracy are 2%

Instrument	Location	Irradiance measured	Spectral Range
Clear dome Eppley Precision Spectral Pyranometer (PSP)	BAe-146 fuselage, upper and lower	Total	$0.3 - 3\mu m$
Red dome Eppley Precision Spectral Pyranometer (PSP)	BAe-146 fuselage, upper and lower	Total	$0.7 - 3\mu m$
ARM Skyrad Pyranometer	Niamey airport, Niger	Direct	$< 4\mu m$
ARM Skyrad Pyranometer	Niamey airport, Niger	Diffuse	$0.4 - 4\mu m$

Table 5.1: *Summary of BAe-146 and ARM pyranometers*

for total shortwave irradiance (Saunders *et al.*, 1991). However, additional uncertainties are encountered through flying the pyranometers on the aircraft. Recent publications cite the accuracy as ranging from ± 5 to $\pm 8\%$ (Haywood *et al.*, 2003, 2001), but are based on previous work by Saunders *et al.* (1992) from an aircraft intercomparison during 1989, when the C-130 aircraft was in use. Saunders *et al.* (1992) estimated the uncertainty in the pyranometer measurements using differences between irradiance measurements from three aircraft under clear skies at an altitude of 5.9km. They found that the accuracy of the upwelling clear dome shortwave irradiance, assumed to be entirely diffuse and therefore isotropic, was $\pm 2\%$ ($< 5 W m^{-2}$) on average. The downwelling irradiance had additional uncertainty because a correction to the direct component for aircraft attitude was required, which increased the uncertainty to $\pm 3\%$. Using standard propagation of error formulae, this results in 2.2% uncertainty due to attitude corrections alone. Uncertainty in the downwelling red dome measurements was estimated to be around $\pm 5\%$. However, differences between downwelling pyranometer measurements and modelling results varied between $2 - 4\%$ for the clear dome pyranometers (with the pyranometers always measuring less irradiance than was modelled) and between $0 - 4\%$ for the red dome pyranometers (with no particular bias in either direction).

Saunders and Barnes (1991) compared the upper and lower pyranometers by moving them from their usual positions to the upper positions and conducting in-flight comparisons at high altitude under clear skies. The results showed that the clear and red dome pyranometers agreed within $6 W m^{-2}$ (0.6%) and $3 W m^{-2}$ (0.8%) respectively. Comparisons against model results showed worse agreement compared with the instrument comparisons, with the clear and red domed pyranometers measuring 2.5% and 8% less than

predicted by model results. If the clear sky above the aircraft is well charactarised and modelled, the agreement between model and pyranometer measurements should be good. Therefore, assuming this to be the case, these percentage differences may outline the accuracy of the pyranomters, when used to compare to model calculations.

Since the work of Saunders *et al.* (1992) the C-130 has been replaced by the BAe-146 and the pyranometer mounting platform has been replaced. No intercomparison of pyranometers has been performed at this time, and estimating the accuracy of the BAe-146 pyranometers is therefore difficult and previous estimates based on measurements made with the C-130 are not necessarily applicable. Based on the previous intercomparisons of Saunders *et al.* (1992) and Saunders and Barnes (1991) of the pyranometers with other aircraft pyranometers and models, the total uncertainty in the clear dome measurements is likely to be up to $\pm 4\%$, and up to $\pm 8\%$ for the red dome measurements, with the uncertainty solely due to attitude corrections being 2.2%.

In this chapter aircraft manoeuvres are used to assess the quality of the pyranometer data, and come from box pattern manoeuvres and pirouette manoeuvres. A description of the manoeuvres and their purposes is as follows:

1. Box Patterns

   Box patterns manoeuvres are carried out at high altitudes (above 550mb or Flight Level (FL) 180 in these examples) under clear sky conditions. Four straight and level runs are carried out; one directed into the sun, one directed across the sun, one directed out of the sun, and the fourth cross-sun, thus forming a box pattern. The high altitude allows irradiances to be measured at an altitude where there is little aerosol (and cloud, since skies are clear) above the aircraft, and the atmospheric profiles of water vapour, ozone, temperature and other components are relatively well known above the aircraft and can be well represented using standard profiles, such as described by McClatchey *et al.* (1971). This means that the irradiance at the altitude of the box pattern can be relatively accurately modelled in order to compare to the pyranometer measurements. Secondly, the box pattern formation itself allows measured irradiances to be compared when the aircraft is at different headings relative to the sun. This is important for estimating pitch and roll offsets,

described later.

2. Pirouettes

   Pirouettes are carried out on the runway before or after take-off. They consist of the aircraft slowly rotating through $360°$. Pirouettes have two purposes: firstly if there is a ground-based pyranometer in the vicinity, then direct comparisons can be made. Secondly they allow measurements of irradiance at different headings relative to the solar azimuth. This can show whether there has been any dirtying or damaging on a particular side of the pyranometer dome, and can be used to estimate pitch and roll offset of the pyranometers relative to the aircraft (see later). The disadvantage of pirouettes compared to box patterns is that there is more atmosphere above the aircraft during pirouettes which can make it difficult to use modelling results for comparison due to lack of knowledge of atmospheric composition and aerosol. Additionally there is high potential for interference by clouds. However, the time taken for pirouette manoeuvres is much less than a box pattern which lowers the flying cost, and allows many pirouettes to be carried out routinely during a campaign, as long as the sky is clear.

Duration	Campaign	Location
11/1/2006 - 2/2/2006	DABEX	Niamey
3/2/2006 - 16/2/2006	DODO1	Dakar
17/2/2006 - 18/7/2006	Aircraft in UK and on other campaigns. Pyranometers removed, calibrated and re-mounted	
20/7/2006 - 20/8/2006	AMMA	Niamey
21/8/2006 - 28/8/2006	DODO2	Dakar

Table 5.2: *Summary of campaigns relevant to pyranometer correction procedures*

The campaigns during which box patterns and pirouette manoeuvres were performed are shown in Table 5.2, and the details of each manoeuvre are shown in Table 5.3. During DABEX two box patterns were carried out, and these can be used to infer the quality of the pyranometer data during DODO1. During DODO2 one box pattern was carried out. Note that between DODO1 and AMMA the pyranometers were removed from the aircraft for a calibration, and then re-mounted. Additionally during AMMA there was

Flight	Date	Campaign	Manoeuvre	Flight Level	Pressure /mb	Comment
b157	16/1/2006	DABEX	Box Pattern	FL180	550	
b167	2/2/2006	DABEX	Box Pattern	FL200	465	
b234	16/8/2006	AMMA	Pirouette	ground level	n/a	Dust present above aircraft. No red dome data available. ARM data available for comparison.
b241	25/8/2006	DODO2	Box Pattern	FL220	428	

Table 5.3: *Summary of flights relevant to pyranometer correction procedures. Note that the pyranometers were removed from the aircraft between DODO1 and AMMA for a calibration. FL stands for flight level.*

one pirouette manoeuvre which was usable. This pirouette was carried out at Niamey airport, where the AMF (ARM (Atmospheric Radiation Measurements) Mobile Facility) was stationed during 2006, and so measured irradiances can be compared to the ARM irradiances. A summary of the BAe-146 pyranometers and the ARM pyranometer data used here are shown in Table 5.1.

For all comparisons between ARM and BAe-146 pyranometers shown here the total irradiance for the ARM pyranometers is calculated using the component sum method: the sum of the direct and diffuse irradiance. This method is used in preference to the ARM pyranometer which measures the total irradiance because the total of the direct and diffuse radiation is more accurate (e.g. Michalsky *et al.*, 1999).

The following sections review the standard corrections that FAAM make to the pyranometer data, assess the amount of dome dirtying that occurred during DODO, estimate the pitch and roll offsets of the pyranometers relative to the aircraft, and assess the uncertainty in the pyranometer data due to these and other factors, and compare the data to other observations and model results.

5.2 Standard Correction Procedure for Pyranometer Measurements

The total downwards irradiance through a horizontal plane is defined according to Equation 5.1, where the total irradiance is composed of a diffuse (I_{diff}) and direct ($I_{dir}(\theta)$)

component (both in Wm^{-2}), where only the direct component depends on the solar zenith angle, θ.

$$I_{tot} = I_{diff} + I_{dir}(\theta) \tag{5.1}$$

Since the BAe-146 pyranometers do not lie in the horizontal during flight the measured direct component of the irradiance must be corrected to allow for the pitch and roll angle of the pyranometer if there is any direct radiation present. This is not the case for the lower pyranometers, where the upwelling shortwave radiation is totally diffuse, but can be important for the upper pyranometers. If the plane of the pyranometer is not horizontal then the measured irradiance becomes

$$I_{tot}(\beta) = I_{diff} + I_{dir}(\theta)\left(\frac{\cos(\beta)}{\cos(\theta)}\right), \tag{5.2}$$

(Saunders *et al.*, 1992), where β is the angle between the solar zenith angle θ and the normal to the pyranometer, defined according to Equation 5.3, and $I_{tot}(\beta)$ is the irradiance measured by the pyranometer.

$$\begin{aligned}\cos(\beta) &= [\sin(dp_{tot})\sin(\theta)\sin(rel\_hdg)] \\ &\quad + [\cos(dr_{tot})\cos(dp_{tot})\cos(\theta)] \\ &\quad - [\cos(dp_{tot})\sin(dp_{tot})\sin(\theta)\cos(rel\_hdg)]\end{aligned} \tag{5.3}$$

dp_{tot} and dr_{tot} are the total pitch and roll of the pyranometers from the horizontal, defined according to $dp_{tot} = dp + dp_{ac}$ and $dr_{tot} = dr + dr_{ac}$, where dp_{ac} and dr_{ac} are the pitch and roll of the aircraft, which change constantly during flight, and dp and dr are the pitch and roll of the pyranometers relative to the aircraft inertial navigation system. rel_hdg is the relative heading of the aircraft relative to the solar azimuth angle, defined as solar azimuth minus aircraft heading.

The raw pyranometer irradiance measurements, $I_{tot}(\beta)$, are processed by FAAM using a program called CRFLUX. If the irradiance is less than a critical threshold, dependent on solar zenith angle, the irradiance is assumed to be totally diffuse, and no corrections for attitude are performed. Otherwise, at least some direct radiation is assumed, and the

measured irradiance is corrected for the pyranometer attitude shown in Equation 5.2 at the same time as a correction for the non-cosine response of the pyranometers. The correction used is shown in Equation 5.4, whereby it is assumed that the ratio of direct to total irradiance (FDIR) is known. C_{eff} is a correction for the non-cosine response of the pyranometers and varies with solar zenith angle, and I_{corr}, the corrected irradiance, equivalent to what would have been measured through a horizontal plane, is obtained.

$$I_{corr} = \frac{I_{tot}(\beta)}{1 - \left\{ FDIR \left[1 - C_{eff} \left(\frac{\cos(\beta)}{cos(\theta)} \right) \right] \right\}}. \tag{5.4}$$

In correcting the measured irradiance, it is necessary to know the values of dp and dr, the pitch and roll offset of the pyranometers relative to the aircraft inertial navigation system for Equation 5.3, and FDIR, the ratio of direct to total radiation, for Equation 5.4. In the FAAM CRFLUX code FDIR is always assumed to be 0.95, though in practice it would be dependent on altitude and solar zenith angle. The pitch and roll of the aircraft itself is constantly changing, and is recorded at 1Hz by the inertial navigation system. Generally the BAe-146 pitch is around $6°$. The pyranometers sit on a mount which is at a pitch offset angle of around $-3°$ relative to the aircraft, but it may be possible that additional variations in the way the pyranometers are bolted onto the mount can result in larger or smaller total pitch offset angles each time they are remounted. Standard FAAM correction procedures for DODO have assumed that pitch and roll offset angles of both clear and red dome pyranometers are as follows:

- clear dome: $dp = -0.87°$, $dr = -0.51°$
- red dome: $dp = 0.02°$, $dr = -0.96°$.

5.3 Determination of Pyranometer Pitch and Roll Offsets

5.3.1 Introduction

As described in Section 5.2 the magnitude of the pitch and roll offset angles of the pyranometers relative to the aircraft is implicit in the standard correction procedure for the

pyranometer data, as described by Equations 5.3 and 5.4. Standard values of pitch and roll offset (dp and dr) are always assumed by FAAM within the CRFLUX program when correcting the pyranometer data (see Section 5.2). However, it became obvious when analysing at the pyranometer data that these standard values of dp and dr are not always appropriate. Additionally small changes in the way the pyranometers are assembled on the aircraft may result in the pitch and roll offset angles changing, which may affect the value of the measured irradiances. Thus every time the pyranometers are removed and re-mounted on the aircraft, the values of dp and dr may change, and therefore an analysis of the following sort should be completed.

5.3.2 Method

The raw irradiance data can be analysed as a function of relative heading, ideally during a pirouette, but also during the box patterns, in order to get a best-estimate of the true values of dp and dr, which may differ from the values used in CRFLUX.

In order to use raw irradiance data, the publicly available BADC irradiance data corrected by FAAM using the CRFLUX code is back-corrected using equations 5.3 and 5.4 and exactly the same values of dp, dr and FDIR as used by CRFLUX. The data is then re-corrected using the same equations, but with appropriate values of dp, dr and FDIR.

Data for the box patterns in b157, b167 and b241 and the pirouette in b234 have all been back-corrected and re-corrected here, in order to estimate the true values of dp and dr. In order to remove another unknown from this method, FDIR has been modelled using the Edwards and Slingo radiation transfer code (Edwards and Slingo, 1996) for the box pattern cases. Standard atmospheric profiles for tropical cases (McClatchey *et al.*, 1971) have been used to determine profiles of water vapour, ozone and temperature. Since the box patterns were performed at high altitudes there should be no aerosol above the aircraft. The box patterns were also performed under cloud-free skies. Therefore the modelled irradiances should be accurate and good for comparisons against the pyranometers, except for uncertainties in water vapour due to departures from the standard tropical profiles. A sensitivity test using Dakar radiosonde data above the aircraft revealed a very low sensitivity to the inclusion of this water vapour data. Although the clear dome pyra-

nometers measure radiation between wavelengths of $0.3-3\mu m$ they are calibrated against radiometers measuring the whole of the shortwave spectrum (personal communication, Ben Johnson). Therefore the modelled irradiances are also over the whole spectrum, between wavelengths of $0.2 - 10\mu m$. Comparisons between the model and red dome pyranometer irradiances use wavelengths of $0.7 - 3\mu m$. Modelling the irradiance at the level of the box patterns in this way allows FDIR for each box pattern to be calculated, and included in the pyranometer corrections.

For the b234 pirouette at Niamey airport, data from the ARM Skyrad pyranometer is used to calculate FDIR. Note that the spectral range of this pyranometer is $0.4 - 4\mu m$, slightly different to the FAAM pyranometers on the BAe-146. Values of FDIR used for each case are shown in Table 5.4.

Once FDIR for each case has been calculated, it is possible to re-correct the pyranometer data using a given value of dp and dr. Using the assumption that the pyranometer should be measuring the same value of irradiance at all headings if the data is de-trended or normalized for a changing solar zenith angle, and that the only variables affecting the re-corrected data are dp and dr, it is possible to vary dp and dr until the standard deviation of the normalized irradiance across a range of relative headings is minimised. Other studies with similar methods of minimizing the variance of de-trended or normalized irradiance over a range of relative headings to estimate dp and dr has been used successfully in other studies, such as Saunders and Barnes (1991), Bannehr and Schwiesow (1993) and Ramana *et al.* (2007), using straight and level runs carried out on different headings, and Boers *et al.* (1996) and Boers *et al.* (1998) who used irradiance measurements from an aircraft 'circle' (orbit).

Figure 5.1 shows an example of a step in the process of estimating dp for the b241 box pattern. Here dr is set to 0.2° and the value of dp is varied from -4.4° to -3.6°. For each case, the standard deviation of the normalised irradiances across the range of relative headings is calculated. For b241 only irradiance measured outside relative headings of $\pm 50^\circ$ is used for the standard deviation calculation as it will not be affected by dome dirtying on its forward side (see Section 5.4). Here the minimum standard deviation occurs when $dp = -4.1^\circ$. For other values of dp the re-corrected irradiance show more

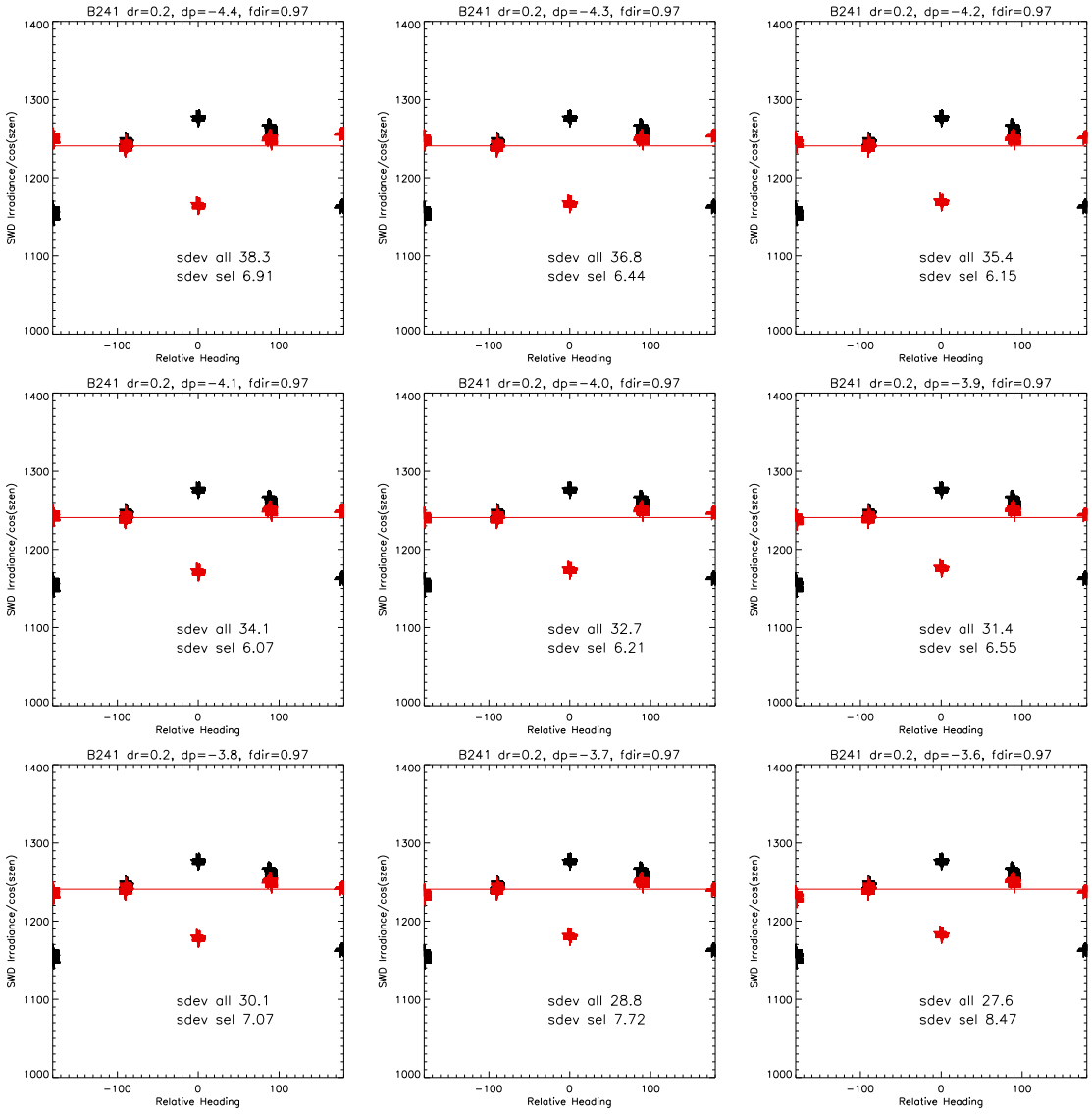

Figure 5.1: *Example of one step in the estimation of dp for the clear dome pyranometer for b241. Irradiance (normalised by cosine of solar zenith angle) is shown as a function of aircraft relative heading (solar azimuth - aircraft heading). For each case the data is re-corrected using $dr = 0.2$ and dp varying between -4.4 to -3.6, as indicated on each plot. Black points represent data re-corrected using only aircraft pitch and roll, red points represent data re-corrected using both aircraft and pyranometer pitch and roll. The red line represents the mean of the red points, excluding data at relative headings between $\pm 50^\circ$ which may be affected by dome dirtying (see Section 5.4). The text in each plot shows the standard deviation of the red points, for all relative headings (sdev all) and relative headings outside $\pm 50^\circ$ (sdev sel). Sdev sel is minimised at $dp = -4.1^\circ$ (middle row, left hand plot) in this case.*

variation across different relative headings. The next step here would be to set $dp = -4.1^\circ$, and vary dr, and iterate this process until there was no more change in dp and dr to within 0.1°.

This process has been carried out for the box patterns in b157, b167 and b241 and the

pirouette in b234, and has allowed dp and dr to be estimated for each case. For any flights affected by dome dirtying/damage (see Section 5.4), measurements for relative headings between $\pm 50^{\circ}$ have not been included in the calculations.

5.3.3 Results and Implications

Table 5.4 shows the best-estimates of dp and dr for the clear and red dome pyranometers for the different flights. During a campaign when the pyranometers have not been removed from the aircraft, the values of dp and dr should remain the same. Between different campaigns, when the pyranometers have been removed and re-mounted, it is possible that dp and dr could change if they are not being attached to their mounts in an identical manner every time. Note that between DODO1 and AMMA (flights b167 and b234) the pyranometers were removed from the aircraft for a calibration. The results in Table 5.4 show that the best-estimates of the pyranometer pitch and roll offset angle as derived from pirouette and box pattern manoeuvres differ significantly from those used in the standard processing of the pyranometer irradiance data (standard values are $dp = -0.87^{\circ}$, $dr = -0.51^{\circ}$ for the clear dome and $dp = 0.02^{\circ}$, $dr = -0.96^{\circ}$ for the red dome).

The irradiances corrected using the standard FAAM values of dp and dr have been compared to the irradiances re-corrected using the best estimates of dp and dr shown in Table 5.4, and are shown in Figures 5.2 and 5.3. It is clear that the data re-corrected using values of dp and dr from Table 5.4 (red lines) result in the smoothest transitions of irradiance values across all the different runs and relative headings adopted during the pirouettes and box patterns. This is an indicator that re-corrected data is behaving physically, in contrast to the FAAM-corrected data (yellow lines), which show large jumps in irradiance between different runs of the box patterns, and on different headings during the pirouette. Note that even the corrected data shows large jumps on some into-sun runs - this is where the pyranometer domes are being affected by dirtying (see Section 5.4).

In many of the flights the difference between the data corrected using values of dp and dr as defined by FAAM and as derived here is very large. Table 5.5 shows the maximum difference between these two correction procedures for each manoeuvre, excluding data

Flight	Dome Type	Flight Pattern	FDIR	dp	dr	FDIR Calculation	Comments
b157	Clear	Box Pattern	0.95	$-5.0°$	$+0.7°$	Model	Flight from DABEX
b157	Red	Box Pattern	0.95	$-3.2°$	$-1.4°$	Model	Flight from DABEX
b167	Clear	Box Pattern	0.95	$-2.6°$	$+0.4°$	Model	Flight from DABEX
b167	Red	Box Pattern	0.95	$-2.3°$	$-1.1°$	Model	Flight from DABEX
b234	Clear	Pirouette	0.68	$-5.0°$	$+0.2°$	ARM data	Flight from AMMA
b234	Red	Pirouette	0.68	n/a	n/a	ARM data	No data available
b241	Clear	Box Pattern	0.97	$-4.1°$	$+0.5°$	Model	Flight from DODO2
b241	Red	Box Pattern	0.97	$-3.6°$	$+6.6°$	Model	Flight from DODO2

Table 5.4: *Best estimates of pitch (dp) and roll (dr) offset of the clear and red dome pyranometers and details of FDIR value (direct/total irradiance ratio) used. Between DODO1 and AMMA (flights b167 and b234) the pyranometers were removed from the aircraft for a calibration.*

which may be affected by dome dirtying. For the clear dome percentage errors range from 3.5-6.3%, and from 4.5-9.0% for the red dome. Errors of this magnitude, which are solely due to errors in dp and dr, are far greater than the uncertainty in measured irradiance of 2.2% due to attitude corrections as found by Saunders *et al.* (1992), and exceed the suggested total error of 4% and 8% (Section 5.1.2) for the clear and red dome pyranometers respectively. Using appropriate values of dp and dr for the pyranometer corrections is therefore extremely important in minimising the error in the measurements and increasing their reliability. Pirouettes and box pattern manoeuvres are of critical value in determining dp and dr if they cannot be determined by any other method.

Table 5.4 also shows that during a single campaign, when the pyranometers have not been removed from the aircraft, the best estimates of dp are uncertain to within $2.4°$ between b157 and b167, and to within $0.9°$ between b234 and b241 for the clear dome. Similarly the best estimates of dr differ by $0.3°$ for b157 and b167, and by $0.3°$ for b234 and b241 for the clear dome. These results suggest that the pitch and roll offsets change significantly between the two campaigns. However, the uncertainties in dp and dr during each campaign are not small enough to unambiguously say that it is the removal and re-

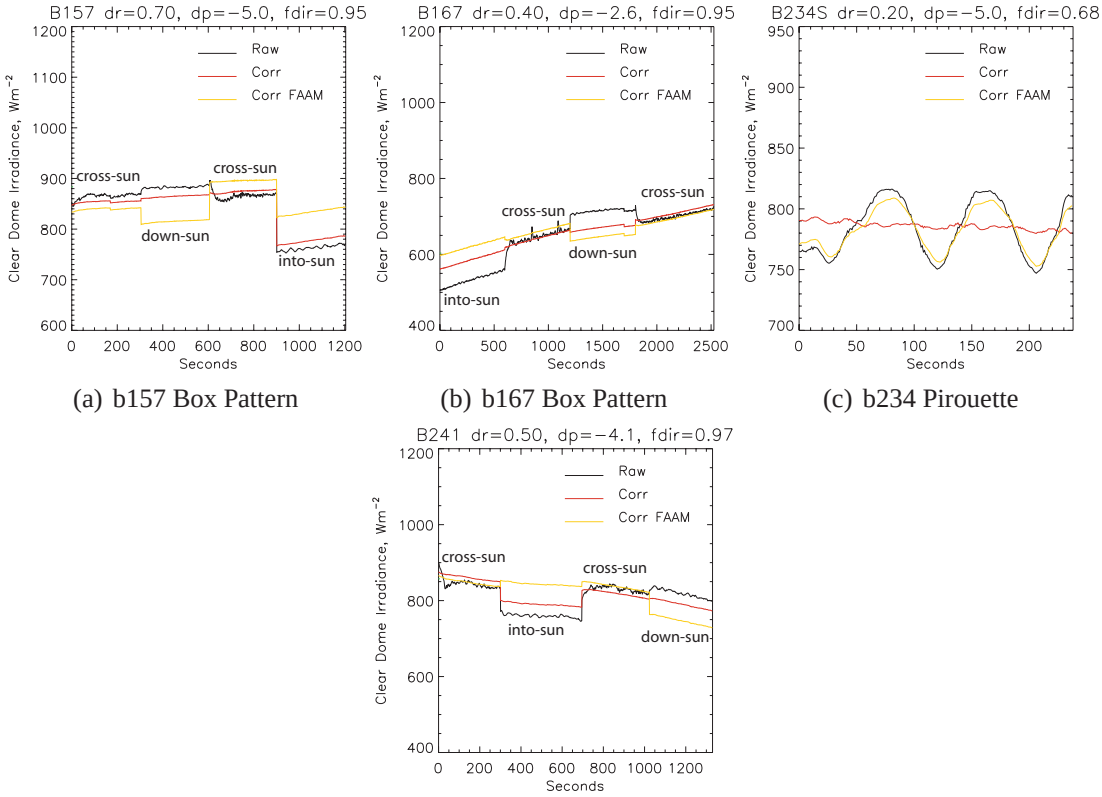

(a) b157 Box Pattern (b) b167 Box Pattern (c) b234 Pirouette

(d) b241 Box Pattern

Figure 5.2: *Clear dome irradiance for box patterns and pirouettes, including raw data (completely uncorrected for pitch and roll) in black, data as corrected by FAAM using standard values of dp and dr, in yellow, and re-corrected data using values of dp and dr as given in Table 5.4, in red.*

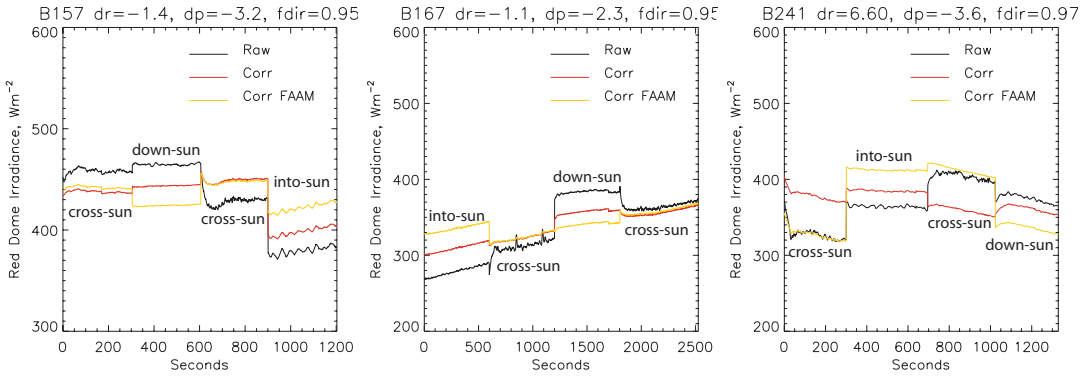

(a) b157 Box Pattern (b) b167 Box Pattern (c) b241 Box Pattern

Figure 5.3: *As for 5.2, but for red dome pyranometer. Note that no data is available for b234.*

mounting that causes this change - it may just be that this method of estimating dp and dr entails large uncertainties. Previous work by Saunders *et al.* (1991) also found that dp estimates changed by up to $0.6°$ when box pattern manoeuvres were repeated and the

Flight	Dome Type	Maximum Percentage Error
b157	Clear	6.0
b157	Red	4.5
b167	Clear	6.3
b167	Red	9.0
b234	Clear	3.5
b234	Red	n/a
b241	Clear	5.8
b241	Red	15.0

Table 5.5: *Maximum percentage difference between irradiances corrected using the standard FAAM values of dp and dr and irradiance corrected using the best-estimate values of dp and dr shown in Table 5.4. Results are based on data shown in Figures 5.2 and 5.3. Data from into-sun runs which may be affected by dome dirtying have not been used.*

pyranometers were not moved. Investigating changes in dp and dr due to removal and remounting of the pyranometers should be straightforward to test by performing pirouettes or box patterns following remounting the pyranometers. Additionally Saunders *et al.* (1991) recommend that dp and dr are recalculated every time the aircraft inertial navigation system is replaced/installed. It is possible that changes to the inertial navigation system between DODO1 and DODO2 could have affected the apparent changes in dp and dr between the two campaigns.

In summary, the implications of this work, which has determined dp and dr for flights relevant to the DODO campaigns, are as follows:

1. It is possible to use both pirouette manoeuvres and box patterns, performed under clear sky conditions, to estimate dp and dr.

2. dp and dr can differ significantly from those used as standard by FAAM.

3. Using the incorrect values of dp and dr can cause large errors in the corrected irradiances, of up to 6.3% for the clear dome and up to 9.0% for the red dome, in the cases examined here. These errors are significantly larger than uncertainty previously associated with uncertainty due to attitude corrections (2.2%), and larger than the total uncertainty estimated in Section 5.1.2 of 4% and 8% for the clear and red dome pyranometers.

4. dp and dr appear to change significantly between the two DODO campaigns, though

the large uncertainties cannot say this is unambiguously. Nevertheless, the current procedure of assuming constant pitch and roll offsets should be viewed with caution.

It is therefore recommended that:

1. Pirouette and/or high level box pattern manoeuvres under clear skies are performed regularly during campaigns where pyranometer measurements are of importance, in order to have the best possible chance of estimating the pitch and roll offsets accurately.

2. The responsibility for correcting the upper pyranometer data using the correct pitch and roll offset angles should be investigated by FAAM, in order to ensure that pyranometer data available on the British Atmospheric Data Centre (BADC) database is the most accurate possible.

3. For scientists analysing the pyranometer data it would be useful to have access to the following information, which FAAM could make available either on the BADC or by other means:

    - Dates when the pyranometers were removed from the aircraft, as this can affect the pitch and roll offsets.
    - How the data was corrected/processed before becoming available on the BADC (e.g. values of assumed pitch and roll offset and the FDIR ratio)
    - To have access to the raw, uncorrected data, as well as that corrected by CRFLUX.

4. Other possibilities could include attempting to measure the offset of pitch and roll angle physically on the aircraft, or installing pyranometers with mounts that automatically adjust to aircraft attitude, as described in Wendisch *et al.* (2001).

5.3.4 Procedure Adopted for DODO Data

For this work the best way forward with the upper pyranometer data is to re-correct all the data for every flight using fixed values of dp and dr for each DODO campaign, for

cases where the direct radiation is greater than a solar zenith angle dependent threshold (Section 5.2). For cases where this is not the case, the irradiance is assumed to be totally diffuse and is therefore not corrected for attitude. This is always the case for the lower pyranometers which measure upwelling irradiance.

Table 5.6 shows the values of dp and dr used for each part of DODO. Since the estimates of dp and dr differ for each flight analysed, mean values of dp and dr for each DODO campaign have been calculated, and errors in dp and dr have been assigned based on the range in dp and dr for the estimates for each flight. This will also allow the uncertainty in the re-corrected irradiances to be calculated, based on the uncertainties in dp and dr (Section 5.5.1). For the red dome pyranometer for DODO2 there was only one estimate of dp and dr since there was no red dome pyranometer data available for b234. Thus the estimates for dp and dr from b241 have been adopted and assigned a large uncertainty of $\pm 2.0^\circ$.

Campaign	Flight	Dome Type	dp	dr	Campaign dp	Campaign dr
DODO1	b157	Clear	-5.0°	0.7°	$-3.8^\circ \pm 1.2^\circ$	$0.6^\circ \pm 0.2^\circ$
	b167		-2.6°	0.4°		
	b157	Red	-3.2°	-1.4°	$-2.8^\circ \pm 0.5^\circ$	$-1.3^\circ \pm 0.2^\circ$
	b167		-2.3°	-1.1°		
DODO2	b234	Clear	-5.0°	0.2°	$-4.6^\circ \pm 0.5^\circ$	$0.4^\circ \pm 0.2^\circ$
	b241		-4.1°	0.5°		
	b234	Red	n/a	n/a	$-3.6^\circ \pm 2.0^\circ$	$6.6^\circ \pm 2.0^\circ$
	b241		-3.6°	6.6°		

Table 5.6: *Values of dp and dr for DODO1 and DODO2, and uncertainties, used to re-correct all the DODO upper pyranometer data. Campaign values of dp and dr are averages of all estimates from flights relevant to each DODO campaign.*

5.4 Dirtying and Sand-blasting of Pyranometer Domes

Flying in heavy aerosol loadings can result in the forward facing side of the pyranometer domes becoming dirty, or even sand-blasted in the case of heavy dust storms. This results in decreased sensitivity of the pyranometer when the sun is on the dirty side of the pyranometer (when the aircraft is heading into the sun, or relative heading is around zero). Decreases in measured irradiance during into-sun runs have been observed in the past (Saunders and Barnes, 1991) following a single profile through a hazy boundary layer in UK-based flights, resulting in a decrease of $40 - 50 W m^{-2}$ (5%).

Dirtying of dome can easily be detected by analysing data from high level box patterns and ground-based pirouettes, where the measured irradiance decreases significantly when the aircraft is facing towards the sun. The domes of the pyranometers are cleaned before every flight, though this may not prevent the build-up of dirt on the domes during the flight itself. However, if the domes are physically damaged due to aerosol impaction then cleaning the domes will not resolve the problem.

Figure 5.4 shows corrected irradiances measured by the upper pyranometers for various box pattern and pirouette manoeuvres during and before DODO. The irradiances have been corrected using appropriate pitch and roll offsets for each flight as described in Section 5.3. The data are plotted as a function of relative heading (solar azimuth angle minus aircraft heading) in order to show how the measured irradiance can be affected when the aircraft heads towards the sun (when relative heading is around zero). Irradiances are normalised by $cos(\theta)$ in order to remove any effects of irradiance decreasing due to changes in the solar zenith angle.

For DODO1 the box patterns were carried out during DABEX in flight b157 near the start of DABEX, and in flight B167, immediately before DODO1 (See Tables 5.2 and 5.3). Figure 5.4(a) for b157 shows a significant decrease in the measured irradiance around relative headings of zero, when the aircraft was heading towards the sun. This is evidence that the front of the clear dome pyranometer was dirty (or damaged) at this point in the flight. The box pattern was carried out at the start of b157 following 3 profiles through aerosol, so it is possible that the dirtying occurred during the flight. The resulting irradiance from the into-sun run from this box pattern decreased by $100 W m^{-2}$ or 11%.

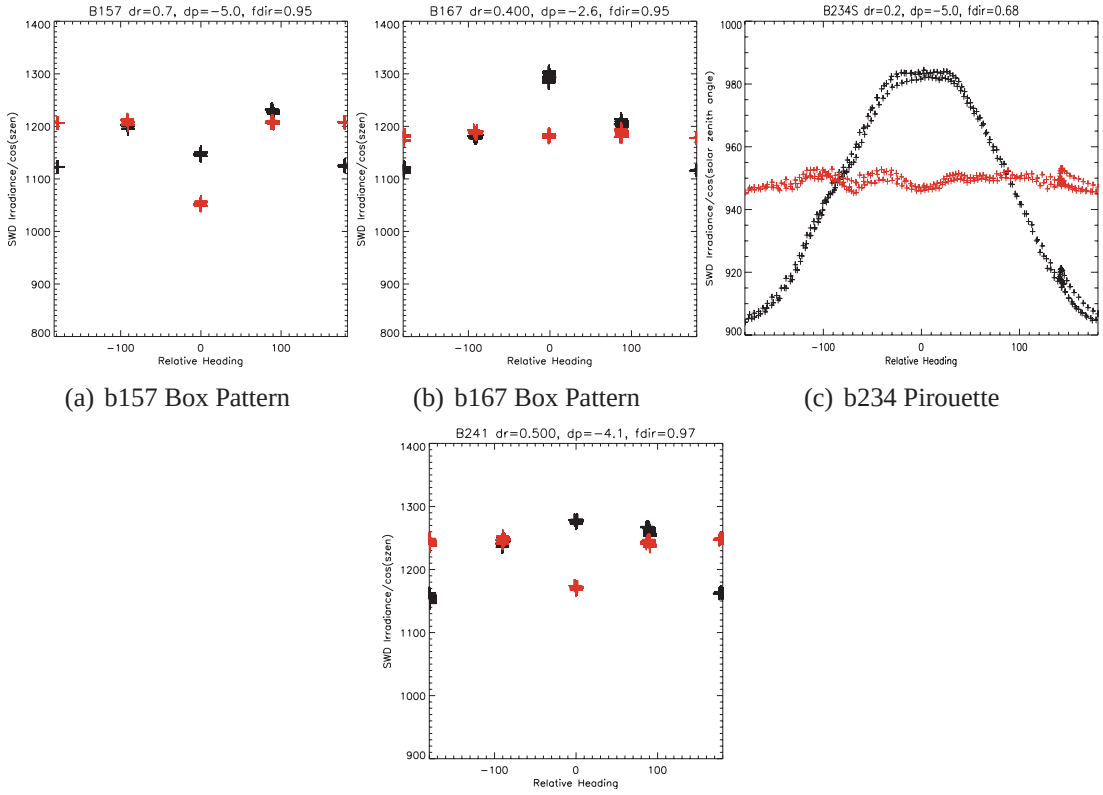

(a) b157 Box Pattern (b) b167 Box Pattern (c) b234 Pirouette

(d) b241 Box Pattern

Figure 5.4: *Clear dome pyranometer measurements from box pattern manoeuvres during b157, b167 and b241 and pirouette manoeuvre during b234. Irradiances are normalised by the cosine of solar zenith angle, and shown as a function of relative heading of the aircraft (0 means aircraft faces into the sun). Black points indicate data corrected for aircraft pitch and roll only, red points indicate data corrected also taking into account pitch and roll offset of the pyranometers relative to the aircraft.*

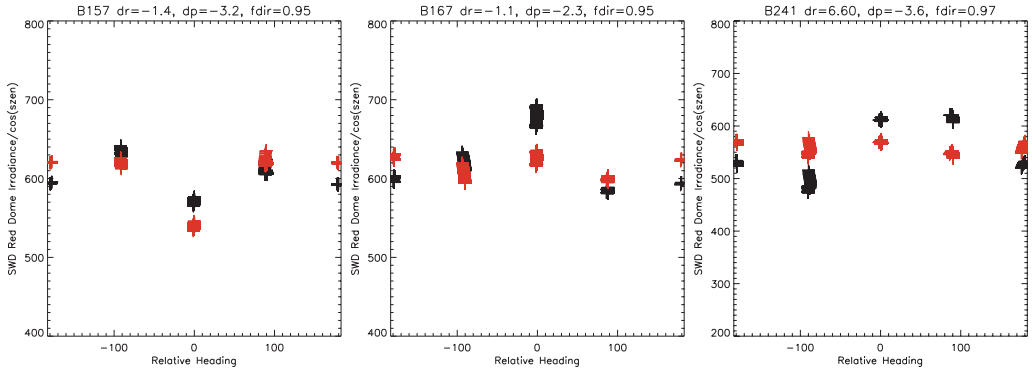

(a) b157 Box Pattern (b) B167 Box Pattern (c) b241 Box Pattern

Figure 5.5: *As in Figure 5.4 but for red dome pyranometer measurements. Note that no red dome pyranometer data are available for flight b234.*

The measurements from the red dome pyranometer (Figure 5.5(a)) also show evidence of dirtying on the front of the dome. As with the clear dome, the measured irradiance drops at relative headings of around zero, in this case by $50Wm^{-2}$ or 11%. Both domes show a much larger decrease in irradiance than that found by Saunders and Barnes (1991).

During b167 the box patterns were also carried out at the start of the flight, following two profiles. In contrast to b157, no dirty dip was evident during the b167 box pattern (see Figure 5.4(b)), as there is no obvious decrease in measured irradiance at relative headings around 0 degrees). The same is true for the red dome pyranometer shown in Figure 5.5(b). This suggests that the decrease in irradiance seen in b157 on both domes was due to dirtying, rather than sand-blasting which would also have effected the b167 data. No pirouettes or box patterns were carried out during the rest of DODO1, so it is not possible to say whether subsequent flying during DODO1 resulted in the pyranometers becoming sand-blasted or dirty. However, it is clear that even small amounts of time spent flying through aerosol can cause the domes to get dirty, and therefore pyranometer data from runs during DODO1 where the aircraft relative heading was close to zero should be discarded.

For DODO2 the pirouette was carried out at the start of flight b234 during AMMA, directly before DODO2 began (see Tables 5.2 and 5.3). Irradiances measured during the b234 pirouette are shown in Figure 5.4(c) and show that there is no significant drop in irradiance at relative headings around zero, which means that there was no dirtying or damaging of the clear dome before DODO2 began. Unfortunately there is no red dome pyranometer data for this flight to allow the same conclusion for the red dome.

The DODO2 box pattern was carried out during flight b241, the penultimate flight of DODO2, when the absence of high cloud meant that the weather conditions were acceptable. The irradiances from the clear dome pyranometer during b241 shown in Figure 5.4(d) show that by the end of DODO2 significant dirtying of the front of the clear dome was evident. During the into-sun run the measured irradiances drop by $55Wm^{-2}$ or 6%. Interestingly there is no significant decrease in measured irradiances for b241 for the red dome pyranometer.

Following DODO2 some analysis of the pyranometer data and domes in the UK

also revealed evidence of dirtying and sand-blasting (personal communication, Jim Haywood). The work described here shows that it is likely that the sand-blasting occurred during DODO2 due to flying in heavy dust conditions, particularly during b238 where concentrations were extremely high and the whole aircraft was dirty on landing. Data from flights and pirouettes in the UK also suggested that although dirtying/damage to the domes is a problem, the irradiances are unaffected at relative headings greater than $\pm 50^{\circ}$. The results from the DABEX and DODO2 box patterns shown here also show that irradiances for the cross-sun and down-sun runs, when relative headings are greater than $\pm 50^{\circ}$, are unaffected by dirtying of the domes. Thus it is clear that dirtying and sand-blasting of the domes can cause the measured irradiance to decrease significantly, but data for relative headings outside $\pm 50^{\circ}$ is unaffected. Therefore for the comparison of modelled and measured irradiances (Chapter 6), pyranometer data for relative headings within $\pm 50^{\circ}$ will be treated with caution.

Both box patterns and pirouettes are useful in detecting the presence of dirtiness and damage on the pyranometer domes. Since pirouettes can be carried out frequently without significant flying cost (given clear skies at take-off and/or landing) it is recommended that for future campaigns pirouettes are carried out regularly during the campaign, if possible before and after each flight, in order to monitor the build-up of dirt/damage on the pyranometer domes. The current procedure of carrying out at least one box pattern during a campaign is also very important. Straight and level runs should be carried out on relative headings outside $\pm 50^{\circ}$ in order to prevent deterioration of data due to dirty and/or damaged domes. Regular cleaning of the pyranometers should be undertaken before every flight.

5.5 Uncertainty in Irradiances due to Attitude Corrections

Equation 5.4 is used to correct the pyranometer data when any direct radiation is incident on the pyranometer. In order to perform this equation, dp and dr must be known to calculate β, and FDIR must be known to attribute the proportion of the total measured irradiance which must be corrected. Uncertainties in dp, dr and FDIR all contribute to uncertainties in the corrected irradiance. This Section will investigate the uncertainty in irradiance due to all these components. The notation δI_{dpdr} will be used to describe the uncertainty in corrected irradiance due to uncertainties in dp and dr, and δI_{FDIR} will be used to describe the uncertainty in the corrected irradiance due to uncertainties in FDIR. The total uncertainty in the corrected beam due to the attitude corrections will be defined as δI_{att}, where $\delta I_{att}^2 = \delta I_{dpdr}^2 + \delta I_{FDIR}^2$, according to standard propagation of error. All errors are fractional percentages, where the percentage error is the percentage change in irradiance due to the known uncertainty in the relevant variable.

5.5.1 Sensitivity of Irradiances to Pitch and Roll Offset

Section 5.3 estimated the values of dp and dr for each DODO campaign, and the associated uncertainties in dp and dr. It is therefore important to test the sensitivity of the corrected irradiances to the values of dp and dr which are used in the correction process.

To do this, the irradiances over the box patterns and pirouettes were re-corrected using firstly the true values of dp and dr for each flight as shown in Table 5.4, and secondly using the average campaign values of dp and dr as shown in Table 5.6. This allows the uncertainty in irradiance solely due to the uncertainty in dp and dr during DODO to be estimated.

Table 5.7 shows the maximum percentage error that occurs for into/down-sun runs and cross-sun runs due to using the campaign average values of dp and dr, rather than the specific values of dp and dr for each flight. The results show that the uncertainty in irradiances are quite small (under 0.5% for the clear dome and under 2.1% for the red dome) if the run is performed cross-sun. For the down-sun/into-sun runs, the errors are

larger, and reach up to 4.0% for the clear dome. This is because the magnitudes of dp are much larger than dr, as are the uncertainties associated with each, and therefore the cross-sun runs show less uncertainty in the re-corrected irradiances as they are less dependent on the values of dp. For the clear dome the uncertainties in dp and dr are smaller for DODO2 than for DODO1, which means that the uncertainties in the re-corrected irradiances are smaller for DODO2 than DODO1. Contrastingly, for the red dome dp and dr are better constrained for DODO1, and so the re-corrected irradiances have more accuracy for the DODO1 red dome pyranometer data.

Campaign	Dome Type	Into/Down-sun Runs	Cross-sun Runs
DODO1	Clear	4.0	0.5
DODO2	Clear	1.0	0.2
DODO1	Red	1.7	0.6
DODO2	Red	1.8	2.1

Table 5.7: *Maximum percentage uncertainty in irradiance (δI_{dpdr}) that occurs due to using the campaign average values of dp and dr, rather than the specific values of dp and dr for each flight. Data excludes runs affected by dome dirtying, and comes from the box patterns and pirouette described in Section 5.1.2. Uncertainties are separated by into/down-sun runs and cross-sun runs since the former are more affected by uncertainty in dp and the latter by uncertainty in dr.*

It should be noted that these values of δI_{dpdr} can only be assumed if the values of dp and dr are estimated as described in Section 5.3. If standard values of dp and dr had been used, the value of δI_{dpdr} would have been much larger, as shown in Section 5.3.

5.5.2 Sensitivity of Irradiances to FDIR

When the pyranometer data is corrected using the standard FAAM procedure, FDIR is assumed to be 0.95 at all altitudes and in all cases. The ARM data in Table 5.4 illustrates that FDIR can drop as low as 0.68 at the surface, and in practice FDIR will vary with solar zenith angle and altitude.

Since the true values of FDIR are not known when the pyranometer data is re-corrected, it is important to assess the error in irradiance that may occur due to using an inappropriate value of FDIR, defined here as δI_{FDIR}. To do this, the pyranometer data for the box patterns and pirouettes has been re-corrected using FDIR values ranging from $0.6 - 1.0$ and the resulting error in the irradiance, δI_{FDIR}, has been recorded. Figure 5.6

shows the resulting irradiances for the clear dome pyranometer for this sensitivity test, along with resulting errors and percentage errors in irradiance.

Campaign	Dome Type	Into/Down-sun Runs	Cross-sun Runs
DODO1	Clear	3.9	1.9
DODO2	Clear	2.1	1.7
DODO1	Red	4.9	2.2
DODO2	Red	2.2	6.8

Table 5.8: *Maximum percentage uncertainty in irradiance (δI_{FDIR}) that occurs due to using the tested range of FDIR values ($0.6 - 1.0$) as opposed to the correctly modelled value of FDIR for each campaign. Data excludes runs affected by dome dirtying, and comes from the box patterns and pirouette described in Section 5.1.2. Uncertainties are separated by into/down-sun runs and cross-sun runs.*

Table 5.8 summarises the maximum percentage error, (δI_{FDIR}), in the irradiance that occurs due to using the range of values of FDIR as illustrated by Figure 5.6 for the clear dome. Note that the amount to which the irradiances are sensitive will depend on the values assumed for dp and dr, and also on the solar zenith angle, and that therefore these results are experimental rather than theoretical.

For the data examined here, the percentage error solely due to using an inappropriate value of FDIR can reach as much as 3.9% for the clear dome and 6.8% for the red dome irradiance. In all cases, when the test value of FDIR is closest to the true value, the percentage error is smaller. Thus for the clear dome during box patterns, the maximum errors are seen when $FDIR = 0.68$ is assumed, and for the pirouette, the maximum error is seen when $FDIR = 0.99$ is assumed. For the clear dome the error for b167 is noticeably larger than the other flights. This is because the solar zenith angle during the box pattern was much larger ($52^\circ - 62^\circ$ compared to between $33^\circ - 45^\circ$ for the other flights). If the sun is lower in the sky, then the pyranometer correction is more sensitive to the value of FDIR used. This implies that the re-corrected pyranometer data for times when the solar zenith angle is large, and FDIR could be much lower than the value used in the corrections, may be much less accurate than data where the solar zenith angle was lower.

For the red dome the errors are much larger than the clear dome. This is due to a combination of factors, including that for b241 dr is very large (6.6°) which makes the data more sensitive to the direct beam, and that for b167 since the solar zenith angle was

large the irradiance is more sensitive to FDIR changing.

Figure 5.6 also shows that for the clear dome, where values of dr are small (between $0.2° - 0.7°$), the uncertainty in irradiance due to FDIR is very small for the cross-sun runs, less than 2.0%. This cannot be said for the red dome data, where the uncertainty is much larger due to the larger estimates of dr (from $-1.4°$ to $6.6°$ for the different flights). Thus the uncertainty in the pyranometer measurements due to uncertainty in FDIR could be minimized by flying cross-sun runs only, provided that the value of dr is small.

In summary, the error in the corrected irradiance solely due to using an incorrect value of FDIR (δI_{FDIR}) can be very large, up to 3.9% for the clear dome and 6.8% for the red dome. However, using data from cross-sun runs will minimise this error to below 2.0% for the cases shown here. Care should be used when analysing data from runs where the solar zenith angle was large as this results in much greater sensitivity of irradiances to the value of FDIR used.

5.5.3 Overall Uncertainty in Corrected Irradiance Data

As described in Section 5.5, the overall uncertainty in the corrected irradiance due to the attitude corrections can be defined as $\delta I^2_{att} = \delta I^2_{dpdr} + \delta I^2_{FDIR}$. If the additional uncertainty in the corrected irradiance due to other factors is defined as δI_{cal}, then the total uncertainty in the corrected irradiance can be calculated using Equation 5.5. Table 5.9 summarises the uncertainty in irradiance due to these different components for the two DODO campaigns, for cross-sun and into/down-sun runs, and also shows the overall uncertainty in the irradiance if any correction for attitude is performed, based on Equation 5.5.

$$\delta I^2_{tot} = \delta I^2_{cal} + \delta I^2_{dpdr} + \delta I^2_{FDIR} \tag{5.5}$$

For the clear dome irradiance, the uncertainties solely due to attitude corrections vary between $1.7 - 5.6\%$. This varies from being within the 2.2% estimate of Saunders *et al.* (1992) to being much greater. The value of δI_{att} from cross-sun runs (maximum 2.0%) is less than that from into/down-sun runs (maximum 5.6%) because the roll offsets are smaller than the pitch offsets. DODO1 shows greater uncertainty than DODO2 becuase

Campaign	Dome Type	Run Type	δI_{dpdr}	δI_{FDIR}	δI_{att}	δI_{cal}	δI_{tot}
DODO1	Clear	I/D	4.0	3.9	5.6	3.3	6.5
DODO1	Clear	Cross	0.5	1.9	2.0	3.3	3.8
DODO2	Clear	I/D	1.0	2.1	2.3	3.3	4.0
DODO2	Clear	Cross	0.2	1.7	1.7	3.3	3.7
DODO1	Red	I/D	1.7	4.9	5.2	4.5	6.9
DODO1	Red	Cross	0.6	2.2	2.3	4.5	5.0
DODO2	Red	I/D	1.8	2.2	2.8	4.5	5.3
DODO2	Red	Cross	2.1	6.8	7.1	4.5	8.4

Table 5.9: *Uncertainties in corrected irradiance due to uncertainty in dp and dr,δI_{dpdr}; uncertainty in FDIR, δI_{FDIR}; and other uncertainty not related to attitude correcitons, δI_{cal} (the uncertainty that would apply to purely diffuse irradiance). δI_{att} is the total uncertainty in corrected irradiance due to attitude corrections ($\delta I_{att} = (\delta I_{dpdr}^2 + \delta I_{FDIR}^2)^{1/2}$). δI_{tot} is the total uncertainty to the corrected irradiance due to all errors, as defined in Equation 5.5. Uncertainty is separated by campaign, clear/red dome and into/down-sun runs (I/D) and cross-sun runs.*

the uncertainty in dp is greater during DODO1.

When the total uncertainty, δI_{tot}, is considered for the clear dome, the uncertainty is within the assumed error (Section 5.1.2) of 4% for all cases other than DODO1 for into/down-sun runs, where the large uncertainty in the value of dp becomes important.

For the red dome irradiance the uncertainties are much larger, mostly because of the greater uncertainties in the values of dp and dr, and because the larger roll offsets make the data more sensitive to changes in FDIR. The uncertainties solely due to attitude corrections, δI_{att}, vary between $2.3 - 7.1\%$, but this time show no clear difference between into/down-sun and cross-sun runs, because for the red dome dr can be as large as dp, which means that the sensitivity to attitude corrections will be high on any relative heading.

The value of δI_{tot} is also much higher for the red dome pyranometers as the error from δI_{att} propagates through. δI_{tot} varies between $5 - 8.4\%$, mostly falling within the 8% uncertainty assumed in Section 5.1.2.

It should be noted that the uncertainties calculated here are partly dependent on the solar zenith angle. Section 5.5.2 showed that the uncertainty due to FDIR increases at larger zenith angles, and data measured under these conditions should therefore be viewed with caution. The data assessed here was measured at zenith angles between $33 - 62°$, and therefore if the solar zenith angle is larger than this, the uncertainties could be con-

siderably greater.

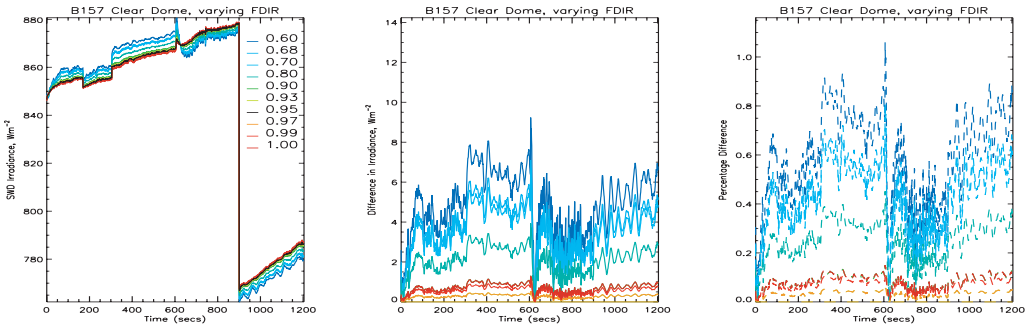

(a) b157 Box Pattern

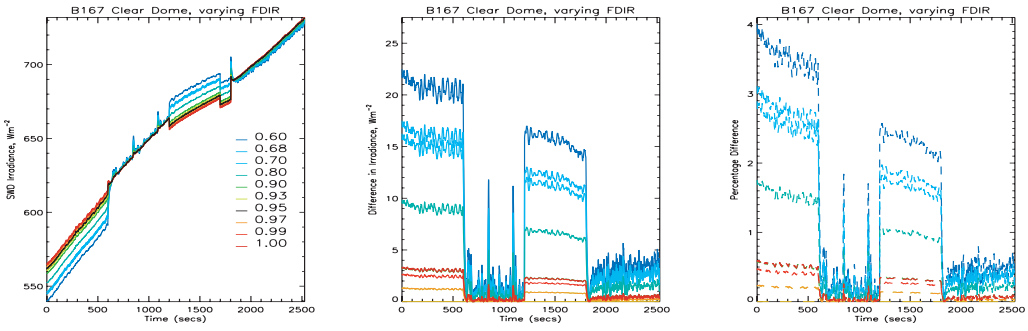

(b) b167 Box Pattern

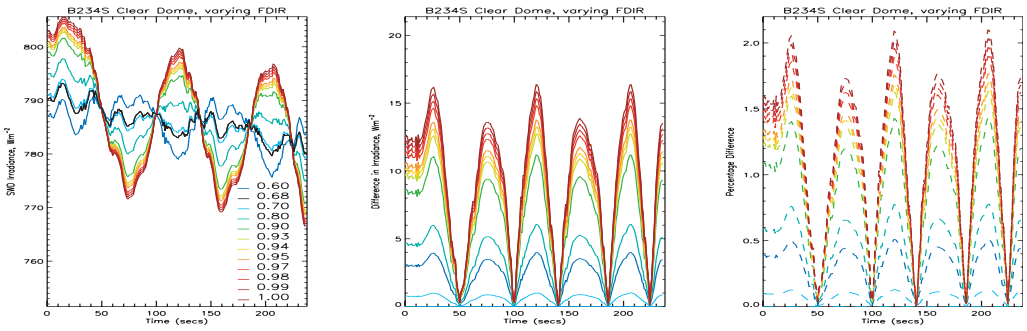

(c) b234 Pirouette

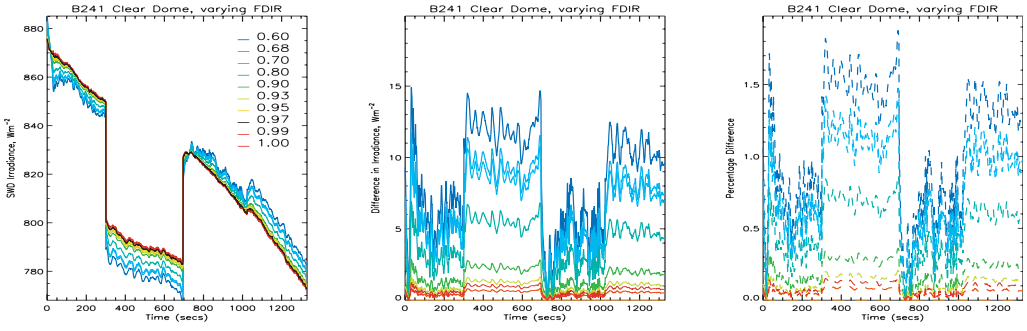

(d) b241 Box Pattern

Figure 5.6: *Irradiances that would result from using different values of FDIR in the re-correction of the clear dome pyranometer data, for the box patterns and pirouette. Left hand side: irradiances; middle: difference in irradiance as compared to the values calculated from the best estimate of FDIR; right hand side: percentage difference in irradiance as compared to the values calculated with the best estimate of FDIR. Black lines show irradiance using the true value of FDIR. The estimates of dp and dr described in Section 5.3 have been used.*

5.6 Comparison of Pyranometer Irradiance to ARM and Model Irradiances

Directly validating the upper pyranometer measurements for past campaigns is not straight forward if no comparisons have been purposefully organised at the time, as with DODO. However, it has proved possible to compare the irradiance measured during the b234 pirouette manoeuvre to the ARM Mobile Facility (AMF) shortwave broadband radiometer data, since the AMF was also stationed at Niamey airport during 2006. Radiative modelling of the measured irradiances has also been carried out for the box patterns, using appropriate solar zenith angles and standard tropical atmosphere profiles from McClatchey *et al.* (1971), as described in Section 5.3.2. Due to the high altitude of the box pattern the results should be accurate, given that there was no cloud or aerosol above the aircraft.

Flight	Dome Type	Maximum percentage error	Direction of difference	Comparison
b157	Clear	4.5	Underestimate	Model
b167		7.5	Underestimate	Model
b234		5.5	Underestimate	ARM
b241		2.5	Overestimate	Model
b157	Red	4.0	Underestimate	Model
b167		9.0	Underestimate	Model
b234		n/a	n/a	n/a
b241		15.0	Underestimate	Model

Table 5.10: *Maximum percentage difference in irradiance between upper pyranometer irradiance and either ARM (for b234 pirouette) or the modelled irradiance (b157, b167 and b234 box patterns). The values of dp, dr and FDIR used are as shown in Table 5.4. Data excludes runs affected by dome dirtying.*

Figure 5.7 and Table 5.10 show that the model data do not always agree with the clear dome pyranometer measurements within the uncertainties defined in Table 5.9. For b241 the agreement is good ($< 2.5\%$), whereas for b157 and b167 the uncertainties overlap with the model data for into/down-sun runs, but do not overlap for the cross-sun runs where the uncertainty in the pyranometer measurements is smaller. The maximum difference between the model and pyranometers is 7.5% for b167, where part of the difference may be due to the greater solar zenith angle during this box pattern, as described in Section

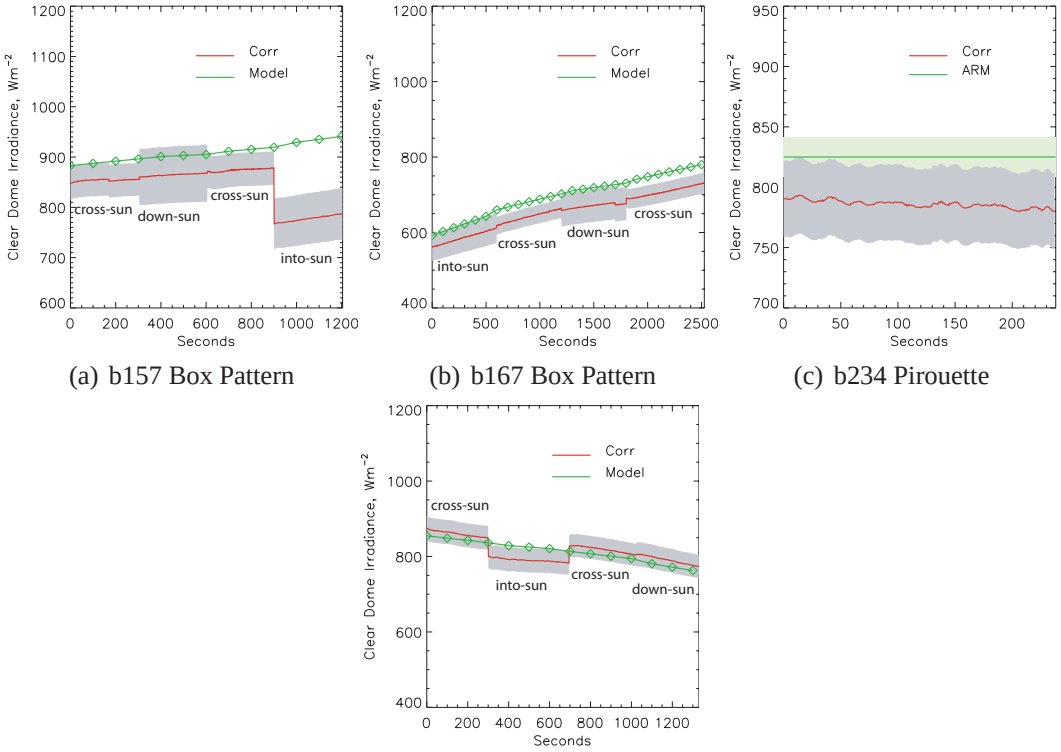

(a) b157 Box Pattern (b) b167 Box Pattern (c) b234 Pirouette

(d) b241 Box Pattern

Figure 5.7: *Upper clear dome pyranometer data compared to modelled irradiances for the box patterns, and compared to ARM data for the b234 pirouette. Red lines represent pyranometer data, green lines represent either model or ARM data as indicated on each figure. Grey shading represents the uncertainty shown in table 5.9, which varies between DODO1 and DODO2, and for into/down-sun and cross-sun headings. Into-sun, down-sun and cross-sun runs are labelled. The values of dp, dr and FDIR used are as shown in Table 5.4. Error in ARM data (estimated at 2% or $16Wm^{-2}$ based on Slingo* et al. *(2006)) is shown by pale green shading.*

5.5.2. There may also be some uncertainty in the model estimates, which are harder to quantify.

At this stage it is important to note that the quality flags for the clear dome upper pyranometer for all the DODO1 and DABEX flights have been flagged as low quality. Investigation of this (personal communication, Phil Rosenberg, FAAM) has revealed that the zero signal for the upper clear dome pyranometer was not recorded at all during the dry season campaigns. This therefore means that noise could be affecting recorded signal, and this noise may easily change as a function of pressure or temperature. Therefore the clear dome upper pyranometer data from DODO1 and DABEX is not reliable. This explains the lack of agreement between the model and pyranometer data shown in Figure 5.7 for b157 and b167. The other pyranometers were unaffected by this problem.

For the DODO2 cases, where the data are not affected by a lack of zero offset recording, and the uncertainties in the pyranometer and ARM measurements during b234 overlap, showing that the data are in agreement within the uncertainties defined in Table 5.9 and by Slingo *et al.* (2006).

Note that in Figure 5.7 the disagreement is particularly bad for the into-sun runs in b157 and b241, where the domes are being affected by dirtying or sand-blasting. For the clear dome the magnitude of the differences as compared to the ARM data and to the model data are of a similar order, though the the BAe-146 clear dome pyranometer measures from $0.3-3\mu m$ whereas the ARM pyranometer measures from $0.4-4\mu m$, and this may account for an unknown amount of the difference in measured irradiance, though it depends on the exact details of the pyranometer calibrations. For all cases other than in b241 for the clear dome, the pyranometers underestimate the amount of irradiance.

For the red dome pyranometer the (dis)agreement is worse, extending to 15% for b241, with worse agreement during b241 compared to DODO1. This is surprising, considering that for the clear dome data, b241 showed the best agreement between the model and the pyranometer data. For b157 the modelled irradiance falls within the uncertainty range of the pyranometer data, and for b167 the data are within the uncertainty limits for the into/down-sun runs, but not the cross-sun runs where the uncertainty is smaller. Considering that the uncertainty already assigned to the red dome data in Table 5.9 is already large ($5.3-8.4\%$), the large percentage differences shown here of up to 15% adds even more uncertainty to the reliability of the red dome pyranometer measurements.

The discrepancies shown here range from being similar to those found in the past through a combination of aircraft intercomparison flights (using the C-130 aircraft, however) and modelling studies, to much larger. For example, agreement between clear dome measured and modelled irradiances of less than 4% were found by Taylor *et al.* (1996), Saunders *et al.* (1992) and Saunders and Barnes (1991). For the red dome pyranometer data model and measurement agreements were found to be within 10% (Taylor *et al.*, 1996), 4% (Saunders *et al.*, 1992) and 8% (Saunders and Barnes, 1991). A recent study by Ramana *et al.* (2007) using pyranometers mounted on unmanned aerial vehicles found agreement of within 1% for incoming clear sky radiation.

In summary, the uncertainties shown in Table 5.9 do not always overlap with modelling estimates of clear sky irradiance. Since the same model is used in Chapter 6 to try and obtain radiative closure with the pyranometer data, this is problematic. Therefore the uncertainty associated with the pyranometer measurements will be increased to cover the maximum percentage difference between the measurements and model data shown here. Thus the uncertainty in clear and red dome pyranometer measurements will be assumed to be 5.5% and 15% respectively, based on the results in Table 5.10. The higher uncertainties shown in Table 5.10 for the dry season flights are not considered, since they are assumed to be related to the faulty recording of the signal.

5.7 Conclusions

5.7.1 Overview of Main Findings

1. Significant sand-blasting/dirtying of the front of the pyranometer domes is evident during both DODO1 and DODO2, causing the measured irradiance to drop by 11% during b157 for both domes, and by 6% for b241. DABEX flights b157 and b167 suggest that this problem resulted from dirt rather than sand-blasting, which resulted from as few as three profiles through aerosol in the case of b157. Runs which are either cross-sun or down-sun do not appear to be affected by the dirtying of the domes.

2. Pitch and roll offset of the pyranometers on the aircraft can be derived from pirouettes and box patterns, and dp and dr can differ significantly from those used in the standard FAAM correction procedure.

3. The corrected pyranometer data is sensitive to the values of dp and dr. Using the standard FAAM values of dp and dr can cause large errors in the corrected irradiances, of up to 6.3% for the clear dome and up to 9.0% for the red dome, in the cases examined here. These errors are significant, and comparable to the official stated accuracy of the pyranometers.

4. The results here suggest that dp and dr change between the two DODO campaigns,

but as errors overlap this cannot be unambiguously confirmed from the results shown here.

5. The BAe pyranometers underestimate the irradiance compared to ARM measurements and modelling results in all cases except for b241 for the clear dome. The underestimation is not always within the estimated pyranometer uncertainty, which varies between runs and campaigns.

5.7.2 Procedure Adopted for Pyranometer Data in Chapter 6

1. Data from runs heading into sun may be affected by dirtying/damage, and will be treated with caution and not used where possible. Runs on relative headings outside $\pm 50^{\circ}$ should be acceptable.

2. The DODO pyranometer data has been re-corrected using the values of dp and dr shown in Table 5.6, and assuming $FDIR = 0.95$ at all altitudes. At solar zenith angles greater than 62° the correction may start to become less accurate, so data from runs performed at large zenith angles will also be viewed with caution.

3. Uncertainty in irradiance solely due to uncertainty in dp and dr has been calculated for runs on different relative headings and for DODO1 and DODO2. The contribution of this error to the total uncertainty can be calculated using standard propagation of error formulae.

4. Uncertainty in irradiance due to the value of FDIR used can reach up to 3.9% and 6.8% for the clear and red dome respectively. Using data from cross-sun runs can minimise this error to below 1.0% however. The contribution of this error to the total uncertainty can also be calculated. Care will be taken when analysing data with solar zenith angle greater than the maximum of 62° from the box patterns, as this can result in much greater sensitivity to the value of FDIR used and greater uncertainty.

5. The total uncertainty in irradiance described in Section 5.5.3 is not always greater than the difference between the pyranometer measurements and the modelling cal-

culations under clear skies. Therefore the uncertainty associated with the pyranometer measurements in Chapter 6 will be extended to cover the discrepancy between the model and pyranometer irradiances for the box pattern manoeuvres. Thus the uncertainty for the clear and red dome pyranometer measurements will be taken as 5.5% and 15% repectively.

5.7.3 Recommendations

1. Performing pirouette manoeuvres regularly during a campaign, before and after a flight, is critical in determining:

   (a) The presence of dirtying or sand-blasting on the front of the pyranometer domes,

   (b) The best-estimate of pitch and roll offset of the pyranometers relative to the aircraft,

   and pirouettes should therefore be carried out regularly during campaigns where pyranometer measurements are of importance, in order to have the best chance of estimating the pitch and roll offsets accurately, and for assessing the degree to which dome dirtying was a problem.

2. High level box patterns are also useful for estimating pitch and roll offsets of the pyranometers. If no ground-based radiometer data is available for using FDIR in the estimation of dp and dr during the pirouettes, then the box patterns have an advantage over the pirouettes as FDIR is more easily modelled at high altitudes. Sand-blasting/dirtying of the pyranometer domes can also be detected using box pattern data.

3. Straight and level runs should be carried out on a cross-sun heading to avoid measuring decreased irradiance due to dome dirtying/damage.

4. Pyranometer domes should be cleaned before each flight.

5. Having ground-based radiation measurements at the airport where the campaign is based (such as the AMF) is extremely useful in validating pyranometer measurements.

6. For scientists using pyranometer irradiance data from the BADC it would be useful to provide information on the following:

   - Dates when the pyranometers were removed/re-mounted on the aircraft, as this can change the values of dp and dr
   - Some information on what processing has been carried out on the pyranometer data on the BADC (including information such as values of dp, dr and FDIR used)
   - Access to uncorrected data on the BADC would also be useful

7. The correction FAAM make to allow for pitch and roll is useful, but can introduce significant errors to the corrected irradiances if the true pitch and roll offsets differ from those used in the corrections. It is important to define who should take the responsibility of calculating the true pitch and roll offsets of each pyranometer each time they are re-mounted, and that the irradiance data is corrected appropriately on the BADC.

8. The possibility of physically measuring the pitch and roll offsets of the pyranometers on the aircraft should be investigated, as comparisons to values of dp and dr derived from the measurements could be carried out.

9. Results from DODO suggest differences between the pyranometer measurements and both modelling results and the ARM measurements. Further testing and comparisons of the pyranometers while mounted on the aircraft could be carried out to explore these discrepancies.

10. It would be possible to conduct experiments to investigate the accuracy of the pyranometers. For example, repeated box patterns could be carried out in order to derive several estimates of dp and dr. A test flight with both clear (or red dome) pyranometers mounted side by side in their upper positions in a similar manner to that used

by Saunders and Barnes (1991) in order to compare the uncertainty between the different pyranometers now they are mounted on the BAe-146. Intercomparison flights between other aircraft with similar pyranometers would also be of value.

Chapter 6

Shortwave Radiative Effect of DODO Dust

6.1 Introduction

It has been shown in Chapter 4 that the optical properties of the dust accumulation mode varied, with ω_0^{550} varying from 0.93 to 0.99 and k_{ext}^{550} varying from $0.75m^2g^{-1}$ to $1.6m^2g^{-1}$. The changes in ω_0^{550} were most likely due to changes in dust source and composition over the two DODO campaigns, while the changes in k_{ext}^{550} appeared to depend on size distribution changes. Additionally there are uncertainties regarding the impact of the coarse mode on these optical properties, and Chapter 4 showed that the coarse mode can cause large decreases in ω_0^{550} and k_{ext}^{550} .

Various studies have highlighted the importance of dust to the climate system and meteorology through the radiative effect and atmospheric heating (e.g. Carlson and Benjamin, 1980). Other studies have also shown that the radiative effect and heating rates are highly uncertain due to uncertainties in dust refractive indices, size distributions and therefore optical properties (e.g. Liao and Seinfeld, 1998; Claquin *et al.*, 1998; Balkanski *et al.*, 2007; Otto *et al.*, 2007). Given the variation in the observed and modelled optical properties during DODO, it is therefore important to determine the contribution of these variations to the radiative effect of the dust. This will give an important insight into the uncertainty in the radiative effect that may result from typical variability in optical properties of Saharan mineral dust. Additionally, the radiative effect of the dust can be validated by the aircraft pyranometer measurements.

This Chapter therefore takes two approaches to investigating the radiative effect of dust observed during DODO. Firstly the change in the radiative effect due to changes in the observed optical properties is investigated using idealised dust profiles over land and ocean surfaces. Secondly, four flights have been selected as case studies for comparing modelled and measured irradiances at various altitudes, in order to ascertain that the radiative modelling is being carried out appropriately. Sensitivity of these results to the surface albedo, to the presence of the coarse mode and to large changes in the refractive index are also tested.

6.1.1 Model Description

The radiative transfer code developed by Edwards and Slingo (1996) is used to calculate irradiances throughout an atmospheric column.

The model (ES96 hereafter) uses the Eddington two-stream approximation, modelling upwards and downwards irradiances. For the purposes of irradiance calculations, the delta-Eddington approximation is used (as recommended) when aerosols are present which exhibit a strong forwards scattering peak. The delta-Eddington scheme in ES96 essentially means that a fraction of the diffuse radiation is added to the direct beam, thus conserving the peak in the forwards part of the phase function when aerosols are present, resulting in more accurate irradiance calculations. However, for the purposes of aerosol optical depth (AOD) calculations attenuation of the direct beam is extremely important and therefore the Eddington scheme is used for AOD calculations.

The spectral resolution of ES96 can be defined by the user. Here a high spectral resolution of 220 bands is used in order to capture the spectral change in aerosol optical properties, and to be consistent with previous aircraft studies (e.g. Haywood *et al.*, 2003). Wavelengths over these bands cover $0.2 - 10\mu m$ and are consistent with the approach used in Chapter 5. For the purpose of AOD calculations, the direct irradiance at 550nm is required. Therefore additional runs of ES96 are carried out over a single wave band spanning from $549 - 556nm$.

The vertical resolution of ES96 can be defined by the user, and is defined here as 51 equal pressure levels, which results in a resolution of around 200-300m at lower altitudes where dust is encountered. This gives good resolution of the aerosol vertical profile without model runs becoming too time consuming. Information on the vertical profiles of mass mixing ratios of temperature, aerosol, water vapour and ozone are required as input, and can be calculated from aircraft vertical profiles. Since most aircraft measurements are made roughly at a resolution of 10m (1Hz) in the vertical, the data are interpolated onto the coarser resolution used for ES96. At altitudes above the range of the aircraft profiles the tropical climatology of McClatchey *et al.* (1971) are used. In cases where the aircraft was unable to get close enough to the land surface due to flying restrictions (e.g. b175 and b238 over the desert) the aerosol, ozone and water vapour are extended to the

surface by assuming a constant profile from the minimum aircraft altitude. For temperature the profile is extended using the lapse rate in the lowest portion of the aircraft profile. The McClatchey *et al.* (1971) profiles were not used at these low altitudes because it was clear that they differed significantly from the observed measurements, whereas at higher altitudes they were close to the aircraft measurements. McClatchey *et al.* (1971) tropical climatology data are also used for carbon dioxide, oxygen, methane, CFCs and N_2O, which the aircraft did not measure.

For simplicity a lambertian surface albedo has been assumed in these experiments. This is calculated based on pyranometer measurements of up and downwelling irradiances from runs performed close to the surface. More details are given in Sections 6.2 and 6.3. Solar zenith angle is specified as appropriate for each test case. The solar irradiance at the top of the atmosphere is also required, and is specified based on standard solar geometry (e.g. Petty, 2006), so that the irradiance changes by day of the year.

Detailed aerosol properties can be included by creating spectrally resolved data offline using a Mie scattering code, at the same wavelength resolution at which ES96 is to be run at. Therefore the various optical properties observed and modelled during DODO can be represented in the model.

Since the model requires input of the vertical aerosol profile in terms of a mass mixing ratio, the vertical profiles of scattering as measured by the aircraft must be converted. Firstly the scattering coefficient is converted to an extinction coefficient ($\sigma_{ext}^{550}, m^{-1}$) profile, as described in Chapter 2 by dividing by ω_0^{550} measured at an appropriate altitude. The extinction coefficient can then be converted to a mass mixing ratio through,

$$MMR = \frac{\sigma_{ext}^{550}}{k_{ext}^{550}\rho_{air}}, \tag{6.1}$$

where MMR is the dust mass mixing ratio (in kg/kg), ρ_{air} is the density of air and can be calculated using the ideal gas law based on aircraft measurements of temperature and pressure. For cases where only the accumulation mode is examined, k_{ext}^{550} can be taken from the Mie code optical property calculations described in Chapter 4. Since the nephelometer is assumed to measure only the accumulation mode, and the value of k_{ext}^{550} also represents that of the accumulation mode, the resulting MMR represents the vertical pro-

file of the accumulation mode only.

It would be plausible to represent the MMR vertical profile of the full size distribution by adjusting the extinction coefficient by an appropriate factor to correct for the larger particles which the nephelometer does not measure, and by dividing by a value of k_{ext}^{550} appropriate for the coarse mode. This would result in a greater mass load for the entire column, and this method is employed and explained further in Sections 6.5 and 6.6.

6.1.2 Pyranometer Data

The pyranometer data from the aircraft has been compared to the modelled irradiances. Due to the problems described in Chapter 5 of the front of the pyranometer domes becoming coated with aerosol particles, the upper pyranometer data has been discarded if measured while heading towards the sun (relative headings of $\pm 50°$). The upwelling radiation is not affected so much since the upwelling radiation is assumed to be completely diffuse, though coating on the pyranometer domes may still result in some reduction in the irradiance measurements.

Data which has been affected by the presence of cloud has also been discarded since the model simulations do not include cloud. This data is detected through examining satellite images, logs from the flights and from the nature of the pyranometer data (rapid fluctutions are likely to result from cloud presence).

Pyranometer data is averaged over runs in order to compare to model data. The uncertainty in the irradiance measurements is 5.5% (from Chapter 5) for the clear dome data, and a total minimum of $5 W m^{-2}$. DODO1 downwelling clear dome pyranometer data are viewed with caution due to the problems described in Chapter 5, though the upwelling data should be reliable since they did not suffer from the same problem.

6.1.3 Definition of terms

The calculations of various parameters described in this Chapter are carried out as follows:

- Aerosol Optical Depth (AOD, τ^{550})

$$\tau^{550} = \cos\theta \ln\left(\frac{I_{sfc}^{clr}}{I_{sfc}^{aer}}\right), \tag{6.2}$$

  where I is direct solar irradiance (Wm^{-2}), sfc indicates it is measured or modelled at the Earth's surface, clr indicates the case with no aerosol and aer indicates the case when aerosol is present and θ is the solar zenith angle. Equation 6.2 is derived from Beer's Law, based on the fact that at the top of the atmopshere (TOA), F^{clr} and F^{aer} will be the same. F is modelled over $549 - 556nm$ in order to represent $550nm$.

- Top of atmosphere direct aerosol radiative effect (ARE_{TOA})

$$ARE_{TOA} = NET_{TOA}^{aer} - NET_{TOA}^{clr}, \tag{6.3}$$

  (Forster *et al.*, 2007), so that the ARE_{TOA} (Wm^{-2}) is the net increase in irradiance for the earth-atmosphere system due to the presence of aerosol. NET irradiance (Wm^{-2}) is defined as being the downwelling minus upwelling irradiance (Forster *et al.*, 2007). ARE_{TOA} can be calculated at specific solar zenith angles (instantaneous ARE), or diurnally averaged over various solar zenith angles, and over the full shortwave spectrum defined in Section 6.1.1. Since dust aerosol is (at least in part) a natural aerosol, these are 'radiative effects' rather than 'radiative forcings' (which would strictly have anthropogenic origins).

- Surface direct aerosol radiative effect (ARE_{SFC})

$$ARE_{SFC} = NET_{sfc}^{aer} - NET_{sfc}^{clr}, \tag{6.4}$$

  so that the ARE_{SFC} (Wm^{-2}) is the net increase in irradiance at the Earth's surface due to the presence of aerosol. As with ARE_{TOA}, ARE_{SFC} can be calculated

as instantaneous or diurnally averaged, and is calculated over the full shortwave spectrum.

- Atmospheric direct aerosol radiative effect (ARE_{ATM})

$$ARE_{ATM} = ARE_{TOA} - ARE_{SFC}, \tag{6.5}$$

so that ARE_{ATM} (Wm^{-2}) is the net heating of the atmosphere due to the presence of aerosol.

- Aerosol radiative efficiency (RE_x)

$$RE_x = \frac{ARE_x}{\tau^{550}}, \tag{6.6}$$

where x represents TOA, SFC or ATM, and so that RE_x is efficiency of the aerosol at causing a radiative effect per unit of aerosol optical depth ($Wm^{-2}\tau^{-1}$). Again, the RE can be calculated as instantaneous or diurnally averaged.

6.2 Sensitivity of the Radiative Effect to the Variations in Optical Properties During DODO

Given the range in optical properties for the accumulation mode described in Chapter 4, it is important to test the sensitivity of the aerosol radiative effect (ARE) due to these variations. This section examines the sensitivity of the ARE to these changes for a typical dust profile.

6.2.1 Method

In order to test the sensitivity of the ARE to the various optical properties observed during DODO, three typical types of optical properties have been tested which represent the range of single scattering albedo values shown in Figure 4.1. These types are described in Table 6.1, and have been chosen to represent the range of ω_0^{550} from DODO, ranging from high to low values.

All cases from flights b173, b174 and b175 in DODO1 were selected, since these represent very high ω_0^{550} values. The runs selected from b237 represent the optical properties of the elevated dust layer, thus representing ω_0^{550} values around mid-values in the range shown in Figure 4.1. The runs from b242 were selected to represent the lower range of ω_0^{550} values.

In order to create optical properties representative of these three types, the accumulation mode size distributions from each run were averaged, and are shown in Figure 6.1. The refractive index at 550nm was also averaged for each type using the values shown in Figure 4.9, and the resulting averages are shown in Table 6.1.

In order to run ES96 over the spectral range described above, it is necessary to provide optical properties over this wavelength range as well. Therefore the refractive index must also be provided over the wavelength range $0.2 - 10\mu m$. The derived refractive indices shown in Chapter 4 represent the values only at 550nm. Therefore the full spectral refractive indices from WCP (1983) (also used by Shettle and Fenn (1979)) have been taken, but scaled so that they are in agreement with the derived values at 550nm. Figure 6.2 shows the real and imaginary refractive indices from WCP (1983) and the full

Dust Type	Runs Used	n_i at 550nm	ω_0^{550}	k_{ext}^{550}	g^{550}
DODO1	b173 (R8,R9), b174 (R3.1-4.5), b175 (R2,R6,R7.1,R7.2)	0.0005	0.99	0.85	0.69
b237 upper	b237 (R2,R3,R6,R7)	0.0017	0.97	1.10	0.69
b242	b242 (R1.1,R5.1)	0.0034	0.95	1.04	0.69
WMO		0.008			

Table 6.1: *Runs used in creating the optical properties for each idealised test case. Also shown is n_i used for each case, and the resulting optical properties at 550nm. n_r^{550} is always assumed to be 1.53. Also shown is the WCP (1983) (WMO) n_i^{550} value.*

spectral refractive indices for each test case. For the real part of the refractive index, the previously assumed value of 1.53 at 550nm is consistent with WCP (1983), so the real refractive indices of WCP (1983) are used directly.

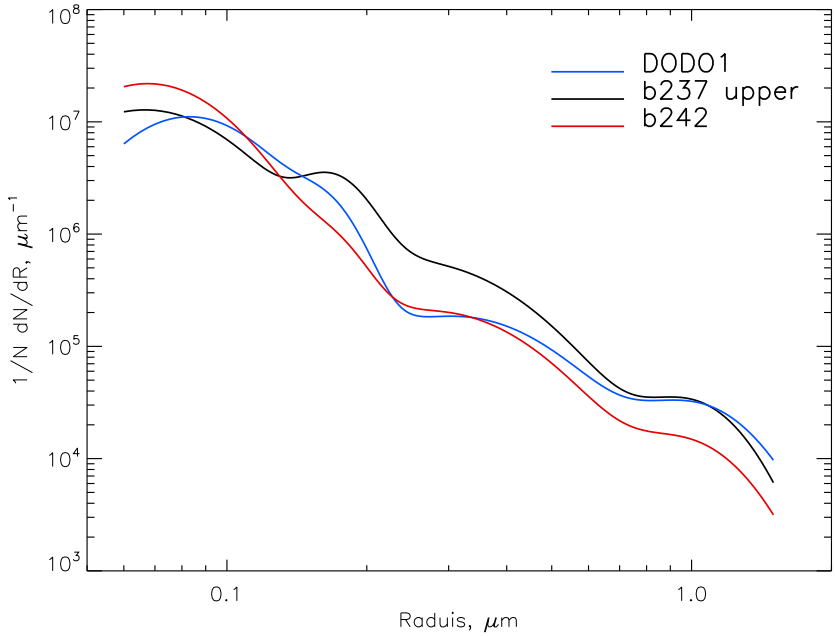

Figure 6.1: *Accumulation mode logfit curve size distributions for each idealised test case, created by averaging the size distribution for each run shown in Table 6.1.*

Using the spectral refractive indices shown in Figure 6.2, and size distributions shown in Figure 6.1, spectral optical properties for each test case were calculated using a Mie scattering code. Spherical particles were assumed. The resulting optical properties are shown in Figure 6.3. It is clear that the differences in the imaginary refractive indices of

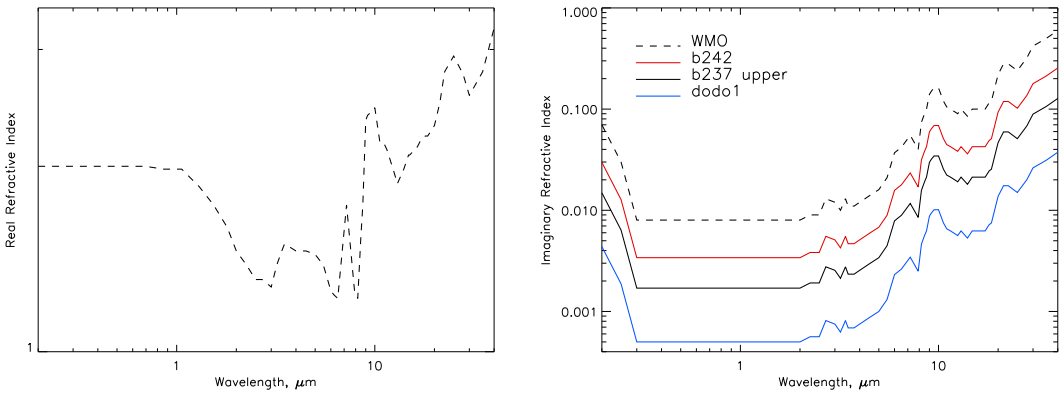

(a) (b)

Figure 6.2: *6.2(a) Real and 6.2(b) imaginary spectral variations of the refractive index used as input to ES96. Black dashed line shows the refractive index of WCP (1983). Coloured lines represent the spectral imaginary refractive index for the idealised test cases of DODO1 dust (blue), the upper layer in b237 (black) and b242 dust (red).*

each case result in different single scattering albedos, with b242 being the most absorbing, and DODO1 the least absorbing. The slightly different size distributions also result in variations in k_{ext} . Changes in g for each case are small.

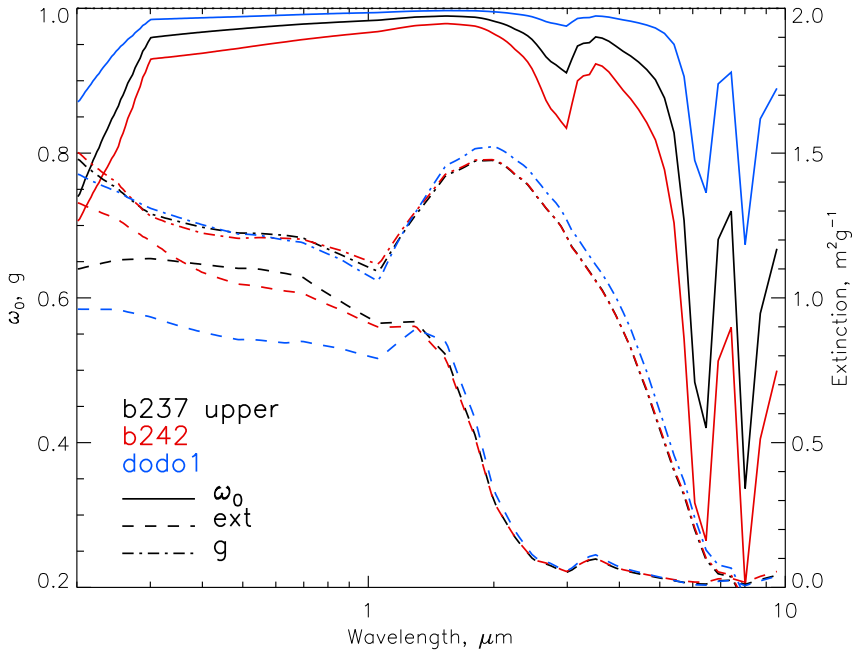

Figure 6.3: *Spectral optical properties for each idealised test case which have been used as input to ES96. Solid lines represent single scattering albedo, dashed lines represent k_{ext} , dot-dashed lines represent the asymmetry parameter. Colours as indicated in the Figure.*

In order to run ES96 the vertical distribution of the dust mass mixing ratio is required. In order to solely test the effect of the changing optical properties for each case, two types of vertical distributions have been tested, and are shown in Figure 6.4. These include a low altitude dust layer, typical of the dry season cases, which has been taken from flight b175. Secondly an elevated dust layer has been used, typical of the dust from DODO2 over the ocean, which has been taken from flight b242. The vertical profiles of dust, water vapour, ozone and temperature have been taken from aircraft measurements for each case and interpolated onto a 50 level vertical grid as described in Section 6.1.1.

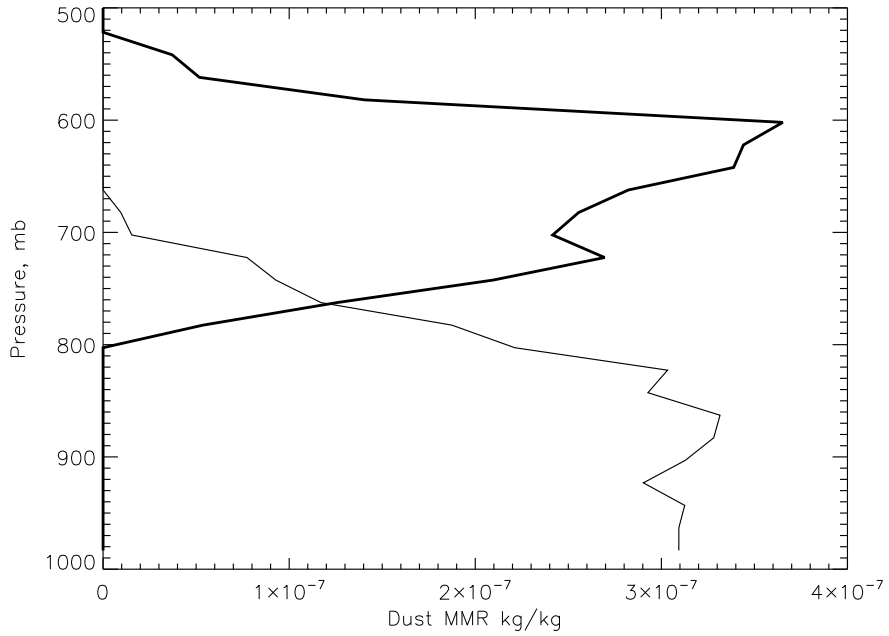

Figure 6.4: *The two vertical profiles of dust mass mixing ratio used in the idealised test cases. The bold line represents the wet season dust in an elevated layer over the ocean (taken from b242 P9) and the thin line represents lower altitude dust typical of the dry season (taken from b175 P8).*

Finally the surface albedo must be defined in order to drive ES96. In order to represent the two typical land surfaces encountered during DODO, two cases are tested. The first is an ocean surface, with an albedo of 0.05, the second a desert surface with an albedo of 0.44. These values are calculated from pyranometer measurements of up and downwelling irradiances when the aircraft was flying close to the surface. The ratio of the upwelling to the downwelling irradiance is taken to represent the surface albedo. Over the ocean this is likely to be accurate, since the aircraft flew as low as 50ft (around 15m)

above the surface, so that the distance over which additional absorption and scattering of radiation could take place was minimal. Over land the closest the aircraft could get to the surface was 500ft (around 150m), so that there is a possibility that the pyranometer measurements of surface albedo may be affected by additional aerosol below the aircraft. Sensitivity to these changes are explored in Section 6.4. Surface albedo is assumed constant throughout the day. This may not be representative of reality (e.g. Jin *et al.*, 2004). However, since the purpose of these tests is to test the sensitivity of the irradiances to the differences in optical properties, it is sufficient for these purposes.

6.2.2 Results

Figure 6.5 shows the results of the effects of the different optical properties tested on the direct aerosol radiative effect (ARE), at the top of atmosphere (TOA) and the surface. The general trends in ARE at both surface and TOA are consistent with those previously examined in sensitivity studies (e.g. Liao and Seinfeld, 1998; Tegen and Lacis, 1996), including a negative ARE (cooling) at the surface due to the absorption and scattering of radiation by the dust in the atmosphere, and a positive or negative ARE at the TOA depending on the amount of absorption occurring and the land surface type.

At the TOA the ARE is always negative (indicating a cooling of the earth atmosphere system) over ocean, but over desert can be negative or positive, implying that the dust can cause an overall warming or cooling. This is because the higher surface albedo over desert results in more radiation being reflected upwards from the surface, allowing the dust to scatter and absorb more radiation. This results in more radiation being reflected back to the surface, causing a less negative surface ARE over desert (compared to ocean). It also results in the dust layer being able to absorb more radiation, causing greater atmospheric heating rates. The greater atmospheric absorption results in a more positive ARE_{TOA}.

The effect of a high versus low altitude dust layer are small, and also affected by the greater mass loading in the low altitude dust layer. However, the vertical profile of the heating rates are strongly dependent on the dust altitude, with most absorption occurring at the altitude where dust is.

The solar zenith angle affects the dust ARE, with both surface and TOA AREs being

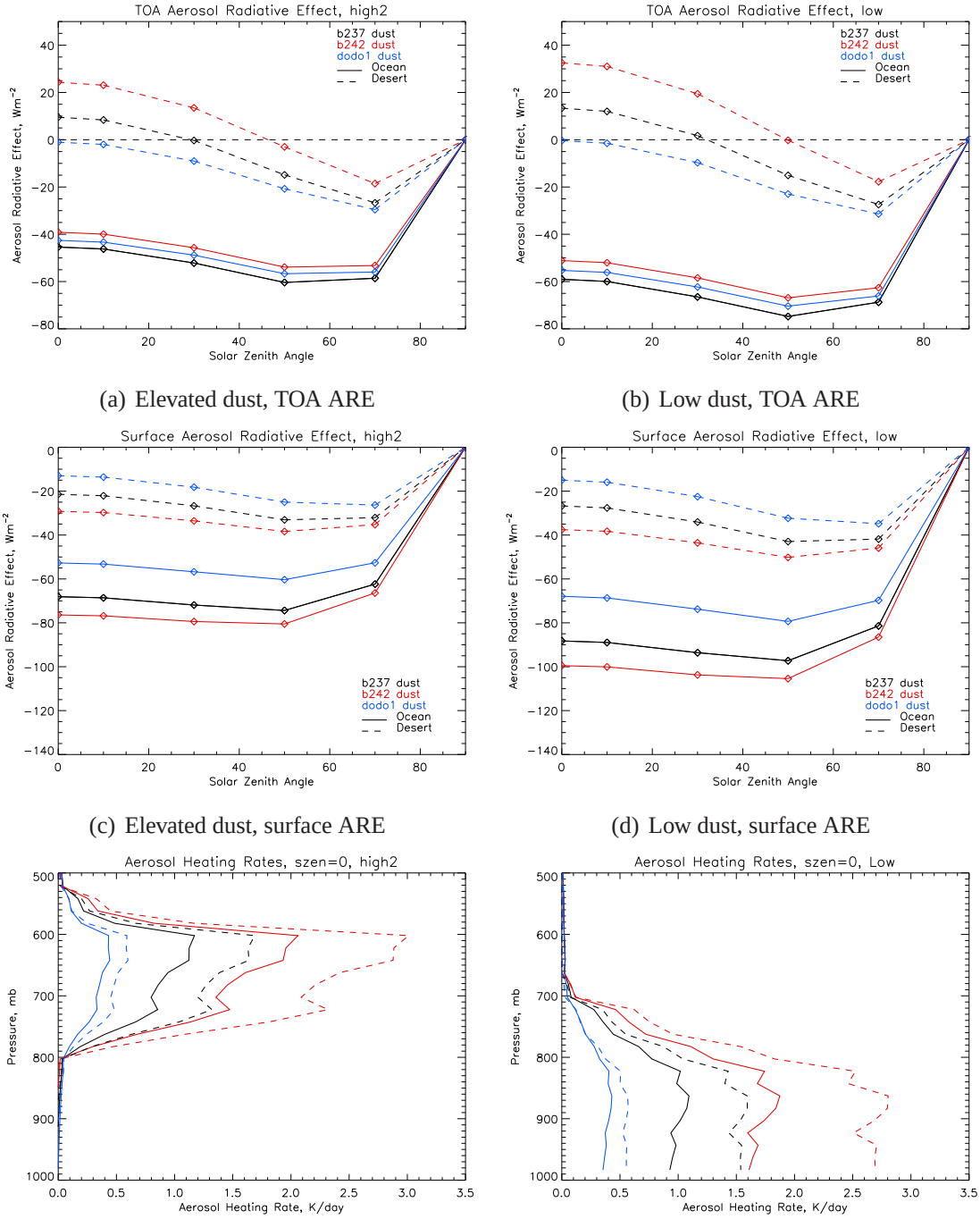

(a) Elevated dust, TOA ARE

(b) Low dust, TOA ARE

(c) Elevated dust, surface ARE

(d) Low dust, surface ARE

(e) Elevated dust, heating rate

(f) Low dust, heating rate

Figure 6.5: *Radiative effect of different idealised dust types for a range of solar zenith angles. Results show radiative effect of elevated dust (6.5(a), 6.5(c), 6.5(e)) and low level dust (6.5(b), 6.5(d), 6.5(f)), at the TOA (top row), surface (middle row), and heating rate profiles at a solar zenith angle of* 0° *(bottom row). Solid lines represent cases over ocean, dashed lines represent cases over desert. Blue lines represent DODO1, black lines represent b237 upper and red lines the b242 case.*

strongest at solar zenith angles of $50°$. This is because of the shape of the phase function - at $50°$ a large proportion of the scattering falls within the upwards hemisphere, allowing the reflected irradiance to reach a maximum. When the sun is overhead more of the scattered radiation falls within the downwards hemisphere, reducing the radiation scattered back out to space, and making the ARE more positive.

Figure 6.5 shows the effects of the different optical properties clearly. At the surface (Figures 6.5(c) and 6.5(d)) the most negative ARE is caused by the most absorbing dust (b242, red lines). The least negative ARE is caused by the least absorbing DODO1 dust (blue lines) which absorbs less radiation. The difference in surface ARE between the different dust types reaches a maximum of around $35Wm^{-2}$ over ocean, and $23Wm^{-2}$ over desert, for low altitude dust (changes of 35% and 60% respectively from the b242 case). The spread in the ARE values for high altitude dust is slightly less due to the smaller absolute values of ARE. Figure 6.5 assumes that the dust particles are spherical. Based on the calculations of Otto *et al.* (2009), the effect of non-spherical particles would be to increase the upwelling irradiance at the TOA by a few percent, therefore making the TOA radiative effect more negative. If this were the case for the data shown in Figure 6.5, then this would not be a large enough effect to outweigh the differences in the radiative effect due to the different optical properties.

Layer Type	DODO1	b237 upper	b242
Elevated	0.47	0.58	0.54
Low	0.61	0.75	0.70

Table 6.2: *Aerosol Optical Depths at 550nm for each idealised dust type.*

The heating rate profiles shown in Figures 6.5(e) and 6.5(f) show a strong dependence on the different optical properties. For example, over desert with a low altitude dust layer, the peak heating rate can vary between $0.55Kday^{-1}$ to $2.8Kday^{-1}$ for the range of optical properties tested - a decrease of 80% from the b242 case.

As a result of the differences in surface ARE and heating rates due to the different optical properties, the TOA ARE can also change significantly. Over ocean, the range in optical properties tested causes a change in ARE of up to $10Wm^{-2}$. Over ocean, the TOA ARE for DODO1 dust (blue line) is the most positive case at the surface. At the TOA,

the ARE does not change much due to the small amount of atmospheric absorption. For the case of b237 dust, the surface ARE was more negative. However, the atmospheric absorption for b237 was larger than that for for DODO1, so that the TOA ARE is still less than that of DODO1, but closer in magnitude. For b242 dust, the very large amount of atmospheric absorption means that the net TOA ARE is more positive than DODO1. Hence the TOA ARE is a balance of how much the surface ARE reduces against how much atmospheric absorption occurs.

Over the desert, more absorbing dust always results in an increase in TOA ARE due to the greater magnitude of atmospheric absorption, despite the ARE_{SFC} being more negative. The changes here are larger and can be up to $35 W m^{-2}$. Additionally the different optical properties are important in determining whether there is a net warming or cooling (positive or negative TOA ARE). The DODO1 dust type never results in a net warming, whereas the b242 dust results in a warming up to solar zenith angles of around 50°.

6.2.3 Conclusions

The aim of this Section has been to examine the importance of the variability in optical properties observed during the DODO campaigns to the shortwave radiative effect of the dust. Section 6.2.2 has clearly shown that these variations are important to not only the magnitude of the radiative effect, but also to its sign over desert surfaces. This high sensitivity of the radiative effect over surfaces with a high albedo is also important over the ocean, where elevated dust layers can occur above stratocumulus or cumulus cloud at the top of the marine boundary layer. Therefore the importance of differing optical properties is important over both the ocean and the desert.

The differences in atmospheric heating rates are also extremely important in driving the local meteorology (e.g. Alpert *et al.*, 1998; Miller and Tegen, 1998). This therefore highlights the importance of the presence, and accurate representation of optical properties, in numerical weather forecast models in regions where dust is dominant.

The differences in irradiances shown in Section 6.2.2 arise largely from the differences in the refractive indices. Given the large range in refractive indices derived during DODO alone, a range which is smaller than the range of estimates and measurements in

the literature, a strong emphasis on obtaining a bank of accurate measurements of refractive indices of dust is needed, including geographical variations, in order to best represent dust in radiative transfer models, general circulation models, and numerical forecast models.

6.3 Comparison of Modelled Irradiances to Pyranometer Measurements

It is necessary to show that the responses of the aerosol radiative effect to the different optical properties shown in Section 6.2 are realistic and reliable, particularly since the model calculations assume that the dust particles are spherical. Therefore this section compares modelled irradiances to the aircraft pyranometer measurements for four different flights.

6.3.1 Model Input

For the comparison of model irradiances and pyranometer measured irradiances, the flights b175, b237, b238 and b242 have been selected. These were selected on the basis of predominantly cloud-free skies (which could otherwise affect the pyranometer measurements), and a well defined dust profile with measurements of optical properties from within the main dust layer. For the DODO1 case (b175) there was no biomass burning aerosol present.

Chapter 4 showed the optical properties for various different runs within a single flight. In order to use one set of optical properties to model the dust for each flight, runs within each flight have been combined to create a typical dust-type for each single flight (see Table 6.3). For the case of b237, where very different optical properties were found in the layer closest to the surface, only optical properties representing the upper layer have been used, as this was where most of the dust mass resided.

Using the selected runs shown in Table 6.3, for each flight an average size distribution for the accumulation mode was calculated and is shown in Figure 6.6(a). The average refractive index at 550nm was also calculated using the data shown in Figure 4.9, and is shown in Table 6.3. This was then converted to a full spectral imaginary refractive index by using the WCP (1983) spectral refractive index, and scaling it down so that it agreed with n_i for each flight. The resulting spectral imaginary refractive indices are shown in Figure 6.6(b). For the real part of the refractive index, the WCP (1983) data were used, and are shown in Figure 6.2(a).

The size distributions and refractive indices shown in Figure 6.6 were then input

Flight	Runs Used	n_i at 550nm	ω_0^{550}	k_{ext}^{550}	g^{550}
b175	R2,R6,R7.1,R7.2	0.0002	0.99	0.82	0.69
b237	R2,R3,R6,R7	0.0017	0.97	1.10	0.69
b238	R3.1-3.4,R4.1,R5.1,R6.1,R7.1	0.0012	0.98	1.10	0.69
b242	R1.1,R5.1	0.0034	0.95	1.04	0.69

Table 6.3: *Details of runs used in creating average optical properties for each flight. Also given is the resulting average n_i at 550nm, and the resulting optical properties at 550nm. n_r^{550} is always assumed to be 1.53.*

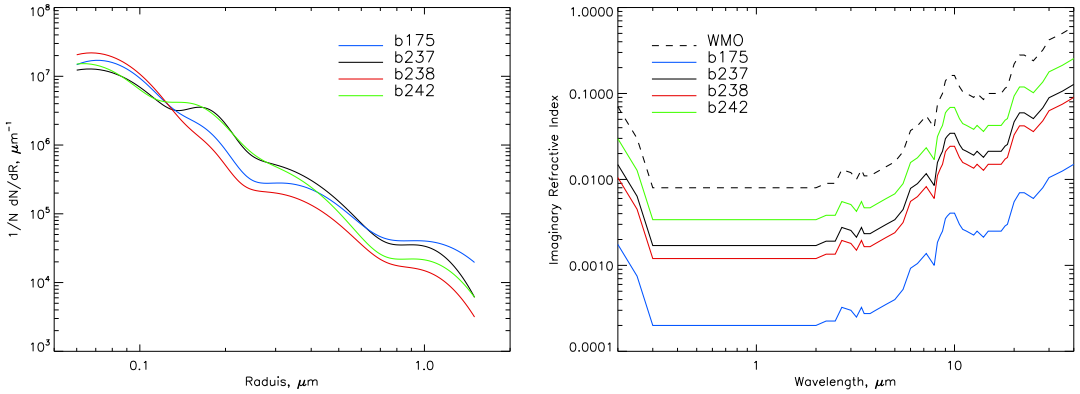

(a) (b)

Figure 6.6: *6.6(a) Averaged logfit size distributions for each flight used to create optical properties specific to each flight. 6.6(b) Refractive indices used to create the optical properties for each flight. Colours represent different flights, as indicated in the Figures.*

into a Mie scattering code in order to calculate the spectral optical properties. Since the size distributions represent the accumulation mode only (up to $r = 1.5\mu m$) the optical properties are only representative of the accumulation mode. Sensitivity to inclusion of the coarse mode is described in Section 6.5. The optical properties are shown in Figure 6.7 along with the optical properties for the runs when treated individually. It is clear that the flight average spectral optical properties fall within the range of values for the different runs. The data for b238 show a greater spread because the optical properties changed dramatically with altitude.

Vertical profiles of dust mass mixing ratios are also used by ES96. These are calculated from the vertical profiles of extinction, as described in section 6.1.1, and are shown in Figure 6.8. For each flight several profiles were performed in the dust layers, and each profile measured slightly different amounts of dust. This is due to spatial variability, and

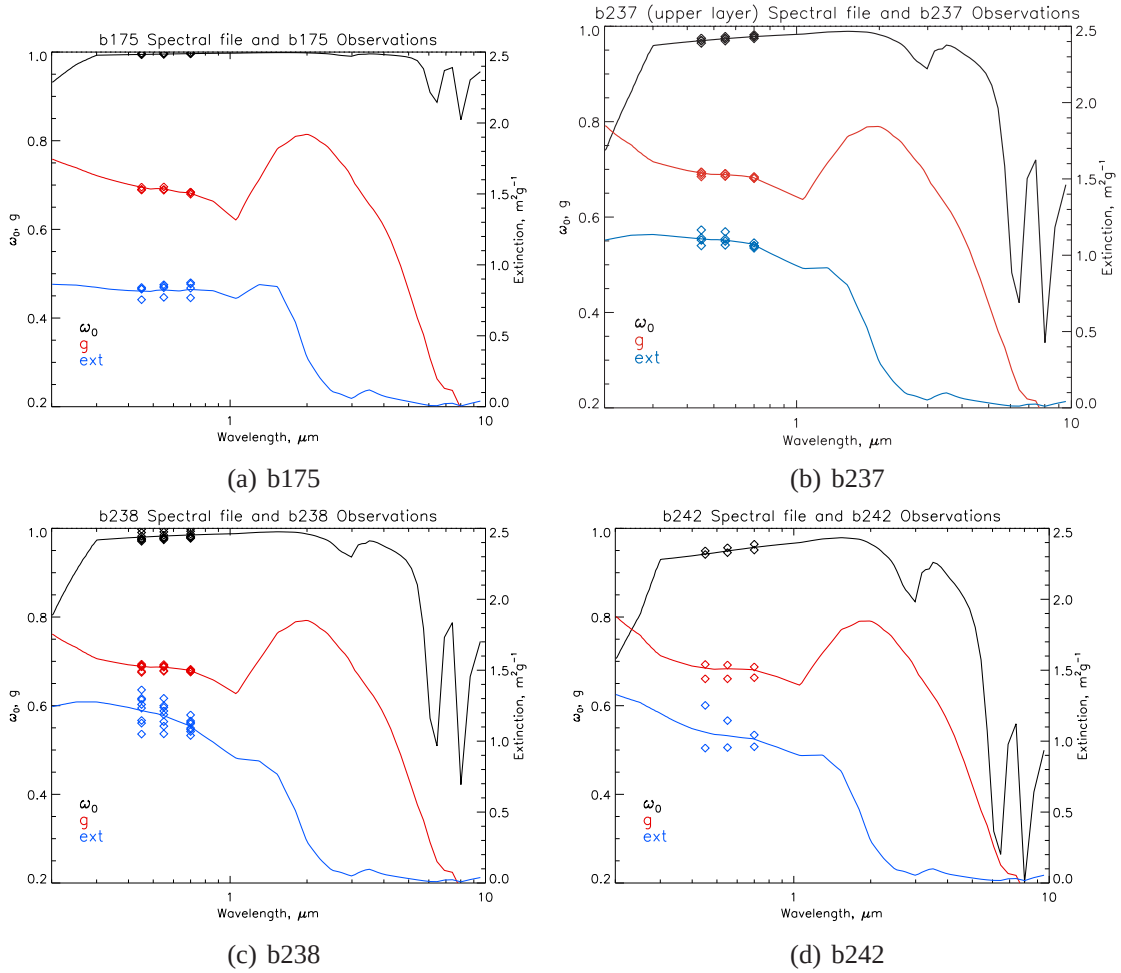

(a) b175 (b) b237

(c) b238 (d) b242

Figure 6.7: *Spectral Optical Properties for the average dust from each flight for the accumulation mode. Black lines indicate ω_0 , red g, and blue k_{ext} . Diamonds indicate the optical properties for individual runs as calculated in Chapter 4.*

development or movement of the dust profile throughout the flight. Therefore each different profile is used, in order to gain an understanding of the uncertainty in the irradiances due to the changes in the vertical profiles observed. In some cases, several shorter vertical profiles which sampled part of the vertical profile have been combined. Note that for flight b242 a latitudinal gradient in the amount of dust was observed, with profiles 6 and 7 being performed further south, and therefore measuring less dust (Figure 6.8(d)). Vertical profiles of water vapour, temperature and ozone are also taken from the aircraft measurements (not shown).

As described in Section 6.2.1, the dust MMR profiles are defined by the amount of aerosol which the nephelometer and PSAP can measure, which is thought to be limited to

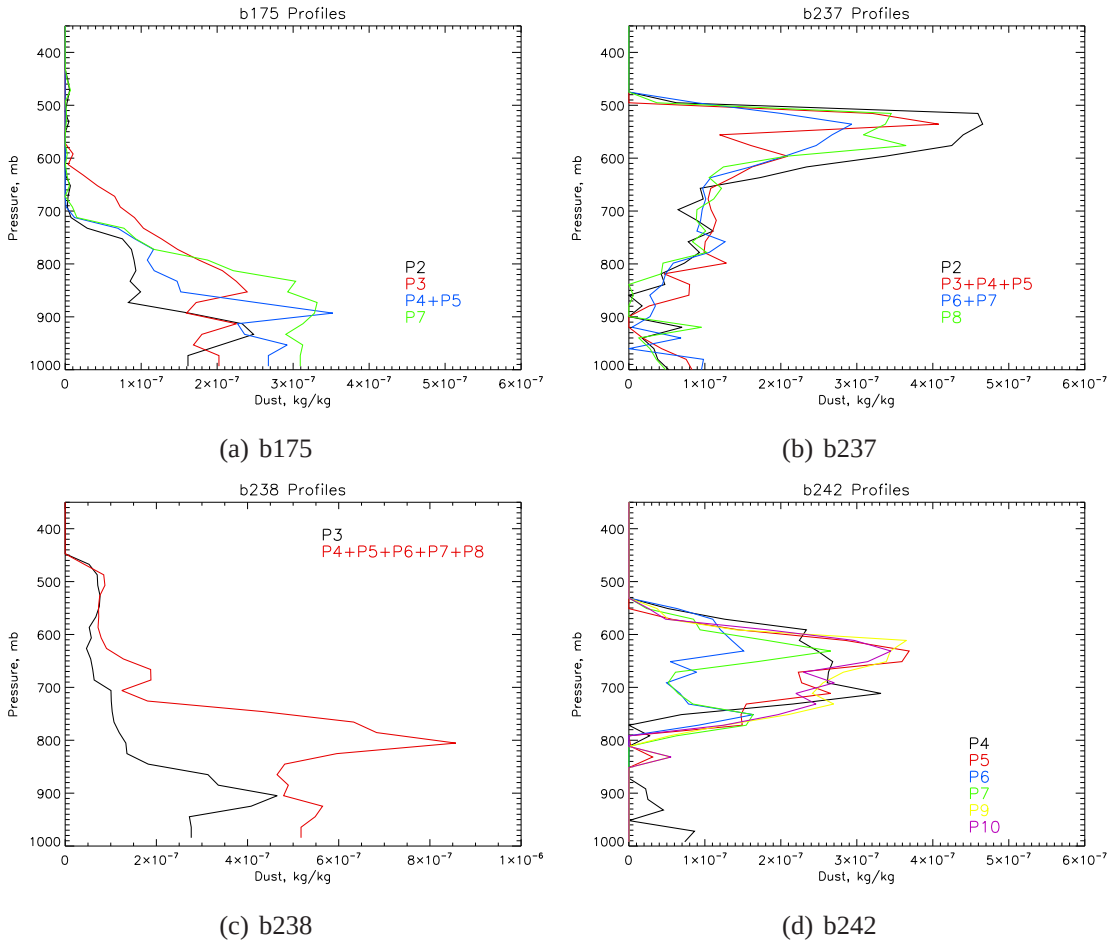

(a) b175 (b) b237

(c) b238 (d) b242

Figure 6.8: *Vertical profiles of dust mass mixing ratio for each flight used for model input. Different mass mixing ratios for different profiles within each flight are shown by different colours, as indicated on each figure. Note the different scale for b238 (Figure 6.8(c)). MMR profiles represent the accumulation mode only.*

the accumulation mode only. The MMR profiles are also limited by value of k_{ext}^{550} used in Equation 6.1, which thus far has been derived using the accumulation mode size distributions, and therefore also represents the accumulation mode. Therefore the MMR profiles described here represent the accumulation mode only.

In order to obtain model irradiances which are comparable to measurements from the pyranometers, it is necessary to use solar zenith angles which are the same as those when pyranometer measurements are made. Pyranometer data from straight and level runs is averaged, and therefore ES96 is run at the average solar zenith angle for each run during each flight. Model results can then be selected at an appropriate pressure level and solar zenith angle so that comparisons with the pyranometer data is appropriate.

6.3.2 Results

The modelled irradiances are compared to the measured ones in Figures 6.9, 6.10, 6.11 and 6.12 for each flight. Each Figure shows a direct comparison of the irradiances through a scatter plot (top rows) for both the shortwave downwelling (SWD, left column) and shortwave upwelling (SWU, right column) irradiances, and through a comparison of the difference in SWD and SWD irradiances as a function of pressure at which the pyranometer measurements were made - in terms of absolute difference (middle rows) and percentage differences with respect to the pyranometer measurements (bottom rows). This is useful as if the percentage differences are within 5.5%, the accepted uncertainty of the pyranomter measurements from Chapter 5, the model and measurements can be seen to be in agreement within the measurement uncertainties. This area of agreement is shown by the grey shading. Since the minimum error on the pyranometers is $5Wm^{-2}$, this is also shown on the absolute difference between the SWU irradiances in Figure 6.10(d) where the differences are less than $5Wm^{-2}$ but greater than 5.5%.

Errors in the model irradiances are less straightforward to define. However, the spread of model results due to the different dust profiles used (different colours in Figures 6.9, 6.10, 6.11 and 6.12) gives an indication of the uncertainty in the model results due to the amount of dust present.

Note that due to the problems experienced with the DODO1 pyranometer data, the SWD measurements should not be considered as reliable for b175. Nevertheless, they are shown for completeness. The SWU DODO1 data are unaffected by this problem, and therefore the b175 case is still of use for comparisons with the model irradiances.

The results in the scatter plots for Figures 6.9, 6.10, 6.11 and 6.12 show that generally the 1:1 ratio between the pyranometer measurements and model results is followed, though the agreement is by no means perfect. Discrepancies between the model and pyranometer are more easily explored through the differences as a function of pressure.

Taking first the measurements of SWD at high altitude, (where good agreement is expected since no aerosol is above the aircraft), the pyranometer and model data are within the pyranometer uncertainty for the DODO2 flights. However, the model always appears to predict less irradiance than the pyranometers by $20 - 40Wm^{-2}$. Examining the SWD

Flight	Profile	Nephelometer τ^{550}	Model τ^{550}
b175	P2	0.31	0.31
	P3	0.49	0.47
	P4+P5	0.49	0.46
	P7	0.61	0.60
b237	P2	0.79	0.82
	P3+P4+P5	0.61	0.65
	P6+P7	0.57	0.63
	P8	0.61	0.64
b238	P3	0.89	0.98
	P4+P5+P6+P7+P8	1.75	2.09
b242	P4	0.56	0.55
	P5	0.56	0.51
	P6	0.27	0.25
	P7	0.32	0.31
	P9	0.67	0.59
	P10	0.67	0.54

Table 6.4: *Aerosol optical depths at 550nm calculated from model irradiances.*

data at lower altitudes, the model and pyranometer data are again in agreement within the pyranometer uncertainties, if the spread of model values for the different dust profiles used is considered. This spread is due to the spatial and temporal variability of the dust profile. Table 6.4 shows the range in AOD for each profile, which causes this spread. Therefore overall the SWD modelled irradiances show good agreement with the pyranometer measurements. It is worth noting that the pyranometer data has been screened, and data from relative headings in the $\pm 50^{\circ}$ range has been removed. Had this data been included, the agreement with the model data would have been much worse.

Agreement is worse between model and pyranometer data for the SWU irradiances. The best agreement is found at low altitudes (runs at pressures over $900mb$), where the differences are within the pyranometer uncertainties and the spread of model results for different dust profiles. This suggests that the values adopted for the surface albedo values are appropriate. At higher altitudes (mostly above the dust), the model results for flights b175, b237 and b238 have too much SWU irradiance compared to the pyranometer measurements. The flights b175, b237 and b242 show a trend of an increasingly positive SWD difference between the model and pyranometers as altitude increases. This suggests that

perhaps the dust in the model is too reflective. This results in the model overestimating the SWU by up to $110Wm^{-2}$, $70Wm^{-2}$, $40Wm^{-2}$ and $15Wm^{-2}$ for flights b175, b237, b238 and b242 respectively.

The overall picture is that the SWD model irradiances fall within the pyranometer uncertainties, whereas the SWU model irradiances at higher altitudes do not. This shows that the model SWU irradiances are less reliable than the SWD irradiances, and that therefore the calculations of surface ARE values in Section 6.2 are more reliable than those at the TOA. The tendency of the model results to overestimate SWU at the TOA will result in the TOA ARE values being more negative (or less positive) - possibly by up to $110Wm^{-2}$ - than reality.

It is possible that the error lies with the lower pyranometer measurements instead of the modelled irradiances. The accuracy of the lower pyranometers was not examined in Chapter 5 due to difficulties in comparing upwelling radiation with model or other measurement data. However, it should be noted that the SWU irradiances between the pyranometer and the model are in agreement at low altitudes, below the dust. This therefore suggests that they are reliable. It is also possible that the lower pyranometer domes get dirty in the same way to the upper pyranometers. However, Saunders and Barnes (1991) estmated that if the whole front hemisphere of the dome was dirty, it would only decrease the measured diffuse irradiance by $1Wm^{-2}$, and this therefore would be unable to explain the differences in SWU at high altitude shown here.

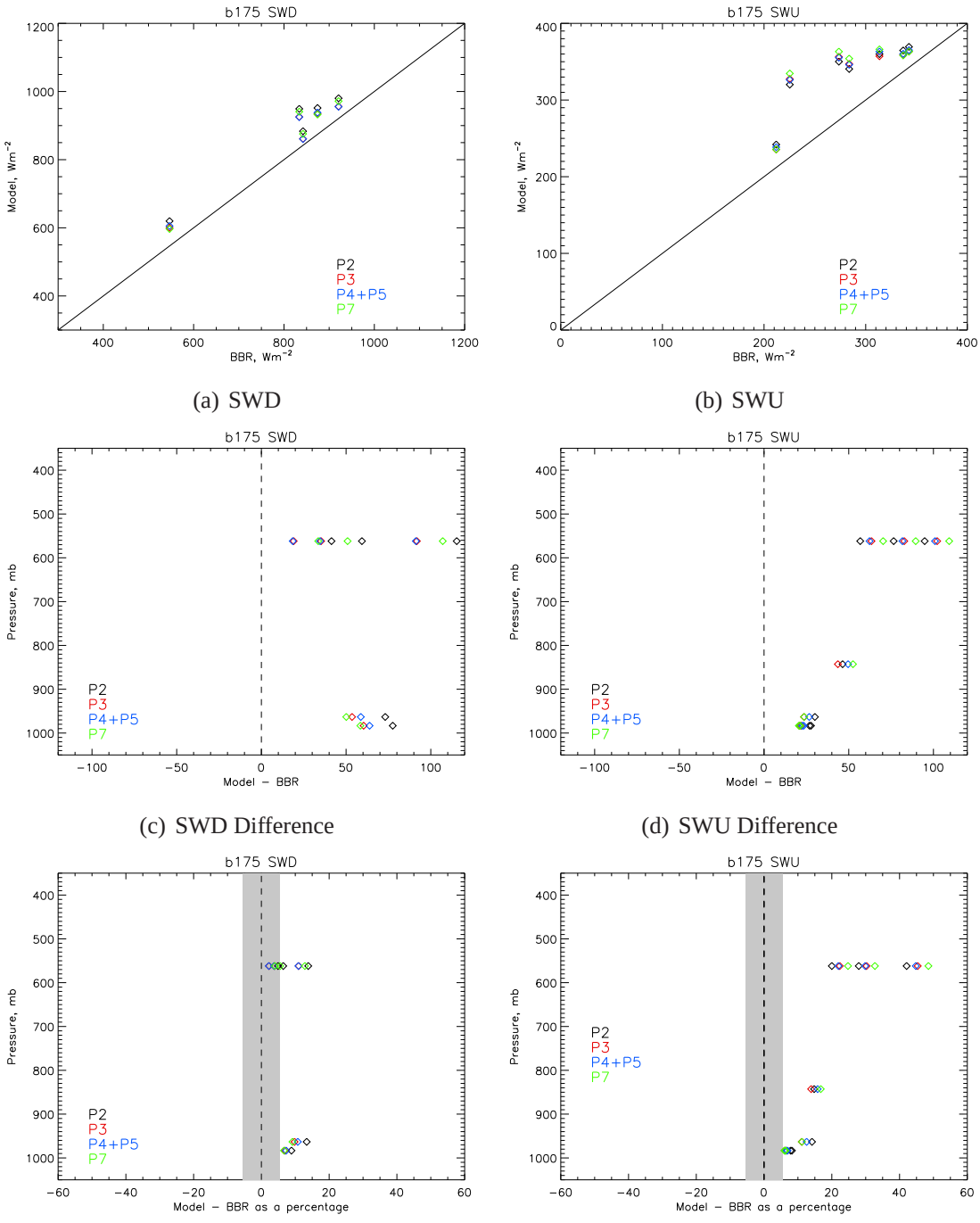

(a) SWD (b) SWU

(c) SWD Difference (d) SWU Difference

(e) SWD Percentage Difference (f) SWU Percentage Difference

Figure 6.9: *Comparison of modelled irradiances to measured irradiances for flight b175. 6.9(a), 6.9(b) Scatter plots of modelled and measured downwelling shortwave (SWD) irradiance and upwelling shortwave (SWU) irradiance; 6.9(c), 6.9(d) Difference between measured and modelled irradiances as a function of the pressure at which the measurements were made; 6.9(e), 6.9(f) Percentage difference between measured and modelled irradiances as a function of the pressure at which the measurements were made. Grey shading shows percentage errors of less than* 5.5%*, representing the uncertainty on the pyranometer measurements.*

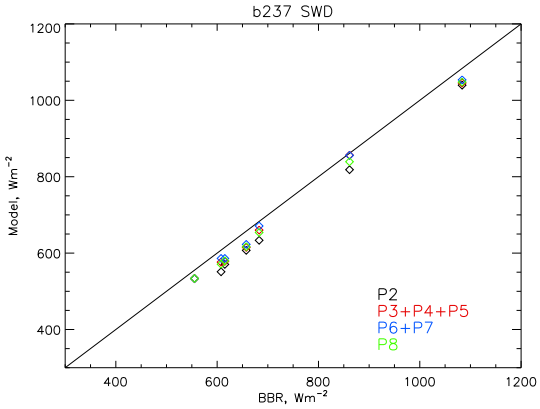

(a) SWD

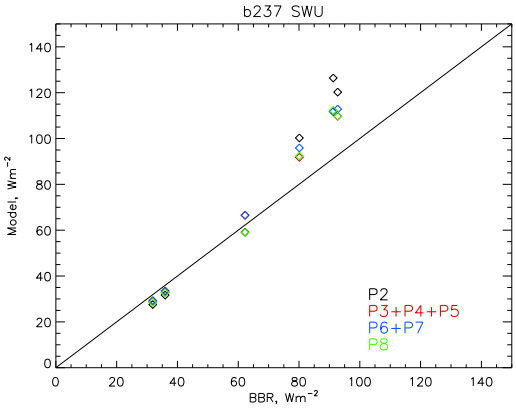

(b) SWU

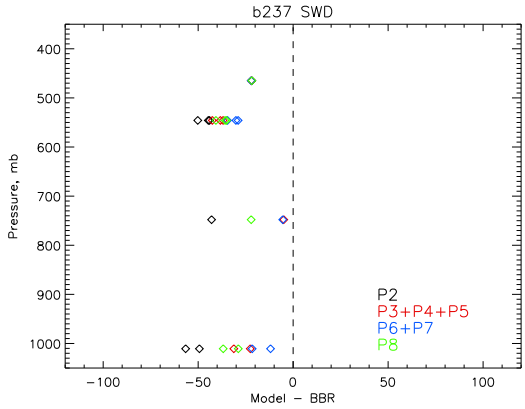

(c) SWD Difference

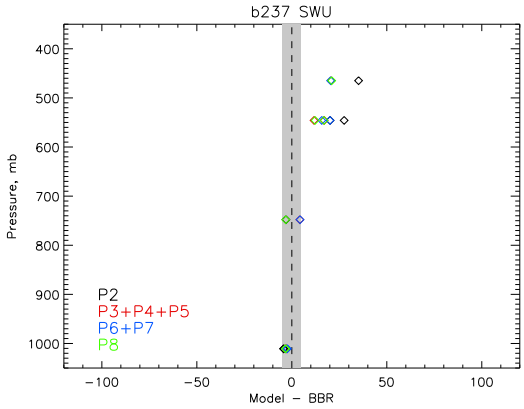

(d) SWU Difference

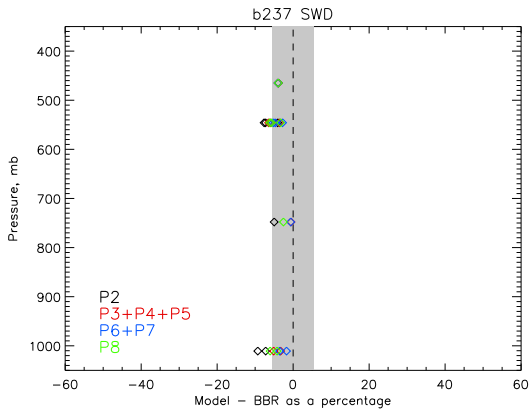

(e) SWD Percentage Difference

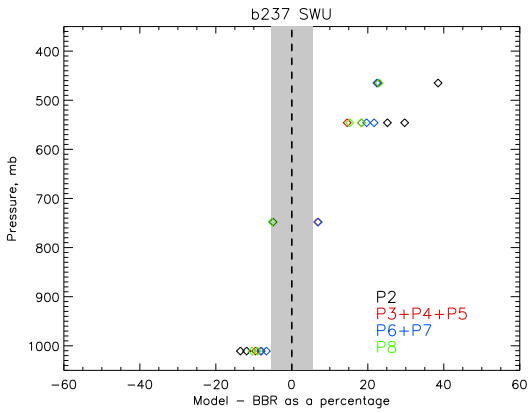

(f) SWU Percentage Difference

Figure 6.10: *As for Figure 6.9, but for flight b237*

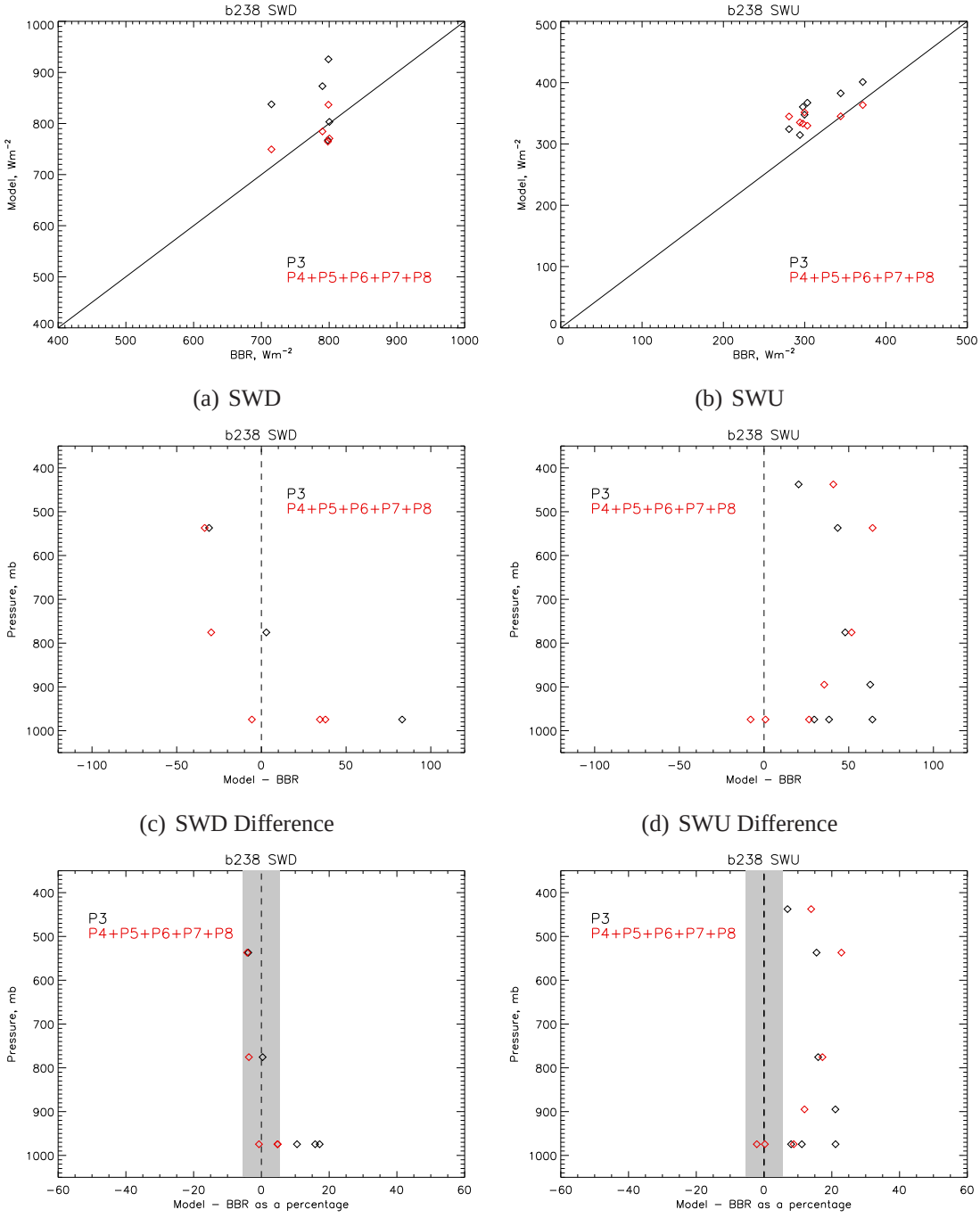

(a) SWD (b) SWU

(c) SWD Difference (d) SWU Difference

(e) SWD Percentage Difference (f) SWU Percentage Difference

Figure 6.11: *As for Figure 6.9, but for flight b238*

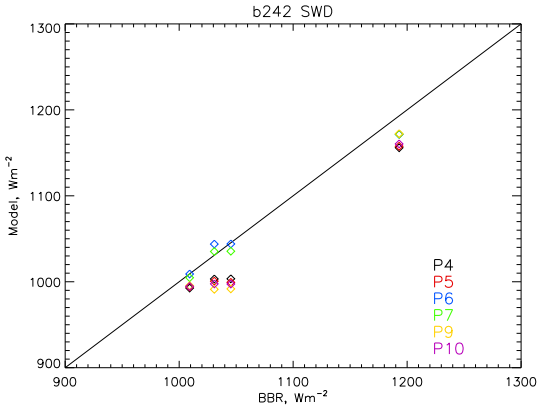

(a) SWD

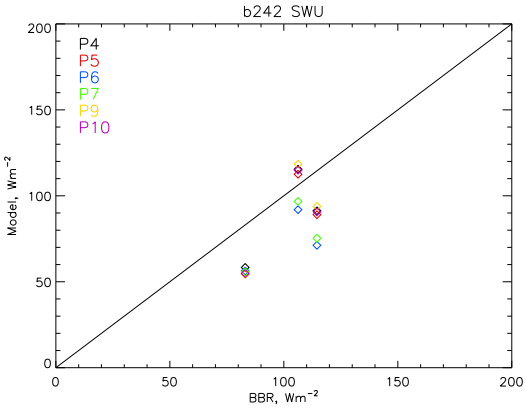

(b) SWU

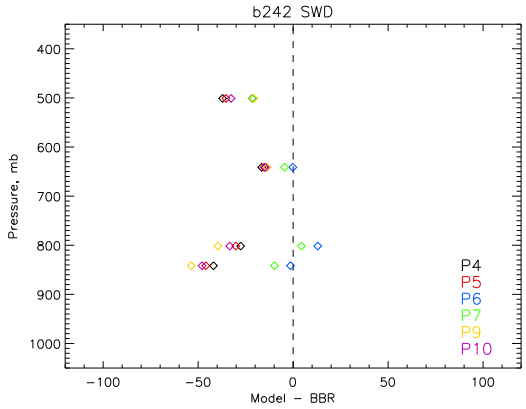

(c) SWD Difference

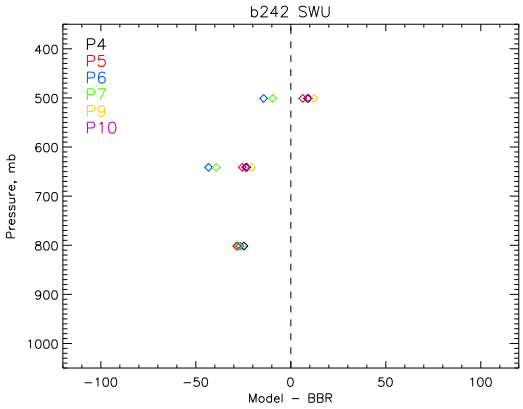

(d) SWU Difference

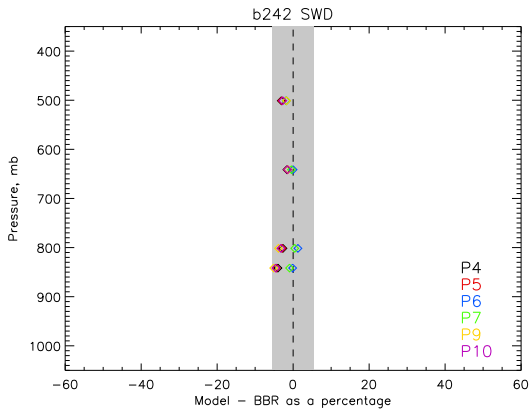

(e) SWD Percentage Difference

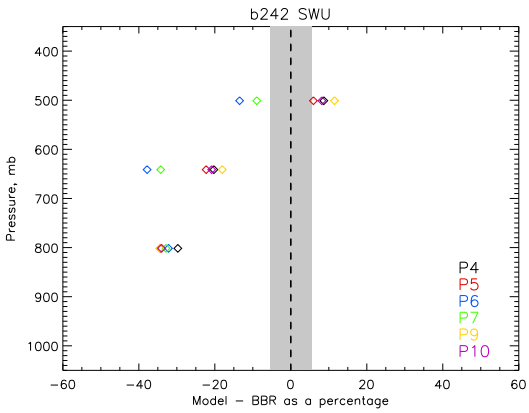

(f) SWU Percentage Difference

Figure 6.12: *As for Figure 6.9, but for flight b242*

6.3.3 Radiative Effect of Case Studies

In order to compare the ARE for each flight to values from the literature, the ARE for each flight has been diurnally averaged using ES96 model output, and is shown in Table 6.5 for the TOA, surface (SFC) and atmosphere (ATM). The diurnal average has been calculated by calculating irradiances at three times during each day, and weighting them based on a gaussian distribution, which varies throughout the year. As recommended by Li *et al.* (2004), the ARE values have also been divided by τ^{550} in order to give the shortwave radiative efficiency (RE) which is independent of solar zenith angle and aerosol amount. Also shown is the ratio of the ARE_{SFC} to the ARE_{TOA} since this gives an indication of the amount of absorption occurring in the atmosphere.

The results from the DODO flights show that the largest ARE at the TOA, surface and in the atmosphere occur for flight b238. This reflects the greater AOD values measured during the b238 profiles. Comparing the radiative efficiencies (RE) removes this dependence on aerosol loading, and results in b175 having the largest TOA RE, probably due to this flight having dust with the highest ω_0 and therefore reflecting the greatest proportion of radiation. Interestingly b175 had the lowest value of k_{ext}^{550} of all the flights (Table 6.3) and it still results in the most negative RE_{TOA}. The smallest RE_{TOA} results from b238, which shows that even though the ARE_{TOA} was highest, the dust is not necessarily the most effective per unit optical depth.

At the surface, the b238 dust also has the smallest RE_{SFC} of the four flights. Again, despite τ^{550} being highest for b238, the RE_{SFC} is the lowest, so that the AOD has increased significantly compared to the other flights without the ARE increasing at the same rate. b242 is an interesting case, where ω_0 is lower than the other flights, and the resulting values of RE_{SFC} are the most negative, RE_{ATM} are the largest, and ARE_{SFC}/ARE_{TOA} are the largest of the four flights examined. Clearly the lower ω_0 for b242 results in more atmospheric absorption (RE_{ATM} is $20.8 Wm^{-2}$, more than double the other flights' values), and therefore RE_{SFC} is more negative, which also results in a larger ratio of ARE_{SFC}/ARE_{TOA}. The differences in ω_0 can also be seen in the differences between b175 with high ω_0 values, and correspondingly low RE_{ATM} and ARE_{SFC}/ARE_{TOA}, in comparison to b237 and b238 with similar ω_0 values, and inter-

Flight/Study	τ^{550}	ARE_{TOA}	ARE_{SFC}	ARE_{ATM}	RE_{TOA}	RE_{SFC}	RE_{ATM}	ARE_{SFC}/ARE_{TOA}
b175	$0.46(0.15)$	$-23.3(6.3)$	$-24.6(6.8)$	$1.3(0.4)$	$-50.9(3.0)$	$-53.8(3.0)$	$2.8(0.3)$	$1.06(0.01)$
b237	$0.67(0.14)$	$-30.2(4.9)$	$-36.9(6.0)$	$6.7(1.1)$	$-44.2(1.3)$	$-54.0(1.7)$	$9.8(0.6)$	$1.22(0.02)$
b238	$1.53(0.56)$	$-54.3(15.0)$	$-68.3(20.3)$	$14.0(5.3)$	$-36.7(3.5)$	$-45.7(3.4)$	$9.1(0.2)$	$1.25(0.03)$
b242	$0.46(0.21)$	$-19.9(7.9)$	$-29.5(12.4)$	$9.6(4.5)$	$-44.1(4.2)$	$-64.9(3.6)$	$20.8(0.6)$	$1.47(0.06)$
Li *et al.* (2004)	0.36 ± 0.16	-12.6 ± 6	2	3	-35 ± 3	-65 ± 3	30 ± 4	1.9
Anderson *et al.* (2005) SHADE	1.48 ± 0.05	-64.54			-24	-38	12	1.6
Balkanski *et al.* (2007) wrt Li *et al.* (2004)					-45 to $-49(-29)$	-65 to $-76(-88)$	16 to $32(60)$	1.3-1.7
Balkanski *et al.* (2007) wrt Anderson *et al.* (2005)					-24 to $-16(4)$	-48 to $-57(-70)$	24 to $41(74)$	2.0-3.6
Christopher and Jones (2007)		-7.75 ± 0.86			-47.91 ± 3.91			

Table 6.5: *ARE and RE values at the surface, top of atmosphere and atmosphere. Results are given for the DODO flights examined, and other cases from the literature (see text for details). DODO values are the average of results for several profiles with different dust amounts, value in parentheses represents the maximum difference of the average from the range for the various profiles. Balkanski* et al. *(2007) values show a range due to changing amounts of hematite included in the refractive index calculations, values in parentheses represent the value obtained using the refractive index data of Patterson* et al. *(1977).*

mediate values of RE_{ATM} and ARE_{SFC}/ARE_{TOA} compared to b175 and b242.

Since the results from these tests are designed to represent the actual dust events during each flight, there are factors for each flight which differ and so the different RE values cannot be directly attributed to the differences in ω_0, though they do seem to explain the differences between flights. Factors such as the surface albedo and the vertical dust distribution may also have impacts on the ARE and RE values. Nevertheless, it appears that the different optical properties observed during the four DODO flights shown here result in signicantly different RE_{SFC}, and particualarly RE_{ATM} values.

Also shown in Table 6.5 are corresponding values from the literature. These values are derived either from satellite measurements (Li *et al.*, 2004; Christopher and Jones, 2007) or from model calculations combined with various methods based on observations (Anderson *et al.*, 2005; Balkanski *et al.*, 2007). The case from Anderson *et al.* (2005) is particularly relevant since the calculations are based on the measurements from SHADE by Haywood *et al.* (2003) (and therefore derived from similar instruments and methods as those presented here), and combined with model calculations in order to obtain a diurnal average. The dust measured during SHADE appears to have had smaller RE_{TOA} and RE_{SFC} values than DODO, though RE_{ATM} was within the range of DODO values. This is logical since the SHADE estimated n_i^{550} was 0.0015: within the range of values for the four DODO flights shown here.

Li *et al.* (2004) used data from MODIS and CERES over the Eastern Atlantic for June-August 2001 to calculate TOA radiative effects. To calculate the surface values they employed a radiative transfer model constrained by the satellite measurements. The results of Li *et al.* (2004) are much closer to the DODO results than those of Anderson *et al.* (2005), with RE_{TOA} and RE_{SFC} falling within the the range of DODO values (and variabilities) shown in Table 6.5. The absolute ARE_{TOA} and ARE_{SFC} are much smaller than the DODO values, presumably since the satellite data spanning more time captures many more smaller dust events than those sampled by the DODO flights. However, the notable difference is that RE_{ATM} is much larger for Li *et al.* (2004) than for DODO. This is likely due to the larger value of n_i adopted compared to the DODO results: Li *et al.* (2004) adopted refractive indices from the OPAC model Hess *et al.* (1998) which

are much more absorbing than those from DODO.

Balkanski *et al.* (2007) investigated how the ARE changes when the refractive index is altered from that of Patterson *et al.* (1977), to one which has varying amounts of hematite, and therefore varying absorption, but still resulting in imaginary refractive indices higher than those estimated for DODO. Balkanski *et al.* (2007) calculated RE values for the same areas as those examined by Li *et al.* (2004) and Anderson *et al.* (2005) using a dust model, and these are shown in Table 6.5. It is clear that the greater n_i values of Patterson *et al.* (1977) result in larger RE_{ATM}, which supports the trend of greater RE_{ATM} for b242 where n_i is larger. It is also interesting to note that the optical properties used by Balkanski *et al.* (2007) were unable to reproduce the low value of RE_{ATM} ($12 W m^{-2}$) measured during SHADE, a value which was not very different from the DODO values. This suggests, combined with the discrepancy in the SWU between the pyranometers and model irradiances for DODO, that perhaps the DODO and SHADE n_i values are underestimates. Generally though, the RE values found by other studies are in line with those calculated for DODO, though there are differences in RE_{ATM} which are likely to be related to n_i differences.

6.4 Sensitivity to Surface Albedo

For the results shown in Section 6.3 a diurnally constant Lambertian surface albedo has been used. The value for the surface albedo (α_s) was calculated from the ratio of upwelling to downwelling irradiance measured by the pyranometers at the lowest altitude possible throughout the duration of the flight. However, it is possible that changes in the surface albedo occur throughout the day due to the solar zenith angle changing, due to the aerosol load changing, and due to the wind speed changing (for the ocean cases) (Jin *et al.*, 2004).

In order to test the sensitivity of the modelled irradiances to the value of α_s used, α_s has been varied and the model irradiances at each α_s have been compared to the pyranometer measurements. It is of interest to examine whether changes in α_s can restore the discrepancy between the modelled and measured SWU irradiances at high altitudes shown in Section 6.3.

The flights b237 and b238 have been selected for the α_s sensitivity tests, since both showed too much SWU at high altitudes, and b237 was over ocean while b238 took place over the desert. Therefore they are good cases to compare. For b237 input profile data from P8 was selected since the dust profile for P8 was around the middle of the range shown in Figure 6.8(b) and therefore the irradiances for this profile were also in the middle of the ranges due to the different dust profiles (Figure 6.10). For b238 the combination of profiles P4+P5+P6+P7+P8 was selected. This profile had significantly more dust than P3 (Figure 6.8(c)), but was performed closer to where the radiation measurements were taken and generally showed better agreement between model results and measurements (Figure 6.11).

For b237 the range of albedo values tested was representative of the range of surface albedo values expected over ocean due to the observed wind speeds ($0 - 15ms^{-2}$), aerosol optical depths and solar zenith angles calculated by Jin *et al.* (2004). Therefore α_s was varied from 0.02 to 0.07 in increments of 0.01. For b238 the surface albedo was varied from 0.1 to 0.7 in increments of 0.1. This covers the range of variations observed during the low-level runs during b238 ($\alpha_s = 0.32 - 0.5$), the variations in α_s measured by Bierwith *et al.* (2009) over the Moroccan desert during SAMUM, and some extreme

values (0.1 and 0.7) to allow a full sensitivity test.

The results for the two sensitivity tests are shown in Figures 6.13 and 6.14. For b237, the changes in α_s cause extremely small changes in the SWD irradiance ($< 5Wm^{-2}$). For the SWU irradiances at the lowest altitude, the best agreement between model and pyranometers occurs with $\alpha_s = 0.055$, as was calculated from the measurements. This suggests that the previously used value of $\alpha_s = 0.055$ is acceptable. However, at higher altitudes the best agreement occurs for a lower α_s of 0.02, though this is still not enough to allow for the SWU discrepancy to be resolved and actually a lower value of α_s than suggested by the conditions of wind speed, AOD and solar zenith angle during the flight from Jin *et al.* (2004). If the results of the correct α_s as suggested by Jin *et al.* (2004) had been used for the comparison of each data point, the change in SWU would have been no greater than $10Wm^{-2}$ - a value too small to solve the SWU discrepancy. Therefore for the case of b237 it appears that although the irradiances are sensitive to the surface albedo, the dust appears to be the principal problem in the SWU differences. (Possible issues with the lower pyranometer are discussed in Section 6.7.2).

For b238 the effects of change α_s are more pronounced, since α_s is higher to begin with and the range of α_s tested covers a greater range than the ocean case. The change in α_s examined now causes changes of around $\pm 100Wm^{-2}$ in SWD at the lowest altitudes, with a range of $\alpha_s = 0.2 - 0.6$ falling within the pyranometer uncertainty. However, at the same altitudes values in the range of $\alpha_s = 0.4 - 0.5$ show agreement between the upwelling model and pyranometer data, which suggests that the best estimate of $\alpha_s = 0.44$ as used in Section 6.3 is acceptable. However, at the highest two altitudes where measurements were made, the best agreement is found for $\alpha_s = 0.3$ where the model irradiances fall within the pyranometer measurement uncertainty. However, this would result in an underestimate of SWU by the model at the lowest altitude of measurements of around $100Wm^{-2}$, which is too low to be acceptable. Therefore the b238 results suggest, as the b237 results did, that the discrepancy in SWU between the model and pyranometer measurements is sensitive to the surface albedo, but that the modelled properties of the dust are more likely to be the main problem.

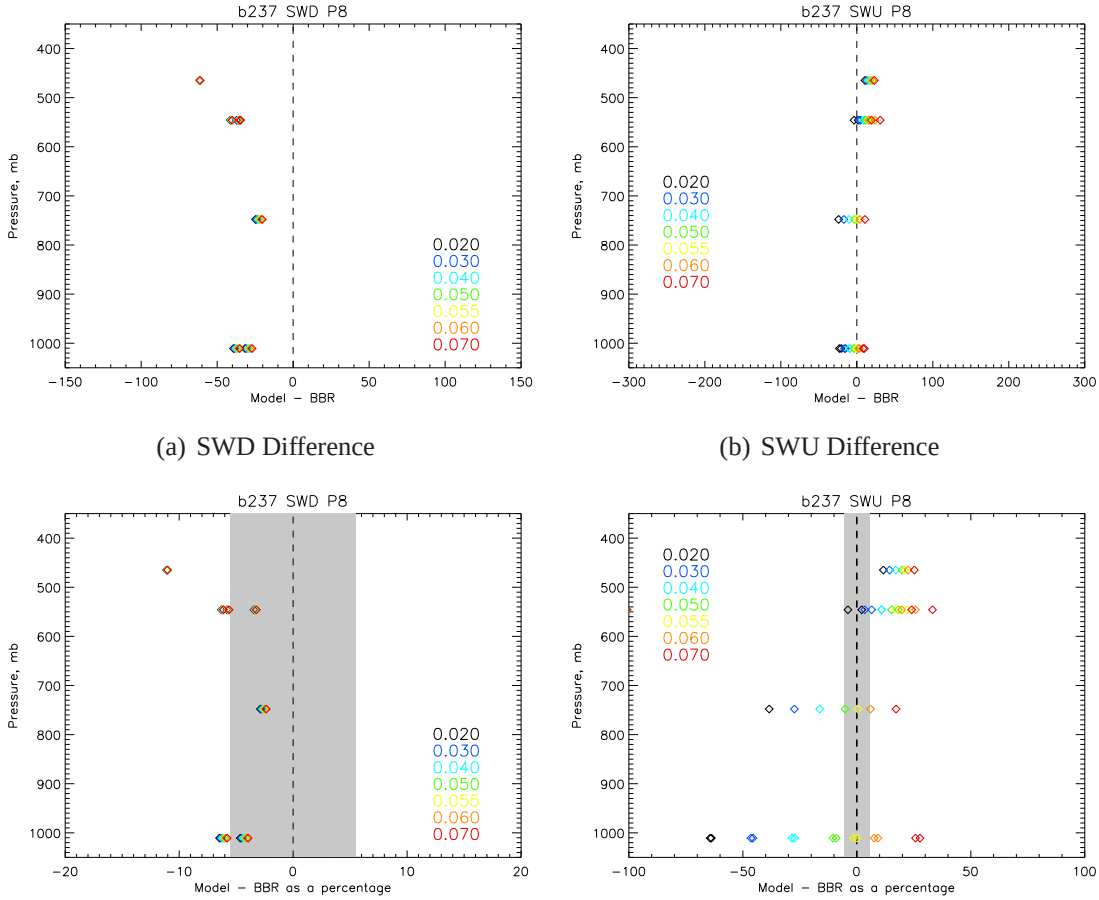

(a) SWD Difference

(b) SWU Difference

(c) SWD Percentage Difference

(d) SWU Percentage Difference

Figure 6.13: *Sensitivity of model irradiances to changes in α_s for flight b237. Different colours represent different α_s values, as indicated in the Figures. The best estimate of α_s from pyranometer measurements is 0.055. (a) and (b) Difference between model and pyranometer irradiances as a function of pressure, (c) and (d) Percentage difference between model and pyranometer irradiances as a function of pressure. (a) and (c) SWD irradiances, (b) and (d) SWU irradiances.*

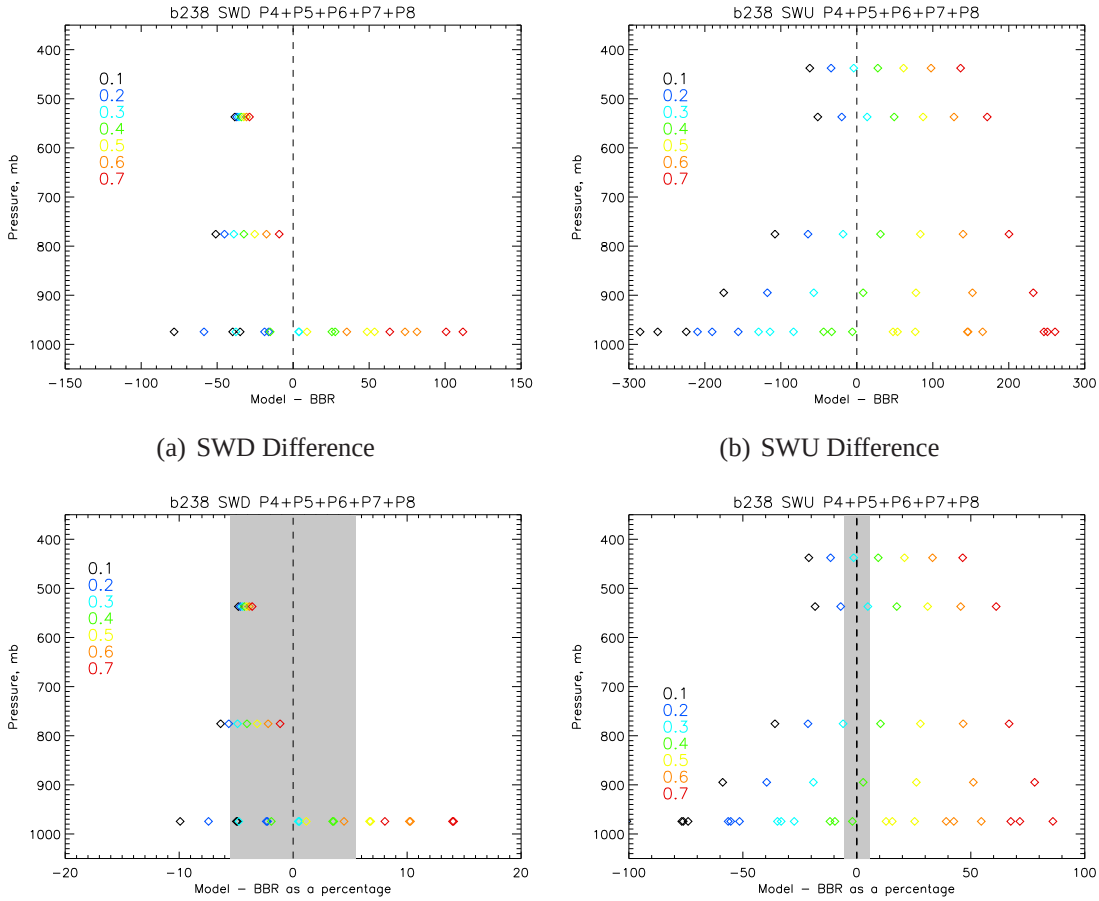

(a) SWD Difference

(b) SWU Difference

(c) SWD Percentage Difference

(d) SWU Percentage Difference

Figure 6.14: *Same as Figure 6.13 but for b238. The best estimate of α_s from pyranometer measurements is 0.44.*

6.5 Sensitivity to Inclusion of Coarse Mode

Chapter 4 showed that the optical properties, particularly ω_0 and k_{ext} , are very sensitive to the presence of a large coarse mode. Therefore this Section investigates the changes in irradiances that might occur had the coarse mode been included in the calculations.

6.5.1 Method

In order to represent the coarse mode in the model calculations, it is necessary to include its effect in two ways:

1. The spectral optical properties of the full size distribution (coarse mode and accumulation mode) must be represented. Therefore the size distribution of the coarse and accumulation modes must be used to calculate the spectral optical properties.

2. The vertical MMR profile of the full size distribution must be represented. In Section 6.3 the vertical dust mass mixing ratio profile had been calculated by taking the extinction profile (based on nephelometer and PSAP measurements) and converting it to a MMR using an appropriate value of k_{ext}^{550} as shown in Equation 6.1. In order to represent the vertical profile of the whole size distribution, the extinction profile should firstly be increased in order to include coarser particles which are not passed by the Rosemount inlets (feeding the nephelometer and PSAP). This increase will be dependent on the amount of coarse mode present (or the amount of particles not measured by the nephelometer and PSAP), a factor which is difficult to determine from the measurements available.

   However, for b237 P8 the aircraft was very close to the Dakar AERONET station. The aircraft-measured AOD was 0.61, whereas the AERONET AOD was 0.64. These values are significantly close to justify not increasing the aircraft extinction profile. For b238 the AERONET measurements are too far away to be comparable, and therefore the extinction profile is not increased for this case either, as it would not be based on any real measurements.

   Secondly, a value of k_{ext}^{550} relevant to the whole size distribution should be used. In both cases of b237 and b238 the extinction profile has been converted to a MMR

profile using k_{ext}^{550} based on optical properties which have included the coarse mode. This means that through including the coarse mode, k_{ext}^{550} decreases, and therefore the MMR increases, representing a greater amount of mass in the vertical column when the coarse mode is included. Further details for each flight are given in Sections 6.5.2 and 6.5.3.

The test cases used are b237 P8 and b238 P4+P5+P6+P7+P8 (the same as in the surface albedo sensitivity tests). The optical properties, vertical profiles and modelled irradiances are dealt with for each flight in turn below.

6.5.2 Flight b237

Figure 6.15 shows the coarse mode size distributions for the runs performed in the upper (main) dust layer from b237, using a combination of the PCASP and CDP size distributions for each run. They are compared to the AERONET-derived size distribution since the dust profile observed during the landing-descent to Dakar during this flight was similar to that from the rest of the flight.

The aircraft-measured size distributions shown in Figure 6.15 have been used in a Mie scattering code, combined with the refractive indices shown in Figure 6.6(b) for b237 in order to calculate spectral optical properties when the coarse mode is included. Since these refractive indices are representative of the accumulation mode only, this may not be entirely accurate, but they are used in the absence of other data. The resulting optical properties are shown in Figure 6.16. It is clear that the addition of the coarse mode size distributions decreases ω_0, decreases k_{ext} and increases g. For Run 3, where there was more coarse mode, the changes are larger. These changes are consistent with those described in Chapter 4, as is the change in optical properties with altitude. For the purposes of the coarse mode sensitivity tests using ES96, the size distribution from b237 Run 2 is selected since it represents the dust at an altitude which contributed most to the optical depth (Figure 6.15). Values of the optical properties for the two cases tested are shown in Table 6.6. Note that there is a small (0.01) decrease in ω_0^{550}, but a larger ($0.5m^2g^{-1}$) decrease in k_{ext}^{550}. Changes in g are largest at wavelengths larger than $1\mu m$ where the solar intensity is lower, and are likely to have less impact on the irradiances.

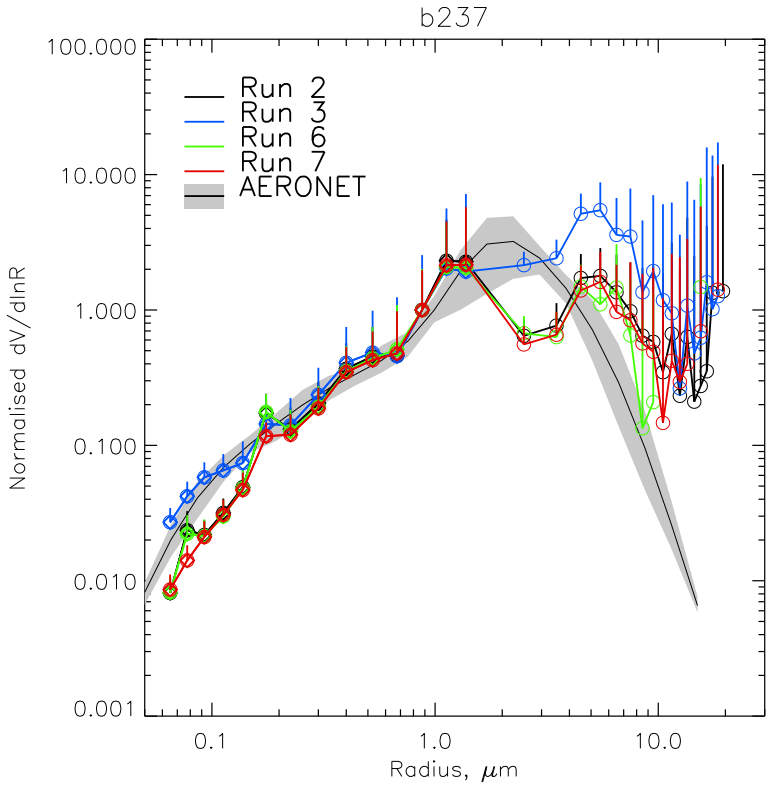

Figure 6.15: *Full normalised volume size distributions for runs in the upper dust layer in flight b237, from PCASP and CDP instruments. Error bars on aircraft measurements show one standard deviation of the variability over the run. The size distributions have been normalised by their value at $r = 1\mu m$ in order to allow a comparison with AERONET derived size distributions from the Dakar AERONET stations, shown by the black line (grey shading represents the maximum and minimum in the derived size distribution over the day). The dust profile observed during landing at Dakar was very similar to that observed during the rest of the flight.*

Size Distribution Used	ω_0^{550}	$k_{ext}^{550}\ /m^2g^{-1}$	g^{550}
b237 accumulation mode only	0.97	1.1	0.69
b237 Run 2 coarse mode	0.96	0.6	0.71

Table 6.6: *Aerosol optical properties at 550nm for the cases used in the coarse mode sensitivity tests for b237. The values of k_{ext}^{550} are used in the vertical MMR profile calculations.*

In order to calculate the vertical profiles of dust MMR Equation 6.1 has been used. To calculate the MMR profile for the accumulation mode, a k_{ext}^{550} value of $1.1m^2g^{-1}$ has been used (see Table 6.6), and is shown by the black line in Figure 6.17 (which is the same as the MMR profile shown in Figure 6.8(b), green line). To calculate the MMR profile for the full size distribution, a value of $0.6m^2g^{-1}$ has been used since this represents the mass

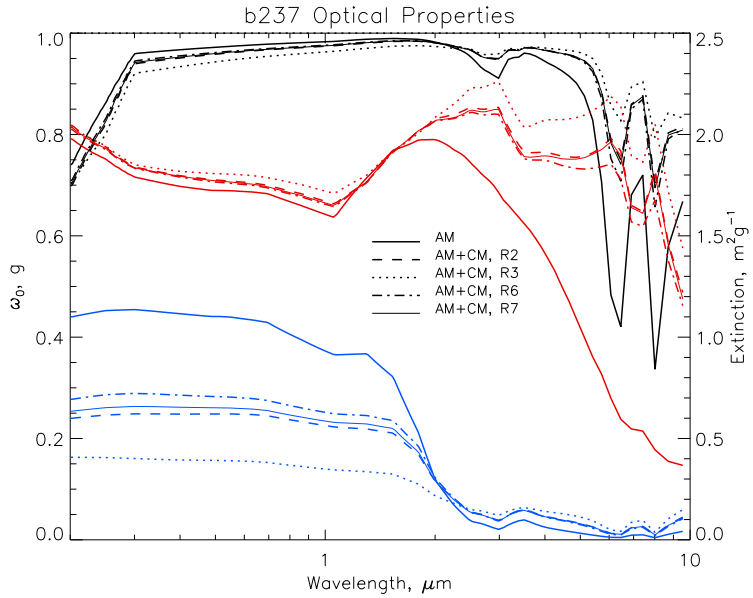

Figure 6.16: *Spectral optical properties for b237, calculated using a spectral refractive index representative of the flight average, and different size distributions: accumulation mode only size distribution ($r < 1.5\mu m$) representative of the b237 average, and coarse mode size distributions ($r > 30\mu m$) for Run 2 (dashed line), Run 3 (dotted line), Run 6 (dot-dashed line) and Run 7 (thin solid line). Black line indicates single scattering albedo, red line indicates asymmetry parameter, and blue line indicates mass specific extinction.*

specific extinction for the full size distribution. This results in a greater mass loading of dust, as is shown by the red line in Figure 6.17, while maintaining the same AOD.

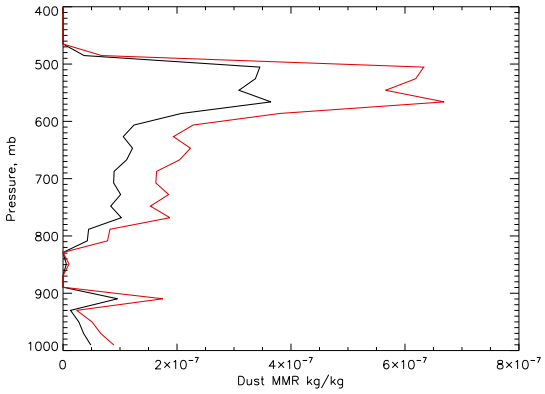

Figure 6.17: *Vertical profiles for dust mass mixing ratios used for the coarse mode sensitivity tests for b237. Black line indicates the profile used for the accumulation mode, red line indicates the profile used for the coarse mode.*

In order to test the sensitivity of the model results to the inclusion of the coarse mode, ES96 has been run for three cases:

1. 'No coarse mode' - model runs are identical to those described in Section 6.3, and contain no representation of the coarse mode in any way.

2. 'opt coarse mode' - model runs are as above, but the optical properties have been calculated using the size distribution for the coarse mode. The MMR profile is not adjusted and still represents the accumulation mode.

3. 'opt coarse mode, hi MMR' - model runs include spectral optical properties derived using the coarse mode size distribution. The MMR profile is calculated using k_{ext}^{550} representative of the coarse mode optical properties ($0.6m^{-2}g^{-1}$). Therefore the MMR profile is larger and represents the full size distribution.

This combination of tests allows the effects of the two changes to be observed individually - firstly the change from using no coarse mode to changing the optical properties to those that represent the coarse mode, and secondly the effect of additionally increasing the MMR dust vertical profile.

Figure 6.18 shows the modelled SWD and SWU irradiances at a solar zenith angle of 27° for each coarse mode test. It can be seen that the addition of the coarse mode optical properties (the change from the black line to the blue line) increases the SWD irradiances due to the lower k_{ext} , while the SWU irradiance decreases due to a combination of lower k_{ext} and ω_0 . The addition of a greater dust MMR profile (change from blue to red line) results in a change in the opposite direction - SWD irradiance now decreases due to more dust in the atmosphere, while SWU increases because there is more dust to reflect irradiance back upwards. The SWU at 400mb is now slightly lower than that for the no coarse mode case. Figure 6.18 also shows the vertical profile of the heating rates. For the 'opt coarse mode' case, the total heating decreases due to the lower k_{ext} , even though ω_0 is lower and potentially more absorption can occur. For the 'opt coarse mode, hi MMR' case, the heating rates are significantly larger than the 'no coarse mode' case due to the combination of more dust being present at the same time as ω_0 being lower.

Figure 6.19 shows how the modelled irradiances for each test compare to the measurements for each of the straight and level runs, and Table 6.7 shows the optical depth at 550nm for each case. The trends shown here reflect those shown in Figure 6.18. This

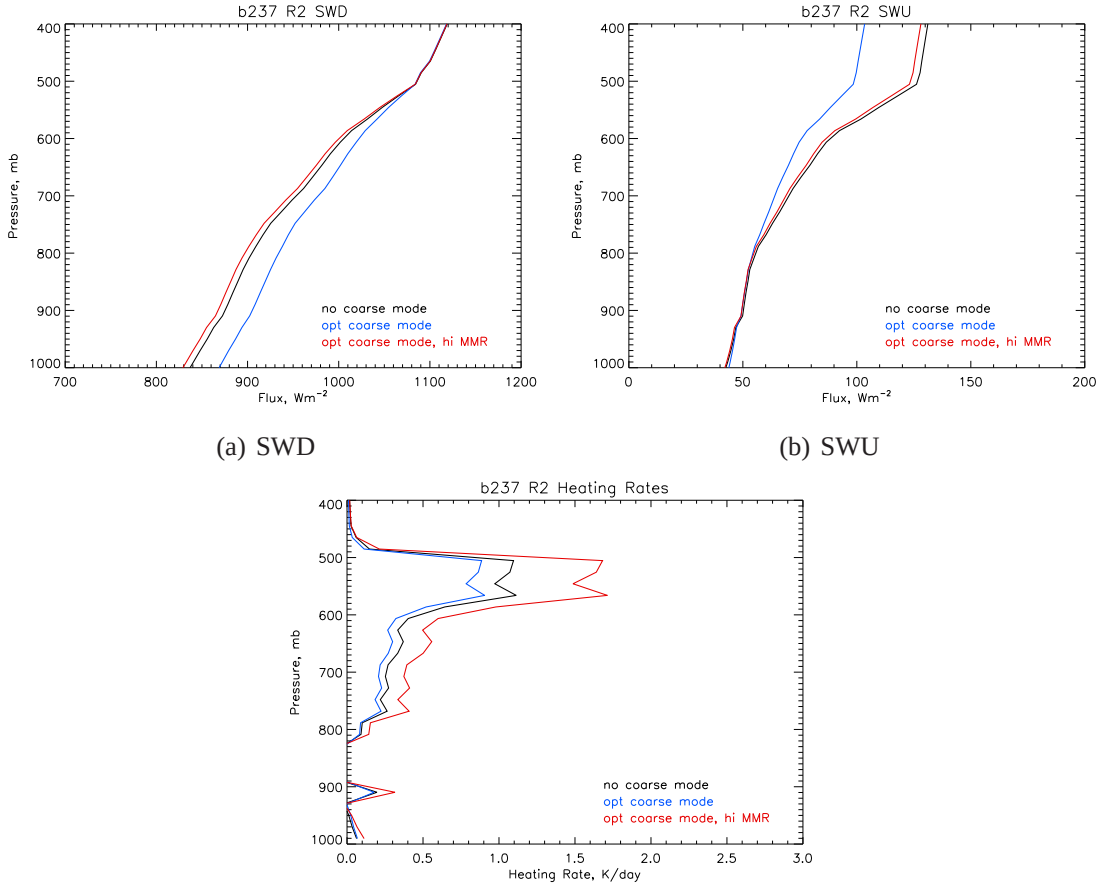

(a) SWD

(b) SWU

(c) Heating Rates

Figure 6.18: *(a), (b) SWD and SWU model irradiances for flight b237 as a function of pressure, for a solar zenith angle of* 27°*. Different colours indicate irradiance profiles for each different coarse mode test case, as indicated in the Figures. (c) Vertical Profiles of heating rates for each test case.*

means that the best agreement appears to occur for the 'opt coarse mode' test, since the SWD at the surface increases slightly and the SWU at higher altitudes decreases, pushing the model irradiances closer to those that were measured. However, Table 6.7 shows that τ^{550} for this case was around 50% too low in comparison to the AERONET value and to that measured by the aircraft nephelometer and PSAP. Therefore although the irradiances give the best agreement, the results are not physical since they assume optical properties relevant to a coarse mode size distribution, but do not use a vertical profile to represent a coarse mode. The results are still included, however, since they illustrate a step in the process of changing the model from including only accumulation mode to including coarse mode as well.

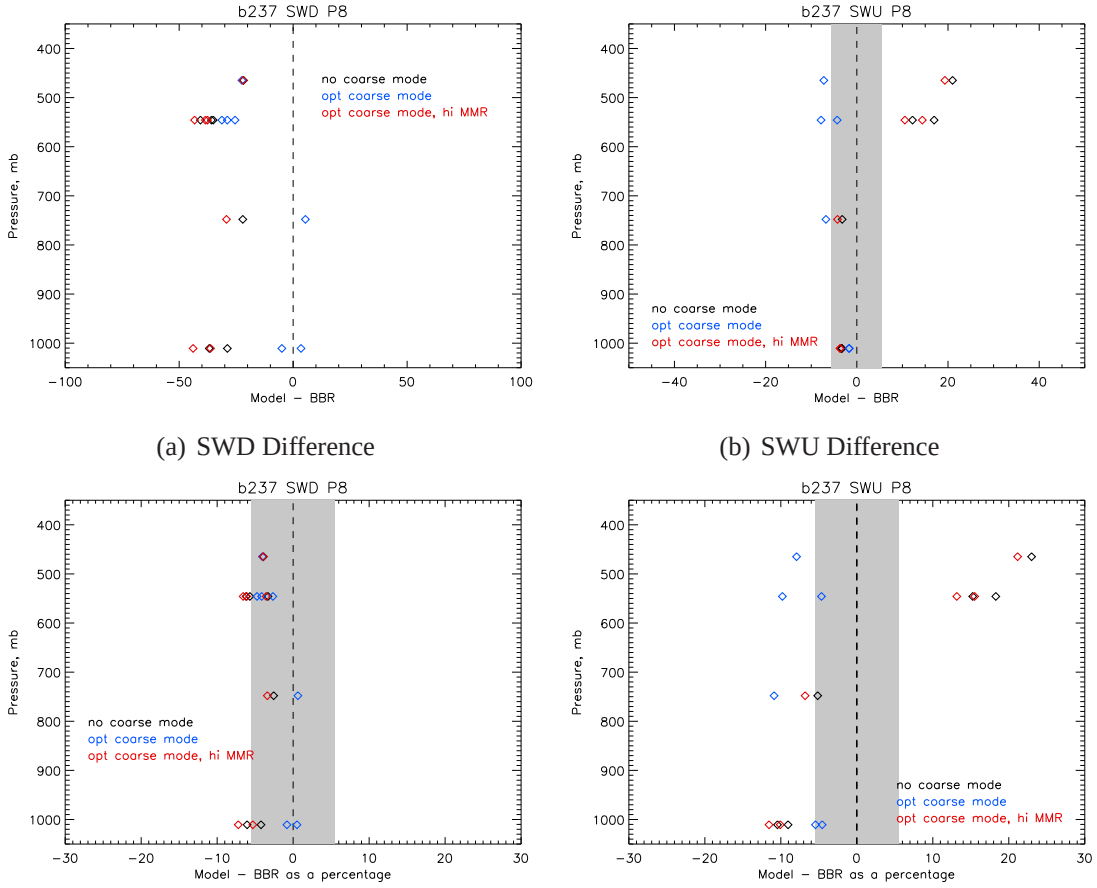

(a) SWD Difference

(b) SWU Difference

(c) SWD Percentage Difference

(d) SWU Percentage Difference

Figure 6.19: *Comparison of measured and modelled irradiances as a function of pressure for each coarse mode test case for b237. (a), (b) Difference between modelled and measured irradiance; (c), (d) Percentage difference between modelled and measured irradiance; left hand column: SWD irradiances; right hand column SWU irradiances.*

Coarse Mode Test	Aircraft τ^{550}	Interpolated τ^{550}	Model τ^{550}	AERONET τ^{550}
no coarse mode	0.61	0.62	0.64	0.64
opt coarse mode	0.61	0.62	0.36	0.64
opt coarse mode, hi MMR	0.61	0.62	0.67	0.64

Table 6.7: *Aerosol optical depths at 550nm (τ^{550}) for each coarse mode sensitivity test for b237. Aircraft τ^{550} results from the high resolution nephelometer/PSAP calcuations, Interpolated τ^{550} is the same data but interpolated onto the 50 level model resolution, model τ^{550} is calculated from direct beam irradiances from the model. AERONET τ^{550} is interpolated linearly between 440nm and 670nm and averaged over times relevant to profile 8 in b237.*

Once the ‘opt coarse mode’ has been excluded on the basis of the inaccurate τ^{550}, the remaining reults show little difference between the ‘no coarse mode’ and ‘opt coarse mode, hi MMR’ cases. The ‘opt coarse mode, hi MMR’ case shows slightly better agree-

ment in SWU with the pyranometer measurements above the dust, by around $5Wm^{-2}$ or a few percent. This is not enough, however, to explain the differences of around $10 - 20Wm^{-2}$ between the modelled and measured irradiances at high altitudes. Therefore it must be concluded, that for flight b237, the inclusion of the coarse mode in an appropriate manner (i.e. for the 'opt coarse mode, hi MMR' case) makes little difference to the modelled irradiances, assuming that the refractive index used is correct, and that the assumption of not adjusting the AOD is correct.

6.5.3 Flight b238

Similar tests to those carried out on b237 have been carried out on flight b238 to test the sensitivity of the irradiances to the inclusion of the coarse mode. The size distribution used for the coarse mode cases is that from R4.1, and shown in Figure 4.15(b) - the same as was used for the coarse mode sensitivity tests in Chapter 4. The accumulation mode size distribution is the same as that used in Section 6.3 and is the average for all the b238 runs within the dust layers. The refractive index used is that shown in Figure 6.2(b) for b238. The resulting optical properties are shown in Figure 6.20, and are in keeping with the changes shown in Chapter 4 due to the addition of the coarse mode. As shown in Figure 3.2(b), the coarse mode decreased with altitude during b238, with its contribution being greatest during R4.1. Therefore the change in optical properties shown in 6.20 are the maximum that would be expected, since there was less coarse mode at other altitudes.

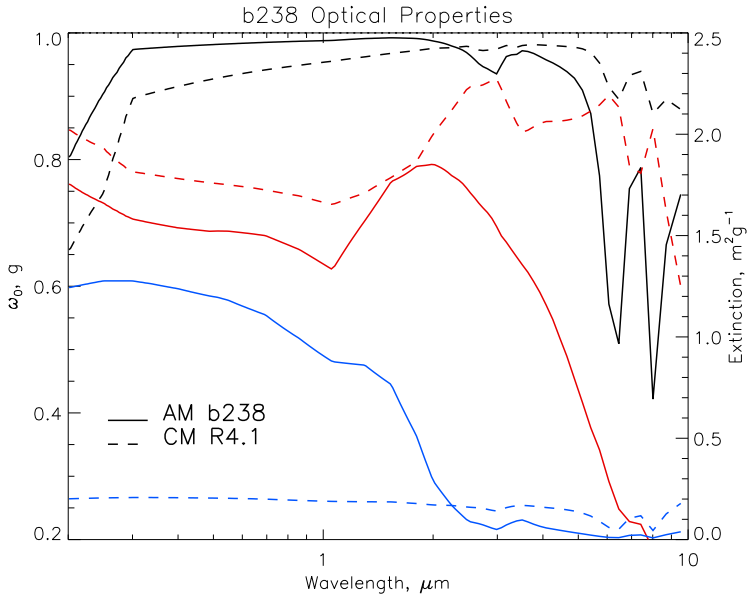

Figure 6.20: *Spectral optical properties for b238, calculated using a spectral refractive index representative of the flight average, and different size distributions: accumulation mode (AM, $r > 1.5\mu m$) only size distribution representative of the b238 average (solid line), and coarse mode size distribution (CM, $r > 30\mu m$) for Run 4.1 (dashed line)*

Figure 6.20 and Table 6.8 show the decrease in ω_0 and k_{ext} and increase in g that occur due to the addition of the coarse mode. However, note that these changes are far larger than those that occurred for b237, due to the greater coarse mode size distribution during b238 R4.1. For b238 the coarse mode results in ω_0^{550} decreasing by 0.05, k_{ext}^{550} decreasing

by $1.0m^2g^{-1}$, and g^{550} increasing by 0.07.

Size Distribution Used	ω_0^{550}	k_{ext}^{550}/m^2g^{-1}	g^{550}
b238 accumulation mode only	0.98	1.2	0.69
b238 Run 4.1 coarse mode	0.93	0.2	0.76

Table 6.8: *Aerosol optical properties at 550nm for the cases used in the coarse mode sensitivity tests for b238. The values of k_{ext}^{550} shown are used in the vertical MMR profile calculations.*

Using the values of k_{ext}^{550} shown in Table 6.8 the dust MMR profiles have been calculated, and are shown in Figure 6.21. As with flight b237, the lower k_{ext}^{550} for the coarse mode results in a greater MMR profile, though the change in b238 is more marked than in b237 due to the larger drop in k_{ext}^{550} when the larger coarse mode is included. It should be noted that when the coarse mode changes strongly with altitude, using one value of k_{ext}^{550} for the whole profile is a simplification - ideally k_{ext}^{550} should increase with altitude as the coarse mode decreases, resulting in a smaller amplification of the dust MMR with altitude. However, one value of k_{ext}^{550} is used here for simplicity.

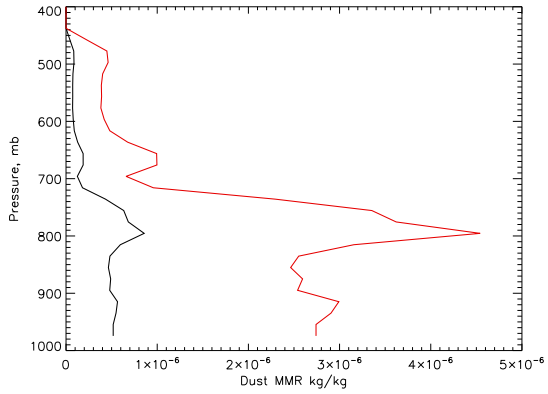

Figure 6.21: *Vertical profiles for dust mass mixing ratios used for the coarse mode sensitivity tests for b238. Black line indicates the profile used for the accumulation mode, red line indicates the profile used for the coarse mode.*

The vertical profiles of dust MMR representing the accumulation mode and the coarse mode, and the optical properties representing the accumulation mode and the coarse mode, were input into ES96 (and therefore using the same combinations as for b237). The results of the vertical irradiance profiles and heating rates are shown in Figure 6.22. As was seen for flight b237, the inclusion of the coarse mode optical properties (change

from black to blue line) results in a larger SWD irradiance at the surface, since k_{ext} is lower. However, due to the large change in optical properties for b238, the SWD decrease at the surface is now on the order of $100Wm^{-2}$ as compared to the $30Wm^{-2}$ increase for b237. This has a larger impact on the SWU irradiance near the surface, combined with the fact that α_s is larger over the desert, and results in an increase of around $50Wm^{-2}$ in the SWU near the surface due to the change in optical properties. At higher altitudes the SWU decreases compared to the case with no coarse mode, since ω_0 has now decreased and the dust is less reflective.

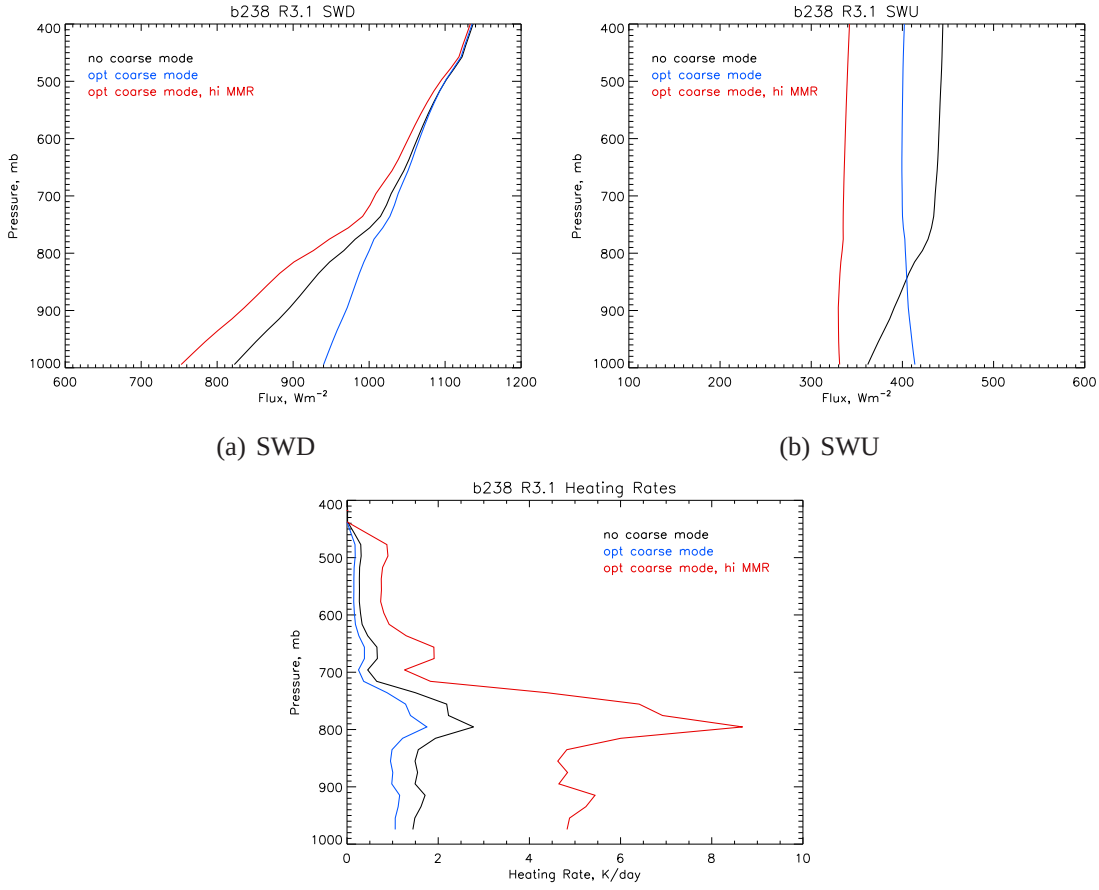

(a) SWD

(b) SWU

(c) Heating Rates

Figure 6.22: *(a), (b) SWD and SWU model irradiances for flight b238 as a function of pressure, for a solar zenith angle of $25°$. Different colours indicate irradiance profiles for each different coarse mode test case, as indicated in the Figures. (c) Vertical Profiles of heating rates for each test case.*

When the MMR profile is also increased (changes from blue to red line), changes in SWD irradiance are similar to those observed for b237: the SWD at the surface decreases.

However, for b238 the decrease is much more significant than that seen in b237 due to the greater increase in the dust MMR profile in b238. As a result, the SWU over the entire column decreases for the 'opt coarse mode, hi MMR' case, by around $60 - 80 Wm^{-2}$ due to the dust mass load being greater at the same time as ω_0 being significantly lower. Therefore the changes in irradiances for b238 due to the addition of the coarse mode are much more significant for b238 than for b237, because the coarse mode is larger and because the flight took place over the desert where the surface albedo is higher.

The changes in heating rates in Figure 6.22 also reflect the changes in optical properties and MMR profiles - when the optical properties are changed and MMR kept constant (black to blue lines), the heating rates decrease, because although ω_0 has dropped, so had k_{ext} . When the MMR inceases, the dust absorbs a lot more radiation and the heating rates therefore increase.

Figure 6.23 shows how well each test case agrees with the pyranometer measurements. Again, the trends reflect the profiles shown in Figure 6.22. At low altitudes, both coarse mode test cases force the model irradiances away from agreement with the pyranometer data, though for the 'opt coarse mode, hi MMR' case the data are still within the uncertainty errors. For the SWU irradiances the model is certainly sensitive to the coarse mode additions, and it appears that the 'opt coarse mode, hi MMR' case results in an improvement at most altitudes. Though the 'opt coarse mode' case shows better agreement with the pyranometer data at high altitudes the agreement is far worse than the other cases at the lowest altitudes, and the resulting optical depth (Table 6.9) is far too low.

Coarse Mode Test	Aircraft τ^{550}	Interpolated τ^{550}	Model τ^{550}
no coarse mode	1.75	1.66	2.09
opt coarse mode	1.75	1.66	0.36
opt coarse mode, hi MMR	1.75	1.66	1.91

Table 6.9: *Aerosol optical depths at 550nm (τ^{550}) for each coarse mode sensitivity test for b238. Aircraft τ^{550} results from the high resolution nephelometer/PSAP calcuations, Interpolated τ^{550} is the same data but interpolated onto the 50 level model resolution, model τ^{550} is calculated from direct beam irradiances from the model.*

Therefore it can be concluded from theses tests that the inclusion of the coarse mode for b238 can have a large impact on the resulting irradiances and how much they agree

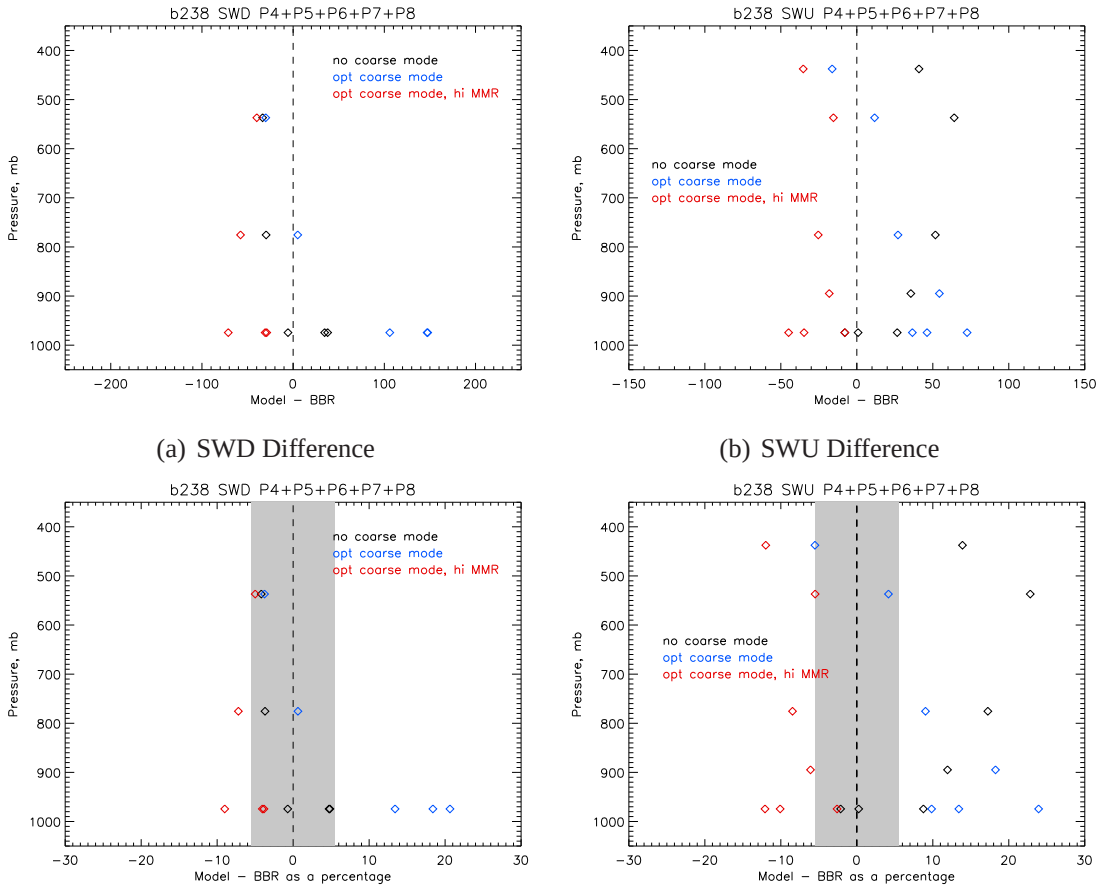

(a) SWD Difference

(b) SWU Difference

(c) SWD Percentage Difference

(d) SWU Percentage Difference

Figure 6.23: *Comparison of measured and modelled irradiances as a function of pressure for each coarse mode test case for b238. (a), (b) Difference between modelled and measured irradiance; (c), (d) Percentage difference between modelled and measured irradiance; left hand column: SWD irradiances; right hand column SWU irradiances.*

with the pyranometer measurements. This conclusion is different to that for b237 due to the greater amount of coarse mode present in b238 and due to the different surface albedo. However, the case for b238 is more complicated due to the large changes of coarse mode with altitude, and the changing optical properties with altitude, which are not represented here. It is likely that if these were included, the agreement between pyranometers and model irradiances might be improved further.

6.6 Sensitivity to Changes in Refractive Index

Refractive index data (both real and imaginary parts) are available for the filter samples for b238 R4.1 courtesy of P. Formenti (LISA, Paris). These have been calculated using a combination of iron oxide measurements and elemental concentrations from PIXE analysis, using a simplified version of the technique described by Lafon *et al.* (2006). The method adopted assumes that all iron oxide is internally mixed in clays, and that there is an external mixture of clays, quartz and calcium carbonate. In the case described here, all the iron oxide has been assumed to be hematite, and all the clay has been assumed to be illite. Other combinations (including goethite and kaolonite) are also possible, and would result in different refractive indices. The hematite/illite combination results in the most absorbing refractive indices (personal communication, P. Formenti).

The availability of this data provides a good opportunity to test the sensitivity of the irradiance results to using a different refractive index - in particular one which stems from the chemical results.

6.6.1 Method

Figure 6.24 shows the refractive indices as obtained from the filter samples (courtesy of P. Formenti), which cover the spectral range of $400 - 800nm$ (green diamonds). In order to use the refractive index data in the Mie scattering code of ES96, it is necessary to have information on the refractive indices across the spectral range shown. Thus some extending of the filters' refractive index data is necessary.

For the real part this is straight forward since the filters data (green diamonds) are very similar to the WCP (1983) data (black line) in Figure 6.24(a). Therefore outside the $400 - 800nm$ range the WCP (1983) values have simply been adopted. The resulting real refractive index used is shown by the blue diamonds.

For the imaginary part extending the refractive index is not so straightforward. Figure 6.24(b) shows that the filters imaginary refractive indices are significantly different from the WCP (1983) data - both in value and spectral variation. Therefore the following method is used in order to avoid unphysical jumps in n_i :

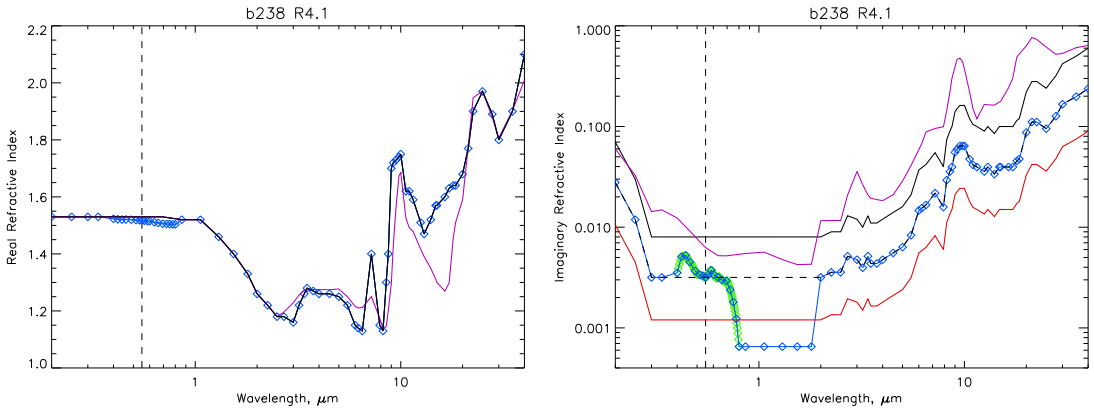

(a) Real Part (b) Imaginary Part

Figure 6.24: *Refractive indices obtained from filter sample calculations courtesy of P. Formenti (green diamonds). Black line represents WCP (1983) refractive index, purple line represents refractive index from Otto* et al. *(2007) which is an average of the values available in the literature. Red line shows the imaginary refractive index previously used for b238, as in Figure 6.6(b). Black dashed line shows the WCP (1983) imaginary refractive index scaled down to equal the value from the filters data at 550nm. Blue line and blue diamonds show the refractive index used in the ES96 calculations.*

1. Over the spectral range $400 - 800nm$ the filters n_i data are used but on a coarser resolution.

2. At wavelengths below $400nm$ and above $2\mu m$ the WCP (1983) data are used, but are scaled down in order to agree with the filters n_i value at 550nm.

3. Over the spectral range $800nm - 2\mu m$ n_i is kept equal to the filters value at $800nm$ in order to produce a spectrally constant n_i over this range. This prevents a sudden increase in n_i which may not be physical, and also reflects the sharp increase in n_i at around $2\mu m$ as shown by the Otto *et al.* (2007) data.

The resulting spectral imaginary refractive index which has been used in the Mie scattering code is shown in blue in Figure 6.24(b). The filters data show a higher n_i than that derived using the Mie code calculations in Chapter 4 by a factor of 0.68 (a change from 0.0019i to 0.0032 at 550nm), as well as significantly more absorption at $400-600nm$ than at $800nm$.

In order to calculate optical properties using the filters refractive index data, the same size distributions as described in section 6.5.3 have been used, in order to have one case representing the accumulation mode only, and another representing the full size distribu-

tion, including the coarse mode. These have been combined with the refractive indices shown in Figure 6.24 for the filter sample data (blue diamonds). These optical properties are compared to those calculated using the refractive index derived previously using Mie code (black line in Figure 6.24(a) and red line in Figure 6.24(b)). The resulting optical properties are shown in Figure 6.25.

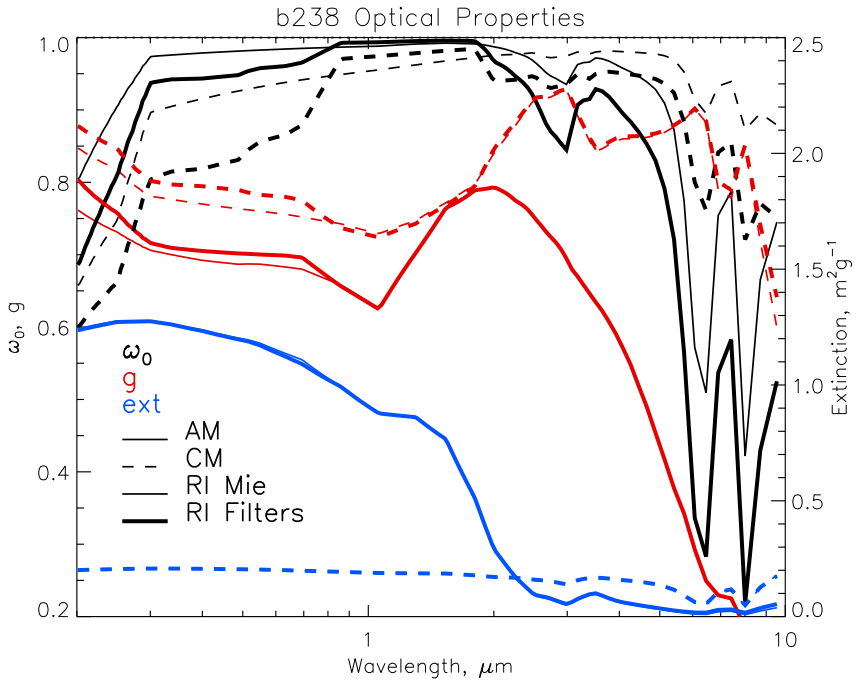

Figure 6.25: *Spectral optical properties calculated using refractive indices derived from Mie code (thin lines) and calculated from filters data assuming a hematite-illite combination (bold lines). Solid lines represent cases for the accumulation mode (AM) only, dashed lines for the full size distribution including coarse mode (CM). Black lines show ω_0 , red lines show g and blue lines show k_{ext} .*

Figure 6.25 clearly shows that the higher n_i from the filter samples results in much lower ω_0 values. Table 6.10 shows that the filters n_i can reduce ω_0^{550} to 0.96, and this can reduce further to 0.86 if the coarse mode size distribution is included. Figure 6.25 also shows that g and k_{ext} are much more sensitive to the addition of the coarse mode than to the change in n_i , with the values of k_{ext}^{550} remaining at $0.2m^2g^{-1}$ when the coarse mode is present for both n_i data sets.

In order to test the effects of the change in refractive indices on the irradiance, four test cases have been used, and are as follows:

1. MIE AM - Optical properties for the accumulation mode only, derived using Mie

Refractive Index	Size distribution	ω_0^{550}	k_{ext}^{550}/m^2g^{-1}	g^{550}
Mie	AM	0.98	1.18	0.69
Mie	CM	0.93	0.20	0.76
Filters	AM	0.96	1.17	0.70
Filters	CM	0.86	0.20	0.78

Table 6.10: *Aerosol optical properties at 550nm for the cases used in the refractive index sensitivity tests for b238. The values of k_{ext}^{550} shown are used in the vertical MMR profile calculations.*

code, have been used (thin solid lines in Figure 6.25). A dust MMR profile calculated using $k_{ext} = 1.18m^2g^{-1}$ (appropriate for the accumulation mode) has been used, resulting in the profile shown in Figure 6.21 by the black line.

2. MIE CM - Optical properties for the coarse mode, derived using Mie code, have been used (bold solid lines in Figure 6.25). A dust MMR profile calculated using $k_{ext} = 0.2m^2g^{-1}$ (appropriate for the coarse mode) has been used, resulting in the profile shown in Figure 6.21 by the red line.

3. FILTERS AM - Optical properties for the accumulation mode only, derived using filters refractive index data, have been used (thin dashed lines in Figure 6.25). A dust MMR profile calculated using $k_{ext} = 1.18m^2g^{-1}$ (appropriate for the accumulation mode) has been used, resulting in the profile shown in Figure 6.21 by the black line.

4. FILTERS CM - Optical properties for the coarse mode, derived using filters refractive index data, have been used (bold dashed lines in Figure 6.25). A dust MMR profile calculated using $k_{ext} = 0.2m^2g^{-1}$ (appropriate for the coarse mode) has been used, resulting in the profile shown in Figure 6.21 by the red line.

Choosing only these combinations of optical properties and MMR profiles avoids using optical properties which are inconsistent with the MMR profile used. Using these four combinations of refractive index and coarse/accumulation modes, irradiances have been computed using ES96.

6.6.2 Results

Figure 6.26 shows the changes in SWD and SWU irradiances and heating rates that occur as a result of using the filters refractive indices (for accumulation mode and coarse mode) in comparison to those as derived by Mie code. The use of the filters refractive indices mean that the dust is more absorbing, and therefore the SWD irradiances are reduced at the surface for the filters data. The decrease in SWD due to the presence of the coarse mode is larger when the filters refractive index is used than when the Mie-derived refractive indices are used, suggesting that if the n_i is lower to start with, the effect of the addition of the coarse mode is greater.

For SWU, the use of the filters refractive indices can reverse the gradient of SWU with altitude. This is because the SWU at the surface is lower due to the reduction in SWD at the surface. Above the dust, the lower ω_0 for the filters n_i data means that less irradiance is reflected back upwards, so the cases with lower ω_0 show minimal increase in SWU above the dust layer (in contrast to the AM cases, where the higher ω_0 means that SWU increases above the dust layer). The change in SWU at 400mb due to using the filters refractive indices for the AM cases is $-38Wm^{-2}$ and $-55Wm^{-2}$ for the CM cases. Therefore the usage of the refractive index calculated from the filter samples is capable of significantly changing the irradiances at both the surface and the TOA, and even more so if a large coarse mode is present. Additionally Figure 6.26 shows the changes in heating rates. Not surprisingly, for the more absorbing filters cases, the heating rates are larger, with the peak heating rate increasing by $2.5Kday^{-1}$ and $4.0Kday^{-1}$ for the AM and CM cases respectively.

Figure 6.27 shows how each test case compares to the pyranometer data irradiances. For the SWD, the FILTERS CM case results in too great a reduction at the surface, whereas the FILTERS AM case is still within the pyranometer uncertainty. For the SWU irradiances the FILTERS CM case still underestimates the irradiance, whereas the FILTERS AM case overestimates the amount of SWU, but not as badly as the MIE AM case. Overall it appears that the best agreement lies somewhere between the MIE CM and FILTERS AM cases.

It is interesting that for the Mie-derived refractive indices the coarse mode case pro-

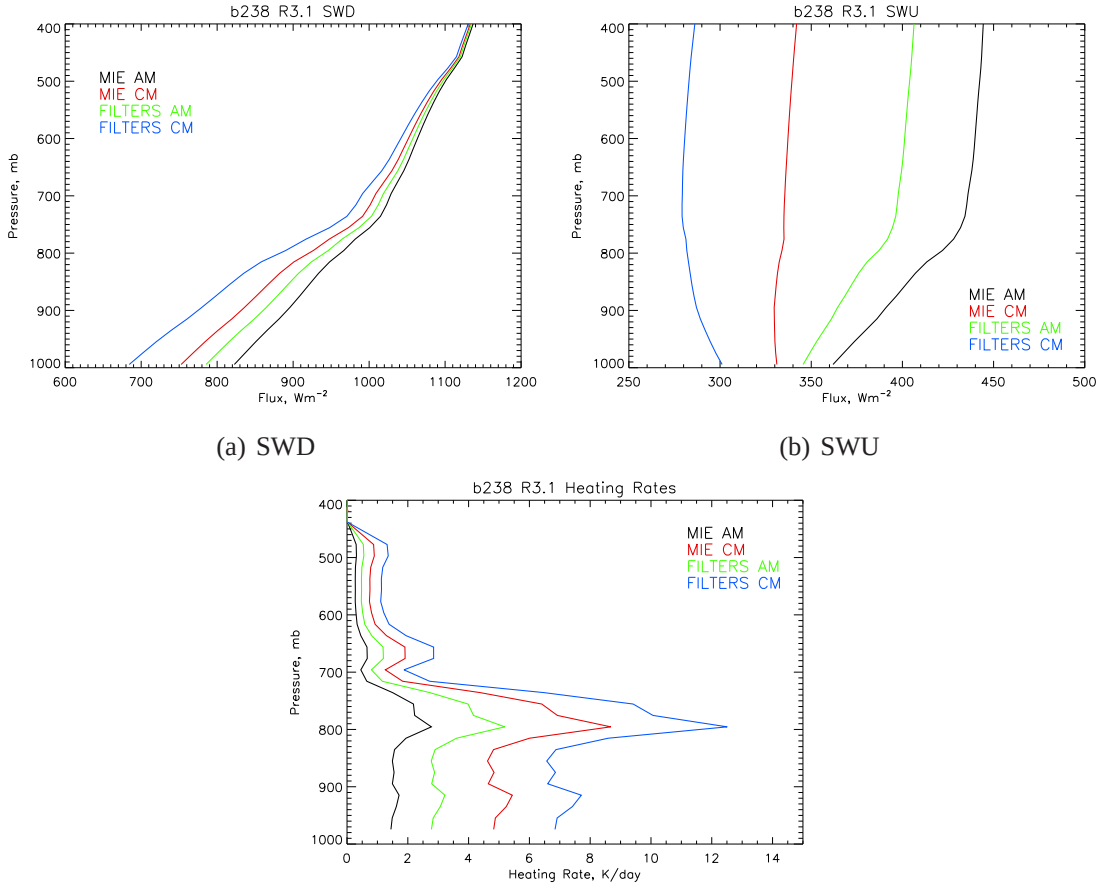

(a) SWD

(b) SWU

(c) Heating Rates

Figure 6.26: *(a), (b) SWD and SWU model irradiances for flight b238 as a function of pressure, for a solar zenith angle of* $25°$*. Different colours indicate irradiance profiles for each test case, as indicated in the Figures. (c) Vertical Profiles of heating rates for each test case.*

vides the best agreement with the pyranometers, while for the filters refractive indices the accumulation mode provides the best agreement. There are many uncertainties in the process of calculating the irradiances from the model, among which is the partitioning of accumulation mode and coarse mode. It is clear that the filter samples do measure at least some of the coarse mode from the SEM size distributions shown in Chapter 4. However, they may not measure the full size range with full efficiency. Additionally the passing efficiency of the Rosemount inlets is not well defined, and difficult to compare to that of the filters inlets. Therefore there are many uncertainties in assigning the size distribution with which it is appropriate to calculate the optical properties with, and secondly in using an appropriate MMR profile.

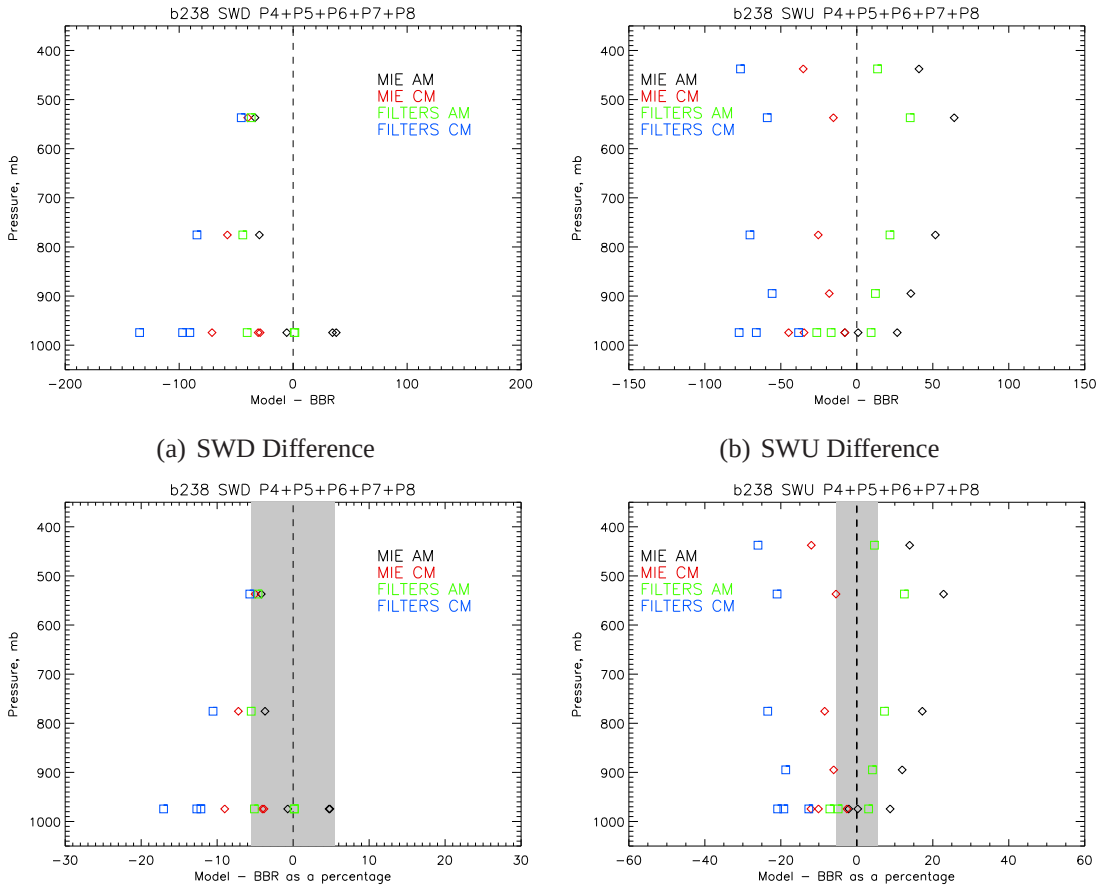

(a) SWD Difference

(b) SWU Difference

(c) SWD Percentage Difference

(d) SWU Percentage Difference

Figure 6.27: *Comparison of measured and modelled irradiances as a function of pressure for each test case for b238. (a), (b) Difference between modelled and measured irradiance; (c), (d) Percentage difference between modelled and measured irradiance; left hand column: SWD irradiances; right hand column SWU irradiances.*

For the CM cases shown here the MMR is calculated with a k_{ext}^{550} value based on a run at 1km altitude, but left constant with altitude in the profile. Since the coarse mode in b238 decreased with altitude, a more realistic system would be for the k_{ext}^{550} used in the MMR calculations to increase with height. This may change the resulting irradiances slightly, and provide more realistic results.

Additionally the assumption that all the iron oxide is hematite, and all the clay is illite results in the most absorbing n_i values. Other combinations, including goethite and kaolonite may result in smaller values of n_i and therefore give irradiance profiles part way between the MIE CM and FILTERS AM cases, resulting in better agreement with the pyranometers.

It is also entirely possible that the refractive index changes with particle size. If the filters inlets are not sampling with 100% efficiency of all sizes, and there is a significant change in refractive index with particle size, then the filters n_i data may be biased, and result in discrepancies with the pyranometer measurements.

In conclusion, the modelled irradiances are extremely sensitive to the change in refractive index from that derived from Mie code to those from the filter samples. These changes are even more marked when a large coarse mode is present. Therefore significant uncertainties in the ARE values shown in Section 6.2 exist.

6.7 Conclusion

6.7.1 Summary

1. The observed variations in the accumulation mode optical properties during DODO can have a large impact on the ARE, and can result in the ARE_{TOA} being either positive or negative. This reflects the changes in n_i during DODO, which determine the amount of absorption that occurs. Over the desert the changes in the optical properties result in ARE_{TOA} differences of up to $32 Wm^{-2}$, and up to $10 Wm^{-2}$ over the ocean. The changes in optical properties from least to most absorbing also result in increases in heating rates by up to 5 times over the ocean and desert for elevated dust layers.

2. The modelled irradiances agree with the measured irradiances within the measurement uncertainty for SWD. SWU irradiances are in agreement at the surface, but not above the dust. Therefore the ARE model calculations at the surface are reliable, whereas the ARE_{TOA} values may be more positive than those calculated, if the pyranometer measurements are taken to be accurate. The discrepancies in the SWU may be due to the dust in the model being too reflective, or due to potential problems with the lower pyranometer.

   Problems with the reliability of the lower pyranometer measurements are possible. This could result from the dome becoming dirty when flying through dust, but this is likely to decrease diffuse upwelling irradiances by only up to $1 Wm^{-2}$ (Saunders and Barnes, 1991). Since the lower pyranometers were not assessed for accuracy in the same way that the upper ones were, their reliability may not be equal to that of the upper ones. The agreement of model and pyranometers for the upwelling irradiance at low altitudes cannot be taken to indicate good agreement, since the surface albedo values have been fixed based on these measurements. It would be possible to compare SWU measurements from the model to satellite irradiances in the future, which would help give a better idea of whether there is a problem with the model SWU or with the lower pyranometer measurements. Additionally, tests involving moving the lower pyranometer to one of the upper mounting points for a

side-by-side comparison with the upper pyranometer would be useful, if conducted in the future by FAAM.

3. The model irradiances are sensitive to the surface albedo used, but changes in α_s are not sufficient to explain the discrepancies between the model and measurements. Therefore the discrepancy is likely to be associated with the way the dust is modelled.

4. The model irradiances are sensitive to the inclusion of coarse mode particles. For the two cases tested (b237 and b238) the sensitivity is different due to the different amounts of coarse mode present in each case. Where more coarse mode is present (b238) the changes in the modelled irradiances are larger and the resulting discrepancy in SWU between the model and measurements is decreased. For b237 when less coarse mode is present, the addition of the coarse mode does not resolve these differences.

5. The modelled irradiances are very sensitive to the changes in the refractive index as suggested by some of the filters data. The larger absorption (higher n_i) results in very different irradiances, particularly when the coarse mode is included. It is not clear that using the refractive index data from the filters samples results in better agreement between the model and measurements. This may be due to the many uncertainties associated with the techniques and methods employed here (see below).

6.7.2 Discussion

Due to instrument uncertainties and other problems, the nature of the work in this Chapter has entailed many assumptions which result in limitations of the findings. These are outlined below.

1. Assigning the fraction of the size distribution measured by each instrument on the FAAM BAe-146 poses a major challenge to this work. Here it has been assumed that the Rosemount inlets, feeding the nephelometer and the PSAP, effectively transport 100% of particles sized below $r = 1.5\mu m$, the same as the sizes

of particles measured by the PCASP. The filters samples have been assumed to measure the full size distribution efficiently. The pyranometers measure irradiance affected by whatever the true size distribution in the atmosphere is. Deciding how to account for particles which are not measured by the nephelometer and PSAP for both the calculation of vertical profiles and optical properties poses challenges since the inlet cut-offs are uncertain. Assigning the composition as measured by the filter samples (representing a bulk measurement) to size distributions which may measure different size ranges of particles also poses a challenge and entails uncertainties.

2. For simplicity the work presented here assumes that optical properties and the amount of coarse mode present are constant with altitude. However, Chapter 4 has shown that this is not the case in many of the DODO2 flights, where optical properties and size distribution do change with altitude. Where there is a significant coarse mode present, the inclusion of this change with altitude may result in different modelled irradiances.

3. For the Mie code work the refractive index has been derived at $550nm$ and for the filters data it is available at wavelengths from $400 - 800nm$. Extending this information spectrally is therefore based on assumptions rather than measurements, and entails uncertainty.

4. The work presented here assumes the dust particles are spherical, when in reality the filter samples (and other studies, (e.g. Chou *et al.*, 2008; Otto *et al.*, 2009)) have shown that they are not. However, since hemispherical flux density (irradiance) is modelled here, the impact of non-sphericity is likely to be small (Mishchenko *et al.*, 1997; Otto *et al.*, 2009) - certainly much smaller than the uncertainties already described in the model, and smaller than the pyranometer measurement uncertainties.

The aim of this chapter was to test the importance of the observed variations of the accumulation mode optical properties during DODO for the aerosol radiative effect. It has been shown that the variation in the optical properties observed during DODO was of importance both for the magnitude of the ARE over ocean and for the magnitude and sign over land. The amount of agreement between the model and pyranometer SWD

irradiances supports these results at the surface, whereas the discrepancy between them for the SWU above the dust means that the ARE_{TOA} values may be up to $100 W m^{-2}$ more positive than those calculated from the model. This would shift the ARE_{TOA} from being mostly cooling to mostly warming - a significant change. The sensitivity tests using the filters refractive index data suggest that the true imaginary refractive index may be higher than that derived from Mie code in Chapter 4, a discrepancy which may result from lack of adequate knowledge of exactly what size distribution is measured by the nephelometer and PSAP.

It is clear that the effect of different imaginary refractive indices and coarse mode size distributions have an important effect on the modelled irradiances, and this may be improved in the future by better constrained coarse mode size distribution measurements on the BAe-146 and experiments designed to measure inlet passing efficiencies. However, it is also clear that the variation in the optical properties observed during the course of DODO results in important changes to the ARE at the surface - changes which can be confirmed by pyranometer measurements.

Chapter 7

Conclusions

7.1 Overview

This thesis has described a detailed investigation into the optical properties of dust measured during the two DODO aircraft campaigns, and the importance of these optical properties to the radiative effect of the dust. This Chapter provides a summary of the key findings of the thesis, a description of the limitations of the work, suggestions for future aircraft campaigns, and discussion of the wider implications of the results.

7.2 Key Findings

7.2.1 Seasonal Differences in Dust Properties

Chapter 3 examined differences in typical vertical profiles between the dry and wet season, and between land (desert) and ocean areas. It was clear that during the dry season the weaker convection and uplift resulted in dust layers lying close to the surface, both over land and ocean. During the wet season the dust was uplifted to greater altitudes over the desert, which allowed it to be transported westwards over the ocean in the Saharan Air Layer, elevated over the marine boundary layer, reaching altitudes of up to $6km$, although dust was also found in the marine boundary layer. Though these profiles are consistent with what would be expected from the seasonal dynamics (e.g. Carlson and Prospero, 1972), they are the first aircraft measurements to report vertical profiles of dust measured using the same aircraft and instrumentation during both seasons, and from both desert and ocean surface types, and are therefore important in supporting theory with a consistent set of measurements.

The potential dust sources for the dust encountered during DODO have been investigated using the NAME model. The dust sources were found to be in the northwest Sahara for DODO1, whereas DODO2 sources were much more variable (ranging from the northwest Sahara to the central Sahara). This was found to be consistent with the meteorology driving the dust uplift and transport in each season: well-defined northeasterly winds in the dry season (the Harmattan), and more localised convection (often connected to mesoscale convective systems) with transport at greater range of altitudes in the wet

season. Therefore it is likely that the microphysical and chemical properties of DODO2 dust will be much more varied due to the greater variation in dust source (likely to affect chemial composition) and transport distances and altitudes (likely to affect size distribution).

Chemical composition data from filter samples has been analysed, incorporating the findings of Formenti *et al.* (2008) relevant to DODO. The elemental ratio data (available for most of the DODO flights) suggested differences in composition between the two seasons based on the amounts of calcium, which could be connected to the dust having different source regions between the two campaigns. There was no difference in the Fe/Al ratios between the DODO campaigns, though this is not necessarily an indicator of absorption. Contrastingly, iron oxide concentrations for four samples were larger for flight b242 where the dust had more Sahelian sources than the other b238 samples examined. Limited amounts of data regarding the mineralogy from SEM and TEM analysis revealed composition differences in the dust between the different campaigns, flights, dust layers at different altitudes and between the accumulation mode and coarse mode for flight b237. This suggests that it may not be appropriate to model the dust using one refractive index for all dust cases and particle sizes.

7.2.2 Optical and Microphysical Properties of DODO Dust

The accumulation mode size distributions measured by the PCASP during the DODO campaigns ($0.01 < r < 1.5\mu m$) have been used to examine how size distributions changed with season and with transport. More variability was found in the DODO2 size distributions, which was found to be due to the greater range in transport altitudes during the wet season in comparison to the dry season. This resulted in a greater fraction of the larger accumulation mode particles to reside in higher altitude dust layers during DODO2. Differences in the accumulation mode size distribution were found between measurements made over land and ocean: fewer particles at $r > 0.2\mu m$ were found over the ocean, due to loss from deposition, which was most marked at greater radii.

The optical properties of dust measured during DODO have been examined. For the accumulation mode only, ω_0^{550} was measured and found to vary between 0.93 to 0.99.

Using measured size distributions, and assuming that $n_r^{550} = 1.53$, Mie code calculations determined values of k_{ext}^{550} from 0.95 to $1.6 m^2 g^{-1}$, g^{550} from 0.56 to 0.70 and n_i^{550} from $0.0001i$ to $0.0046i$. The measurements of ω_0^{550} fall at the high end of those in the literature, though they are similar in value to the numerous measurements and estimates of Tanré *et al.* (2001); Kaufman *et al.* (2001); Dubovik *et al.* (2002); Haywood *et al.* (2003); Todd *et al.* (2007); Kandler *et al.* (2007); Osborne *et al.* (2008).

The factors contributing to the variability in ω_0^{550} and k_{ext}^{550} observed during the DODO campaigns have also been examined. An important question was whether the composition or the size distribution had more influence over the optical properties. It was found that variations in ω_0^{550} were dominated by changes in n_i^{550} , and that changes in the accumulation mode size distribution had no discernible influence on ω_0^{550} . This was despite significantly more variability in the accumulation mode size distribution during DODO2 compared to DODO1. Contrastingly, k_{ext}^{550} was highly dependent on the size distribution. Due to changes in the size distribution with dust transport, this would mean that k_{ext}^{550} may change substantially across the Atlantic, whereas ω_0^{550} would be more dependent on the dust source region, and these results suggest that it would be reasonably stable during transport across the Atlantic. For example, during b173 and b174 (where the same dust outbreak was sampled on consecutive days), derived n_i^{550} values did not change, whereas the size distribution was different during the two flights. These findings confirm that representing both size distributions and composition are important for the accurate modelling of dust in terms of optical properties.

Variations in n_i and ω_0^{550} could be linked to variations in dust source regions, showing that the particular dust source which is activated has an important effect on the optical properties of the transported dust. Pinpointing particular dust sources was not possible due to the limitations of the NAME results since they indicate potential uplift only, and do not attempt to consider properties which affect dust mobilisation, such as surface moisture or low level wind speeds, for example. Both ω_0^{550} and n_i^{550} showed more variability during DODO2, which was connected to more variable dust sources due to the meteorology of the wet season. Therefore the seasonal meteorology has an effect on the variability of the optical properties of transported dust. Previous studies have shown that the chemical

composition is related to the dust source location. The dependence of ω_0 on the chemical composition has been demonstrated here, confirming the importance of the source location in determining the optical properties of dust.

The effect of the coarse mode size distribution on the optical properties has also been assessed for a case study from flight b238. Inclusion of the coarse mode resulted in a significant decrease in ω_0^{550} and k_{ext} and an increase in g^{550} . The magnitude of these changes was dependent on the amount of coarse mode measured, which changed for different measurement techniques. The largest coarse mode measurements resulted in ω_0^{550} decreasing from 0.98 to 0.90. This change highlights two issues: firstly, the importance of accurate, consistent measurements of the coarse mode on research aircraft (see Section 7.3) due to the high sensitivity of the optical properties to the coarse mode. Secondly, the addition of the coarse mode lowers ω_0^{550} , bringing it more towards the range of lower measurements and estimates of ω_0^{550} by studies such as Carlson and Benjamin (1980); Hess *et al.* (1998); Otto *et al.* (2007, 2009) (values from 0.76 to 0.837). It is likely that if n_i^{550} had been lower, even further reductions in ω_0^{550} would have occurred for the b238 case study. Changes in n_i as a function of particle size were not accounted for in this thesis due to a lack of data, even though it is likely that n_i does change with particle size (e.g. Kandler *et al.*, 2007), and the mineralogy for b237 showed differences between the accumulation mode and coarse mode.

7.2.3 Pyranometer Measurements

Chapter 5 described a detailed investigation into the quality and accuracy of the BAe-146 upper pyranometer measurements. This was necessary due to a lack of investigation of this type since the move from the previous C-130 aircraft to the BAe-146, which meant that an up-to-date estimate of the uncertainty was not available. It was also required in order to be able to rely on the pyranometer measurements for the purpose of model comparisons.

Firstly an investigation into the standard values of pitch (dp) and roll (dr) offset of the pyranometers relative to the aircraft as used by FAAM during the processing of DODO data was performed. dp and dr were found to be significantly different from

the values used by FAAM, which entailed large errors in the resulting irradiances. The DODO pyranometer data was processed using different dp and dr values, calculated from pirouette and box pattern manoeuvres. The total uncertainty in the upper pyranometer measurements resulting from the combined uncertainty in dp, dr, $FDIR$ and calibration error was calculated. Comparisons against model and ARM data were then made, and the resulting discrepancies were defined as the pyranometer uncertainties to be adopted for the analysis of DODO data. The uncertainties adopted were 5.5% and 15% for the clear and red dome pyranometers respectively, and for both upper and lower pyranometers.

Investigations into the dirtying of the front of the pyranometer domes during DODO were also carried out. As a result of this problem, significant decreases in the measured signal of up to 11% were found when the aircraft was heading into the sun. Therefore DODO data obtained on relative headings of $\pm 50^{\circ}$ were discarded.

These investigations into the quality and accuracy of the upper pyranometer measurements made during DODO allowed the data to be processed appropriately, and allowed an uncertainty to be applied to the measurements. Recommendations were made based on the problems encountered with the DODO data and based on the techniques applied to the DODO pyranometer data. Some of these recommendations have since been adopted by FAAM, and others are being considered for the future.

7.2.4 Radiative Effect of DODO Dust

Chapter 6 investigated how important the variability in the optical properties observed during DODO were to the dust shortwave radiative effect, and attempted to validate the model calculations by comparing them to pyranometer measurements.

The variations in ω_0 and n_i were found to cause significant changes in the instantaneous top of atmosphere, surface and atmospheric radiative effects. They also resulted in a change of sign of the radiative effect from negative to positive at the top of the atmosphere, thus resulting in the effect of the dust changing from a net cooling of the earth-atmosphere system to a net warming in the shortwave spectrum. Changes in instantaneous ARE_{TOA} due to the increase of n_i tested resulted in increases (more positive, or less negative) of $32 Wm^{-2}$ over the desert and $10 Wm^{-2}$ over land, whereas the in-

stantaneous ARE_{SFC} decreased by $23Wm^{-2}$ over the desert and $35Wm^{-2}$ over land. Peak instantaneous atmospheric heating rates were observed to increase by a factor of 5. Therefore the observed variations in the single scattering albedo during DODO have an important role in determining the shortwave radiative effect of the dust.

Comparisons of modelled irradiances with measured irradiances from the aircraft pyranometers were performed as a function of altitude, for both up and downwelling irradiance. The results showed that the model irradiances agreed with the measurements within instrument uncertainties and model uncertainty (due to the spatial and temporal variability of the dust) for the shortwave downwelling irradiance at high and low altitudes. The shortwave upwelling irradiances were in agreement at low altitudes below the dust, but not at higher altitudes above the dust. This reveals that the model estimates of ARE_{SFC} are valid, but that the ARE_{TOA} values from the model may be too negative, since the model was overestimating the amount of upwelling irradiance at the top of the atmosphere.

Sensitivity tests were performed in order to investigate assumptions in the modelling work and to investigate reasons for the discrepancy in shortwave upwelling irradiance between the model and pyranometer measurements. The upwelling shortwave irradiances were found to be most sensitive to the inclusion of the coarse mode size distribution, and to large changes (increases) in the imaginary part of the refractive index. A combination of including a significantly larger imaginary refractive index and the coarse mode size distribution leads to dust which is more absorbing, less reflective, and has a lower extinction per unit mass. This can significantly reduce the shortwave upwelling irradiance at high altitudes.

These sensitivity tests suggest that in the model calculations the values of ω_0 used are too high. This is probably a limitation associated with a lack of adequate knowledge of the aircraft inlet cut-offs for the inlets leading to the nephelometer, PSAP and filter samples, which creates problems in assigning a vertical dust profile and optical properties representative of the real dust in the atmosphere. These limitations are discussed further in Section 7.3. Nevertheless, the agreement of the model and pyranometer irradiances at low altitudes supports the importance of the variations in the DODO optical properties

for the ARE at the surface. The overestimate of the model upwelling irradiances at high altitudes is likely to result in an even greater dependence of the ARE_{TOA} on the optical properties than has been shown here from the model results.

The radiative modelling carried out here also assumed that the dust particles were spheres, allowing the use of Mie theory. However, the SEM filter samples clearly show that the particles are non-spherical, so this assumption therefore entails uncertainties. However, it has been shown that although non-spherical particles have significantly different phase functions to spherical particles, the net effect on parameters ω_0 , g and k_{ext} which are integrated over all scattering angles are small if the particles are randomly orientated in the atmosphere (Mishchenko *et al.*, 1997). For example, Otto *et al.* (2009) found that the correct representation of particles as oblate spheroids for a SAMUM dust event resulted in changes of ω_0 of up to 1%, g of up to 4% and τ^{550} of up to 3.5% in comparison to the values resulting from spherical particles. In comparison to the changes in optical properties shown in the DODO case study sensitivity tests for the coarse mode and refractive index, these are small changes. Otto *et al.* (2009) also found that non-spherical particles result in significantly increased back-scatter, causing a more negative ARE_{TOA} by 29% over the desert and 167% over the ocean. This effect could be important for the DODO results. However, increased upwelling shortwave irradiance at the top of the atmosphere due to non-spherical particles would actually increase the discrepancy between the model and pyranometer measurements for the DODO results.

7.3 Limitations and Suggestions for Future Work

The work in this thesis has been able to use aircraft measurements of mineral dust from the BAe-146 during the DODO campaigns, obtained over remote areas over the Mauritanian desert and from over the Atlantic ocean where ground-based instrumentation is absent, and in-situ measurements to validate satellite data are useful. The results have provided an insight into the variability of the optical properties of transported mineral dust and its radiative effect. However, there are some limitations to the results which mostly stem from measurement uncertainties. These are described below, along with suggestions for future aircraft campaigns.

1. Rosemount inlet cut-off

   One of the key assumptions in this study is that the cut-off radius of the Rosemount inlets (feeding the nephelometer and the PSAP) was at $r = 1.5\mu m$; the same as the maximum size measured by the PCASP. This was assumed based on previous findings (Haywood *et al.*, 2003) that the aerosol optical depths derived from the nephelometer and PSAP measured in dust during SHADE were a factor of 1.5 too small compared to AERONET measurements. This also represented the current thinking at the time of the DODO campaigns (e.g. Osborne *et al.*, 2008; Johnson *et al.*, 2008; McConnell *et al.*, 2008).

   Lack of knowledge of the inlet cut-off radius is a problem when supermicron size particles are present, as with dust. This is appreciated at FAAM, and therefore for an upcoming dust campaign the operation of two nephelometers side by side in the BAe-146 is planned, one with a cyclone-impactor which will allow a known cut-off radius to be applied to the measured aerosol particles. This should provide extra information on what sized particles are being measured. During SAMUM, aircraft measurements of dust absorption were made by a PSAP, which was connected to the same sampling line as a condensation particle counter. This allowed knowledge of the size distribution measured by the PSAP, which was determined to be $d < 2.5\mu m$, Petzold *et al.* (2009). This technique could be applied on the BAe-146 and would provide valuable information on the size distribution measured by the nephelometer and PSAP.

2. Chemical Composition

   Spectral refractive index data calculated from filter samples is an important part of radiative closure. The refractive index data available for flight b238 has been extremely useful in this respect. However, due to the likely differences in size distributions measured by the filter inlets, and the nephelometer and PSAP, comparing the chemical refractive indices and the Mie code derived refractive indices is not straightforward. Refractive index data as a function of size from the filter samples (e.g. Otto *et al.*, 2009) would significantly improve this problem, though obtaining

the data would involve extensive laboratory work and this has not been possible during DODO. Data of this type would be extremely valuable in future campaigns.

3. Coarse mode size distributions

   During DODO, difficulties in measuring the coarse mode size distribution were encountered. This was partly due to the key instrument for coarse mode size distributions measurements (SID (Small Ice Detector)) being struck by lightning. As a result other experimental instruments had to be relied upon. During SHADE an FFSSP (Fast Forward Scattering Spectrometer Probe) was operated successfully to measure coarse mode, and this has been operated during the recent GERBILS dust campaign on the BAe-146. It is recommended that effort is made to ensure that the coarse mode size distribution can be adequately measured by reliable, calibrated instruments during future aircraft campaigns measuring dust. This thesis has shown that the optical properties of dust in the shortwave are strongly influenced by the coarse mode size distribution. Additionally the coarse mode size distribution is important in determining the longwave radiative effect.

7.4 Final Comments

Chapter 1 showed that the values of ω_0 for dust reported in the literature cover a large range due to uncertainties in the refractive index, size distribution and morphology. In particular, the imaginary part of the refractive index at $550nm$ varied by nearly two orders of magnitude from $0.0004i$ to $0.01i$. This thesis has added to the volume of data available on the magnitude of the single scattering albedo, mass specific extinction, asymmetry parameter and the imaginary part of the refractive index. The data resulting from this study placed ω_0^{550} at the higher range of the values in the literature, from $0.93 - 0.99$, with correspondingly low values of n_i^{550} from $0.0001i - 0.0046i$. However, these values represent only the accumulation mode sized particles and are sensitive to the amount of coarse mode present, which can decrease ω_0^{550}. Additionally the n_i^{550} results are dependent on the size distribution measured by the nephelometer and PSAP.

The recent number of dust field campaigns are leading to a growing amount of emerg-

ing data concerning dust ω_0 and n_i. Although values of measured ω_0 still vary greatly, recent publications rarely find values of $n_i^{550} > 0.006i$. Lower measurements of ω_0^{550} are generally attributed to the number of large particles present (e.g. Otto *et al.*, 2009) rather than high imaginary refractive indices. Therefore it appears likely that the high, but widely adopted n_i^{550} value of $0.008i$ in dust models (Shettle and Fenn, 1979; WCP, 1983; Hess *et al.*, 1998) is an overestimate. Variations in the remaining range of n_i values are likely to be due to the composition of the dust, such as the proportion of absorbing iron oxides (Lafon *et al.*, 2006). This thesis has shown that the optical properties and imaginary refractive index during DODO changed with the dust source. Numerous studies have shown that composition changes with dust source (e.g. Chiapello *et al.*, 1997; Claquin *et al.*, 1999; Caquineau *et al.*, 1998, 2002). Due to the strong dependence of ω_0 on the imaginary refractive index of dust, as shown in this thesis, determining and parameterising the composition of the different Saharan (and Sahelian) dust sources is extremely important for the accurate modelling of the radiative effect of transported dust. Using accurate values of n_i for dust in satellite retrievals will have similar implications.

This thesis has shown that the range of optical properties of dust measured during DODO result in significantly different radiative effects. Considering this, it is important to continue to explore, constrain and attribute the variability in the optical properties of dust. The DODO project focused on West Africa in the coastal region around Senegal and Mauritania, and the results were limited to flights carried out over a total time of around two weeks. Further studies in different locations, and for longer time periods, could add useful information on how the optical properties of dust vary on much larger timescales and spatial areas. Recent and upcoming aircraft campaigns will no doubt add to these results, as will the new observatory at Cape Verde which aims to monitor atmosphere-ocean interactions, including dust transport and deposition.

Aircraft field campaigns allow the combination of chemical, scattering and absorption, size distribution and radiative measurements to fully explore the relationships between dust composition, microphysical and optical properties, through to the full radiative effect. In this respect they can obtain valuable in-situ measurements of dust which ground-based and satellite retrievals are unable to obtain. However, the DODO results

were limited by several instrumentation issues and lack of knowledge regarding instrument inlet efficiencies. If future aircraft field campaigns are able to make use of well-calibrated, accurate instruments, there is real potential for future studies to further the knowledge of the magnitudes and variability of dust optical properties.

Due to the small-scale nature of dust uplift, which can often be at a lower resolution than that of regional dust models, challenges remain in order for dust models to represent reality accurately (e.g. Washington *et al.*, 2006; Heinold *et al.*, 2009). However, the recent North-African dust campaigns (DODO, DABEX, AMMA, SAMUM and GERBILS) have enabled significant improvements in the accuracy of dust models through better understanding of the dust uplift mechanisms and through comparisons with aircraft data (e.g. Ackerley *et al.*, 2009; Heinold *et al.*, 2009). As dust models improve and develop in terms of the dynamics enabling dust uplift, and in terms of the size distributions uplifted and transported, the representation of the chemical composition for different source areas should not be bypassed, since this is an important governor of dust optical properties. A combination of aircraft, ground and satellite measurements should continue to be used for assessing model accuracy. Recent developments in using satellite data to determine the locations of dust sources (e.g. Schepanski *et al.*, 2007; Koven and Fung, 2008) should be valuable in including the effects of varying composition with source in dust models.

The deposition of dust to the ocean can have a large impact on climate. Aircraft measurements can be used to validate and improve dust models through comparing size distributions of transported dust, for example, which leads to improved model estimates of dust deposition. Aircraft measurements also provide data on the chemical composition of transported dust, such as iron content, which is important for deposition to the ocean. Research cruises (e.g. Rijkenberg *et al.*, 2008) provide key information on the amount, composition and effects in the upper ocean of dust which has been depostited. Measurements of this type can be linked to longer term data, from satellites, ground-based observatories (such as the one at Cape Verde), and possibly in future also from buoy measurements (e.g. Singer *et al.*, 2003), allowing short-term intensive field campaign measurements to be applied to a longer time scale.

Dust has an important place in the climate system through interactions with both

shortwave and longwave radiation, and through deposition to the surface of the Earth. Although much dust is of natural origin, a significant proportion may be anthropogenic (Mahowald *et al.*, 2005), and this proportion may change in the future. Therefore, if dust emissions alter due to climate change or changing global land use, understanding the impacts of dust on the climate is of great significance. This thesis suggests that in terms of the shortwave direct radiative effect of Saharan dust, one of the priorities should be to determine how dust composition varies across specific sources in North Africa, since this has a large impact on the radiative effect.

References

Abel, S. (2007). CDP airflow modelling and droplet shadowing on the FAAM 146. Presented at the FAAM cloud user group meeting at Manchester University, available at http://www.web.mac.com/mccssmwg1/CIUG/Presentations_1.html.

Ackerley, D., Highwood, E., Harrison, M., McConnell, C., Joshi, M., Walters, D., Milton, S., Greed, G., and Brooks, M. (2009). The development of a new dust uplift scheme in the Met Office's Unified Model. *Meteorological Applications*. Submitted.

Alfaro, S., Lafon, S., Rajot, J., Formenti, P., Gaudichet, A., , and Maille, M. (2004). Iron oxides and light absorption by pure desert dust: an experimental study. *Journal of Geophysical Research*, **109**(D08208). doi:10.1029/2003JD004374.

Alpert, P., Kaufman, Y., Shay-El, Y., Tanré, D., da Sliva, A., Schubert, S., and Joseph, J. (1998). Quantification of dust-forced heating of the lower troposphere. *Nature*, **395**, 367–370.

Anderson, T. and Ogren, J. (1998). Determining aerosol radiative properties usuing the TSI 3563 integrating nephelometer. *Aerosol Sci. and Technol.*, **29**, 57–69.

Anderson, T., Charlson, R., Bellouin, N., Boucher, O., Chin, M., Christopher, S., Haywood, J., Kaufman, Y., Kinne, S., Ogren, J., *et al.* (2005). An A-Train Strategy for Quantifying Direct Climate Forcing by Anthropogenic Aerosols. *Bulletin of the American Meteorological Society*, **86**(12), 1795–1809.

Andreae, M., Elbert, W., Gabriel, R., Johnson, D., Osborne, S., and Wood, R. (2000). Soluble ion chemistry of the atmospheric aerosol and SO2 concentrations over the eastern North Atlantic during ACE-2. *Tellus B*, **52**(4), 1066–1087.

Arimoto, R., Ray, B., Lewis, N., Tomza, U., and Duce, R. (1997). Mass-particle size distributions of atmospheric dust and the dry deposition of dust to the remote ocean. *Journal of Geophysical Research*, **102**(D13), 15867–15874.

Athanassiadou, M., Flocas, H., Harrison, M., Hort, M., Witham, C., and Watkin, S. (2006). The dust event of 17 april 2005 over athens, greece. *Weather*, **61**(5), 125–131.

Baker, A. and Jickells, T. (2006). Mineral particle size as a control on aerosol iron solubility. *Geophysical Research Letters*, **33**(L17068). doi:10.1029/2006GL026557.

Balkanski, Y., Schulz, M., Claquin, T., and Guibert, S. (2007). Reevaluation of mineral aerosol radiative forcings suggests a better agreement with satellite and AERONET data. *Atmospheric Chemistry and Physics*, **7**, 81–95.

Bannehr, L. and Schwiesow, R. (1993). A Technique to Account for the Misalignment of Pyranometers Installed on Aircraft. *Journal of Atmospheric and Oceanic Technology*, **10**(5), 774–777.

Berthier, S., Chazette, P., Couvert, P., Pelon, J., Dulac, F., Thieuleux, F., and Moulin, C. (2006). Desert dust aerosol coumnar properties over ocean and continental Africa from Lidar in-Space Technology Experiment (LITE) and Meteosat synergy. *Journal of Geophysical Research*, **111**(D21202). doi:10.1029/JD006999.

Bierwith, E., Wendisch, M., Ehrlich, A., Heese, B., Tesche, M., Althausen, D., Schladitz, A., Muller, D., Otto, S., Trautmann, T., Dinter, T., von Hoyningen-Heune, W., and Kahn, R. (2009). Spectral surface albedo over morocco and its impact on radiative forcing of saharan dust. *Tellus B*, **61**, 252–269.

Boers, R., Jensen, J., Krummel, P., and Gerber, H. (1996). Microphysical and short-wave radiative structure of wintertime stratocumulus clouds over the Southern Ocean. *Quarterly Journal of the Royal Meteorological Society*, **122**, 1307–1340.

Boers, R., Mitchell, R., and Krummel, P. (1998). Correction of aircraft pyranometer measurements for diffuse radiance and alignment errors. *Journal of Geophysical Research*, **103**(D13), 16,753–16,758.

Bohren, C. and Huffman, D. (1983). *Absorption and scattering of light by small particles*. Wiley, New York.

Bond, T., Anderson, T., and Campbell, D. (1999). Calibration and intercomparison of filter-based measurements of visible light absorption by aerosols. *Aerosol Sci. and Technol.*, **30**, 582–600.

Burns, S., Khelif, D., Friehe, C., Hignett, P., Williams, A., Grant, A., Hacker, J., Hagan, D., Serra, Y., Rogers, D., *et al.* (2000). Comparisons of aircraft, ship, and buoy radiation and SST measurements from TOGA COARE. *Journal of Geophysical Research*, **105**(D12), 15,627–15,652.

Burpee, R. (1972). The origin and structure of Easterly Waves in the Lower Troposphere of North Africa. *Journal of the Atmospheric Sciences*, **29**, 77–90.

Cakmur, R., Miller, R., and Tegen, I. (2001). A comparison of seasonal and interannual variability of soil dust aerosols over the Atlantic Ocean as inferred by the TOMS AI and AVHRR AOT retrievals. *Journal of Geophysical Research*, **106**, 18287–18303. doi:10.1029/2000JD900525.

Calzolai, G., Chiari, M., García Orellana, I., Lucarelli, F., Migliori, A., Nava, S., and Taccetti, F. (2006). The new external beam facility for environmental studies at the Tandetron accelerator of LABEC. *Nuclear Inst. and Methods in Physics Research, B*, **249**(1-2), 928–931.

Caquineau, S., Gaudichet, A., Gomes, L., Magonthier, M., and Chatenet, B. (1998). Saharan dust: Clay ratio as a relevant tracer to assess the origin of soil-derived aerosols. *Geophysical Research Letters*, **25**(7), 983–986.

Caquineau, S., Gaudichet, A., Gomes, L., and Legrand, M. (2002). Mineralogy of Saharan dust transported over northwestern tropical Atlantic Ocean in relation to source regions. *J. Geophys. Res*, **107**(D15), 4251.

Carlson, T. (1979). Atmospheric Turbidity in Saharan Dust Outbreaks as Determined by Analyses of Satellite Brightness Data. *Monthly Weather Review*, **107**, 322–335.

Carlson, T. and Benjamin, S. (1980). Radiative Heating Rates for Saharan Dust. *Journal of the Atmospheric Sciences*, **37**(1), 193–213.

Carlson, T. and Caverly, R. (1977). Radiative characteristics of Saharan dust at solar wavelengths. *Journal of Geophysical Research*, **82**(21), 3141–3152.

Carlson, T. and Prospero, J. (1972). The Large-Scale Movement of Saharan Air Outbreaks over the Northern Equatorial Atlantic. *Journal of Applied Meteorology*, **11**, 283–297.

Carrico, C., Kus, P., Rood, M., Quinn, P., and Bates, T. (2003). Mixtures of pollution, dust, sea salt and volcanic aerosol during ACE-Asia: Radiative properties as a function of relative humidity. *Journal of Geophysical Research*, **108**(D23), 8650. doi:10.1029/2003JD003405.

Chiapello, I., Bergametti, G., Gomes, L., Chatenet, B., Dulac, F., Pimenta, J., and Suares, E. S. (1995). An additional low layer transport of Sahelian and Saharan dust over the North-Eastern Tropical Atlantic. *Geophysical Research Letters*, **22**(23), 3,191–3,194.

Chiapello, I., Bergametti, G., Chatenet, B., Bousquet, P., Dulac, F., and Suares, E. S. (1997). Origins of African dust transported over the northeastern tropical Atlantic. *Journal of Geophysical Research*, **102**(D12), 13,701–13,709.

Chiapello, I., Prospero, J., Herman, J., and Hsu, N. (1999). Detection of mineral dust over the North Atlantic Ocean and Africa with the Nimbus 7 TOMS. *Journal of Geophysical Research*, **104**(D8), 2977–9292.

Chiari, M., Lucarelli, F., Mazzei, F., Nava, S., Paperetti, L., Prati, P., Valli, G., and Vecchi, R. (2005). Characterization of airborne particulate matter in an industrial district near Florence by PIXE and PESA. *X-Ray Spectrometry*, **34**, 323–329.

Chou, C., Formenti, P., Maille, M., Ausset, P., Helas, G., Harrison, M., and Osborne, S. (2008). Size distribution, shape and composition of mineral dust aerosols collected during the African Moonsoon Multidisciplinary Analysis Special Observation Period 0: Dust and Biomass Burning Experiment field campaign in Niger, January 2006. *Journal of Geophysical Research*, **113**(DC00C10). doi:10.1029/2008JD009897.

Christopher, S. and Jones, T. (2007). Satellite-based assessment of cloud-free net radiative effect of dust aerosols over the Atlantic Ocean. *Journal of Geophysical Research*, **34**(L02810). doi:10.1029/2006GL027783.

Claquin, T., Schulz, M., Balkanski, Y., and Boucher, O. (1998). Uncertainties in assessing radiative forcing by mineral dust. *Tellus B*, **50**(5), 491–505.

Claquin, T., Schulz, M., and Balkanski, Y. (1999). Modeling the mineralogy of atmospheric dust sources. *Journal of Geophysical Research*, **104**(D18), 22,243–22,256.

Colarco, P., Toon, O., and Holben, B. (2003). Saharan dust transport to the Caribbean during PRIDE: 1. Influence of dust sources and removal mechanisms on the timing and magnitude of downwind aerosol optical depth events from simulations of in situ and remote sensing observations. *Journal of Geophysical Research*, **108**(D19), 8589.

Cullen, M. (1993). The unified forecast/climate model. *Meteor. Mag.*, **122**, 81–93.

D'Almeida, G. and Schtz (1983). Number, mass and volume distribution of mineral aerosol and soils of the Sahara. . *J. Climate Appl. Meteor.*, **22**, 233–243.

d'Almeida, G., Koepke, P., and Shettle, E. (1991). *Atmospheric Aerosols: Global Climatology and Radiative Characteristics*, chapter A Global Aerosol Climatology, page 561. A. Deepak, Hampton, Va.

Das, P. (1986). Monsoons. In *WMO*. WMO no. 613 5th IMO lecture.

DeMott, P., Sassen, K., Poellot, M., Baumgardner, D., Rogers, D., Brooks, S., Prenni, A., and Kreidenweis, S. (2003). African dust aerosols as atmospheric ice nuclei. *Journal of Geophysical Research*, **30**(14), 1,732.

Dubovik, O., Holben, B., Eck, T., Smirnov, A., Kaufman, Y., King, M., Tanre, D., and Slutsker, I. (2002). Variability of Absorption and Optical Properties of Key Aerosol Types Observed in Worldwide Locations. *Journal of the Atmospheric Sciences*, **59**, 590–608.

Edwards, J. and Slingo, A. (1996). Studies with a flexible new radiation code .1. Choosing a configuration for a large-scale model. *Quarterly Journal of the Royal Meteorological Society*, **122**(531), 689–719. Part A.

Engelstaedter, S. and Washington, R. (2007a). Atmospheric controls on the annual cycle of North African dust. *Journal of Geophysical Research*, **112**(D03103). doi:10.1029/2006JD007195.

Engelstaedter, S. and Washington, R. (2007b). Temporal controls on global dust emissions: the role of surface gustiness. *Geophysical Research Letters*, **34**(L15805). doi:10.1029/2007GL029971.

Engelstaedter, S., Washington, R., and Tegen, I. (2006). North African dust emissions and transport. *Earth Science Reviews*, **79**(1-2), 73–100.

Evan, A., Dunion, J., Foley, J., Heidinger, A., and Velden, C. (2006). New evidence for a relationship between Atlantic tropical cyclone activity and African dust outbreaks. *Geophysical Research Letters*, **33**(L19813). doi:10.1029/2006GL026408.

Field, P., Mohler, O., Connolly, P., Kramer, M., Cotton, R., Heymsfield, A., Saathoff, H., and Schnaiter, M. (2006). Some ice nucleation characteristics of Asian and Saharan desert dust. *Atmospheric Chemistry and Physics*, **6**, 2991–3006.

Formenti, P., Elbert, W., Maenhaut, W., Haywood, J., and Andreae, M. (2003). Chemical composition of mineral dust aerosol during the Saharan Dust Experiment (SHADE) airborne campaign in the Cape Verde region, September 2000. *Journal of Geophysical Research*, **108**. doi:10.1029/JD002648.

Formenti, P., Rajot, J., Desboeufs, K., Caquineau, S., Chevaillier, S., Nava, S., Gaudichet, A., Journet, E., Triquet, S., Alfaro, S., Chiari, M., Haywood, J., Coe, H., and Highwood, E. (2008). Regional variability of the composition of mineral dust from Western Africa: results from the AMMA SOP0/DABEX and DODO field campaigns. *Journal of Geophysical Research*, **113**(D00C13). doi:10.1029/2008JD009903.

Forster, P., Ramaswamy, V., Artaxo, P., Berntsen, T., Betts, R., Fahey, D., Haywood, J., Lean, J., Lowe, D., Myhre, G., Nganga, J., Prinn, R., Raga, G., Schulz, M., and Dorland, R. V. (2007). *Climate Change 2007: The Physical Science Basis. Contribution of Working Group I to the Fourth Assessment Report of the Intergovernmental Panel on Climate Change*, chapter Changes in Atmospheric Constituents and in Radiative Forcing, pages 130–234. Cambridge University Press, Cambridge, United Kingdom and New York, NY, USA. . (ed. [Solomon, S., D. Qin, M. Manning, Z. Chen, M. Marquis, K.B. Averyt, M.Tignor and H.L. Miller] .

Fouquart, Y., Bonnel, B., Roquai, M., Santer, R., and Cerf, A. (1987a). Observations of Saharan Aerosols: Results of ECLATS Field Experiment. Part I: Optical Thicknesses and Aerosol Size Distributions. *Journal of Applied Meteorology*, **26**(1), 28–37.

Fouquart, Y., Bonnel, B., Brogniez, G., Buriez, J., Smith, L., Morcrette, J., and Cerf, A. (1987b). Observations of Saharan Aerosols: Results of ECLATS Field Experiment. Part II: Broadband Radiative Characteristics of the Aerosols and Vertical Radiative Flux Divergence. *Journal of Applied Meteorology*, **26**(1), 38–52.

Ginoux, P., Chin, M., Holben, B., Lin, S., Tegen, I., Prospero, J., and Dubovik, O. (2001). Sources and distributions of dust aerosols simulated with the GOCART model. *Journal of Geophysical Research*, **106**(D17), 20.

Gloster, J., Mellor, P., Manning, A., Webster, H., and Hort, M. (2007). Assessing the risk of windborne spread of bluetongue in the 2006 outbreak of disease in northern Europe. *Veterinary record*, **160**(2), 54–56.

Godbole, R. and Shukla, J. (1981). Global analysis of Janjary and July sea level pressure. NASA Technical Memorandum 82097, Goddard Space Flight Centre, Greenbeld, Maryland. pp52.

Gomes, L. (1990). *Approche géochimique du soulvément des aérosoles á l'interface sol-atmosphére en zone désertique*. Ph.D. thesis, Université Paris 7.

Goudie, A. and Middleton, N. (2001). Saharan dust storms: nature and consequences. *Earth Science Reviews*, **56**(1-4), 179–204.

Greed, G. (2005). Upgrades to crisis area mesoscale model service. Technical Report 464, UK Met Office, Met Office, Exeter, UK. Forecasting Res. Tech. Rep.

Greed, G., Haywood, J., Milton, S., Keil, A., Christopher, S., Gupta, P., and Highwood, E. (2008). Aerosol optical depths over North Africa: 2. Modeling and model validation. *J. Geophys. Res*, **113**(D00C05). doi:10.1029/2007JD00945.

Hastenrath, S. (1991). *Climate dynamics of the tropics*, chapter Regional circulation systems, pages 114–208. Kluwer Academic Publishers.

Haywood, J. and Osborne, S. (2000). Corrections to be applied to the PSAP and nephelometer for accurate determination of the absorption coefficient, scattering coefficient and single scattering albedo. Technical report, UK Meteorological Office. MRF Tech. Note No. 31.

Haywood, J., Francis, P., Glew, M., and Taylor, J. (2001). Optical properties and direct radiative effect of Saharan dust: a case study of two Saharan dust outbreaks using aircraft data. *Journal of Geophysical Research*, **106**(D16), 18417–18430.

Haywood, J., Francis, P., Osborne, S., Glew, M., Loeb, N., Highwood, E., Tanré, D., Mhyre, G., Formenti, P., and Hirst, E. (2003). Radiative properties and direct radiative effect of Saharan dust measured by the C-130 aircraft during SHADE: 1. Solar spectrum. *Journal of Geophysical Research*, **108**(D18). doi:10.1029/2002JD002687.

Haywood, J., , Pelon, J., Formenti, P., Bharmal, N., Brooks, M., Capes, G., Chazette, P., Chou, C., Christopher, S., Coe, H., Cuesta, J., Derimian, Y., Desboeufs, K., Greed, G., Harrison, M., Heese, B., Highwood, E., Johnson, B., Mallet, M., Marticorena, B., Marsham, J., Milton, S., Myhre, G., Osborne, S., Parker, D., Rajot, J., Schulz, M., Slingo, A., Tanré, D., and Tulet, P. (2009). Overview of the Dust and Biomass-burning Experiment and African Monsoon Multidisciplinary Analysis Special Observing Period-0. *Journal of Geophysical Research*, **113**(D00C17). doi:10.1029/2008JD010077.

Heinold, B., Tegen, I., Esselborn, M., Kandler, K., Knippertz, P., Müller, D., Schladitz, A., Tesche, M., Weinzerl, B., Ansmann, A., Althausen, D., Laurent, B., Petzold, A., and Schepanski, K. (2009). Regional dust modelling during the SAMUM 2006 campaign. *Tellus B*, **61B**, 307–324.

Herman, J., Bhartia, P., Torres, O., Hsu, C., Seftor, C., and Celarier, E. (1997). Global distribution of UV-absorbing aerosols from Nimbus 7/TOMS data: Passive Remote Sensing of Tropospheric Aerosol and Atmospheric Corrections From the New Generation of Satellite Sensors. *Journal of geophysical research*, **102**(D 14), 16911–16922.

Hess, M., Koepke, P., and Schult, I. (1998). Optical Properties of Aerosols and Clouds: The Software Package OPAC. *Bulletin of the American Meteorological Society*, **79**(5), 831–844.

Highwood, E., Haywood, J., Silverstone, M., Newman, S., and Taylor, J. (2003). Radiative properties and direct effect of Saharan dust measured by the C-130 aircraft during Saharan Dust Experiment (SHADE): 2. Terrestrial spectrum. *Journal of Geophysical Research*, **108**. doi:10.1029/2002JD002552.

Holben, B., Vermote, E., Kaufman, Y., Tanre, D., and Kalb, V. (1998). AERONET: a federated instrument network and data archive for aerosol characterization. *Remote Sens. Environ*, **66**(1), 1–16.

Hsu, N., Tsay, S., King, M., and Herman, J. (2004). Aerosol properties over bright-reflecting source regions. *IEEE Transactions on Geoscience and Remote Sensing*, **42**(3), 557–569.

Husar, R., Prospero, J., and Stowe, L. (1997). Characterization of tropospheric aerosols over the oceans with the NOAA advanced very high resolution radiometer optical thickness operational product. *J. Geophys. Res*, **102**(16), 889–16.

Ivlev, L. and Andreev, S. (1986). *Opticheskie svoistva atmosfernykh aerozolei (Optical Properties of Atmospheric Aerosols)*. Leningrad State University, Leningrad.

Janowiak, J. (1988). An investigation into interannual rainfall variability in africa. *Journal of Climate*, **1**, 240–255.

Jeong, M., Tsay, S., Ji, Q., Hsu, C., Hansell, R., and Lee, J. (2008). Ground-based measurements of Saharan dust in marine environment during the NAMMA field experiment. *Geophysical Research Letters*, **35**(L20805). doi:10.1029/2008GL035587.

Jickells, T., An, Z., Andersen, K., Baker, A., Bergametti, G., Brooks, N., Cao, J., Boyd, P., Duce, R., Hunter, K., Kawahata, H., Kubilay, N., laRoche, J., Liss, P., Mahowald, N., Prospero, J., Ridgwell, A., and Torres, R. (2005). Global Iron Connections Between Desert Dust, Ocean Biogeochemistry and Climate. *Science*, **308**, 67–71.

Jin, Z., Charlock, T., Smith Jr, W., and Rutledge, K. (2004). A parameterization of ocean surface albedo. *Geophysical Research Letters*, **31**. doi:10.1029/2004GL021180.

Johnson, B., Osborne, S., Haywood, J., and Harrison, M. (2008). Aircraft measurements of biomass burning aerosol over West Africa during DABEX. *Journal of Geophysical Research*, **113**(D00C06). doi:10.1029/2007JD00945.

Jones, C., Mahowald, N., and Luo, C. (2004). Observational evidence of African desert dust intensification of easterly waves. *Geophysical Research Letters*, **31**. doi:10.1029/2004GL020107.

Kahn, R., Li, W., Moroney, C., Diner, D., Martonchik, J., and Fishbein, E. (2007). Aerosol source plume physical characteristics from space-based multiangle imaging. *J. Geophys. Res*, **112**(D11205). doi:10.1029/2006JD007647.

Kalashnikova, O. and Kahn, R. (2008). Mineral dust plume evolution over the Atlantic from MISR and MODIS aerosol retrievals. *Journal of Geophysical Research*, **113**(D24204). doi:10.1029/2008JD010083.

Kandler, K., Benker, N., Bundke, U., Cuevas, E., Ebert, M., Knippertz, P., Rodríguez, S., Schütz, L., and Weinbruch, S. (2007). Chemical composition and complex refractive index of Saharan Mineral Dust at Izaña, Tenerife (Spain) derived by electron microscopy. *Atmospheric Environment*, **41**(37), 8058–8074.

Karyampudi, V., Palm, S., Reagen, J., Fang, H., Grant, W., Hoff, R., Moulin, C., Pierce, H., Torres, O., Browell, E., *et al.* (1999). Validation of the Saharan Dust Plume Conceptual Model Using Lidar, Meteosat, and ECMWF Data. *Bulletin of the American Meteorological Society*, **80**(6), 1045–1075.

Kaufman, Y., Tanre, D., Dubovik, O., Karnieli, A., and Remer, L. (2001). Absorption of sunlight by dust as inferred from satellite and ground-based remote sensing. *Geophysical Research Letters*, **28**(8), 1479–1482.

Kaufman, Y., Koren, I., Remer, L., Tanré, D., Ginoux, P., and Fan, S. (2005). Dust transport and deposition observed from the Terra-Moderate Resolution Imaging Spectroradiometer (MODIS) spacecraft over the Atlantic Ocean. *J. Geophys. Res*, **110**, D10S12. doi:10.1029/2003JD004436.

Koepke, P., Hess, M., Schult, I., and Shettle, E. (1997). Global Aerosol Data Set (GADS). *Max-Planck Institute for Meteorology*, **243**, 1–44.

Koven, C. and Fung, I. (2008). Identifying global dust source areas using high-resolution land surface form. *Journal of Geophysical Research*, **113**(D22). doi:10.1029/2008JD010195.

Lafon, S., Sokolik, I., Rajot, J., Caquineau, S., and Gaudichet, A. (2006). Characterization of iron oxides in mineral dust aerosols: Implications for light absorption. *J. Geophys. Res*, **111**. doi:10.1029/2005JD007016.

Levin, Z., Joseph, J., and Mekler, Y. (1980). Properties of Sharav (Khamsin) dust - comparison of optical and direct sampling data. *Journal of the Atmospheric Sciences*, **37**(4), 882–891.

Li, F., Vogelmann, A., and Ramanathan, V. (2004). Saharan Dust Aerosol Radiative Forcing Measured from Space. *Journal of Climate*, **17**(13), 2558–2571.

Li-Jones, X. and Prospero, J. (1998). Variations in the size distribution of non-sea-salt sulfate aerosol in the marine boundary layer at Barbados: Impact of African dust. *Journal of Geophysical Research*, **103**(D13), 16–073.

Li-Jones, X., Maring, H., and Prospero, J. (1998). Effect of relative humidity on light scattering by mineral dust aerosol as measured in the marine boundary layer over the Tropical Atlantic Ocean. *Journal of Geophysical Research*, **108**(D23), 31,113–31,121.

Liao, H. and Seinfeld, J. (1998). Radiative forcing by mineral dust aerosols: sensitivity to key variables. *Journal of Geophysical Research*, **103**(31), 31,637–31,645.

Lindberg, J. and Laude, L. (1974). Measurement of Absorption-coefficient of atmospheric dust. *Applied Optics*, **13**(8), 1923–1927.

Liu, D., Wang, Z., Liu, Z., Winker, D., and Trepte, C. (2008a). A Height Resolved Global View of Dust Aerosols from the First Year CALIPSO Lidar Measurements. *Journal of Geophysical Research*, **113**(D16214). doi:10.1029/2007JD009776.

Liu, Z., Omar, A., Vaughan, M., Hair, J., Kittaka, C., Hu, Y., Powell, K., Trepte, C., Winker, D., Hostetler, C., *et al.* (2008b). CALIPSO lidar observations of the optical properties of Saharan dust: A case study of long-range transport. *Journal of Geophysical Research*, **113**(D7). doi:10.1029/2007JD008878.

Magi, B. and Hobbs, P. (2003). Effects of humidity on aerosols in southern Africa during the biomass burning season. *Journal of Geophysical Research*, **108**(D13). doi:10.1029/2002JD002144.

Mahowald, N. and Dufresne, J. (2004). Sensitivity of TOMS aerosol index to boundary layer height: Implications for detection of mineral aerosol sources. *Geophysical Research Letters*, **31**. doi:10.1029/2003GL018865.

Mahowald, N., Baker, A., Bergametti, G., Brooks, N., Duce, R., Jickells, T., Kubilay, N., Prospero, J., and Tegen, I. (2005). Atmospheric global dust cycle and iron inputs to the ocean. *Global Biogeochemical Cycles*, **19**(GB4025). doi:10.1029/2004GB002402.

Maring, H., Savoie, D., Izaguirre, M., McCormick, C., Arimoto, R., Prospero, J., and Pilinis, C. (2000). Aerosol physical and optical properties and their relationship to aerosol composition in the free troposphere at Izaña, Tenerife, Canary Islands, during July 1995. *Journal of Geophysical Research*, **105**(D11).

Maring, H., Savoie, D., Izaguirre, M., Custals, L., and Reid, J. (2003a). Mineral dust aerosol size distribution change during atmospheric transport. *J. Geophys. Res*, **108**, 8592.

Maring, H., Savioe, D., Izaguirre, M., Custals, L., and Reid, J. (2003b). Vertical distributions of dust and sea-salt aerosols over Puerto Rico during PRIDE measured from a light aircraft. *J. Geophys. Res*, **108**, 8587.

Mason, B. (1966). *Principles of Geochemistry*. John Wiley, Hoboken, N.J.

McClatchey, R., Fenn, R., Selby, J., Volz, F., and Garing, J. (1971). Optical properties of the atmosphere. *ARCRL-71-0279*. Air Force Geophysics Lab, Bedford, MA.

McConnell, C., Highwood, E., Coe, H., Formenti, P., Anderson, B., Osborne, S., Nava, S., Desboeufs, K., Chen, G., and Harrison, M. (2008). Seasonal variations in the physical and optical characteristics of Saharan mineral dust: results from the Dust Outflow and Deposition to the Ocean experiment. *Journal of Geophysical Research*, **113**(D14S05). doi:10.1029/2007JD009606.

McFarquhar, G. and Heymsfield, A. (1998). The definition and significance of an effective radius for ice clouds. *Journal of the Atmospheric Sciences*, **55**, 2039–2052.

McMeeking, G., Rosenberg, P., Morgan, W., and Coe, H. (2008). An examination of the passive cavity aerosol spectrometer probe (PCASP) performance during EUCAARI-LONGREX. Internal report, correspondence to: gavin.mcmeeking@manchester.ac.uk.

McNaughton, C. S., Clarke, A. D., Howell, S. G., Pinkerton, M., Anderson, B., Thornhill, L., Hudgins, C., Winstead, E., Dibb, J. E., Scheuer, E., and Maring, H. (2007). Results from the DC-8 Inlet Characterization Experiment (DICE): Airborne Versus Surface Sampling of Mineral Dust and Sea Salt Aerosols. *Aerosol Science and Technology*, **41**, 136–159. doi:10.1080/02786820611184406.

Michalsky, J., Dutton, E., Rubes, M., Nelson, D., Stoffel, T., Wesley, M., Splitt, M., and DeLuisi, J. (1999). Optimal measurement of surface shortwave irradiance using current instrumentation. *Journal of Atmospheric and Oceanic Technology*, **16**, 55–69.

Miller, R. and Tegen, I. (1998). Climate response to soil dust aerosols. *Journal of Climate*, **11**, 3247–3267.

Mishchenko, M. (1993). Light-scattering by size shape distributions of randomly oriented axially-symmetrical particles of a size comparable to a wavelength. *Applied Optics*, **32**(24), 4652–4666.

Mishchenko, M., Lacis, A., Carlson, B., and Travis, L. (1995). Nonsphericity of dust-like tropospheric aerosols: Implications for aerosol remote sensing and climate modeling. *Geophys. Res. Lett*, **22**(9), 1077–1080.

Mishchenko, M., Travis, L., Kahn, R., and West, R. (1997). Modeling phase functions for dustlike tropospheric aerosols using a shape mixture of randomly oriented polydisperse spheroids. *Journal of Geophysical Research*, **102**(16), 831–16.

Moulin, C., Lambert, C., Dulac, F., and Dayan, U. (1997). Control of atmospheric export of dust from North Africa by the North Atlantic Oscillation. *Nature*, **387**, 691–694.

Osborne, S., Johnson, B., Haywood, J., and McConnell, C. (2008). Physical and optical properties of mineral dust aerosol during the Dust and Biomass Experiment (DABEX). *Journal of Geophysical Research*, **113**(D00C03). doi:10.1029/2007JD009551.

Otterman, J., Fraser, R., and Bahethi, O. (1982). Characterization of Tropospheric Desert Aerosols at Solar Wavelengths by Multispectral Radiometry From Landsat. *Journal of Geophysical Research*, **87**, 1270–1278.

Otto, S., de Reus, M., Trautmann, T., Thomas, M.Wendisch, and Borrmann, S. (2007). Atmospheric radiative effects of an in situ measured Saharan dust plume and the role of large particles. *Atmospheric Chemistry and Physics*, **7**, 4887–4903.

Otto, S., Bierwith, E., Weinzierl, B., Kandler, K., Esselborn, M., Tesche, M., Schladitz, A., Wendisch, M., and Trautmann, T. (2009). Solar radiative effects of a Saharan dust plume observed during SAMUM assuming speroidal model particles. *Tellus B*, **61B**, 270–296.

Patterson, E., Gillette, D., and Stockton, B. (1977). Complex index of refraction between 300 and 700 nm for Saharan aerosols. *Journal of Geophysical Research*, **82**(21), 3153–3160.

Petty, G. (2006). *A first course in atmospheric radiation*, chapter Regional and seasonal distribution of insolation. Sundog Publishing, Madison, Wisconsin, 2nd edition edition.

Petzold, A., Rasp, K., Weinzierl, B., Esselborn, M., Hamburger, T., Dörnbrack, A., Kandler, K., Schütz, L., Knippertz, P., and Fiebig, M. (2009). Saharan dust absorption and refractive index from aircraft-based observations during SAMUM 2006. *Tellus B*, **61B**, 118–130.

Pierangelo, C., Mishchenko, M., Balkanski, Y., and Chédin, A. (2005). Retrieving the effective radius of Saharan dust coarse mode from AIRS. *Geophys. Res. Lett*, **32**. doi:10.1029/2005GL023425.

Prospero, J. and Lamb, P. (2003). African Droughts and Dust Transport to the Caribbean: Climate Change Implications. *Science*, **302**(5647), 1024–1027.

Prospero, J., Ginoux, P., Torres, O., Nicholson, S., and Gill, T. (2002). Environmental characterization of global sources of atmospheric soil dust identified with the NIMBUS 7 Total Ozone Mapping Spectrometer (TOMS) absorbing aerosol product. *Reviews of Geophysics*, **40**(1), 1002. doi:10.1029/2000RG000095.

Rajot, J., Formenti, P., Alfaro, S., Desboeufs, K., Chevaillier, S., Chatenet, B., Gaudichet, A., Journet, E., Marticorena, B., Triquet, S., Maman, A., Mouget, N., and Zakou, A. (2008). AMMA dust experiment: An overview of measurements performed during the dry season special observation period (SOP0) at the Banizoumbou (Niger) supersite. *J. Geophys. Res*, **113**. doi:10.1029/2008JD009906.

Ramana, M., Ramanathan, V., Kim, D., Roberts, G., and Corrigan, C. (2007). Albedo, atmospheric solar absorption and heating rate measurements with stacked UAVs. *Quarterly Journal of the Royal Meteorological Society*, **133**(629), 1913.

Redelsperger, J., Thorncroft, C., Diedhiou, A., Lebel, T., Parker, D., and Polcher, J. (2008). African monsoon multidisciplinary analysis: an international research project and field campaign. *Bulletin of the American Meteorological Society*, **87**(12), 1739–1746. doi:10.1175/BAMS-87-12-1739.

Reid, E., Reid, J., Meier, M., Dunlap, M., Cliff, S., Broumas, A., Perry, K., and Maring, H. (2003a). Characterization of African dust transported to Puerto Rico by individual particle and size segregated bulk analysis. *Journal of Geophysical Research*, **108**(D19).

Reid, J., Westphal, D., Livingston, J., Savoie, D., Maring, H., Jonsson, H., Eleuterio, D., Kinney, J., and Reid, E. (2002). Dust vertical distribution in the Caribbean during the Puerto Rico Dust experiment. *Geophysical Research Letters*, **29**(7), 55–1.

Reid, J., Jonsson, H., Maring, H., Smirnov, A., Savoie, D., Cliff, S., Reid, E., Livingston, J., Meier, M., Dubovik, O., *et al.* (2003b). Comparison of size and morphological measurements of coarse mode dust particles from Africa. *J. Geophys. Res*, **108**, 8593.

Reid, J., Reid, E., Walker, A., Piketh, S., Cliff, S., Al Mandoos, A., Tsay, S., and Eck, T. (2008). Dynamics of southwest Asian dust particle size characteristics with implications for global dust research. *J. Geophys. Res*, **113**. doi:10.1029/2007JD009752.

Remer, L. and Kaufman, Y. (2006). Aerosol direct radiative effect at the top of the atmosphere over cloud free ocean derived from four years of MODIS data. *Atmospheric Chemistry and Physics*, **6**, 237–253.

Richardson, M., DeMott, P., Kreidenweis, S., Cziczo, D., Dunlea, E., Jimenez, J., Thomson, D., Ashbaugh, L., Borys, R., Westphal, D., *et al.* (2007). Measurements of heterogeneous ice nuclei in the western United States in springtime and their relation to aerosol characteristics. *Journal of Geophysical Research*, **112**. doi:10.1029/2006JD007500.

Rijkenberg, M., Powell, C., Dall'Osto, M., Nielsdottir, M., Patey, M., Hill, P., Baker, A., Jickells, T., Harrison, R., and Achterberg, E. (2008). Changes in iron speciation following a Saharan dust event in the tropical North Atlantic Ocean. *Marine Chemistry*, **110**(1-2), 56–67.

Ryall, D. and Maryon, R. (1998). Validation of the UK Met Office's NAME model against the ETEX dataset. *Atmospheric Environment*, **32**, 4265–4276.

Salisbury, G., Williams, J., Gros, V., Bartenbach, S., Xu, X., Fischer, H., Kormann, R., de Reus, M., and Zollner, M. (2006). Assessing the effect of a Saharan dust storm on oxygenated organic compounds at Izana, Tenerife (July-August 2002)(DOI 10.1029/2005JD006840). *Journal of Geophysical Research*, **111**(D22), 22303.

Sassen, K. (2000). *Light scattering by nonspherical particles: theory, measurements, and applications*, chapter Lidar Backscatter Depolarization Technique for Cloud and Aerosol Research, page 393. Academic Press.

Saunders, R. and Barnes, J. (1991). Intercomparison flights of pyranometers and pyrgeometers ont he mrf c-130. Technical report, Met Office, Exeter, UK. Internal Note no. 56.

Saunders, R., Foot, J., Kilsby, C., and Seymour, J. (1991). Report of broad-band radiative fluxes working group. Technical report, UK Met Office. MRF Technical note no. 5.

Saunders, R., Brogniez, G., Buriez, J., Meerkötter, R., and Wendling, P. (1992). A Comparison of Measured and Modeled Broadband Fluxes from Aircraft Data during the ICE'89 Field Experiment. *Journal of Atmospheric and Oceanic Technology*, **9**(4), 391–406.

Schepanski, K., Tegen, I., Laurent, B., Heinold, B., and Macke, A. (2007). A new Saharan dust source activation frequency map derived from MSG-SEVIRI IR-channels. *Geophysical Research Letters*, **34**. doi:10.1029/2007GL030168.

Schmetz, J., Pili, P., Tjemkes, S., Just, D., Kerkmann, J., Rota, S., and Ratier, A. (2002). An Introduction to Meteosat Second Generation (MSG). *Bulletin of the American Meteorological Society*, **83**(7), 977–992.

Schütz, L. and Sebert, M. (1987). Mineral aerosols and source identification. *Journal of the Atmospheric Sciences*, **18**(1), 1–10.

Seinfeld, J. and Pandis, S. (2006). *Atmospheric Chemistry and Physics*, chapter Properties of the Atmospheric Aerosol. Wiley, 2nd edition edition.

Shettle, E. and Fenn, R. (1979). Models for the Aerosols of the Lower Atmosphere and the Effects of Humidity Variations on their Optical Properties. Technical Report AFGL-TR-79-0241, AFGL. AFGL Tech. Report.

Singer, A., Ganor, E., Dultz, S., and Fischer, W. (2003). Dust deposition over the Dead Sea. *Journal of Arid Environments*, **53**(1), 41–59.

Slingo, A., Ackerman, T., Allan, R., Kassianov, E., McFarlane, S., Robinson, G., Barnard, J., Miller, M., Harries, J., Russell, J., and Dewitte, S. (2006). Observations of the impact of a major Saharan dust storm on the atmospheric radiation balance. *Journal of Geophysical Research*, **33**(L24817). doi:10.1029/2006GL027869.

Sokolik, I. and Toon, O. (1996). Direct radiative forcing by anthropogenic airborne mineral aerosols. *Nature*, **381**(6584), 681–683.

Sokolik, I. and Toon, O. (1999). Incorporation of mineralogical composition into models of the radiative properties of mineral aerosol from UV to IR wavelengths. *Journal of geophysical research*, **104**(D 8), 9423–9444.

Sokolik, I., Andronova, A., and Johnson, T. (1993). Complex refractive index of atmospheric dust aerosols. *Atmospheric Environment*, **27A**(16), 2495–2502.

Solomon, S., Qin, M., Manning, Z., Chen, Z., Marquis, M., Averyt, K., M.Tignor, and Miller, H., editors (2007). *Climate Change 2007: The Physical Science Basis. Contribution of Working Group I to the Fourth Assessment Report of the Intergovernmental Panel on Climate Change*, chapter IPCC, 2007: Summary for Policymakers. Cambridge Univerity Press, UK.

Stuut, J., Zabel, M., Ratmeyer, V., Helmke, P., Schefuß, E., Lavik, G., and Schneider, R. (2005). Provenance of present-day eolian dust collected off NW Africa. *J. Geophys. Res*, **110**. doi:10.1029/2004JD005161.

Tanré, D., Kaufman, Y., Holben, B., Chatenet, B., Karineli, A., Lavenu, F., Blarel, L., Dubovik, O., and Remer, L. (2001). Climatology of dust aerosol size distribution and optical properties derived from remotely sensed data in the solar spectrum. *Journal of Geophysical Research*, **106**(D16), 18,205–18,217.

Taylor, J., Edwards, J., Glew, M., Hignett, P., and Slingo, A. (1996). Studies with a flexible new radiation code. II: Comparisons with aircraft short-wave observations. *Quarterly Journal of the Royal Meteorological Society*, **122**, 839–862.

Tegen, I. and Fung, I. (1995). Contribution to the atmospheric mineral aerosol load from land surface modification. *Journal of Geophysical Research*, **100**(D9), 18,707–18,726.

Tegen, I. and Lacis, A. (1996). Modeling of particle size distribution and its influence on the radiative properties of mineral dust aerosol. *Journal of Geophysical Research*, **101**(D14).

Tegen, I., Werner, M., Harrison, S., and Kohfeld, K. (2004). Relative importance of climate and land use in determining present and future global soil dust emission. *Geophysical Research Letters*, **31**(5). doi:10.1029/2003GL019296.

Todd, M., Washington, R., Martins, J., Dubovik, O., Lizcano, G., M'Bainayel, S., and Engelstaedter, S. (2007). Mineral dust emission from the Bodélé Depression, northern Chad, during BoDEx 2005. *J. Geophys. Res*, **112**. doi:10.1029/2006JD007170.

Torres, O., Bhartia, P., Herman, J., Ahmad, Z., and Gleason, J. (1998). Derivation of aerosol properties from satellite measurements of backscattered ultraviolet radiation: Theoretical basis. *Journal of Geophysical Research*, **103**(D14), 17099–17110.

Torres, O., Tanskanen, A., Veihelmann, B., Ahn, C., Braak, R., Bhartia, P., Veefkind, P., and Levelt, P. (2007). Aerosols and surface UV products from Ozone Monitoring Instrument observations: An overview. *J. Geophys. Res*, **112**.

Wang, H., Shi, G., Li, S., Li, W., Wang, B., and Huang, Y. (2006). The impacts of optical properties on radiative forcing due to dust aerosol. *Advances in Atmospheric Sciences*, **23**(3), 431–441.

Washington, R. and Todd, M. (2005). Atmospheric controls on mineral dust emission from the Bodele Depression, Chad: The role of the low level jet. *Geophysical Research Letters*, **32**. doi:10.1029/2005GL.

Washington, R., Todd, M., Middleton, N., and Goudie, A. (2003). Dust-storm source areas determined by the total ozone monitoring spectrometer and surface observations. *Annals of the Association of American Geographers*, **93**(2), 297–313.

Washington, R., Todd, M., Engelstaedter, S., Mbainayel, S., and Mitchell, F. (2006). Dust and the low-level circulation over the Bodélé Depression, Chad: Observations from BoDEx 2005. *J. Geophys. Res*, **111**, D03201.

WCP, editor (1983). *WMO Report of the Experts' Meeting on Aerosols and their Climatic Effects*, number WCP-55, Geneva, Switzerland. World Meteorol. Org.

Webster, H., Carroll, E., Jones, A., Manning, A., and Thomson, D. (2007). The Buncefield oil depot incident: a discussion of the meteorology. *WEATHER-LONDON*, **62**(12), 325.

Wendisch, M., Müller, D., Schell, D., and Heintzenberg, J. (2001). An Airborne Spectral Albedometer with Active Horizontal Stabilization. *Journal of Atmospheric and Oceanic Technology*, **18**(11), 1856–1866.

Winker, D., Pelon, J., and McCormick, M. (2003). The CALIPSO mission: Spaceborne lidar for observation of aerosols and clouds. In *Proc. SPIE*, volume 4893, page 11.

Winker, D., Hunt, W., and McGill, M. (2007). Initial performance assessment of CALIOP. *Geophys. Res. Lett*, **34**.

Witham, C. and Manning, A. (2007). Impacts of Russian biomass burning on UK air quality. *Atmospheric Environment*, **41**(37), 8075–8090.

Yoshida, M. and Murakami, H. (2008). Dust absorption averaged over the Sahara inferred from moderate resolution imaging spectroradiometer. *Applied Optics*, **47**(12), 1995–2003.

Yoshioka, M., Mahowald, N., Dufresne, J., and Luo, C. (2005). Simulation of absorbing aerosol indices for African dust. *Journal of Geophysical Research*, **110**. 10.1029/2004JD005276.

Zhang, J. and Christopher, S. (2003). Longwave radiative forcing of Saharan dust aerosols estimated from MODIS, MISR, and CERES observations on Terra. *Geophys. Res. Lett*, **30**(23), 2188.

Zhu, A., Ramanathan, V., Li, F., and Kim, D. (2007). Dust plumes over the Pacific, Indian, and Atlantic oceans: Climatology and radiative impact. *Journal of Geophysical Research*, **112**. 10.1029/2007JD008427.

Appendix A

Paper published in the Journal of Geophysical Research

JOURNAL OF GEOPHYSICAL RESEARCH, VOL. 113, D14S05, doi:10.1029/2007JD009606, 2008

Seasonal variations of the physical and optical characteristics of Saharan dust: Results from the Dust Outflow and Deposition to the Ocean (DODO) experiment

C. L. McConnell,[1] E. J. Highwood,[1] H. Coe,[2] P. Formenti,[3] B. Anderson,[4] S. Osborne,[5] S. Nava,[6] K. Desboeufs,[3] G. Chen,[4] and M. A. J. Harrison[5]

Received 15 November 2007; revised 20 March 2008; accepted 24 April 2008; published 28 June 2008.

[1] North African dust is important for climate through its direct radiative effect on solar and terrestrial radiation and its role in the biogeochemical system. The Dust Outflow and Deposition to the Ocean project (DODO) aimed to characterize the physical and optical properties of airborne North African dust in two seasons and to use these observations to constrain model simulations, with the ultimate aim of being able to quantify the deposition of iron to the North Atlantic Ocean. The in situ properties of dust from airborne campaigns measured during February and August 2006, based at Dakar, Senegal, are presented here. Average values of the single scattering albedo (0.99, 0.98), mass specific extinction (0.85 $m^2\ g^{-1}$, 1.14 $m^2\ g^{-1}$), asymmetry parameter (0.68, 0.68), and refractive index (1.53−0.0005i, 1.53−0.0014i) for the accumulation mode were found to differ by varying degrees between the dry and wet season, respectively. It is hypothesized that these differences are due to different source regions and transport processes which also differ between the DODO campaigns. Elemental ratios of Ca/Al were found to differ between the dry and wet season (1.1 and 0.5, respectively). Differences in vertical profiles are found between seasons and between land and ocean locations and reflect the different dynamics of the seasons. Using measurements of the coarse mode size distribution and illustrative Mie calculations, the optical properties are found to be very sensitive to the presence and amount of coarse mode of mineral dust, and the importance of accurate measurements of the coarse mode of dust is highlighted.

Citation: McConnell, C. L., E. J. Highwood, H. Coe, P. Formenti, B. Anderson, S. Osborne, S. Nava, K. Desboeufs, G. Chen, and M. A. J. Harrison (2008), Seasonal variations of the physical and optical characteristics of Saharan dust: Results from the Dust Outflow and Deposition to the Ocean (DODO) experiment, *J. Geophys. Res.*, *113*, D14S05, doi:10.1029/2007JD009606.

1. Introduction

[2] Mineral dust is an important species in the Earth's atmosphere. Picked up from the surface around the globe, the majority of this dust is a natural aerosol although models suggest that 5−7% of the global dust loading is anthropogenic in origin [*Tegen et al.*, 2004] and this may be between 0 and 15% in the North African region [*Yoshioka et al.*, 2005]. Activities such as land use change and overgrazing increase the dust available for uplift [e.g., *Tegen and Fung*, 1995]. Dust is lifted from land surfaces across the globe, but Saharan mineral dust accounts for an annual source of 400−700 Tg a^{-1} [*Washington et al.*, 2003], a large proportion of the total. Dust is emitted from sources within North Africa, of which the Sahara forms the major part [e.g., *Woodward*, 2001], and can be advected across the Atlantic toward the southeast USA and South America [*Prospero*, 1999; *Formenti et al.*, 2001; *Reid et al.*, 2003]. Some of this dust advection occurs during Africa-wide outbreaks [e.g., *Slingo et al.*, 2006]; there has been somewhat less focus on the properties of airborne dust during less extreme outbreaks and throughout the year.

[3] The most direct way in which mineral dust can influence global climate is by scattering and absorbing radiation, affecting both regional and global energy balance. Mineral dust, perhaps most interestingly of all aerosols, can affect both solar and terrestrial radiation. In the shortwave part of the spectrum, dust scatters radiation back to space but depending on the albedo of the underlying surface it can either increase (over ocean) or make little difference (over desert) to the total albedo. The impact in the longwave depends crucially on the surface temperature and the altitude of the dust layer. Radiation from the ground is absorbed in the dust layer and reemitted back toward the ground thereby potentially increasing the surface temperature. For dust over the ocean surface the result is usually dominated by the solar effect, however for dust at altitude

[1]Department of Meteorology, University of Reading, Reading, UK.
[2]School of Earth, Atmosphere and Environmental Science, University of Manchester, Manchester, UK.
[3]LISA, CNRS, Universités Paris 12 et Paris 7, Créteil, France.
[4]NASA Langley Research Center, Hampton, Virginia, USA.
[5]Met Office, Exeter, UK.
[6]National Institute of Nuclear Physics, Florence, Italy.

0148-0227/08/2007JD009606$09.00

over a desert surface the longwave effect can dominate the flux changes at the top of the atmosphere. It is also important to distinguish between the effect at the top of the atmosphere and at the surface, since the direct solar radiation reaching the ground can be dramatically reduced while the diffuse component increases substantially during major dust outbreaks. The impact of dust on longwave radiation is important for satellite retrievals of sea surface temperature and the spectral signal within the 8–12 μm region can be used to infer the mineralogy of the dust [*Highwood et al.*, 2003]. The Saharan Dust Experiment (SHADE) surveyed the optical properties and radiative impact of Saharan dust during September 2000 [*Haywood et al.*, 2003]. Magnitudes for the local direct radiative effect over the ocean reached as much as -130 W m^{-2} at the top of the atmosphere for an individual dust storm. *Slingo et al.* [2006] also showed top of atmosphere shortwave flux increased by 100 W m^{-2} while the surface downward solar flux at Niamey reduced by as much as 300 W m^{-2} for the dust storm of early March 2006. These are considerable perturbations to the local energy balance. In terms of global climate change, the IPCC 2007 report considered the anthropogenic dust top of the atmosphere radiative forcing to range between -0.3 W m^{-2} and $+0.1$ W m^{-2} [*Forster et al.*, 2007]. Key parameters for determining the radiative effect of dust include the single scattering albedo (ω_0), the asymmetry parameter (g), and the mass specific extinction (k_{ext}), which are dependent on size distribution and refractive index.

[4] Other impacts of North African dust on the climate system are less well studied and quantified. Even small concentrations of mineral dust are thought to be able to significantly affect cold cloud properties including the radiative properties of cirrus, dehydration of the tropopause and convective cloud dynamics. Laboratory studies show that dust might act as ice nucleii and have shown dust to exhibit complex primary and secondary nucleation at varying ice supersaturations [e.g., *Field et al.*, 2006]. Accordingly, *DeMott et al.* [2003] results from CRYSTAL-FACE (The Cirrus Regional Study of Tropical Anvils and Cirrus Layers–Florida Area Cirrus Experiment) showed that Saharan dust plumes were associated with elevated ice nuclei counts across Florida, while *Richardson et al.* [2007] showed a proportionately high contribution to ice nuclei by mineral dust over the continental USA. It has also been hypothesized that dust may provide a surface for heterogeneous chemical reactions to take place. For example, ozone can be destroyed on pure calcium carbonate particles. *Salisbury et al.* [2006] found that daily cycles and absolute concentrations of some oxygenated species were different during dust storms in the MINATROC (Mineral dust aerosol and tropospheric chemistry) project. However, it was impossible to unequivocally attribute this to heterogeneous reactions on the dust itself.

[5] Airborne North African dust is of great interest to marine biologists. Much of the dust leaving the western coast of Africa is deposited in the Atlantic Ocean where it provides a flux of nutrients such as iron and phosphorus to the ocean. This deposition stimulates nitrogen fixation and relieves iron limitation of phytoplankton activity. The resulting growth of marine biological organisms results in ocean sequestration of carbon dioxide and fluxes of halocarbons, alkylnitrate and DMS between atmosphere and ocean. Iron from mineral dust therefore plays an indirect route in carbon and other mass fluxes between atmosphere and ocean [*Jickells et al.*, 2005].

[6] One climate impact which has received much interest in recent years has been the role of North African dust in tropical storm and hurricane formation. *Jones et al.* [2004] reported indirect observations of modification of African Easterly Waves (the forerunner disturbances of some hurricanes) via the radiative impacts of dust. *Evan et al.* [2006] showed that mean dust coverage as measured by satellites and tropical cyclone activity are strongly correlated over the North Atlantic. Particular highlight has been given to the contrasting North Atlantic hurricane seasons of 2005 (active, fewer dust outbreaks than normal) and 2006 (less active, more dust outbreaks than normal). However, this is not in itself enough to suggest that the dust is directly influencing the tropical cyclones. Various mechanisms including the radiative impact on sea surface temperature, and alteration of vertical shear regions, and the entrainment of dust laden dry air have been proposed. However, none of these have been shown to be a predominant governor of cyclone activity, with N. Atlantic sea surface temperatures playing a very large role in determining the cyclone activity. The correlation between dust and cyclone activity may stem from them both being driven by a third party, for example Sahelian rainfall in the previous season.

[7] Because of the significant destructive capacity of hurricanes, there is considerable interest in summer season dust uplift and transport. The mechanisms of dust production and uplift are rather different between dry season (November to March) and the wet season (July–September). During the dry season, dust in western Africa is mainly found at low altitudes and its uplift often results from activity along trailing cold fronts associated with systems passing through the Mediterranean region. Orography and local advection effects then magnify the dust uplift [e.g., *Slingo et al.*, 2006]. The winter season, therefore, tends to produce very dramatic dust outbreaks that last a few days. During the wet season, dust tends to be uplifted in convection over the African continent and then transported westward at altitude. The different transport mechanisms between seasons could have an effect on the size distribution of dust, and hence result in different optical properties. The vertical profiles of dust also vary substantially between seasons [e.g., *Karyampudi et al.*, 1999; *Zhu et al.*, 2007], which will also have an impact on the radiative effect.

[8] In addition, there is evidence that the African source regions may differ throughout the year [e.g., *Schepanski et al.*, 2007; *Washington et al.*, 2003; *Chiapello et al.*, 1997]. The Bodélé Depression in Chad is perhaps the major source region for mineral dust, but there are significant sources in the western Sahara which also influence the dust flowing toward the Atlantic. As shown by *Washington and Todd* [2005] and *Engelstaedter and Washington* [2007], there is evidence that the uplift from these different sources responds to different parts of the atmospheric dynamics. In the case of the Bodélé Depression the presence and strength of the low-level jet is important, while dust production from the western Sahara seems to be more closely related to the degree of low-level convergence. Differing mineralogy at these sources may influence the

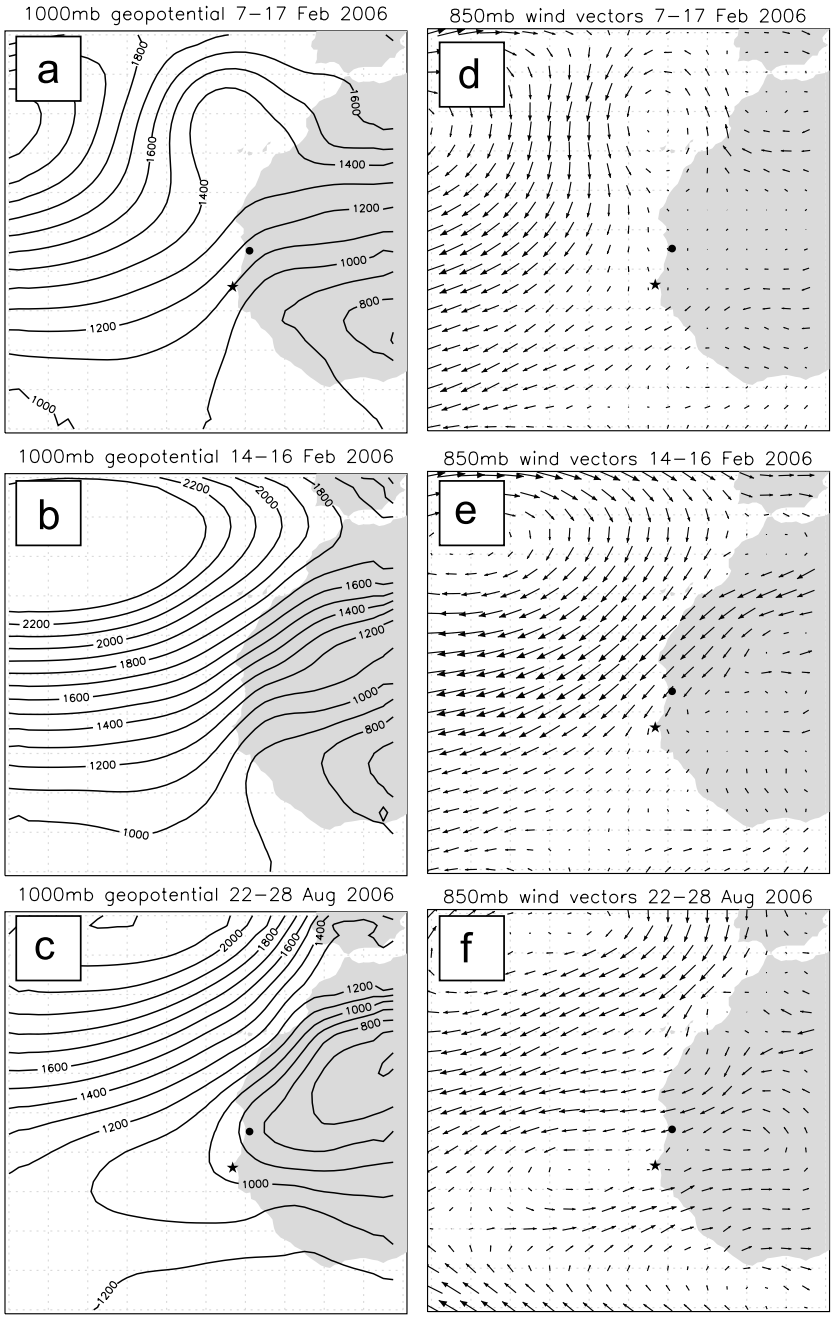

Figure 1. DODO campaign meteorology from ERA operational analyses. The 1000 mbar geopotential (m^2 s^{-1}) for (a) DODO1 period 7–17 February 2006, (b) DODO1 period 14–16 February 2006, and (c) DODO2 period 22–28 August 2006. The 850 mbar wind vectors for (d) DODO1 period 7–17 February 2006, (e) DODO1 period 14–16 February 2006, and (e) DODO2 period 22–28 August 2006. Locations of Dakar and Nouakchott are indicated by a star and circle, respectively.

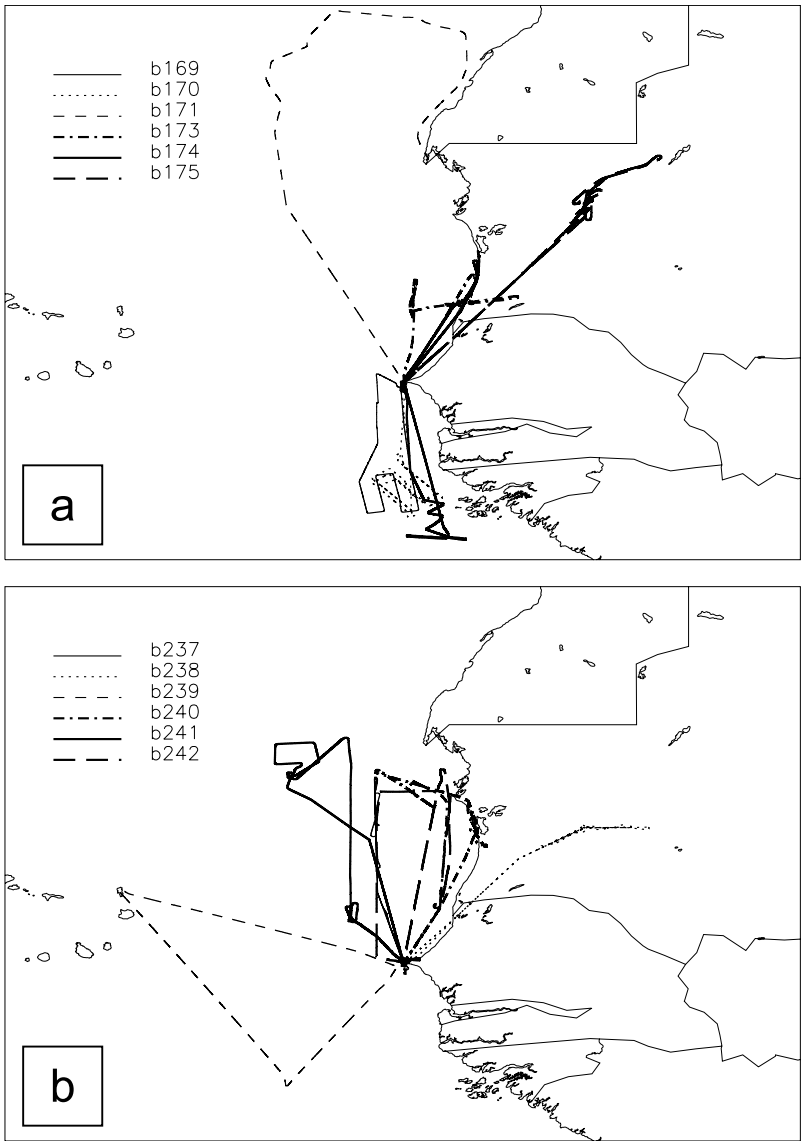

Figure 2. Flight tracks for (a) DODO1 and (b) DODO2 campaigns based in Dakar, Senegal.

composition of mineral dust [*Claquin et al.*, 1999; *Formenti et al.*, 2008] and its microphysics, and thus the radiative impact [e.g., *Todd et al.*, 2007; *Highwood et al.*, 2003].

[9] It is important to remember that dust is not the only aerosol that affects sub Saharan Africa. During the dry season, considerable biomass burning activity along the coast of the Gulf of Guinea and convection there results in a ubiquitous layer of biomass burning aerosol at higher altitudes above the dust, and this complicates retrieval of aerosol properties from AERONET (Aerosol Robotic Network) and satellite methods as biomass burning aerosol has quite different properties to dust. The interaction of dust and biomass during January–February 2006 was examined in detail by the Dust and Biomass Experiment (DABEX) of the UK Met Office [*Johnson et al.*, 2008; J. M. Haywood et al., Overview of the Dust and Biomass Burning Experiment and African Monsoon Multidisciplinary Analysis Special Observing Period-0, submitted to *Journal of Geophysical Research*, 2008] and parallels between dust and biomass found during that campaign and those reported here are discussed by *Osborne et al.* [2008].

[10] In terms of understanding the climate impact of dust throughout the year there is clearly a need to establish whether the likely seasonal differences in uplift and trans-

Table 1. Summary of Flights During DODO1 and DODO2 Campaigns

Flight Number	Date	Takeoff, Landing	Operating Area	Objectives
DODO1				
B169	7 Feb 2006	112228, 141834	over ocean south of Dakar	instrument shake-down, biomass burning aerosol sampling
B170	11 Feb 2006	095447, 145335	over ocean south of Dakar	in situ biomass aerosol collection
B171 (B172)	12 Feb 2006	084911, 130656	north of Nouadhibou, over ocean	model validation for major dust storm to north of region; aircraft lost science power during refuel therefore no data available from B172
B173	14 Feb 2006	094953, 143615	coastal region, Dakar-Nouackchott	in situ sampling of local dust source
B174	15 Feb 2006	094400, 131354	over sea north and south of Dakar	in situ sampling of dust advected over ocean and biomass aerosol
B175	16 Feb 2006	085143, 141538	land regions in northern Mauritania	in situ sampling and radiometric measurements over land, moderate dust loading
DODO2				
B237	22 Aug 2006	135855, 182401	over ocean northwest of Dakar	in situ and radiation measurements of dust over ocean off Senegal/Mauritania coast
B238	23 Aug 2006	130025, 173152	land regions in northern Mauritania	sample heavy dust loadings over land in Mauritania forecast by dust models and visible in satellite imagery
B239	24 Aug 2006	095141, 135328	over ocean, between and to the south of Dakar and Sal	in situ measurements of dust forecast over ocean to south of Dakar-Sal area
B240	24 Aug 2006	151619, 193645	over ocean northwest of Dakar	mapping of in situ dust to north of Dakar for comparison with B239
B241	25 Aug 2006	135438, 183200	over ocean between Nouadhibou and Dakar	intercomparison flight with NASA DC8 and high-level calibration of radiometers
B242	28 Aug 2006	110243, 153338	over ocean northwest of Dakar	in situ and radiation measurements of moderate dust loadings to north of Dakar

port processes lead to any discernible influence in radiative or microphysical properties. From a biogeochemical point of view, these may also lead to differences in nutrient deposition to the ocean. The Dust Outflow and Deposition to the Ocean (DODO) project was conceived to use aircraft measurements of airborne dust to constrain model estimates of dust deposition to the ocean. The microphysical and optical properties and the vertical structure the dust that were measured during the two major fieldwork periods in Africa are described in this paper. Section 2 describes the airborne campaigns and instrumentation in more detail, including measurement correction procedures based on an intercomparison flight with the NASA DC-8 aircraft. The characteristics of dust found during both DODO campaigns are described in sections 3, 4 and 5. The paper ends with discussion in section 6. The project is ongoing, and model results will be reported elsewhere in due course.

2. Methodology

2.1. DODO Meteorology and Flight Patterns

[11] In order to characterize airborne North African dust and outflow to the ocean in both the dry season and the wet season, two airborne campaigns based in Dakar, Senegal, were organized. DODO1 took place during the dry season from 7 to 16 February 2006, while DODO2 followed in the wet season from 22 to 28 August. Both campaigns were also associated with the AMMA (African Monsoon Multidisciplinary Analysis) project [*Redelsperger et al.*, 2006]. The 1000 mbar geopotential and 850 mbar wind vectors are shown in Figure 1, for the whole of DODO1 (Figures 1a and 1d), the last 3 days of DODO1 (Figures 1b and 1e), and the whole of DODO2 (Figures 1c and 1f). During DODO1 the flow changed substantially: for the first week the flow was dominated by an anomalous low-pressure system located over the Canary Islands, shown by the geopotential lines in Figure 1a, which resulted in little offshore flow in the region between Dakar and Nouakchott (Figure 1d). This is contrary to the predominantly easterly flow that would be expected from climatology [e.g., *Hastenrath*, 1991] and no dust was sampled during this period. The flow changed during the three final days of the campaign, becoming more climatological with northerly/northeasterly flow to the north of Dakar (Figures 1b and 1e), advecting light dust loadings toward Dakar. During this period the dust samples discussed in this study were collected on flights B173, B174 and B175 (Figure 2a). This flow pattern is not reflected in the DODO1 averages (Figures 1a and 1d) because of its short time duration. To the south of Dakar the flow was offshore (see Figure 1d) giving rise to the advection of biomass aerosol (originating from southern West Africa) at midlevels in the troposphere, this being sampled during three of the six DODO1 flights which operated to the south of Dakar (see Figure 2a).

[12] The geopotential in Figure 1c shows the Saharan heat low positioned over Algeria during DODO2. The wind vectors at 850 mbar suggest offshore flow to the north of Dakar, with a recirculation to the south of the region. However, it is important to note that these mean circulation patterns are a combination of flow patterns from a succession of African easterly waves that passed over Dakar during this time, bringing relatively large meridional excursions of alternately dry and moist airflow over Dakar. The six flights during DODO2 concentrated mainly on the ocean and land areas to the north of Dakar (Figure 2b), reflecting the largest likelihood of dust sampling. During DODO2, Dakar itself was frequently affected by clouds associated with Mesoscale Convective Systems which passed mainly to the south of the main operating area. A summary of the

Table 2. Summary of Aerosol-Related Instruments on Board the FAAM BAe146 Operated During the DODO Campaigns

Type of Measurement	Instrument	Size Range (Optically Equivalent Radius), Wavelengths, etc.	Comment
Aerosol microphysics	PMS PCASP, GRIMM OPC, DMT CDP	0.05–1.5 μm, 0.15–20 μm, 2.5–20 μm	
Aerosol optical properties	TSI nephelometer, PSAP	λ = 0.45, 0.55, 0.7 μm; λ = 0.567 μm	particle scattering coefficient, particle absorption coefficient
Aerosol chemical composition	bulk filters, Aerodyne AMS, VACC	90-mm Nuclepore 0.4 μm pore size; quartz; Particle sizes 50–500 nm; temperature range 50–300°C, PCASP 0.05–1.5 μm	inorganics (elements and water soluble fraction), carbon (EC and OC), volatile and semivolatile aerosols, water and volatile material
Trace gas chemistry	O_3, CO		O_3 and CO are sampled using online analyzers
Thermodynamics	AVAPS		temperature, pressure, winds, GPS

location, duration and nature of the flights in both DODO campaigns is given in Table 1.

[13] In this study results are presented for aircraft maneuvers consisting of vertical profiles, measuring the vertical distribution of aerosol, and straight and level runs, measuring in situ aerosol for a duration of between 5 and 30 min at a constant altitude. Vertical profiles range from either ground level (in the case of takeoff or landing) or the aircraft's minimum safe altitude of 50ft over sea or approximately 500ft over land, to above the aerosol layer. The aircraft flies at 110 m s^{-1} but ascends/descends at 5 m s^{-1} and therefore covers considerable horizontal distance during a profile, which means that the straight and level run data is valuable in terms of showing the horizontal variation. Most instruments on the BAe146 (including the nephelometer) sample at least 1Hz, giving good resolution of data in the vertical and horizontal. Straight and level runs will hereafter be referred to as "runs."

2.2. BAe146 Instrumentation

[14] The core instrumentation on the UK community Facility for Airborne Atmospheric Measurements (FAAM) BAe146 is described by Haywood et al. (submitted manuscript, 2008). Details of the most relevant instrumentation for aerosol and dust measurements are given in Table 2. Key instruments included the wing-mounted Passive Cavity Aerosol Spectrometer Probe (PCASP), TSI integrating nephelometer model 3563 and Radiance Research Particle Soot Absorption Photometer (PSAP) (corrected according to standard procedures as in the work by *Bond et al.* [1999]) in terms of aerosol microphysical and optical properties for the accumulation mode.

[15] Bulk filters were used to collect samples of airborne dust. The aerosol sampling system used on board the BAe146 is identical to that previously used on board the UK Met Office C-130 and is described in detail by *Andreae et al.* [2000], who estimated the inlets to the filters to sample 35% of the coarse mode by mass. Aerosol particles were sampled by filtration onto two stacked filter units (SFUs) mounted in parallel. Each SFU can hold a maximum of three filters on sequential 47-mm diameter polyethylene supports, but only one stage was used during DODO. Samples were collected only during horizontal flight legs lasting not less than 20–30 min in order to guarantee sufficient loading of the filter samples. One SFU consisted of a Nucleopore filter (nominal pore size 0.4 μm) measuring the inorganic composition. The second SFU was used for measuring carbonaceous aerosols on one quartz filter.

2.2.1. Nephelometer Corrections Using the DC-8 Intercomparison

[16] During DODO2, the BAe146 flew a wing tip to wing tip comparison flight (B241) with the NASA DC-8. Flight B241 included 3 straight and level runs within the Saharan Air Layer over the Atlantic Ocean to the north of the Cape Verde Islands (see Figure 2b). This provided an opportunity to compare the nephelometers on board both aircraft. The BAe146 was operating a TSI 3563 nephelometer running from a Rosemount inlet, which has been estimated by *Haywood et al.* [2003] to have an upper limit for dust particles at around 3 μm in terms of optical diameter, although the true cutoff is not well defined. The DC-8 operated a TSI 3563 nephelometer behind the NASA LaRC type inlet. This inlet has been shown to give a 50% loss of dust particles above 3.6 μm aerodynamic diameter (giving an optically equivalent diameter of 2.0 μm [*McNaughton et al.*, 2007]).

[17] Figure 3 shows the scattering from the DC-8 and the BAe146 TSI nephelometers during one of the three straight and level runs from flight B241. In each case, both nephelometers measured dry scattering at low values of relative humidity and the data has been corrected as advised by *Anderson and Ogren* [1998]. Relative humidity during these runs varied between 52% to 69% and so no attempt

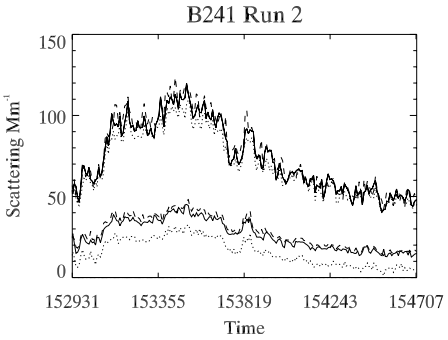

Figure 3. Nephelometer measurements of scattering in Mm^{-1} from intercomparison flight B241 (BAe146 run 2) at 2100 m within dust layer. Heavy lines are BAe146 measurements corrected according to *Anderson and Ogren* [1998]. Light lines are DC-8 TSI nephelometer data corrected similarly. Dotted lines are 450 nm, solid lines are 550 nm, and dashed lines are 700 nm.

Table 3. Linear Pearson Correlation Coefficients (r) Between DC-8 and BAe146 Data During Three Wing Tip to Wing Tip Straight and Level Runs Within Dust Layers During DODO2 Flight B241

Channel	Run 1	Run 2	Run 3
0.45 μm	0.93	0.96	0.93
0.55 μm	0.82	0.97	0.94
0.70 μm	0.80	0.94	0.91

has been made to account for any hygroscopic growth, which is thought to be small for dust particles within this range of humidities [e.g., *Li-Jones et al.*, 1998; *Carrico et al.*, 2003] It is apparent that the two nephelometers are sampling similar variability in the aerosol layer (i.e., spatial variability) however there is a significant offset between the two instruments, with the BAe146 scattering being substantially lower than the DC-8. In addition, the 450 nm channel on the BAe146 nephelometer is reading relatively much lower than other frequencies compared to the DC-8. The ratio between DC-8 and BAe146 values is approximately 2.5 in each of the 3 runs. Table 3 shows the linear Pearson correlation coefficients (r) for scattering measured by the two systems at the three different wavelengths during the three different straight and level runs within dust. The average ratios of the DC-8 to BAe146 scattering across the three runs were 7.3, 2.36 and 2.4 at 450, 550 and 700 nm respectively.

[18] The combined evidence of (1) high correlation between the two nephelometers at all wavelengths and in all three runs, (2) higher scattering measured by the DC-8 nephelometer by a factor of 2.5, and (3) underestimation of aerosol optical depth by the nephelometer and PSAP compared to AERONET by an average factor of 3.1 (see following paragraph), point to a fault with the BAe146 nephelometer, suggesting a sensitivity loss perhaps due to the high dust loadings experienced during an immediately preceding campaign where the nephelometer was not closely monitored and which may have resulted in the detectors becoming dirty. On the basis of the similar inlet cutoff diameters on the two aircraft and the large differences in scattering between the two nephelometers, it is thought unlikely that the differences in scattering are due to the DC-8 inlet having a greater passing efficiency.

[19] It was therefore decided that for DODO2, the BAe146 nephelometer data would be scaled to agree with the DC-8 TSI data. A linear fit was used to fit the BAe146 data to the DC-8 data. The resulting corrections using the average fit parameters across all three runs for 450, 550 and 700 μm channels of the BAe146 scattering data are shown below.

$$\sigma_{corr}^{450}\left(\text{in m}^{-1}\right) = 33.2 \times 10^{-6} + 7.3 \times \sigma^{450} \quad (1)$$

$$\sigma_{corr}^{550}\left(\text{in m}^{-1}\right) = 11.3 \times 10^{-6} + 2.36 \times \sigma^{550} \quad (2)$$

$$\sigma_{corr}^{700}\left(\text{in m}^{-1}\right) = 10.1 \times 10^{-6} + 2.4 \times \sigma^{700} \quad (3)$$

Note that a larger correction for blue wavelengths is required because of the very low scattering at blue wavelengths compared to red and green wavelengths. Figure 4 shows the effect of this correction for one of the straight and level runs, the triangles representing the correlation of the original BAe146 data with the DC-8 data, and the diamonds the improved correspondence when the fits in equations (1)–(3) above are applied. It should be noted that the uncertainty in passing efficiency of the BAe146 Rosemount inlet relative to the DC-8 LaRC type inlet results in a small amount of uncertainty in applying the scaling factor from the intercomparison flight B241 to the other DODO2 flights where the aerosol size distributions and optical properties may be different.

[20] The underestimation of scattering by the BAe146 nephelometer can also be shown by comparing optical depths measured by the Dakar AERONET station at Mbour to those obtained by integrating the vertical profiles of scattering in the vicinity of the only AERONET station, according to the expression:

$$\tau_{550} = \int_0^z \frac{\sigma_{corr}^{550}}{\omega_0^{550}}\, dz \quad (4)$$

where ω_0^{550} is the single scattering albedo calculated from a horizontal run in a dust layer at an appropriate altitude. PSAP data is only used for straight and level runs when the flow rate has been manually set to 3 L per minute and integration of absorption measured by the PSAP during profiles is not possible as the flow rate is not recorded on the BAe146. The comparison of calculated AODs with those measured by AERONET is shown in Table 4. DODO1 profiles (assumed to be unaffected by the nephelometer issues, but still affected by any inlet losses) underestimate AOD compared to AERONET by a factor of 1.54 which is consistent with previous experience during SHADE [*Haywood et al.*, 2003], this being attributed to loss of coarse mode particles in the instrument inlet. The DODO2 comparison using data corrected using the DC-8

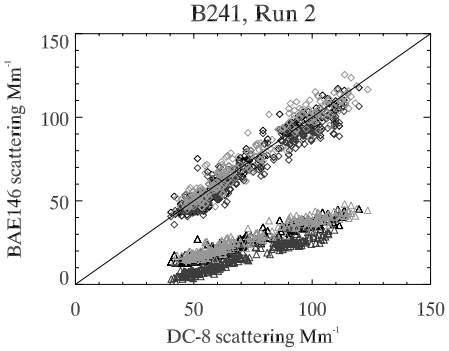

Figure 4. Correlation plot of DC-8 and BAe146 nephelometer measurements from BAe146 runs 1–3 of flight B241. Triangles show BAe146 data with correction only according to *Anderson and Ogren* [1998]. Diamonds show BAe146 data corrected according to a linear fit against the DC-8 data at each of three wavelengths and averaged across all three runs. Heaviest symbols are 550 nm, and palest are 700 nm.

Table 4. Correction Factors Obtained From Comparing AERONET Optical Depths at Dakar With Integrated Extinction From Accumulation Mode Measurements During Aircraft Profiles at Dakar

Flight	Profile	Aircraft-Based Optical Depth τ^{550}	AERONET Optical Depth at 550 nm $\tau_{AERONET}$	$C = \tau_{AERONET}/\tau^{550}$
DODO1				
B168	P17	0.21	0.38	1.83
B169	P1	0.30	0.24	0.81
B171	P1	0.11	0.11	1.00
B173	P1	0.09	0.12	1.34
B174	P10	0.05	0.11	2.03
B175	P1	0.12	0.15	1.19
B175	P8	0.04	0.11	2.56
Mean				1.54
DODO2				
B236	P10	0.33	0.23	0.71
B237	P8	0.61	0.64	1.06
B238	P1	0.38	0.68	1.80
B238	P9	0.42	0.48	1.16
B242	P1	0.18	0.42	2.30
B242	P11/P12	0.27	0.29	1.08
Mean				1.35

data gives a similar underestimate, whereas using data not corrected in equation (2) the aerosol optical depth was underestimated by a factor of 3.1.

[21] The variability of the underestimation of aerosol optical depth shown in Table 4 is assumed to be related to differing amounts of coarse mode aerosol being present, although some of the variation may be explained by discrepancies in inlet passing efficiency between the two aircraft which would result in a different scaling factor being required for different size distributions. As concerns hygroscopic growth, few estimates of hygroscopicity of Saharan dust exist, but it is likely that relative humidity effects are small. When dust is mixed with large amounts of other aerosols, humidity can be more important, but using the hygroscopic growth values for submicron Asian dust mixtures of *Carrico et al.* [2003] and biomass burning aerosol hygroscopic growth characteristics from *Magi and Hobbs* [2003] with our profiles resulted in AOD estimates far larger than those from AERONET. Therefore we do not account for hygroscopic growth here, but acknowledge that this could result in small increases in the calculation of AOD. The average distance between the mean profile location and the AERONET station varies between 29 and 254 km (mean of 114 km). Despite some of the profiles being further away from the AERONET station there is no correlation between distance to the AERONET station and the ratios of the AODs, so this is unlikely to be the main cause of differences in AOD.

[22] The comparison of AERONET and aircraft-measured AODs points to a consistency between approaches and supports that the scaling of the BAe146 nephelometer to the DC-8 nephelometer. Further examination, on a flight by flight basis, of the nephelometer behavior during the AMMA airborne campaign immediately prior to the DODO2 campaign suggests that the instrument apparently developed a problem just before deployment in DODO2, a problem that we were not able to rectify in the field. Unfortunately it is not possible from these comparisons to ascertain precisely the problem with the BAe146 nephelometer during DODO2, although loss in the inlets of larger particles is certainly a contributing factor, and this is partly responsible for the underestimation of AOD in both DODO campaigns. No further attempts were made to adjust the nephelometer scattering data for hygroscopic growth for the cases presented here, based on low relative humidity values during runs sampling dust (46% on average during the whole of DODO) and low expected hygroscopic growth rates for dust particles [e.g., *Li-Jones et al.*, 1998; *Carrico et al.*, 2003].

2.2.2. Measurement of Size Distribution

[23] The accumulation mode is measured by a wing-mounted PCASP which measures particles sized between 0.05 and 1.5 μm optically equivalent radius. It is assumed to sample at 100% efficiency at all sizes because of the short sampling lines and relatively small maximum size. Errors in the PCASP-measured size distribution due to nonspherical particles [*Osborne et al.*, 2008] are moderate compared to other sources of uncertainty affecting the optical properties presented here.

[24] Measurements of the coarse mode size distribution are much less well defined than those for the accumulation mode [e.g., *Reid et al.*, 2003], and measurement techniques on the FAAM BAe146 are less well validated. During DODO2 the coarse mode was measured by a Droplet Measurement Technology cloud droplet probe (CDP-100) (see Table 2) and by particle counting software used on scanning electron microscope (SEM) analysis images from filter samples (see Table 2). An internal optical probe was run but line losses prevented any meaningful numbers being used for the supermicron sizes. Limitations of each technique for measuring the coarse mode and the processing of the size distributions in order to allow comparisons are as follows:

[25] 1. The CDP is mounted nonoptimally 10 cm away from the aircraft skin which resulted in some initial uncertainty in the sample volume as a function of particle size [*Abel*, 2007]. Subsequent comparisons with several cloud instruments, including FSSP-100, Johnson-Williams, Small Ice Detector and Nevzorov were used to determine the sample volume which showed a consistent behavior for droplet sizes below 20 μm radius [*Abel*, 2007]. On the basis of these comparisons the CDP number concentration for

particles up to a radius of 20 μm has been adjusted by a factor of 0.35 to account for uncertainties in the sample volume. Above 20 μm radius the CDP has a shadowing effect due to its position on the aircraft and hence data from sizes larger than this has been discounted. The lower edge of the smallest CDP size bin is not well characterized and has also been discounted. To create a full size distribution the CDP size distribution has simply been joined onto the PCASP size distribution, and in most cases the transition from PCASP to CDP size distribution appears smooth.

[26] 2. Filter samples were also used to obtain another estimate of the coarse mode size distribution. SEM analysis was performed at the Laboratoire Interuniversitaire des Systèmes Atmospheriques (LISA) in Créteil, France. Particle counting software was used on SEM images of dust samples to obtain a size distribution (as described by *Chou et al.* [2008]). The smallest 4 size bins from the SEM size distribution were defined to be the same as the largest 4 bins from the PCASP, so that the PCASP and SEM size distributions overlap. The SEM number distribution was higher than that of the PCASP in the four overlapping bins and a scaling factor was necessary to match the two. The whole SEM size distribution was then scaled down accordingly. The SEM technique is a 2-D procedure which measures geometrical diameter, and may overestimate particle diameters if the dust particles are nonspherical. Thus the scaling down of the SEM size distribution can partly be interpreted as accounting for this overestimation of diameter, as well as a conversion from geometrical to optical diameter. Errors in the PCASP size distribution due to the refractive index and particle shape might also intervene as estimated by *Osborne et al.* [2008], but are not able to account for the difference between the SEM and PCASP size distributions.

[27] Because of limitations with each technique we regard the various estimates of the coarse mode as a range of possibilities.

2.3. Dispersion Modeling Using NAME

[28] To identify potential dust sources, investigations were undertaken using the UK Met Office Numerical Atmospheric-dispersion Modeling Environment (NAME). This is a Lagrangian particle model [*Ryall and Maryon*, 1998] in which emissions from pollutant sources are represented by parcels released into a model atmosphere driven by the meteorological fields from the Met Office's numerical weather prediction model, the Unified Model [*Cullen*, 1993]. Each parcel carries the mass of one or more pollutant species and evolves by various physical and chemical processes during its lifespan. Although originally designed as an emergency response tool, NAME has subsequently been developed for a wide range of applications [e.g., *Middleton et al.*, 2008; *Gloster et al.*, 2007; *Webster et al.*, 2007; *Witham and Manning*, 2007].

[29] In this work two approaches have been taken. First, to identify potential source regions of the dust measured during DODO, NAME was initiated at a location where the aircraft had measured dust, and the air mass was run backward in time over 5 days in order to identify locations where the air mass had been in the lower boundary layer, within 200 m of the surface. While this technique highlights regions from which the air originated, it does not indicate where dust was actually uplifted. In recent years a dust scheme has been developed [*Athanassiadou et al.*, 2006] in which dust is dynamically lifted, transported and deposited on the basis of the surface properties and meteorology. Therefore second, the relative contribution to the dust observed by the aircraft originating from different parts of the model domain have been identified by altering the extent of the modeled domain.

3. Identification of Aerosol Types

[30] The dominant aerosol types encountered during DODO were mineral dust (both campaigns) and biomass burning aerosols (DODO1 only). In order to isolate runs where the accumulation mode was dominated by dust only, we first removed runs where scattering from the nephelometer at 450 nm was greater than 550 nm and 700 nm, indicating the presence of biomass burning aerosol. For the remaining runs, we then looked at data from the aerosol mass spectrometer (AMS) and at the analysis of filter samples using scanning electron microscopy (SEM) and transmission electron microscopy (TEM). Analysis of air mass origin (see section 5) was not part of the selection criteria for dust cases, but the results support the hypothesis that the selected cases were dust aerosol, having sources in the Sahara and Sahel. However, we note that air mass origins do indicate that dust sampled during flights B173 and B174 had air mass origins around Spain and Portugal as well as in the northwest Sahara.

[31] Analysis of filter samples does not suggest any mixing of aerosol types or the presence of other components. Submicron mass loadings of organics and sulfates for DODO1 were determined using AMS data [see *Capes et al.*, 2008]. The dust cases described in this study have less than 15% of the submicron mass constituted by sulphates and organics, and can therefore be considered as dominated by dust in the accumulation mode, with the exception of run 3.1 in flight B174 where higher mass loadings of sulphates were found. On this basis, the aerosol samples presented are referred to as dust, on the assumption that mineral dust is almost certainly the dominant aerosol type and that mixing with other components is thought to be unlikely for the runs that have been selected.

4. Characteristics of Dust in DODO1 and DODO2

4.1. Vertical Profiles

[32] Figure 5 shows the variety of vertical profiles of dust (and biomass burning aerosol) found during the DODO campaigns. In each case, the scattering coefficient at 550 nm, Angstrom exponent (calculated using the 550 and 700 μm channels of the nephelometer), and ozone mixing ratio are shown. Small or even negative Angstrom exponent values imply larger particles (more likely to be dust), while larger positive values suggest small particles (more likely to be biomass burning or anthropogenic aerosol).

[33] Over land, close to the source, vertical profiles are quite similar for both the dry and wet season (Figures 5a and 5c), both showing a dust layer close to the surface. Figure 5a in the dry season (flight B175) shows a thick dust

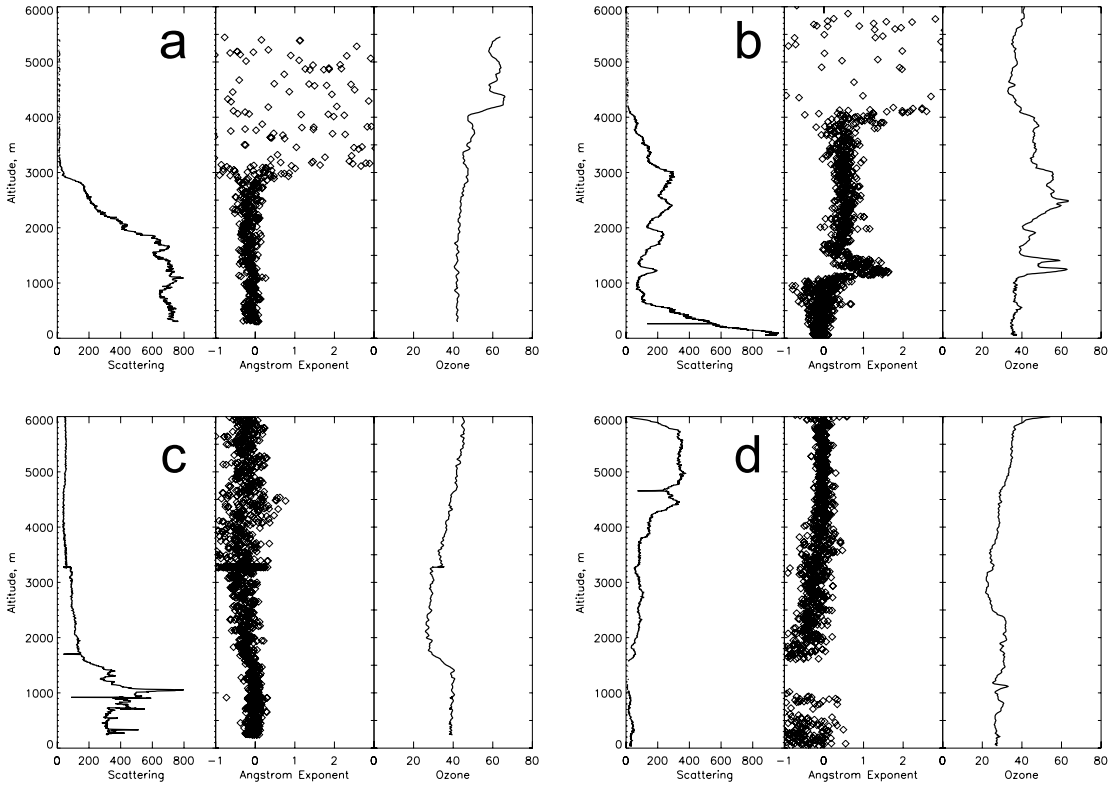

Figure 5. Vertical profiles of corrected 550 nm scattering (Mm^{-1}), ozone mixing ratio (ppbv) and 550–700 nm Angstrom exponent for (a) B175 profile 7 (Mauritania, dry season), (b) B174 profile 6 (over ocean, dry season), (c) B238 profile 3 (Mauritania, wet season), and (d) B237 profile 2 (over ocean, wet season).

layer from the surface extending to 3000 m with the largest scattering toward ground level. The wet season (Figure 5c, flight B238) shows a similar layer also extending to around 3000 m, but with peak scattering at around 1000 m. Above 3000 m low scattering values (<100 Mm^{-1}) extend up to 6000 m, whereas in the dry season no aerosol was seen above 3000 m. Temperature and dew point temperature values (not shown) indicate that the boundary layer heights for to these two profiles correspond to the altitude at which the scattering drops sharply, at around 3000 m for Figure 5a and around 6000 m for Figure 5c, although there is a minor inversion at around 1500 m, just above the scattering peak at 1000 m. Thus it appears that the differences in the vertical profiles of dust are due to seasonal variations in the height of the boundary layer, although the location of the profiles relative to the sources may also be a contributing factor.

[34] Figures 5b and 5d are profiles over the ocean from dry season (flight B174) and wet season (flight B237) respectively. During the dry season (Figure 5b) the scattering shows multiple layers of aerosol with one below 1000 m, and a second thicker layer, itself with considerable vertical structure, between 1500 m and 4000 m. The Angstrom exponent suggests different aerosol characteristics between these two layers with larger particles in the lower-altitude layer. Ozone concentration is also positively correlated with the scattering in the upper layer, but not in the lower layer. This type of profile was common particularly during the more southerly flights in DODO1 and consists of a low-altitude layer of dust (present to varying degrees) and a higher-altitude layer of biomass burning aerosol (most likely mixed with some dust [e.g., *Johnson et al.*, 2008]). In contrast, during the wet season over the ocean (Figure 5d), there is no biomass aerosol present and instead there is a layer of weaker scattering from particles with a low Angstrom exponent between 4000 and 6000 m. The ozone shows an increase, as would be expected at altitude, but no positive correlation with the scattering as was observed in the winter season. The 4000 to 6000 m layer is presumably the Saharan Air Layer (SAL), containing mineral dust, which is uplifted by dry or moist convective activity over source regions to higher potential temperature surfaces, and then advected out over colder layers above the ocean. There is some evidence that the angstrom exponent decreases toward the ocean surface, suggesting the deposition of larger particles. The seasonal variation in aerosol profiles over the ocean will have important effects in terms of the longwave radiative effect, which depends on the altitude of the dust layer [e.g., *Highwood et al.*, 2003], and also in

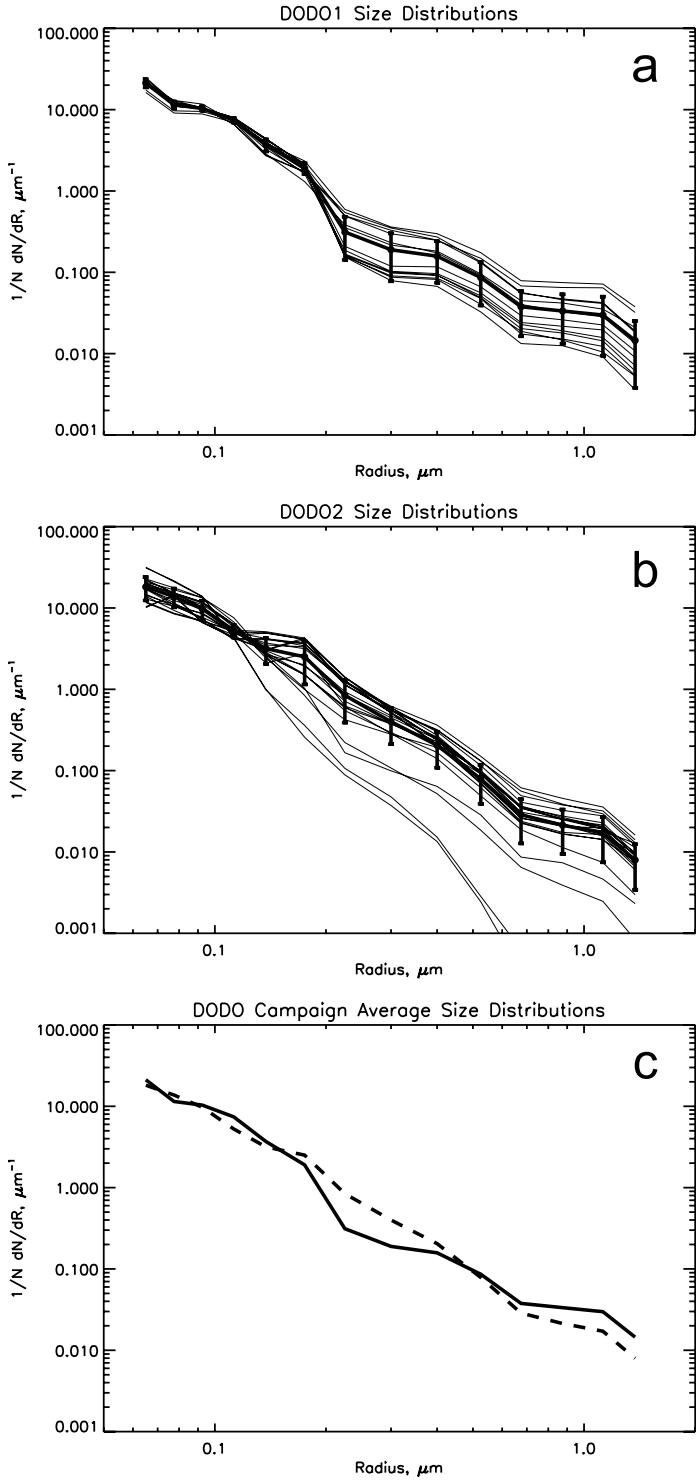

Figure 6. Size distributions measured by the PCASP on all runs dominated by dust, along with the average (heavy line) and errors (one standard deviation over each campaign) for (a) DODO1 and (b) DODO2. (c) Average size distributions for DODO1 (solid line) and DODO2 (dashed line).

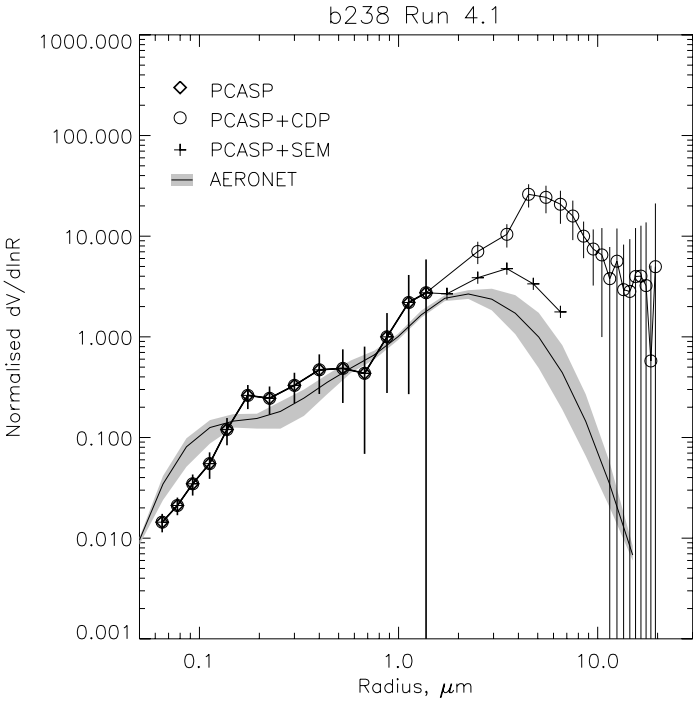

Figure 7. Volume size distributions for B238 run 4.1 at 1 km altitude on 23 August 2006 over Mauritania. The coarse mode was measured by a Cloud Droplet Probe (CDP) and by particle counting software used on Scanning Electron Microscope (SEM) imagery from filter samples. Size distributions from AERONET retrievals (Level 1.5, Version 2) are also shown. In order to compare distributions more meaningfully, in particular with AERONET, each distribution has been normalized by the value at 1 μm radius (see text for details of processing).

terms of dust deposition to the ocean, a process which might be expected to take longer from a higher-altitude dust layer.

[35] Broadly the dust profiles are illustrative of what is known about the large-scale dynamics of this region of the atmosphere, clearly showing the elevated SAL in the wet season and low-level dust transport in the dry season [e.g., *Chiapello et al.*, 1995], although considerable variability within this idealized picture is evident, such as a deeper dust layer observed over land during the dry season (Figure 5b). A ubiquitous biomass burning haze was detected by the instrumentation and clearly visible by eye during almost all the flights throughout the dry season. The difference between vertical profiles of aerosol over land and ocean is apparent. Since determining vertical profiles of aerosol loading via remote sensing is challenging without recent developments in lidar technology, these profiles will provide a valuable opportunity for comparison with dust model results subsequently within the DODO project and beyond.

4.2. Size Distribution

[36] Accumulation mode size distributions measured by the PCASP instrument for various straight and level runs in both DODO1 and DODO2 are shown in Figures 6a and 6b, with heavy lines showing campaign average size distributions. The average size distributions for DODO1 and DODO2 show small differences in the accumulation mode between 0.2 and 0.6 μm and 0.7–1.5 μm radius (Figure 6c) between the two campaigns. Greater variability is seen in the DODO2 size distributions which can be at least partly associated with greater changes in size distribution over height of the dust layer.

[37] A significant coarse mode of dust is also present in some cases. Figure 7 shows the coarse mode size distributions, in terms of volume density, from run 4.1 at 1 km altitude during flight B238 (DODO2). This run is selected as an example when dust concentrations were high and data from both coarse mode instruments available. It should be noted that we are comparing optically equivalent sizes for the PCASP and CDP with geometric sizing from the SEM. Since most of the optical instruments are calibrated using latex spheres, if the aerosol being measured is substantially absorbing, then a correction will need to be made. DODO dust has been shown to be mainly scattering (see section 4.3) so we are assuming that the correction needed would be small, and within the considerable errors already described.

[38] The size distributions retrieved by inverting the scattered sky radiances measured by the Dakar AERONET site for the corresponding day are also shown, though it should be noted that these are column integrated measurements at a location around 580 km from the aircraft sampling region, and so could at best only be expected to

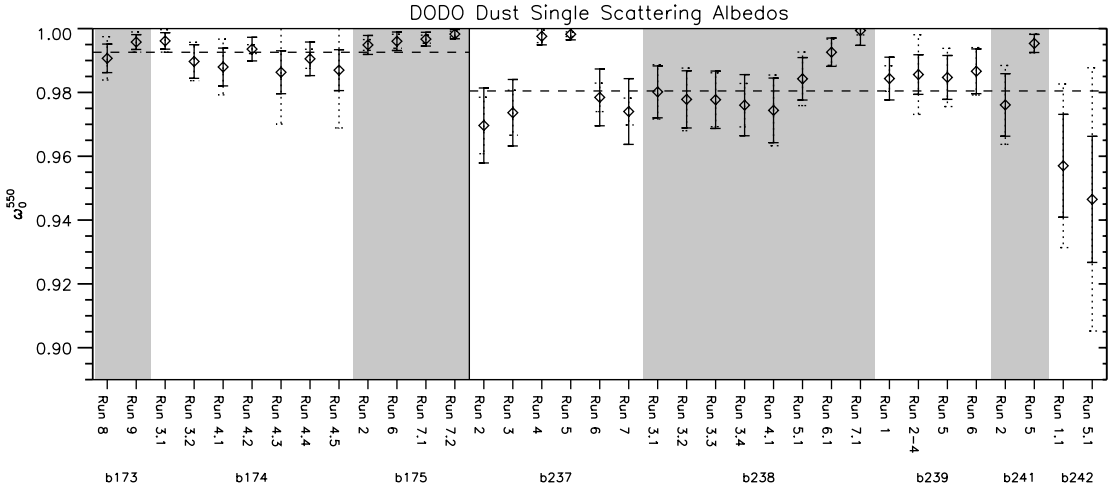

Figure 8. Accumulation mode single scattering albedos at 550 nm for each run in dust throughout the DODO campaigns, with errors estimated from variability across each run (dotted error bars) and from instrumental errors (solid error bars). Shaded/clear areas mark successive flights. Dashed horizontal lines show the campaign mean values of single scattering albedo as shown in Table 6. Single scattering albedos were calculated using absorption from the PSAP and scattering from the nephelometer, neither including contributions from the coarse mode.

be broadly similar to the aircraft measurements. In order to allow comparison between the in situ measurements and AERONET, each size distribution in Figure 7 is normalized by the value at 1 μm. This avoids normalizing to the smallest bin of the PCASP which is known to be the least reliable of the PCASP size bins, or normalizing to the peak of the volume distribution which places too much faith in the coarse mode measurements given the large range shown.

[39] Although there are limitations associated with each measurement technique, it is important to note the large range of coarse mode volume distributions shown in Figure 7. The effects of this uncertainty arising from the different measurements of the coarse modes on optical properties are considered in section 4.4. The CDP and SEM size distributions show a different coarse mode both in terms of mode radius and magnitude, centered around 4.5 μm and 3.5 μm radius respectively. Considering the distance to the Dakar AERONET site, a distance greater than the assumed length scale of the dust outbreak indicated from satellite imagery (not shown), it is unsurprising that AERONET retrieves less coarse mode than the SEM and CDP. The accumulation modes show comparatively better agreement: at radii greater than 0.2 μm agreement is achieved between AERONET and the PCASP size distributions within the bounds of the errors and variability shown. Below 0.2 μm more particles are measured by AERONET than the aircraft.

4.3. Optical Properties

[40] Figure 8 shows the single scattering albedo values of dust-dominated cases from both campaigns, associated errors and campaign average single scattering albedos (see also Table 5). Results shown are averages measured during different aircraft runs which have been determined to be dominated by dust (see section 3). As the PSAP and the nephelometer most likely measure absorption and scattering from the accumulation mode only, these results only show optical properties for the accumulation mode. Measured dust single scattering albedos were consistently high (always greater than 0.98) during DODO1, but showed greater variation during DODO2 ranging from 0.95 to 0.99. The variation observed during DODO2 could be attributed to both the variation in size distribution with altitude and to different dust sources and chemical composition. Although mixing or coating of dust with/by other aerosols or chemicals is a possibility, this was not evident from filter sample analysis.

[41] The campaign average mineral dust single scattering albedos for DODO1 and DODO2 accumulation mode were 0.99 ± 0.004 and 0.98 ± 0.012 respectively, with errors representing one standard deviation of the variability around the mean (see Table 5), (as opposed to the range of observed values shown in Figure 8). Hence DODO1 dust is slightly

Table 5. Lognormal Parameters for DODO Average Size Distributions (Accumulation Mode Only)

Mode	r_g (μm)	σ	w
	DODO1		
1	0.083	1.36	0.815
2	0.160	1.16	0.095
3	0.310	1.50	0.067
4	1.000	1.31	0.023
	DODO2		
1	0.061	1.47	0.797
2	0.165	1.18	0.104
3	0.230	1.54	0.089
4	0.960	1.32	0.010

Table 6. Campaign Average Optical Properties From DODO, DABEX, and SHADE Campaigns[a]

	DODO1, Feb 2006		DODO2, Aug 2006		DABEX, Jan 2006 [*Osborne et al.*, 2008]: AM (AM + CM)	SHADE, Sep 2000 [*Haywood et al.*, 2003]: AM (AM + CM)
	Observations: AM	Mie: AM	Observations: AM	Mie: AM		
ω_0^{550}	0.99 ± 0.004	0.99	0.98 ± 0.013	0.98	0.99 (0.98)	0.97 (0.95)
Refractive index (550 nm)		1.53−0.0005i		1.53−0.0014i	1.53−0.0004i	1.53−0.0015i
g^{550}		0.68		0.68	0.71 (0.75)	0.72 (0.74)
k_{ext}^{550} (m^2 g^{-1})		0.85		1.14	0.76 (0.33)	0.70 (0.42)

[a]DODO observations are taken from the nephelometer and PSAP data, while the Mie results are from calculations using the observed size distributions for fine and accumulation mode particles only, assuming spherical dust and a refractive index to match the observed single scattering albedo. Errors on observed ω_0^{550} indicate one standard deviation around the mean of values shown in Figure 8. CM indicates coarse mode, and AM indicates accumulation mode.

more scattering than DODO2 dust, though the errors do overlap. In comparison to other recent aircraft campaigns measuring North African dust, DABEX (January 2006, Niamey) measured consistently high ω_0^{550} values with an average of 0.99 [*Osborne et al.*, 2008], and SHADE (September 2000 around the Capo Verde Islands) measured an average ω_0^{550} of 0.97 with a range of 0.95–0.99 [*Haywood et al.*, 2003] (both campaigns accounting only for accumulation mode). These results, where dust has been determined to be the dominant aerosol type, suggest that the dry season dust has a higher ω_0^{550} value than the wet season dust, for which ω_0^{550} values seem to be more variable.

[42] The DODO measurements of ω_0^{550} are at the upper end of previous estimates of ω_0. Values of ω_0^{670} for global dust range from 0.90 to 0.99, with an IPCC central global estimate of 0.96 [*Forster et al.*, 2007], with long-term AERONET estimates of ω_0^{670} at 0.95 for Saharan dust [*Dubovik et al.*, 2002]. Note that the DODO calculations of single scattering albedo do not include the coarse mode contribution, the effect of which most likely decreases ω_0 by variable amounts (see section 4.4), depending on assumptions made about the composition of the coarse mode compared to the accumulation mode. Higher values of ω_0^{550} impact the direct radiative effect in the shortwave by increasing the magnitude of the negative radiative effect at the TOA [*Forster et al.*, 2007].

[43] Table 6 shows the average optical properties (with associated errors) for both DODO1 and DODO2 calculated from Mie scattering code, as well as comparison to previous measurement campaigns. The measured size distributions (Figure 6) were fitted with four lognormal curves to produce a best fit curve (see Table 5). These were input into a Mie scattering code together with an inferred refractive index (constant with wavelength in the visible). The optical properties were retrieved, and the refractive index was chosen so that the single scattering albedo from Mie code matched that from observations. A density of 2.65 g cm^{-3} was assumed [*Tegen and Fung*, 1995] in order to calculate the mass specific extinction.

[44] The inferred refractive indices (Table 6) show that the DODO2 dust was more absorbing (higher imaginary part) than DODO1 dust. This suggests that the different campaign average single scattering albedos are explained by the dust composition (see section 5), since the size distributions are similar in the accumulation mode (see Figure 6c). Interestingly the refractive indices show similarities to the SHADE and DABEX campaigns both in terms of location and season: both DODO1 and DABEX have low imaginary refractive indices showing very little absorption. In contrast, the wet season campaigns based around the West African coast produced higher imaginary refractive indices showing more absorption. These differences may be due to different dust sources having different mineralogy (in particular iron oxide amounts giving more absorption in the UV and midvisible parts of the spectrum in DODO2). Broadly the refractive indices from DODO fit in with the emerging picture from recent studies that North African dust has very low absorption [e.g., *Kaufman et al.*, 2001; *Dubovik et al.*, 2002; *Haywood et al.*, 2003; *Osborne et al.*, 2008].

[45] The asymmetry parameter calculated from Mie code for both DODO campaigns is 0.68, indicating that most radiation is scattered in a forward direction, and appears to differ little between campaigns. The mass specific extinction for the accumulation mode is significantly higher during DODO2 (1.14 m^2 g^{-1}) showing that DODO2 accumulation mode dust is more efficient at extinguishing radiation per unit mass of aerosol. Mass specific extinction for DODO1 (0.85 m^2 g^{-1}) is similar to that measured during SHADE and DABEX (0.76 m^2 g^{-1} and 0.70 m^2 g^{-1}). The higher value seen in DODO2 is possibly due to a greater proportion of mass between radii of 0.2–0.4 μm where the dust is optically more efficient at extinguishing radiation.

4.4. On the Role of the Coarse Mode for Calculation of Optical Properties

[46] Previous studies have shown that inclusion of the coarse mode when calculating optical properties of dust has a small effect, except in the calculation of mass specific extinction which drops significantly because of the large increase in mass when the coarse mode is included [*Haywood et al.*, 2003]. A sensitivity test was carried out to analyze the importance of the large coarse mode observed in flight B238 run 4.1 in calculating the optical properties, using the different measurements of coarse mode as shown in Figure 7.

[47] As described in section 4.3, Mie code was used to calculate the optical properties using the measured size distributions shown in Figure 7. Five lognormal modes were fitted to the measured size distributions using the coarse mode from each instrument as a sensitivity test in varying the amount of coarse mode present. The first four modes were fitted to the PCASP size distribution (repre-

Table 7. Optical Properties for B237 Run 4.1 at 1 km Altitude During DODO2, Showing the Effect of Including the Coarse Mode in the Calculation of Optical Properties[a]

Instrument Measuring Coarse Mode	ω_0^{550}	g^{550}	K_{ext}^{550} (m^2 g^{-1})
No coarse mode (PCASP only)	0.98	0.69	1.22
SEM	0.96	0.72	0.46
CDP	0.90	0.77	0.20

[a]PCASP only results exclude the effect of the coarse mode, and use four lognormals to fit to the size distribution. Size distributions using the SEM and CDP use the same four lognormal modes for the accumulation mode but include a fifth to fit the coarse mode which is derived from each measurement.

senting the accumulation mode) and remained identical in each case. The fifth mode was fitted to the coarse mode from each instrument and the parameters of this mode changed depending on which instrument was measuring the coarse mode. The refractive index was calculated specifically for the accumulation mode dust sampled in run 4.1 and was applied to the whole size distribution.

[48] Table 7 shows the results of the effects of the different coarse modes on the optical properties of the dust. As found previously, the addition of the coarse mode decreases ω_0^{550}, increases g and decreases k_{ext}^{550} [*Haywood et al.*, 2003]. The DODO results show that the changes in the optical properties are more marked when a greater amount of coarse mode is present, as with the CDP. For example, ω_0^{550} decreases from 0.98 to 0.90 with the addition of the CDP coarse mode, a substantial change. Less of a decrease in ω_0^{550} is observed when less coarse mode is measured. The mass specific extinction changes similarly with the varying amounts of coarse mode. Thus the optical properties in this case are extremely sensitive to the amount and presence of the coarse mode. In this illustrative example it has been assumed that the refractive index of the dust (and therefore the composition) of coarse and accumulation modes are the same. If there were dramatically different sources or composition then the impact on the optical properties could be different to that described. SEM and TEM analysis on a small number of particles for this case showed some differences of composition between the accumulation and coarse modes. In particular the accumulation mode contained iron oxides which were not measured in the coarse mode. Iron oxides such as hematite and goethite are responsible for absorption of UV and visible light [*Sokolik and Toon*, 1999; *Lafon et al.*, 2006]. Future work will involve a more sophisticated representation of refractive index with particle size. Meanwhile these results show that accurate measurement of the coarse mode in mineral dust is extremely important and so in future aircraft studies effort must be made in operating fully calibrated aerosol probes that can measure particles sizes up to 10−20 μm radius.

5. Dust Source Identification

[49] Elemental concentrations for the combined accumulation and coarse modes were measured by particle induced X-ray emission (PIXE) at the Laboratorio di Tecniche Nucleari per i Beni Culturali (LABEC) [*Chiari et al.*, 2005; *Calzolai et al.*, 2006]. Ratios of elemental concentrations usually associated with dust have been calculated for the same cases as those described in sections 3 and 4, and are shown in Table 8. Average elemental ratios for Si/Al are 2.7 ± 0.2 for DODO1 and 2.6 ± 0.3 for DODO2. These are all somewhat higher than previous SHADE results from *Formenti et al.* [2003], and from the range of results for different origins given by *Chiapello* [1996], but less than the value in crustal rock [*Mason*, 1966]. It is possible that transport as well as source regions affects this ratio, since some of DODO1 and DODO2 samples were much closer to the source of the dust than those in the previous studies. It is also possible that the source area of the dust has different characteristics.

[50] DODO1 shows substantially higher Ca/Al ratio (1.1 ± 0.4) compared to DODO2 (0.5 ± 0.2), indicating that the DODO1 samples had sources based more toward the northern Sahara than DODO2 [e.g., *Formenti et al.*, 2008; J. L. Rajot et al., AMMA dust experiment: An overview of measurements during the dry season special observation period (SOP 0) at the Banizoumbou (Niger) supersite, submitted to *Journal of Geophysical Research*, 2008]. The K/Al ratio is 0.3 ± 0.1 for DODO1 and 0.2 ± 0.1 for DODO2: again DODO2 is similar to results for Saharan dust from *Chiapello* [1996]. Finally, Fe/Al ratios are 0.7 ± 0.1 for both DODO1 and DODO2, slightly higher than was found during SHADE by *Formenti et al.* [2003] and by *Chiapello* [1996]. *Formenti et al.* [2008] have shown than the Fe/Al ratio is not that sensitive to the source region. Conversely, these authors indicate that the iron oxide to iron ratio is more sensitive to source region.

[51] The elemental analysis of filter samples and optical property results suggest some differences in source characteristics between DODO1 and DODO2, and between different dust samples collected from different (and sometimes the same) flights. NAME was run for several cases for both DODO campaigns in order to determine potential dust source regions. Figure 9 shows air mass origins from the NAME for dust sampled during different runs from two flights (B175 in DODO1 and B238 in DODO2) over Mauritania.

[52] For the flights and runs shown, the dust encountered during DODO1 straight and level runs originated (over a 5 day period) from more geographically limited regions than that encountered during DODO2. Figure 9a shows the air mass origin from B175 (run 7.2 at 170 m above ground level), and suggests potential dust sources originating from the boundary layer in Algeria and Mauritania. Dust found at similar altitudes and geographical locations during DODO2 flight B238 (run 3.3) suggested that the air mass originated from more coastal regions of western Sahara and Morocco (Figure 9b). There is a substantial difference in single scattering albedo between these runs, with that from DODO2 being lower. Although mixing with anthropogenic aerosol from Spain or Portugal could be a factor (though it was not

Table 8. Mean Elemental Ratios Measured by PIXE for Filter Samples From DODO[a]

	Si/Al	Ca/Al	K/Al	Fe/Al
DODO1 dust	2.7 (0.2)	1.1 (0.4)	0.3 (0.1)	0.7 (0.1)
DODO2 dust	2.6 (0.3)	0.5 (0.2)	0.2 (0.1)	0.7 (0.1)

[a]Values in parentheses represent one standard deviation.

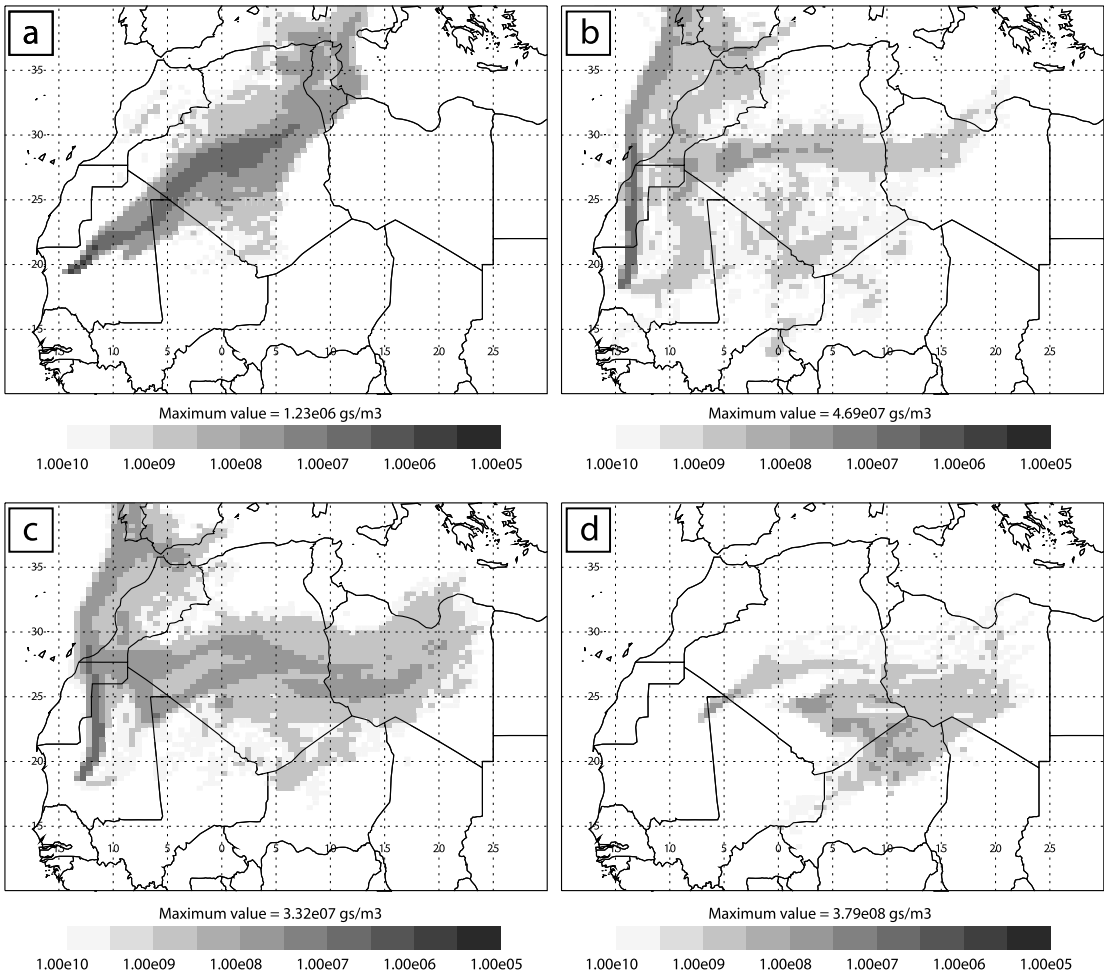

Figure 9. Five day particle release experiments from the UK Met Office NAME model, indicating the likely origin (within the lowest 200 m) of dust encountered during straight and level runs of the BAe146 aircraft. (a) DODO1 B175 run 7.2 at 175 m above ground level (agl), (b) DODO2 B238 run 3.3 at 175 m agl, (c) DODO2 B238 run 5.1 at 2 km agl, and (d) DODO2 B238 run 7.1 at 5 km agl.

evident on filter samples), the lower single scattering albedo is likely due to the mineralogy of the dust since *Formenti et al.* [2008] found high values of absorbing iron oxides for this run.

[53] Analysis of air mass origins for dust encountered during other straight and level runs in flight B238 over northern Mauritania suggests different source regions for each dust layer at different altitudes. At around 2 km (run 5.1) the dust appears to have originated from a mixture of locations including a well-defined area within Mauritania, coastal regions around Morocco, and central Algeria and western Libya (Figure 9c). Dust from within the highest altitude in the SAL at around 5.2 km (run 7.1) has 5 day origins further west around northern Niger, southern Algeria and southwest Libya (Figure 9d). Thus for the case of B238 dust encountered higher up in the atmosphere is likely to have originated from sources further east than sources at lower altitudes.

[54] NAME simulations for the other flights (not shown) show similar patterns in the air mass origins. DODO1 dust (dry season) was always transported by air masses originating from the north to northwest within a narrow plume (as shown in Figure 9a), whereas the DODO2 (wet season) potential dust sources were much more widespread over North Africa, as indicated by the variation in potential sources shown in Figures 9b–9d. This difference could be explained by the small number of dust events encountered during DODO1, with similar meteorology during each, rather than being a truly seasonal effect.

[55] Different dust sources are expected to have different mineralogy and therefore different optical properties [e.g., *Claquin et al.*, 1999; *Caquineau et al.*, 2002]. It is therefore interesting that both the single scattering albedos shown in Figure 8 and the potential dust sources for DODO2 dust cases show more variability than those for DODO1, and suggests that the dust mineralogy or source region is having

an important effect on the optical properties observed. Notably the air mass origins for dust sampled during flight B242 (not shown) appear to be from further south than those for other flights, with potential sources being centered around southern Algeria, eastern Mali and northwestern Niger. This coincides with single scattering albedos for this flight being much lower than those for other flights. It is possible that the mineralogy of dust sampled during this flight is rather different to others, possibly because of higher concentrations of absorbing iron oxides in sources located further south [*Claquin et al.*, 1999; *Alfaro et al.*, 2004; *Lafon et al.*, 2006]. Further work will examine the mineralogy from flight B242 in more detail.

[56] Care must be taken in interpreting these results, since although the air masses may have passed through these potential source areas this does not necessarily mean that dust has been uplifted. In order to account for this for the case of flight B238, forward model runs were undertaken incorporating the dust uplift scheme. Results indicate that essentially all the dust observed at low altitude (run 3.3) originated from the region west of 0E. This region accounted for approximately 80% of the dust observed at mid levels (run 5.1) but only 10% of that observed at high levels (run 7.1), with the remainder having been transported from further east. Therefore the hypothesis that for the case of flight B238 the high-altitude dust had been transported over larger distances than the dust sampled at lower altitudes, and that the high-altitude dust had different dust sources to the dust at low altitudes, as indicated by the air mass origins from NAME, is supported by the dust model results.

6. Discussion and Future Plans

[57] Aircraft observations of North African dust during the DODO project reveal some interesting differences between wet and dry season dust during 2006. Differences in the measured accumulation mode ω_0^{550} for dust between the dry and wet season campaigns suggest higher values of ω_0^{550} are more prevalent during the dry season (0.99 (0.98–0.999), DODO1), while wet season ω_0^{550} values are more variable (0.98 (0.94–0.999) DODO2) and slightly lower on average. This range of observed single scattering albedos will be important in terms of the radiative effect. Potential dust sources suggested by NAME are also more variable during DODO2, whereas during DODO1 they were more confined in area and located in the northwest Sahara. Of the elemental ratios examined those of Ca/Al were the most variable between the DODO campaigns, with higher values observed during DODO1, also suggesting dust sources further toward the northern Sahara. Changes in such ratios also have implications for minerals deposited to the ocean. The size distributions for the accumulation mode were less variable between campaigns and flights. Thus the available data suggests that the different optical properties of the accumulation mode between the two DODO campaigns are related to the chemical composition of the dust and the potential dust sources. This also is reflected in the different derived refractive index for the accumulation mode between campaigns; 1.53–0.0005i for DODO1 and 1.53–0.0014i for DODO2. Mineralogical information will be used to confirm the consistency of our inferred refractive indices with the observed composition. We note that the correction of the BAe146 nephelometer based on the DC-8 nephelometer involves some uncertainty based on the uncertainty in the passing efficiency of the Rosemount inlets on the BAe146 relative to those of the DC-8, and that there is therefore a degree of uncertainty in the measured optical properties for the DODO2 accumulation mode results.

[58] Aerosol optical depth estimates from the aircraft extinction profiles in general underestimated those from AERONET (values shown in Table 4). Differences were within a factor of 1.5 for DODO1, and to within 1.35 during DODO2 once correction had been made to DODO2 values on the basis of a poorly behaving nephelometer and comparison with the NASA DC-8. These ratios to AERONET are consistent with previous work from SHADE [*Haywood et al.*, 2003] and are attributed to loss of coarse mode particles in the aircraft inlets. During DABEX, *Osborne et al.* [2008] found that once corrected for missing scattering based on measurements of the coarse mode the aircraft extinction tended to overestimate dust optical depth compared to AERONET data at Banizoumbou.

[59] The importance of the coarse mode in affecting radiative properties is apparent in DODO, as is the lack of adequately validated airborne measurements. While the single scattering albedo for the accumulation mode was measured directly, we must rely on size distribution measurements in order to calculate the single scattering albedo for the combined accumulation and coarse modes. We have presented size distributions from two different techniques for measuring the coarse mode, both of which have limitations. We illustrate that the uncertainty from different coarse mode size distributions results in a large variation in the single scattering albedo of dust (0.90 with the largest coarse mode to 0.98 with no coarse mode present), although here we make the simple assumption that the coarse mode composition is the same as that of the accumulation mode. This is an area where development is required in order to reduce the uncertainty in key properties such as the single scattering albedo and hence the radiative effect of dust. Large-scale dust events such as the March 2006 dust storm are likely to have a substantial coarse mode, which could lead to significantly different values of single scattering albedo and may explain differences previously reported [*Slingo et al.*, 2006; *Haywood et al.*, 2003].

[60] The vertical profiles measured during DODO are qualitatively consistent with what would be expected on the basis of the differing meteorology of the two seasons. (e.g., *Chiapello et al.* [1995] (winter transport at low altitudes) and *Karyampudi et al.* [1999] (wet season transport in SAL), and *Zhu et al.* [2007] (comparison of dust plumes in different seasons)). When present, dry season dust was always found at low altitudes, whereas wet season dust was found to be transported up to altitudes of 6 km. However, during one flight in the dry season dust was found in a layer extending up to around 3 km over the land (flight B175), implying that there may be substantial variability in the idealized picture. A ubiquitous layer of biomass burning aerosol was found aloft during the dry season to the south of Dakar.

[61] The optical properties of dust aerosol are crucial in determining the radiative effect of dust accurately [*Haywood and Shine*, 1995] and so variations in the single scattering

albedo such as those presented here are extremely important. Further work will assess the radiative effect of the dust sampled during both DODO campaigns, using both radiometer data from the aircraft and a radiative transfer code. Finally, the iron content will be assessed in more detail as this is relevant for converting the deposition of dust in general to the ocean to a contribution of iron.

[62] There are obvious limitations to using only 1 year for a comparison. However, we believe the results presented here are of winder applicability since the flow during DODO2 was climatological and during DODO1 the analysis of dust samples was completed on days when the flow was climatological. Additionally, the campaign suffered from some major uncertainties in the behavior of key instrumentation. However, having made best attempts with independent data to quantify and assess the reasons for necessary corrections, these observations add to the available data on North African dust. The case studies are being used to constrain numerical models of dust uplift and transport which will ultimately be used to assess the deposition of dust to the Atlantic Ocean. Dust is a crucial part of the climate system, acting as a forcing and involved in feedbacks between anthropogenic and natural climate change mechanisms. However, the processes involved in dust uplift are many and occur at small spatial scales and are often episodic in nature. The use of integrated airborne, ground and remote sensing measurements to constrain models is a vital step forward in our ability to model dust distributions, and for this there must be a continuation of long-term monitoring of dust properties such as by AERONET and AMMA dust stations, supplemented by in situ aircraft campaigns covering as many seasons and locations as is feasible.

[63] **Acknowledgments.** DODO is funded by NERC via the SOLAS directed program (grant NE/C517276/1). The aircraft campaigns would not have been possible without the professional and enthusiastic staff of FAAM, DirectFlight, and Avalon Engineering. We also acknowledge the support and staff of the Met Office who were involved in these campaigns and in discussion of the analysis. FAAM is jointly funded by the Natural Environment Research Council and the Met Office. The financial support of the French API-AMMA national program to the chemical and microscopy analysis of the bulk filter samples is also acknowledged. The CDP is not a core FAAM instrument and we would like to acknowledge the provision of the CDP data by Martin Gallagher through the support of the IAGOS project. We thank the AERONET PI Didier Tanré for his effort in establishing and maintaining the Dakar AERONET site.

References

Abel, S. (2007), CDP airflow modelling and droplet shadowing on the FAAM 146, paper presented at FAAM Cloud Instrument User Group Meeting, Univ. of Manchester, Manchester, U. K., 10 Oct. (Available at http://web.mac.com/mccssmwg1/CIUG/Presentations_1.html)

Alfaro, S. C., S. Lafon, J. L. Rajot, P. Formenti, A. Gaudichet, and M. Maille (2004), Iron oxides and light absorption by pure desert dust: An experimental study, *J. Geophys. Res.*, *109*, D08208, doi:10.1029/2003JD004374.

Anderson, T. L., and J. A. Ogren (1998), Determining aerosol radiative properties using the TSI 3563 integrating nephelometer, *Aerosol Sci. Technol.*, *29*(1), 57–69, doi:10.1080/02786829808965551.

Andreae, M. O., et al. (2000), Soluble ion chemistry of the atmospheric aerosol and SO_2 concentrations over the eastern North Atlantic during ACE-2, *Tellus, Ser. B*, *52*(4), 1066–1087, doi:10.1034/j.1600-0889.2000.00105.x.

Athanassiadou, M., H. Flocas, M. A. J. Harrison, M. C. Hort, C. S. Witham, and S. Watkin (2006), The dust event of 17 April 2005 over Athens, Greece, *Weather*, *61*(5), 125–131.

Bond, T. C., T. L. Anderson, and D. Campbell (1999), Calibration and intercomparison of filter-based measurements of visible light absorption by aerosols, *Aerosol Sci. Technol.*, *30*, 582–600, doi:10.1080/027868299304435.

Calzolai, G., M. Chiari, I. García Orellana, F. Lucarelli, A. Migliori, S. Nava, and F. Taccetti (2006), The new external beam facility for environmental studies at the Tandetron accelerator of LABEC, *Nucl. Instrum. Methods in Phys. Res., Sect. B*, *249*, 928–931.

Capes, G., B. T. Johnson, G. McFiggans, P. I. Williams, J. M. Haywood, and H. Coe (2008), Aging of biomass burning aerosols over West Africa: Aircraft measurements of chemical composition, microphysical properties and emission ratios, *J. Geophys. Res.*, doi:10.1029/2008JD009845, in press.

Caquineau, S., A. Gaudichet, L. Gomes, and M. Legrand (2002), Mineralogy of Saharan dust transported over northwestern tropical Atlantic Ocean in relation to source regions, *J. Geophys. Res.*, *107*(D15), 4251, doi:10.1029/2000JD000247.

Carrico, C. M., P. Kus, P. K. Quinn, and T. S. Bates (2003), Mixtures of pollution, dust, sea salt, and volcanic aerosol during ACE-Asia: Radiative properties as a function of relative humidity, *J. Geophys. Res.*, *108*(D23), 8650, doi:10.1029/2003JD003405.

Chiapello, I. (1996), Les aérosols atmosphériques au-dessus de l'Atlantique nord tropical: Approche physico-chimique et météorologique. Evaluation de la contribution de différentes espèces à l'épaisseur optique en aérosol, Ph.D. thesis, Univ. Paris VII, Paris.

Chiapello, I., G. Bergametti, L. Gomes, B. Chatenet, F. Dulac, J. Pimenta, and E. Santos Suares (1995), An additional low layer transport of Sahelian and Saharan dust over the northeastern tropical Atlantic, *Geophys. Res. Lett.*, *22*(23), 3191–3194, doi:10.1029/95GL03313.

Chiapello, I., G. Bergametti, B. Chatenet, P. Bousquet, F. Dulac, and E. Santos Soares (1997), Origins of African dust transported over the northeastern tropical Atlantic, *J. Geophys. Res.*, *102*(D12), 13,701–13,709, doi:10.1029/97JD00259.

Chiari, M., F. Lucarelli, F. Mazzei, S. Nava, L. Paperetti, P. Prati, G. Valli, and R. Vecchi (2005), Characterization of airborne particulate matter in an industrial district near Florence by PIXE and PESA, *X Ray Spectrom.*, *34*(4), 323–329, doi:10.1002/xrs.825.

Chou, C., P. Formenti, M. Maille, P. Ausset, G. Helas, M. Harrison, and S. Osborne (2008), Size distribution, shape and composition of mineral dust aerosols collected during the AMMA SOP0/DABEX field campaign in Niger, January 2006, *J. Geophys. Res.*, doi:10.1029/2008JD009897, in press.

Claquin, T., M. Schulz, and Y. J. Balkanski (1999), Modeling the mineralogy of atmospheric dust sources, *J. Geophys. Res.*, *104*(D18), 22,243–22,256, doi:10.1029/1999JD900416.

Cullen, M. J. P. (1993), The unified forecast/climate model, *Meteorol. Mag.*, *122*, 81–93.

DeMott, P. J., K. Sassen, M. R. Poellot, D. Baumgardner, D. C. Rogers, S. D. Brooks, A. J. Prenni, and S. M. Kreidenweis (2003), African dust aerosols as atmospheric ice nuclei, *Geophys. Res. Lett.*, *30*(14), 1732, doi:10.1029/2003GL017410.

Dubovik, O., B. Holben, T. F. Eck, A. Smirnov, Y. Kaufman, M. D. King, and D. Tanré (2002), Variability of absorption and optical properties of key aerosol types observed in worldwide locations, *J. Atmos. Sci.*, *59*, 590–608.

Engelstaedter, S., and R. Washington (2007), Atmospheric controls on the annual cycle of North African dust, *J. Geophys. Res.*, *112*, D03103, doi:10.1029/2006JD007195.

Evan, A., J. A. Dunion, J. A. Foley, A. K. Heidinger, and C. S. Velden (2006), New evidence for a relationship between Atlantic tropical cyclone activity and African dust outbreaks, *Geophys. Res. Lett.*, *33*, L19813, doi:10.1029/2006GL026408.

Field, P. R., O. Mohler, P. Connolly, M. Kramer, R. Cotton, A. J. Heymsfield, H. Saathoff, and M. Schnaiter (2006), Some ice nucleation characteristics of Asian and Saharan desert dust, *Atmos. Chem. Phys.*, *6*, 2991–3006.

Formenti, P., M. O. Andreae, L. Lange, G. Roberts, J. Cafmeyer, I. Rajta, W. Maenhaut, B. N. Holben, P. Artaxo, and J. Lelieveld (2001), Saharan dust in Brazil and Suriname during the Large-Scale Biosphere-Atmosphere Experiment in Amazonia (LBA)–Cooperative LBA Regional Experiment (CLAIRE) in March 1998, *J. Geophys. Res.*, *106*(D14), 14,919–14,934, doi:10.1029/2000JD900827.

Formenti, P., W. Elbert, W. Maenhaut, J. Haywood, and M. O. Andreae (2003), Chemical composition of mineral dust aerosol during the Saharan Dust Experiment (SHADE) airborne campaign in the Cape Verde region, September 2000, *J. Geophys. Res.*, *108*(D18), 8576, doi:10.1029/2002JD002648.

Formenti, P., et al. (2008), Composition of mineral dust from western Africa: Results from the AMMA SOP0/DABEX and DODO field campaigns, *J. Geophys. Res.*, doi:10.1029/2008JD009903, in press.

Forster, P., et al. (2007), Changes in atmospheric constituents and in radiative forcing, in *Climate Change 2007: The Physical Science Basis—Contribution of Working Group 1 to the Fourth Assessment Report of*

the Intergovernmental Panel on Climate Change, edited by S. Solomon et al., pp. 130–234, Cambridge Univ. Press, New York.

Gloster, J., P. S. Mellor, A. J. Manning, H. N. Webster, and M. C. Hort (2007), Assessing the risk of windborne spread of bluetongue in the 2006 outbreak of disease in northern Europe, *Vet. Rec.*, *160*, 54–56.

Hastenrath, S. (1991), *Climate Dynamics of the Tropics*, Kluwer Acad., Dordrecht, Netherlands.

Haywood, J., and K. Shine (1995), The effect of anthropogenic sulfate and soot aerosol on the clear sky planetary radiation budget, *Geophys. Res. Lett.*, *22*(5), 603–606, doi:10.1029/95GL00075.

Haywood, J., P. Francis, S. Osborne, M. Glew, N. Loeb, E. Highwood, D. Tanré, G. Myhre, P. Formenti, and E. Hirst (2003), Radiative properties and direct radiative effect of Saharan dust measured by the C-130 aircraft during SHADE: 1. Solar spectrum, *J. Geophys. Res.*, *108*(D18), 8577, doi:10.1029/2002JD002687.

Highwood, E. J., J. M. Haywood, M. D. Silverstone, S. M. Newman, and J. P. Taylor (2003), Radiative properties and direct effect of Saharan dust measured by the C-130 aircraft during Saharan Dust Experiment (SHADE): 2. Terrestrial spectrum, *J. Geophys. Res.*, *108*(D18), 8578, doi:10.1029/2002JD002552.

Jickells, T. D., et al. (2005), Global iron connections between desert dust, ocean biogeochemistry, and climate, *Science*, *308*(5718), 67–71, doi:10.1126/science.1105959.

Johnson, B. T., S. R. Osborne, and J. M. Haywood (2008), Aircraft measurements of biomass burning aerosols over West Africa during DABEX, *J. Geophys. Res.*, doi:10.1029/2007JD009741, in press.

Jones, C., N. Mahowald, and C. Luo (2004), Observational evidence of African desert dust intensification of easterly waves, *Geophys. Res. Lett.*, *31*, L17208, doi:10.1029/2004GL020107.

Karyampudi, V. M., et al. (1999), Validation of the Saharan Dust Plume conceptual model using Lidar, Meteosat and ECMWF Data, *Bull. Am. Meteorol. Soc.*, *80*, 1045–1074, doi:10.1175/1520-0477(1999)080<1045:VOTSDP>2.0.CO;2.

Kaufman, Y. J., D. Tanré, O. Dubovik, A. Karneili, and L. A. Remer (2001), Absorption of sunlight by dust as inferred from satellite and ground-based remote sensing, *Geophys. Res. Lett.*, *28*(8), 1479–1482.

Lafon, S., I. N. Sokolik, J. L. Rajot, S. Caquineau, and A. Gaudichet (2006), Characterization of iron oxides in mineral dust aerosols: Implications for light absorption, *J. Geophys. Res.*, *111*, D21207, doi:10.1029/2005JD007016.

Li-Jones, X., H. B. Maring, and J. M. Prospero (1998), Effects of relative humidity on light scattering by mineral dust aerosol as measured in the marine boundary layer over the tropical Atlantic Ocean, *J. Geophys. Res.*, *103*(D23), 31,113–31,121, doi:10.1029/98JD01800.

Magi, B. I., and P. V. Hobbs (2003), Effects of humidity on aerosols in southern Africa during the biomass burning season, *J. Geophys. Res.*, *108*(D13), 8495, doi:10.1029/2002JD002144.

Mason, B. (1966), *Principles of Geochemistry*, 3rd ed., John Wiley, Hoboken, N. J.

McNaughton, C. S., et al. (2007), Results from the DC-8 inlet Characterisation Experiment (DICE): Airborne versus surface sampling of mineral dust and sea salt aerosols, *Aerosol Sci. Technol.*, *41*(2), 136–159, doi:10.1080/02786820601118406.

Middleton, D. R., A. R. Jones, A. L. Redington, D. J. Thomson, R. S. Sokhi, L. Luhana, and B. E. A. Fisher (2008), Lagrangian modelling of plume chemistry for secondary pollutants in large industrial plumes, *Atmos. Environ.*, *42*, 415–427, doi:10.1016/j.atmosenv.2007.09.056.

Osborne, S., B. Johnson, J. Haywood, C. McConnell, A. J. Baran, and M. A. J. Harrison (2008), Physical and optical properties of mineral dust aerosol during the Dust and Biomass Experiment (DABEX), *J. Geophys. Res.*, doi:10.1029/2007JD009551, in press.

Prospero, J. M. (1999), Long-term measurements of the transport of African mineral dust to the southeastern United States: Implications for regional air quality, *J. Geophys. Res.*, *104*(D13), 15,917–15,927.

Redelsperger, J.-L., C. D. Thorncroft, A. Diedhiou, T. Lebel, D. J. Parker, and J. Polcher (2006), African monsoon multidisciplinary analysis: An international research project and field campaign, *Bull. Am. Meteorol. Soc.*, *87*(12), 1739–1746, doi:10.1175/BAMS-87-12-1739.

Reid, J. S., et al. (2003), Analysis of measurements of Saharan dust by airborne and ground-based remote sensing methods during the Puerto Rico Dust Experiment (PRIDE), *J. Geophys. Res.*, *108*(D19), 8586, doi:10.1029/2002JD002493.

Richardson, M. S., et al. (2007), Measurements of heterogeneous ice nuclei in the western United States in springtime and their relation to aerosol characteristics, *J. Geophys. Res.*, *112*, D02209, doi:10.1029/2006JD007500.

Ryall, D. B., and R. H. Maryon (1998), Validation of the UK Met Office's NAME model against the ETEX dataset, *Atmos. Environ.*, *32*, 4265–4276, doi:10.1016/S1352-2310(98)00177-0.

Salisbury, G., J. Williams, V. Gros, S. Bartenbach, X. Xu, H. Fischer, R. Kormann, M. de Reus, and M. Zöllner (2006), Assessing the effect of a Saharan dust storm on oxygenated organic compounds at Izaña, Tenerife (July–August 2002), *J. Geophys. Res.*, *111*, D22303, doi:10.1029/2005JD006840.

Schepanski, K., I. Tegen, B. Laurent, B. Heinold, and A. Macke (2007), A new Saharan dust source activation frequency map derived from MSG-SEVIRI IR-channels, *Geophys. Res. Lett.*, *34*, L18803, doi:10.1029/2007GL030168.

Slingo, A., et al. (2006), Observations of the impact of a major Saharan dust storm on the atmospheric radiation balance, *Geophys. Res. Lett.*, *33*, L24817, doi:10.1029/2006GL027869.

Sokolik, I. N., and O. B. Toon (1999), Incorporation of mineralogical composition into models of the radiative properties of mineral aerosol from UV to IR wavelengths, *J. Geophys. Res.*, *104*, 9423–9444, doi:10.1029/1998JD200048.

Tegen, I., and I. Fung (1995), Contribution to the atmospheric mineral aerosol load from land surface modifications, *J. Geophys. Res.*, *100*, 18,707–18,726, doi:10.1029/95JD02051.

Tegen, I., M. Werner, S. P. Harrison, and K. E. Kohfeld (2004), Relative importance of climate and land use in determining present and future global soil dust emission, *Geophys. Res. Lett.*, *31*, L05105, doi:10.1029/2003GL019216.

Todd, M. C., R. Washington, M. Vanderlei, O. Dubovik, G. Lizcano, S. M'Bainayel, and S. Engelstaedter (2007), Mineral dust emission from the Bodélé Depression, northern Chad, during BoDEx 2005, *J. Geophys. Res.*, *112*, D06207, doi:10.1029/2006JD007170.

Washington, R., and M. C. Todd (2005), Atmospheric controls on mineral dust emission from the Bodélé Depression, Chad: The role of the low level jet, *Geophys. Res. Lett.*, *32*, L17701, doi:10.1029/2005GL023597.

Washington, R., M. Todd, N. J. Middleton, and A. S. Goudie (2003), Dust-storm source areas determined by the Total Ozone Monitoring Spectrometer and surface observations, *Ann. Assoc. Am. Geogr.*, *93*, 297–313, doi:10.1111/1467-8306.9302003.

Webster, H. N., E. B. Carroll, A. R. Jones, A. J. Manning, and D. J. Thomson (2007), The Buncefield oil depot incident: A discussion of the meteorology, *Weather*, *62*(12), 325–330, doi:10.1002/wea.164.

Witham, C., and A. Manning (2007), Impacts of Russian biomass burning on UK air quality, *Atmos. Environ.*, *41*(37), 8075–8090, doi:10.1016/j.atmosenv.2007.06.058.

Woodward, S. (2001), Modeling the atmospheric life cycle and radiative impact of Mineral dust in the Hadley Centre Climate Model, *J. Geophys. Res.*, *106*(D16), 18,155–18,166, doi:10.1029/2000JD900795.

Yoshioka, M., N. Mahowald, J.-L. Dufresne, and C. Luo (2005), Simulation of absorbing aerosol indices for African dust, *J. Geophys. Res.*, *110*, D18S17, doi:10.1029/2004JD005276.

Zhu, A., V. Ramanathan, F. Li, and D. Kim (2007), Dust plumes over the Pacific, Indian, and Atlantic oceans: Climatology and radiative impact, *J. Geophys. Res.*, *112*, D16208, doi:10.1029/2007JD008427.

B. Anderson and G. Chen, NASA Langley Research Center, Hampton, VA 23681, USA.

H. Coe, School of Earth, Atmosphere and Environmental Science, University of Manchester, Manchester M13 9PL, UK.

K. Desboeufs and P. Formenti, LISA, CNRS, Universités Paris 12 et Paris 7, 61 Avenue du Général de Gaulle, F-94010 Créteil, France.

M. A. J. Harrison and S. Osborne, Met Office, Exeter EX1 3PB, UK.

E. J. Highwood and C. L. McConnell, Department of Meteorology, University of Reading, Reading RG6 6BB, UK. (c.l.mcconnell@reading.ac.uk)

S. Nava, National Institute of Nuclear Physics, I-50019 Florence, Italy.

Appendix B

List of Abbreviations

AEJ	African Easterly Jet
aer	Aerosol present
AERONET	Aerosol Robotic Network
AEW	African Easterly Wave
AI	Aerosol Index
AM	Accumulation Mode
AMF	ARM Mobile Facility
AMS	Aerosol Mass Spectrometer Probe
AMMA	African Monsoon Multidisciplinary Analyses
AOD	Aerosol Optical Depth
ARE	Aerosol Radiative Effect
ARM Program	Atmospheric Radiation Measurement Program
AVHRR	Advanced very high resolution imaging spectrometer
BADC	British Atmospheric Data Centre
BODEX	Bodélé Depression Experiment
BSRN	Baseline Surface Radiation Network
CALIOP	Cloud-Aerosol Lidar with Orthogonal Polarization
CALIPSO	Cloud-Aerosol Lidar and Infrared Pathfinder Satellite Observation
CAMM	Crisis Area Mesoscale Model
clr	clear skies (no aerosol present)
CDP	Cloud Droplet Probe
CM	Coarse Mode
DABEX	Dust and Biomass Burning Experiment
DMS	Dimethyl sulphate
DODO	Dust Outflow and Deposition to the Ocean
ECLATS	Etudes Climatiques dans l'Atlantique Tropical
ECMWF	European Centre for Medium Range Weather Forecasting
ERA	ECMWF ReAnalyses
ES96	Edwards and Slingo Radiative Transfer Code
FAAM	Facility for Atmospheric Airborne Measurements
FL	Flight Level
GATE	GARP Atlantic Tropical Experiment
IPCC	International Panel on Climate Change
ITCZ	Intertropical Convergence Zone
MCS	Mesoscale Convective System
MINATROC Project	Mineral dust aerosol tropospheric chemistry project
MODIS	Moderate resolution imaging spectrometer
MSG	Meteosat Second Generation
NAME	(Met Office) Numerical Atmospheric-dispersion Modelling Environment
NAMMA	NASA AMMA
OMI	Ozone Monitoring Instrument
PCASP	Passive Cavity Aerosol Spectrometer Probe
PIXE	Particle Induced X-ray Emission
PSAP	Particle Soot Absorption Photometer
PSP	Precision Spectral Pyranometer

RE	Radiative Efficiency
SAL	Saharan Air Layer
SAMUM	Saharan Mineral Dust Experiment
SeaWIFS	Sea-viewing Wide Field-of-view Sensor
SEM	Scanning Electron Microscope
SEVIRI	Spinning Enhanced Visible and Infrared Imager
SFC	Surface of the Earth
SHADE	Saharan Dust Experiment
SWU	Shortwave Upwelling Irradiance
SWD	Shortwave Downwelling Irradianc
TEM	Transmission Electron Microscope
TOA	Top of Atmosphere
TOMS	Total Ozone Monitoring Instrument
WCP	World Climate Program

Appendix C

List of Symbols and Units

α_s	Surface Albedo
$\dot{A}$	Angstrom exponent, no units
β	Angle between solar zenith angle and normal to a pyranometer, degrees
C_{ext}, C_{scat}, C_{abs}	Single-particle extinction, scattering and absorption cross section, m^2
dN/dr	Size distribution measurement: number of particles per cubic centimetre in the size interval r to $r + dr$, $cm^{-3}m^{-1}$
dp	pitch of pyranometer relative to aircraft inertial navigation system, degrees
dr	roll of pyranometer relative to aircraft inertial navigation system, degrees
dp_ac	pitch of aircraft, degrees
dr_ac	roll of aircraft, degrees
dp_{tot}	total pitch of pyranometer from the horizontal, degrees
dr_{tot}	total roll of pyranometer from the horizontal, degrees
$FDIR$	Ratio of direct downwelling irradiance to total downwelling irradiance, no units
g	Asymmetry parameter, no units
I	Irradiance, Wm^{-2}
I_{diff}	Diffuse downwelling irradiance, Wm^{-2}
I_{dir}	Direct downwelling irradiance, Wm^{-2}
I_{tot}	Total downwelling irradiance, Wm^{-2}
k_{ext}^{λ}	Mass specific extinction at wavelength λ, m^2g^{-1}
MMR	Mass mixing ratio, kg/kg
N	Number of particles per cubic metre, m^{-3}
n_i^{λ}	Imaginary part of the refractive index at wavelength λ, no units
n_r^{λ}	Real part of the refractive index at wavelength λ, no units
N_{tot}	See N
ω_0^{λ}	Single scattering albedo at wavelength λ, no units
P	Phase function, sr^{-1}
r	Particle radius
ρ_{aer}	density of an aerosol particle, m^{-3}
ρ_{air}	Density of air, kgm^{-3}
r_{eff}	Effective Radius, m
r_g	Geometric median radius in a lognormal size distribution, m
rel_hdg	relative heading (solar azimuth minus aircraft heading), degrees
σ_{ext}	Extinction coefficient, m^{-1}
σ_g	Geometric standard deviation in a lognormal size distribution, no units
τ^{λ}	Aerosol optical depth at wavelength λ, no units
θ	Solar zenith angle, or scattering angle, in degrees or radians
vf	Volume Fraction - volume of dust per cubic metre air, no units
z	Altitude, m